Grain Boundary Segregation of P and its Interaction with Cr and Mo in Ni-base Alloys

BY

JINSEN TIAN

A thesis submitted to the University of Birmingham for the degree of

DOCTOR OF PHILOSOPHY

School of Metallurgy and Materials

College of Engineering and Physical Science

University of Birmingham

February 2019

Preface

This research was carried out by Jinsen Tian in School of Metallurgy and Materials, University of Birmingham (from October 2014 to October 2018), under the supervision of Dr. Yu-Lung Chiu and Prof. Ian Jones.

The present work is original and no part of the work has been submitted for another degree at any other university. Wherever other researchers' work has been drawn from or cited, it is acknowledged in the text and the references are listed.

Acknowledgements

I am grateful for a Li Siguang PhD scholarship jointly awarded by the China Scholarship Council and the University of Birmingham.

I want to thank my supervisors Prof. Ian Jones and Dr. Yu-Lung Chiu for their guidance and encouragement throughout the project. I benefit quite a lot from discussions with them and their comments and advices.

Special thanks are to Dr. Rengen Ding for his help both in the thesis and in daily life. Trainings and help from Paul Stanley, Theresa Morris, David Price, Andy Bradshaw, Geoff Sutton and Tim Perry are also acknowledged.

Group members, Dr Yu Lu, Dr Bo Pang, Dr Jing Wu, Dr Gnanavel Thirunavukkarasu, Dr Leifeng Liu, Dr Mingshi Wang, Dr Xinyu Lyu, Ryan Ameen, Zhaoran Liu, Daniel Higgins, Gareth Douglas, Subash Rai, Siben Jiang, Ubaid-Ur-Rehman Ghori, Shanshan Si, Yang Lyu, Mark Elliot, Jianbing Zhang, Peng Lin and Wanqi Chen, are acknowledged for their help and tolerance. I also want to thank my friends Yuan Cao, Qingbin Liu, Qi Wei, Yulin Ju et al.. It is like a family being here with them.

Finally, I want to thank my families for their support and understanding.

Abstract

The behaviour of phosphorus (P) segregation to grain boundary during cooling and aging and its interaction with chromium (Cr) and molybdenum (Mo) in Ni-base alloys have been investigated using transmission electron microscopy.

P segregation takes place during cooling and aging. The segregation width was several nanometres, much wider than the grain boundary thickness. This indicated a non-equilibrium mechanism. The effect of grain boundary misorientation angle and grain size on the segregation level has been investigated. The grain boundary P concentration increased with increasing misorientation angle until about 45°. A further increase in the grain boundary misorientaion angle resulted in a decline of the segregation level. Compared with random high angle grain boundaries, special grain boundaries displayed much lower segregation. This can be related to the free volume dependence on the misorientation angle. When the effective time during cooling is shorter than a certain critical time, increasing grain size reduced the grain boundary segregation level because of the higher mass transfer coefficient close to the grain boundary in samples with smaller grain size.

Segregation level during cooling at different rates and after aging for different times was obtained. A critical cooling rate and aging time existed where the grain boundary P concentration reached a maximum, indicating a non-equilibrium segregation pattern. Calculations based on Faulkner's [1, 2] and Xu's [3] and Wu's [4] theory were conducted and compared with the experimental results. As regard the effect of grain size, the results based on Wu's theory were consistent with our experimental results.

The elemental interaction between P and Cr or Mo was investigated. On samples without P addition, no segregation of Cr and Mo was observed after cooling and aging due to the low

binding energy between vacancies and Cr or Mo. With P addition, P segregated to the grain boundary while Cr and Mo were depleted at the grain boundary. With increasing P concentration, the grain boundary Cr and Mo concentrations decreased in a linear manner due to the repulsive relative interaction coefficient between P and Cr or Mo in Ni-base alloys.

List of figures

List of tables

Contents

Chapter 1. Introduction

Ni-based superalloys have been widely used in the aerospace industry due to their excellent properties, such as high strength, creep rupture life and oxidation resistance, especially at high temperature [5]. Impurities, such as P and S, are detrimental to the mechanical properties even at a very low concentration due to grain boundary segregation [6, 7]. Recently, however, some evidence has shown that P can be beneficial to the stress rupture properties while keeping the tensile properties unaffected, especially for the wrought superalloys [8-11]. The proposed mechanisms are also related to the segregation of P [8, 12-15]. Since both detrimental and beneficial effects of P on the mechanical properties can be attributed to the segregation, this indicates the importance of grain boundary segregation.

Grain boundary segregation can be divided into equilibrium segregation (ES) and non-equilibrium segregation (NES). ES thermodynamics and kinetics are well understood [16]. Factors such as solubility, temperature, grain size, and misorientation have been discussed [17]. Among these factors, grain size and misorientation have been a hot topic as they are the key parameters of grain boundary engineering [18]. By controlling the grain size and misorientation, the mechanical properties can be modified. However, the effect of grain size and misorientation angle on NES was seldom reported considering their importance.

It has been reported that the effect of P on mechanical properties also depends on the P concentration [8]. An optimised P concentration leads to a maximum stress rupture life [8]. Investigation of the kinetics during cooling or aging enables a better understanding of the segregation mechanism and can be used to control the segregation level and thus to optimise the mechanical properties by heat treatment.

Commercial superalloys are complex systems with more than ten different alloying elements or significant impurities. In such a system, elemental interaction is an important factor influencing the segregation level. The interaction between P and Cr or Mo has been reported in both steels and Ni-base alloys [19-22]. However, all the alloys studied contain C, B or N, which also interacts with Cr and Mo. It was impossible to isolate the interaction between P and Cr or Mo.

The aim of this thesis is to investigate the NES kinetics during cooling and aging in simplified model Ni-base alloys and the effect of grain size, misorientation angle and elemental interaction on the segregation level.

Chapter 2 contains the literature review. Previous work, such as the effect of P on the mechanical properties, ES and NES theories, factors influencing the segregation level, elemental interaction and methods to measure the segregation are outlined.

The experimental procedure of alloy preparation, heat treatment and microscopy is reported in Chapter 3.

Chapter 4 describes the grain boundary and triple junction segregation of P in Ni-Al-P alloy during cooling and subsequent aging. The effect of grain size and misorientation angle, cooling rate and aging time on the segregation level is discussed in detail. Calculations based on Faulkner's [1, 2] and Xu's [3] and Wu's [4] theory were carried out and the results compared with the experimentally obtained results.

Chapter 5 focusses on the segregation behaviour of Cr and Mo in samples with and without P. Possible mechanisms of Cr and Mo segregation including equilibrium segregation, non-equilibrium segregation and elemental interactions are discussed. Interactions between P and Cr or Mo are assessed by calculating the relative interaction coefficient and compared with previous results.

The effect of experimental parameters, such as probe size, acquisition time and specimen thickness on the chemical analysis using EDS are discussed in Chapter 6. An optimised condition is proposed.

The main conclusions of this work together with suggestions for future work are summarized in Chapter 7.

Chapter 2. Literature Review

2.1 Effect of P on mechanical properties

Ni-based superalloys have been widely used for aircraft gas turbines and electricity power plant due to their excellent mechanical properties, such as high strength, stress rupture life and oxidation and corrosion resistance, especially at high temperature [5].

P, just like S, has been regarded as a detrimental impurity and is strictly limited in conventional cast Ni-base superalloys [6, 7]. With increasing P concentration from 0.0008 wt% to 0.032 wt%, tensile strength and ductility of cast alloy 718 at room temperature and 650 °C as well as the stress rupture life at 650 °C/620 MPa all decrease (figure 2.1) [7].

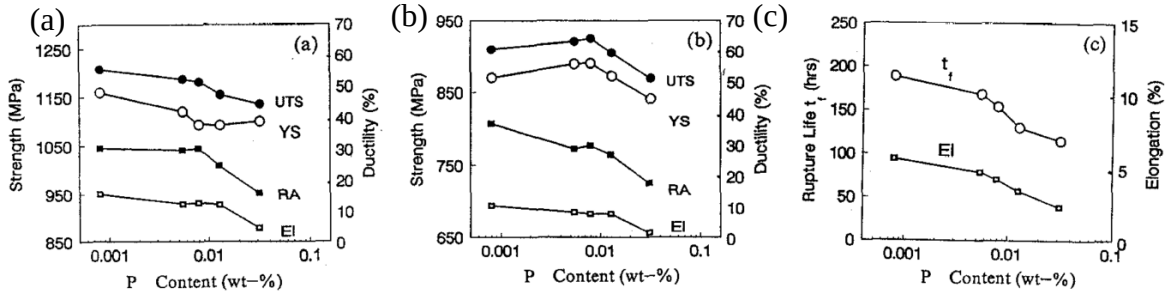

Figure 2.1 Effect of P content on the tensile and stress rupture properties of cast alloy 718 (a) at room temperature (b) at 650 °C (c) at 650 °C/620 MPa [7]

Generally, the mechanism of the deleterious effect of P can be outlined as below. First, P segregates strongly to GB as its solubility in the superalloy matrix is extremely low, resulting in a decline of the cohesion strength at the GB. This phenomenon has been explained by Seah by considering both the difference in sublimation heat and the bond length between nearest neighbours using first-principles calculation [23]. This is inconsistent with the molecular dynamics simulation that P increases grain boundary cohesion [24, 25]. Simulation by first principles of a tensile test indicated that the effect of P on the grain boundary strength depended

on the grain boundary concentration. With an optimum concentration, the strength can be as strong as that of a clean grain boundary [26]. Second, the segregation of P may result in the formation of a low melting point eutectic such as Ni-Ni_3P or promote the precipitation of a harmful phase [27].

However, the effect of P was complicated in wrought Ni-base superalloys. The mechanisms mentioned above can also be applied to wrought superalloys. The detrimental effect of P does exist and has been demonstrated by experiments, for example the strong segregation to the GB [28, 29], the promotion of harmful Laves phase [30, 31], the deterioration of the interfacial cohesion of the intergranular β-NiAl and γ matrix [32] and the increase in segregation of other alloying elements [33]. On the other hand, experimental evidence for the beneficial effects of P have increasingly been found in wrought Ni-base superalloys over recent years [34]. Addition of P up to 130 ppm had almost no influence on tensile strength and ductility at room temperature and 650 °C, while it improved both stress rupture life and ductility at 650 °C of γ′′ strengthened Inconel 718 [8, 35]. This was consistent with Cao et al. [13, 36] with a P content less than 220 ppm, Wang et al. with a P content less than 190 ppm [10], Xie et al. [37] and Sun et al. [8] with P contents less than 130 ppm and Song et al. [38] with P contents of 30 and 200 ppm. One example is shown in figure 2.2 [10]. The effect was quite similar in γ′ strengthened wrought superalloys GH761 and IN706 even though the microstructures of these two alloys were different from that of IN718 [9, 12, 14, 33, 35, 39].

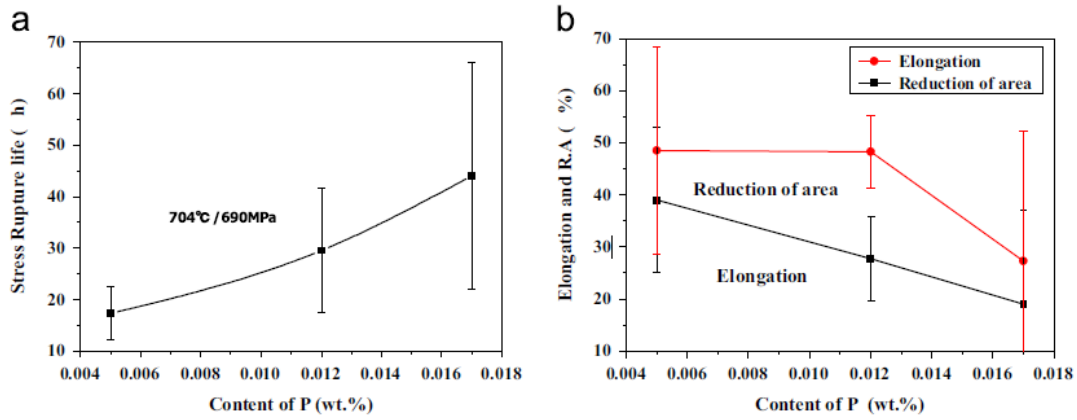

Figure 2.2 (a) The stress rupture life and (b) elongation and reduction of area of 718Plus alloy with different P contents [10].

Some experiments have been carried out to reveal the mechanism of the effect of P on mechanical properties and several have been proposed for both γ′ and γ′′ strengthened wrought superalloy. P addition retarded the movement of dislocations and decreased the creep rate [7, 9]. P segregation reduced the GB energy [26], and thus the critical nucleation radius of GB precipitates. This promoted the nucleation of GB precipitates, such as carbides and δ phase. Small round and evenly distributed precipitates can relieve the stress concentration and strengthen the GBs [8, 11, 12]. However, other results indicated that the size and quantity of GB precipitates did not vary with P concentration [13]. The main mechanism was considered to be the interaction between P and B. Both P and B increased the GB cohesion and co-segregation of P-B further increased the GB strength [13]. This is inconsistent with the calculations [23, 26]. Due to site competition, P segregation inhibited the segregation and diffusion of oxygen at the GB, thus improving the oxidation resistance and creep elongation [14, 15]. However, this contradicts the results in [11] which showed that elongation is not affected by P content.

Although much research has been carried out, the mechanism of the effect of P on mechanical properties is arguable and alloy specific up to now. Notwithstanding this, most of the

mechanisms, such as the morphological optimization of the grain boundary precipitates [8, 12], the synergistic effect with B [13] and the effect on intergranular oxidation [14, 15] relate to the grain boundary segregation of P. A knowledge of grain boundary segregation is therefore essential for a deep understanding of the effects of P on nickel-based alloys.

2.2 GB structure and properties

GB is a thin area (several atomic layers [40]) where two adjacent grains with different orientation join together. The typical characteristics of a GB is an irregular atomic configuration (including compression sites and expansion sites), a lower coordination number and a higher energy than the insides of the grain.

2.2.1 Types of GB

To describe a GB, five independent parameters (macroscopic degrees of freedom, DOFs) are needed [41]. A rotation axis $\boldsymbol{o}$ (2 DOFs) and rotation angle θ (1 DOF) are used to specify the misorientation of the mutual grains, while the normal $\boldsymbol{n}$ to the GB plane (2 DOFs) is used to describe its specific orientation. Besides these five DOFs, three other microscopic parameters represented by a vector T exist to describe the rigid translation of both grains relative to each other, parallel (2 parameters) or perpendicular (one parameter) to the GB. However, these three parameters are controlled by energetic factors and cannot be chosen in an arbitrary way. According to the rotation angle or misorientation, GBs can be divided into small angle GBs ($\theta<15^{\circ}$) and large angle GBs ($\theta>15^{\circ}$) [42]. Based on the relationship between $\boldsymbol{n}$ and $\boldsymbol{o}$, GBs can be divided into tilt GBs ($\boldsymbol{o}\perp\boldsymbol{n}$) and twist GBs ($\boldsymbol{o}//\boldsymbol{n}$) or mixed (in other cases). Also, if the adjacent grains are mirror symmetrical, the GB is called symmetrical, otherwise asymmetrical. This kind of categorization is simplified. Due to the symmetry of the lattice, the same GB can be described in several different ways.

Small angle GBs can be described as dislocation arrays when the misorientation angle is small, as it can be accommodated by an array of dislocations [43, 44]. It can be divided into tilt GBs and twist GBs, the former composed of edge dislocations and the latter of screw dislocations.

Compared with small angle GBs, large angle GBs are much more complex. There are several models to describe large angle GBs, among which the coincidence site lattice (CSL) is most commonly used. When tilting or twisting to a specific angle, a plane crossing the GB from one grain to the other exists. Namely, some sites in the GB coincide with the ideal atomic sites in both grains and are called the CSL. They form another lattice whose unit cell is bigger than the original lattice. The ratio of the primitive cell volume of the CSL to that of crystal lattice, Σ, is used to characterize the CSL. In cubic lattices, Σ can be simply derived from the GB normal [45]

$$\Sigma = \delta(h^2 + k^2 + l^2) \qquad 2.1$$

where $\delta=1$ if $h^2 + k^2 + l^2$ is odd and $\delta =1/2$ if $h^2 + k^2 + l^2$ is even because in cubic systems, whenever an even number is obtained, there is a coincidence lattice site in the centre of the cell which then means that the true area ratio is half of the apparent quantity.

GBs with low Σ contain a high density of coincidence sites and can be regarded as special GBs or CSL GBs. These GBs have lower free energy and hence have a higher possibility to exist from the energy point of view. This is consistent with experimental data.

Problems arise when the tilt angle deviates from the exact value needed to form a CSL GB because a small deviation results in a dramatic change in coincidence and consequently a change of Σ. To compensate, secondary GB dislocations are introduced. Then the characterization as a CSL GB can be conserved even with a small angle of deviation. The maximum deviation is empirically calculated by

$$\nu_{m=\frac{\nu_0}{\Sigma^{\xi}}} \quad 2.2$$

where ν_0=15° is commonly used. ξ is a constant and 1/2 is used by the most commonly adopted criterion proposed by Brandon[46]. Other values such as 1 [47] and 2/3 [48] are also used by other authors.

As will be shown in the next part, GB misorientation has an effect on the GB segregation. A precise determination of the GB misorientation should be done at the same time as measuring the GB segregation. Jang [49] has proposed a detailed method using the electron diffraction in a TEM to determine the grain orientation, including the Σ value, misorientation and the normal to the GB plane. The basic procedure is firstly to determine precisely the orientation of each grain, followed by the determination of GB misorientation. In this project, this method will be used.

2.2.2 GB energy

By applying the dislocation model proposed by Read and Shockley [50], the GB energy can be calculated exactly as the total energy of all the dislocations in the GB. For tilt GBs, it has been shown that the energy of a dislocation of unit length can be expressed by

$$E_d = \frac{\mu b^2}{4\pi(1-\nu)} ln\frac{D}{r_0} + E_c \quad 2.3$$

where ν is the Poisson ratio, μ the shear modulus, D the dislocation spacing, $r_0 \approx b$ the magnitude of the Burgers vector, and E_c the energy of the dislocation core. According to Read and Shockley [50], the limiting distance of the dislocation stress field is about D. So the dislocation density of unit GB length can be approximated to 1/D. The GB free energy with a misorientation of θ can then be expressed as

$$\sigma = \frac{\theta}{|b|}\left[\frac{\mu b^2}{4\pi(1-\nu)} ln\frac{1}{\theta} + E_c\right] = \theta(A - Bln\theta) \qquad 2.4$$

where $A=E_c/|\boldsymbol{b}|$ and $B=\mu|\boldsymbol{b}|/4\pi(1-\nu)$ [50]. This model has been verified by experiment. It should be noted here that this model can only be applied when θ is small enough. With the increase of θ, the dislocation spacing decreases. When D decreases to an extent that two dislocations are too close and lose their identity, the dislocation model cannot be used anymore. Generally, the transition θ between small-angle and large-angle GB lies roundabout 13-15° [51-53].

Another model was proposed by Sakaguchi [54] using molecular dynamics and statics, the sink strength (GB energy) dependence on the misorientation was calculated and the result indicated that the GB energy increased with misorientation except the CSL GB, where a local minimum was present [54].

2.2.3 GB free volume

The free volume is an interatomic region with low electron density that aids the mobility of neighbouring atoms, enabling GB sliding, grain rotation and GB dislocation emission [52]. It affects the segregation as it serves as the segregation site for the solute. It has been shown that GB free volume depends on the misorientation angle. By atomistic molecular dynamics simulation, GB free volume has been found to increase with misorientation angle until 50°, and then to decrease. The result is shown in figure 2.3 [55]. This is consistent with the results by first-principle calculations [56].

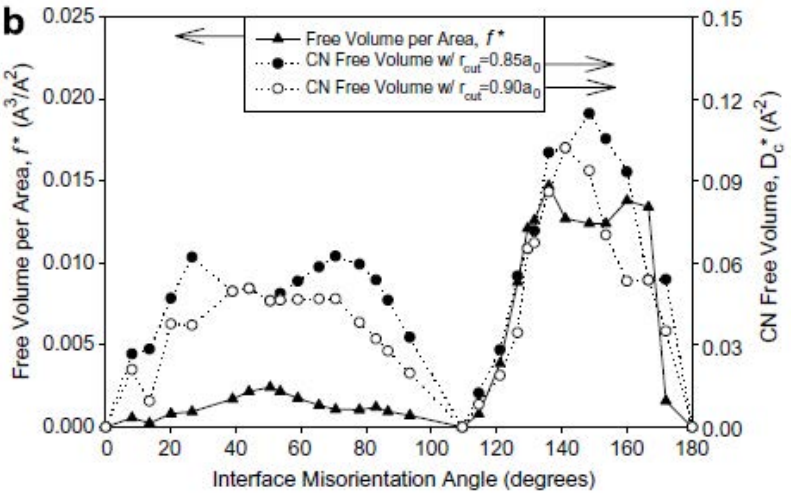

Figure 2.3 Calculated free volume for <110> symmetric tilt GBs. a_0 is the lattice parameter, r_{cut} is the cut off distance and CN means coordination normalized [55].

2.2.4 GB diffusion

Diffusion has been investigated both experimentally and theoretically as it is involved in many processes, such as sintering, segregation and creep. The volume and GB diffusion of Cr in Ni-Cr-Fe alloys was measured using radioactive tracer ^{51}Cr [57]. The GB diffusion coefficient over a temperature range 585-1150 °C is 3-5 orders of magnitude higher than that in the lattice and the ratio decreases with temperature. Similar results have also been reported for Zn in Al [58]. The GB diffusion coefficient is misorientation dependent. Using molecular dynamics and statics, the vacancy diffusion activation energy along CSL boundaries was calculated [59]. It was found that the activation energies were different for different boundaries. This is consistent with the experimental results in Al bicrystals (figure 2.4) [60, 61].

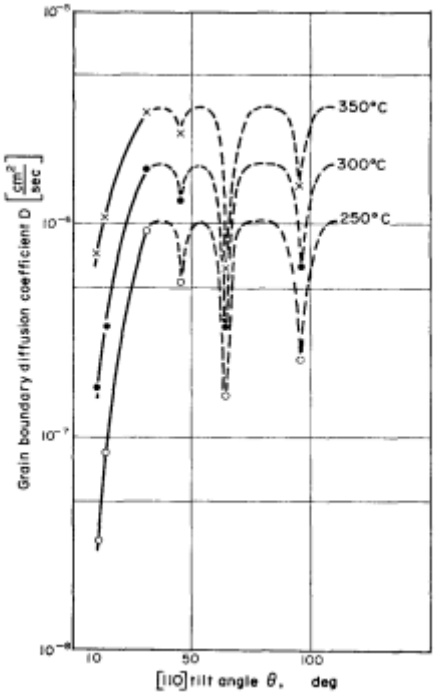

Figure 2.4 GB diffusion coefficient along [110] tilt boundaries in Al as a function of the tilt angle [60].

The different structures in the GB and the grain interior affect the GB segregation by supplying sites for the solute atoms or by acting as a defect sink.

2.3 Equilibrium segregation (ES)

The thermodynamics and isothermal kinetics theory of ES were first set up by McLean [16] and then developed by Guttmann [62]. Ogura [63] further developed the theory to calculate the segregation level during non-isothermal processes such as cooling.

2.3.1 Mechanism

It has been stated in section 2.2 that a GB is composed of an irregular atomic configuration including compression and expansion sites. So, solute atoms or impurities occupying the GB sites raise the system free energy less than those in the grain interior. The energy difference ΔG, the segregation free energy, acts as the force driving the solutes to diffuse to the GB.

The diffusion mechanisms for interstitial and substitutional atoms are different. Interstitial atoms are free to move to any adjacent interstice. So, the diffusion coefficient is controlled by how easily an interstitial atom can move to the adjacent interstice. Substitutional atoms diffuse via a position swap with a vacancy. Therefore, the diffusion coefficient is controlled by the ease with which a vacancy can form and the atom exchange with the vacancy. Normally the coefficient of interstitial diffusion is higher than that of substitutional diffusion. It has been confirmed that Al, Cr and Mo are substitutional, while B, C, O and N are interstitial in Ni [64]. Based on the assumption that P occupies a substitutional site, the segregation energy has been calculated and the result is consistent with the experimental results [26, 65]. By calculating the energy change when the solute elements take the substitutional or interstitial sites using first-principle calculations, it is found that P prefers the substitutional site [64]. Also, the relaxation volume when the solute atom is introduced to the lattice has been evaluated. A slight decrease (about 0.1%) of the volume is expected if P is located at the substitutional site, while a 0.7% or 1% increase would be expected with P atoms taking the tetrahedral or octahedral interstitial sites, respectively [64]. XRD results show that the lattice parameter of the γ phase in IN706 alloy decreases from 0.35988nm to 0.35953nm with P content increasing from 0.002% to 0.025%, indicating that P occupies substitutional sites [39]. P introduced lattice parameter reduction has also been observed by XRD in austenitic iron, which has a very similar structure to that of Ni [66]. The diffusion coefficients of several elements at 700 ºC are listed in table 2.1 [67, 68]. Ni, Al, Cr, Mo and P diffuse much more slowly than C, indicating that Al, Cr, Mo and P are substitutional while C is interstitial. This is consistent with [64].

Table 2.1 Diffusion coefficients of Ni, Al, Cr, C, P and S in Ni [67, 68].

Elements	Ni	Al	Cr	C	P	S

D (700ºC)(m^2/s)	$1.20*10^{-19}$	$1.20*10^{-18}$	$2.55*10^{-19}$	$5.11*10^{-13}$	$6.14*10^{-18}$	$2.45*10^{-16}$

2.3.2 Thermodynamics.

Based on statistical mechanics, McLean [16] proposed an expression to describe the ES. As this is expressed in the form of a Langmuir absorption isotherm [69], the expression is often called the Langmuir-McLean equation. The equilibrium concentration of the segregant at the GB can be written as (see Appendix equation A8)

$$\frac{C_{gb}^{m}}{1-C_{gb}^{m}} = \frac{C_0}{1-C_0}\exp\left(-\frac{\Delta G}{RT}\right) \qquad 2.5$$

where C_{gb}^{m} is the equilibrium concentration at the GB, C_0 the concentration inside the grain and ΔG the segregation free energy. Guttmann [62] modified McLean's model by considering the interaction between solute atoms and impurities and assuming that the same area was occupied by all of the elements. For a multicomponent system with a limited number of segregation sites, the segregation equation can be expressed as

$$\frac{C_I^{\emptyset}}{C^{0\emptyset}-\sum_{J\neq M}^{M} C_J^{\emptyset}} = \frac{C_I}{1-\sum_{J\neq M}^{M} C_J}\, exp(-\Delta G_I/RT) \qquad 2.6$$

where M is the solvent, I and J are two of the solute atoms, $C_I^{\emptyset}$ and C_I are the concentrations of solute I at the GB and inside the grain and $C^{0\emptyset}$ the fraction of the total available sites. The segregation free energy ΔG_I is given by (see Appendix equation A56)

$$\Delta G_I = \Delta G_I^0 - \alpha_{IM}^{M}\left(1-2X_I^{\emptyset}\right) + \sum\nolimits_{J\neq I} \alpha'_{IJ} X_J^{\emptyset} \qquad 2.7$$

Where ΔG_I^0 is the segregation energy of I without interaction with M, α_{IM}^M is the binary I-M interaction coefficient in M, α_{IJ}' is the relative interaction between I and J and can be calculated as (see Appendix equation A57)

$$\alpha_{IJ}' = \alpha_{IJ} - \alpha_{IM} - \alpha_{JM} \qquad 2.8$$

2.3.3 Kinetics

To obtain equilibrium segregation, a long enough time is needed, which is not easy to reach under practical conditions. So, the kinetics are analysed and often used. As it is a process of diffusion, the dependence on time is controlled by the diffusivity of the solute atoms or of the impurities in the matrix. McLean [16] analysed the kinetics by using Fick's Law to describe the diffusion. The diffusion process can be simplified as diffusion in two half-infinite crystals with uniform solute contents. The segregation equation can be expressed as (see Appendix equation A18)

$$\frac{C_{gb}(t) - C_{gb}(0)}{C_{gb}(\infty) - C_{gb}(0)} = 1 - exp\left(\frac{4Dt}{\alpha^2\theta^2}\right) \text{erfc}\left(\frac{2\sqrt{Dt}}{\alpha\theta}\right) \qquad 2.9$$

where $C_{gb}(t)$ is the GB content after time t, $C_{gb}(0)$ is the GB concentration at t=0, $C_{gb}(\infty)$ is the equilibrium content at GB, D is the diffusivity of solute in the matrix, θ is the thickness of the GB and α is given by $\frac{C_{gb}(\infty)}{C_0}$ with C_0 the concentration in the bulk sample. The character of the kinetics is that with the increase of time, the GB concentration increases monotonically until it reaches the equilibrium level.

2.3.4 Important factors in ES

There has been much research concerning the effect of various factors on ES:

(a) Temperature. It has been shown thermodynamically that with an increase of temperature, the equilibrium concentration at the GB decreases. Kinetically, though the expression does not

explicitly contain a temperature term, temperature does affect the segregation kinetics by its effect on diffusivity. When the temperature is too low, a high segregation concentration is expected, but the low temperature results in slow diffusion and thus a longer time to achieve equilibrium. Practically it is hard to reach the equilibrium state at temperatures below a certain temperature which is dependent on the melting point T_m [17].

(b) Solid solubility. Without considering inter-element interactions, the segregation equation can be simplified to the Langmiur-McLean absorption isotherm with a segregation free energy of [70]

$$\Delta G_I = \Delta H_I^0 - T\Delta S_I^0 = \Delta H_I^* + RTlna_I - T\Delta S_I^0 = \Delta H_I^* + vRTlnX_I^* - T\Delta S_I^0 \qquad 2.10$$

where ΔH_I^* corresponds to the extrapolated segregation enthalpy of a solute with unlimited solubility in the matrix, a_I is the activity of solute I at the solubility limit X_I^* and v is a constant. This simplification has been verified for several systems, especially dilute alloys. Relevant parameters have been measured for Ni-S [71], Ni-In [72] and α-Fe-Si [73]. The results showed that $T|\Delta S_I^0| \ll |\Delta H_I^0|$. Thus neglecting the term $T\Delta S_I^0$, a direct relationship between free energy and solid solubility X_I^* can be deduced as $\Delta G_I = \Delta H_I^* + vRTlnX_I^*$ [70]. A decrease in solubility causes a decrease in free energy, eventually enhancing GB segregation. Ni strongly reduced the solubility of Sb. Clayton and Knott [74] found that in a steel with 200ppm Sb, there is no susceptibility to embrittlement at 520ºC when the Ni content is 0.5%, while the ductile-brittle transition temperature increased dramatically under the same conditions for higher Ni content (2%, 5%).

(c) GB misorientation. As discussed in 2.2, GB misorientation has a close relationship with the GB energy. Also, the energy difference between the GB and the grain interior is the driving force for equilibrium GB segregation. Therefore, a tight dependence of equilibrium GB segregation on the grain orientation is expected. However, little research has been done on this

topic. Powell [75, 76] found that the GB segregation in a Cu-Bi alloy was misorientation dependent and they thought that the anisotropy was caused by the GB structure. However, no quantitative or even qualitative relations were proposed, mainly because polycrystalline samples were used and the mean segregation content of several GBs was obtained. By using α-Fe-Si and α-Fe-Sn bicrystals, Watanabe [77] found that the amount of segregation increased with increasing tilt angle. However, the results were not consistent with those of Hoffmann [78], who obtained scattered data concerning the dependence of GB segregation of P, C and Si on the misorientation angle in [100] symmetrical tilt bicrystals of Fe-Si. The probable reason is the elemental interactions between C, P and Si due to site competition or co-segregation [79-81].

(d) Grain size. The relation between the matrix concentration C_m and the GB concentration C_{gb} of the solute can be described as

$$\mathrm{C}_{gb} f + \mathrm{C}_m(1-f) = \mathrm{C}_0 \qquad 2.11$$

where C_0 is nominal concentration and f is the volume fraction of GB which can be calculated by

$$\mathrm{f} = \frac{\left(\frac{\theta}{2}\right) 4\pi\bar{R}^2}{4/3\pi\bar{R}^3} = 3\theta/2\bar{R} \qquad 2.12$$

where θ is the GB thickness and $\bar{R}$ is the average grain radius. By combining 2.5, 2.11 and 2.12, the GB concentration can be obtained by [82]

$$\frac{\mathrm{C}_{gb}}{1-\mathrm{C}_{gb}} = \frac{\mathrm{C}_0 - \frac{3\theta}{2\bar{R}}\mathrm{C}_{gb}}{1-\mathrm{C}_0}\exp(-\frac{\Delta G}{kT}) \qquad 2.13$$

When $\mathrm{C}_0 \gg \frac{3\theta}{2\bar{R}}\mathrm{C}_{gb}$, the effect of grain size can be neglected. This has been confirmed in a Fe-0.17wt%P alloy. There is essentially no difference in the ES level of P when the grain size is

in the range 10 – 1000 μm [83]. However, the grain size effect is quite remarkable if C_0 and $\frac{3\theta}{2\bar{R}}C_{gb}$ are comparable. GB concentration increases with grain size, especially at low temperature [82]. This has been confirmed by using AES in interstitial-free steel aged at 600 °C and 680 °C and in a 2.25Cr-1Mo steel aged at 520 °C and 560 °C [84]. This is consistent with experimental results which indicated that the Y content at GBs in alumina increased with grain size when the Y content was not high enough to be saturated or to form precipitates [85]. Similar results for Ca and Si have also been reported in ZrO_2 [86].

(e) Elemental interaction. According to Guttmann's model [62], elemental interaction affects GB segregation via its effect on the segregation free energy. A positive value of interaction coefficient or attractive interaction between elements I and J results in a much more negative free energy and therefore increases their tendencies to segregate to the GB. This is called 'co-segregation'. Using AES, Dong [22] found that P segregates to the GB in Ni-base alloy 718 and both Mo and Nb co-segregate to the GB, with their contents increasing with the increase of P content at the GB. When the attractive interaction was strong enough, 2-D interfacial compounds were expected to form, which has been confirmed by Menyhard [87]. On the other hand, inter-elemental repulsion supressed the GB segregation. A strong repulsive interaction between P and Si has been detected in a P doped Fe-Si alloy by Lejcek [81]. In some other cases, there is no interaction between solutes. Even in this case, the segregation of elements can be affected by the others. Because the total number of sites available for the solutes to occupy is limited, the total segregation content should also be limited. Generally, the stronger segregant will remove the weaker segregant from the GB when they compete for the same segregation sites. This is called site competition and was observed for the GB segregation of P and C in Fe [79, 80], and for S and Si in an Fe-Si alloy [88].

ES has been widely used to describe the segregation of impurities and to interpret the mechanical properties of various alloys. Considering both the sublimation enthalpies and atom sizes, Seah [23] proposed a theory to evaluate the effect of various elements on GB cohesion. The result showed that P, S and several other elements decreased the cohesion, causing GB embrittlement, while N, B and C were beneficial to GB cohesion. Using first principles calculations, Briant [89] drew the conclusion that P with strong electronegativity extracted electrons from the surrounding metallic atoms and weakened the metal-metal bonds, resulting in GB fracture. However, it is hard to interpret the intermediate temperature embrittlement of metals and alloys and the reverse temper embrittlement, because some phenomena are contrary to the models. For example, research shows that with increasing aging time at 540 °C, the segregation content of P and the degree of embrittlement in a 12Cr1MoV steel first increased and then decreased [90].

2.4 Non-equilibrium segregation (NES)

Aust [88] found in 1968 that in Zn with 100ppm Al air cooled from 350 °C, there was excess hardening in the GB relative to the grain interior. Two typical characteristics of the hardening were: (a) it increased with increasing solid solution heat treatment temperature; (b) the hardening spread several microns into the grains from the GB. Both of these could not be rationalized by ES. This is called NES. Other research papers [91, 92] have since been published, confirming the existence of NES. Radiation induced segregation (RIS) is another type of NES, which has been observed in steels [93, 94].

2.4.1 Models and mechanism

Both cooling and radiation induce supersaturated vacancies. Solute diffuses to or away from the grain boundary via the diffusion of the vacancy flux. Two possible mechanisms have been proposed based on whether the solute diffuses via solute-vacancy exchange (i.e. inverse Kirkendall effect) or solute-vacancy complexes.

As described in [93], a vacancy gradient between the grain interior and the GB generates a vacancy flux, J_v, towards the GB. A balanced atom flux (J_A+J_B) with equal magnitude is induced away from the GB, where J_A and J_B are the fluxes of elements A and B. If the diffusion coefficients of A and B equal each other, the GB concentration of A and B will not change. Otherwise, the faster diffusion component will be depleted at the GB. According to table 2.1, the diffusion coefficients of P, Al, Cr and Mo are quite close. Also, calculations in dilute Ni alloys indicated that inverse Kirkendall effects are dominant when the binding energy between solute and vacancy is lower than 0.2 eV, while complex diffusion is dominant with a binding energy above 0.2 eV [95]. The binding energy between P and vacancy has been calculated to be ~0.33 eV in Ni by strain field method [96], suggesting that the inverse Kirkendall effect is not the dominant mechanism.

A solute-vacancy complex theory of NES was proposed by Aust [97] and Anthony [98] based on an assumption of local equilibrium between vacancies, solutes and the vacancy-solute complex at a given temperature. Song [99] described theoretically the mechanisms for the complex diffusion for both substitutional and interstitial solutes in fcc and bcc crystals. Based on the diffusion coefficients of the solutes, the activation energy for complex diffusion can be evaluated. Here only substitutional and interstitial solutes in an FCC matrix are shown. There are two possible migration paths for the substitutional atom to diffuse, as shown in figure 2.5. A vacancy is denoted by □, while a solute atom is marked as ●. For the first path (figure 2.5a), the vacancy jumps from site A to site B and then to site C. Finally, the position of the vacancy and solute interchange. Another mechanism involves a vacancy jumping from A to D and C, finally interchanging with the solute. The new position after jumping is shown in figure 2.5c. By both mechanisms, the complexes can diffuse to the GB. During the jumping shown in 2.5a, the distance between the vacancy and solute atom changes from 0.707 a_0 (site A) to 1 a_0 (site B) and then to 0.707 a_0 (site C), where a_0 is the lattice parameter. So partial dissociation and

re-combination of the vacancy-solute complex are required in this process. This is called the dissociation mechanism. The migration energy of the complex is the sum of the vacancy-solute binding energy and the migration energy of the vacancy (the energy for the vacancy to jump to the solvent atom site), or the migration energy of the solute (the energy for the vacancy to jump to the solute atom site). The selection of the former or latter depends on which is larger. For the second mechanism, the distance between vacancy and solute is 0.707 a_0 no matter whether the vacancy takes site A, D or C. This is referred as the non-dissociation mechanism. The migration energy by this mechanism is the larger of the vacancy migration energy or the solute migration energy. Compared with the dissociation mechanism, the non-dissociation mechanism is more energetically favourable as no dissociation and recombination of the vacancy-solute complex is required.

For an interstitial atom, two jump sequences are shown in figure 2.6. The solute atom jumps from site A to site B and then the vacancy jumps from site C to site D. The new position is shown as figure 2.6b. Another sequence has a solute jumping from site A to site B and a vacancy jumping from site C to site E. For both mechanisms, no dissociation or recombination is required. So the migration energy is the larger of the vacancy migration energy and solute migration energy.

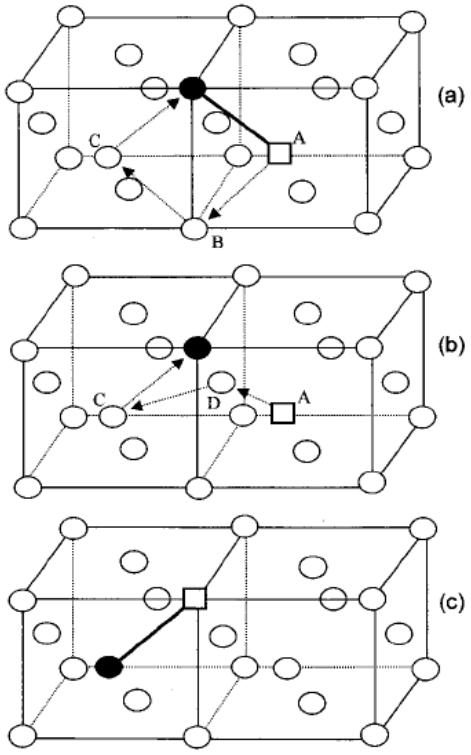

Figure 2.5 Schematic drawings of the migration processes of vacancy–substitutional solute complexes in fcc crystals with (a) dissociation and (b) non-dissociation mechanisms, and (c) the new position of the complex after the vacancy jumps [99].

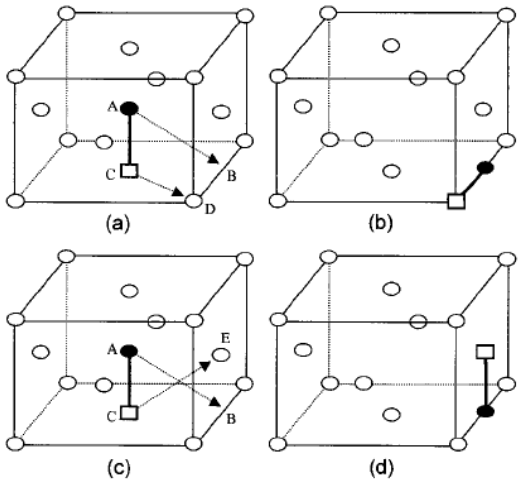

Figure 2.6 Schematic diagrams of the migration processes of vacancy–interstitial solute complexes in fcc crystals via two different ways (a and c); (b) and (d) are the new positions of the complex after the jumps illustrated in (a) and (c), respectively [99].

For interstitial and substitutional solutes, the migration energy can be different. Also, the vacancy jump frequency for each jump of the complex is different. The vacancy jumps three times during the complex diffusion to a new site for a substitutional solute, while only one jump of a vacancy is required for an interstitial solute. This will result in a different pre-exponential factor, and finally a different diffusion coefficient for the complex.

The diffusion coefficient of the complex formed by the substitutional solute P and vacancy can then be calculated as below. The self-diffusion coefficient of Ni can be written as [100]

$$D_{self}^{Ni} = D_0 \exp\left(-\frac{E_A}{kT}\right) = 1.27 \times 10^{-4}\exp(-2.9\ \text{eV/kT})\ m^2 s^{-1} \qquad 2.14$$

where D_0 is a pre-exponential factor which corresponds to the vacancy jump frequency and E_A is the diffusion activation energy. According to [101], E_A is the sum of the vacancy formation energy (E_f) and the vacancy migration energy (E_m). E_f is 1.5 eV [68] in Ni. Thus, the vacancy migration energy can be calculated as

$$E_m = E_A - E_f = 2.9eV - 1.5eV = 1.4\ eV \qquad 2.15$$

The diffusion coefficient of a vacancy in Ni is therefore

$$D_v = D_0 \exp\left(-\frac{E_A - E_f}{kT}\right) = 1.27 \times 10^{-4}\exp(-1.4\ \text{eV/kT})\ m^2 s^{-1} \qquad 2.16$$

Diffusion coefficient of P in Ni is given by [64]

$$D_P = 1.0 \times 10^{-8} \exp\left(-\frac{1.78\ eV}{kT}\right) m^2 s^{-1} \qquad 2.17$$

The activation energy (E_A^i) is the sum of the vacancy formation energy and the solute migration energy. The solute migration energy can then be calculated as E_m^i=E_A^i-E_v^f=0.28 eV. According to the above discussion, the activation energy of the complex is the larger of the vacancy migration energy or solute migration energy. The pre-exponential factor of the complex is one third of the pre-exponential constant of the vacancy diffusion as the vacancy jumps three times

for each migration step of the complex. So, the diffusion coefficient of the complex can be written as

$$D_c^{Ni} = \frac{\mathrm{D}_0}{3} * \exp\left(-\frac{\mathrm{E}_m^c}{kT}\right) = 4.23 \times 10^{-5}\exp\left(-\frac{1.4\ \mathrm{eV}}{\mathrm{kT}}\right) m^2 s^{-1} \quad 2.18$$

Considering an equilibrium between vacancies V, solute atoms P and V-P complexes

$$[\mathrm{V}] + [\mathrm{P}] \leftrightarrow [\mathrm{C}] \quad 2.19$$

The concentration of vacancies and complexes can be calculated by [92]

$$[\mathrm{V}] = k_V \exp(-\frac{E_f}{kT}) \quad 2.20$$

$$[\mathrm{C}] = k_C[\mathrm{V}][\mathrm{P}]\exp(\frac{E_b}{kT}) \quad 2.21$$

where E_f and E_b are the vacancy formation energy and vacancy-solute binding energy.

Table 2.2 Equilibrium concentrations of vacancies and complexes and the diffusion coefficients of P and the V-P complexes at high temperature (1000 ºC) and low temperature (500 ºC) in Ni.

Temperature	1000 ºC	500 ºC
Vacancy concentration [V]	4.67×10^{-6}	6.78×10^{-10}
Complex concentration [C]	1.13×10^{-6}	1.13×10^{-9}
Diffusion coefficient of P D_P, m^2s^{-1}	9.11×10^{-16}	2.54×10^{-20}
Diffusion coefficient of complex D_c, m^2s^{-1}	3.68×10^{-10}	9.64×10^{-14}
Diffusion coefficient of vacancy D_v, m^2s^{-1}	1.10×10^{-9}	2.89×10^{-14}

Table 2.2 shows the equilibrium concentrations of vacancies and complexes and the diffusion coefficients of P and the complexes at 1000 ºC and 500 ºC in Ni. When held at 1000 ºC for some time, equilibrium between the solutes, vacancies and complexes can be achieved both at

the GB and in the grain interior. The concentration profile is shown in figure 2.7 [102]. After quenching to a lower temperature 500 ºC, a new equilibrium at the GB can be reached immediately because the GBs are vacancy sinks. Removing the vacancies causes complexes to decompose to vacancy and solute, lowering the concentration of the complex. In the grain interior, vacancy concentration will remain unchanged. This results in an increase of the complex concentration according to equation 2.21 and the formation of a concentration gradient between the GB and the grain interior (figure 2.7). Complexes diffuse to the GB and decompose in the GB, resulting in an increase of solute. At the same time, solutes build up at the GB and form another gradient (figure 2.7). This gradient drives solute to the grain interior via vacancies.

The flux of the complexes to the GB and the back-diffusion of the solute can be calculated by

$$\mathrm{J}_c = -D_c \nabla C_c = -D_c \frac{\partial C_c}{\partial x} \qquad 2.22$$

$$\mathrm{J}_i = -D_i \nabla C_i = -D_i \frac{\partial C_i}{\partial x} \qquad 2.23$$

Initially, the diffusion of the complexes to the GB is dominant because the concentration gradient of the solute is low and the diffusion coefficient of the solute is also lower than that of the complex. With the build-up of the solute at the GB, the concentration gradient increases for the solute and decreases for the complex. This leads to an increase of the solute flux and a decrease of the complex flux. At a specific time, these two fluxes equal each other and the solute concentration at the GB reaches a maximum. After that, back-diffusion of the solute is dominant and the GB concentration of the solutes decreases.

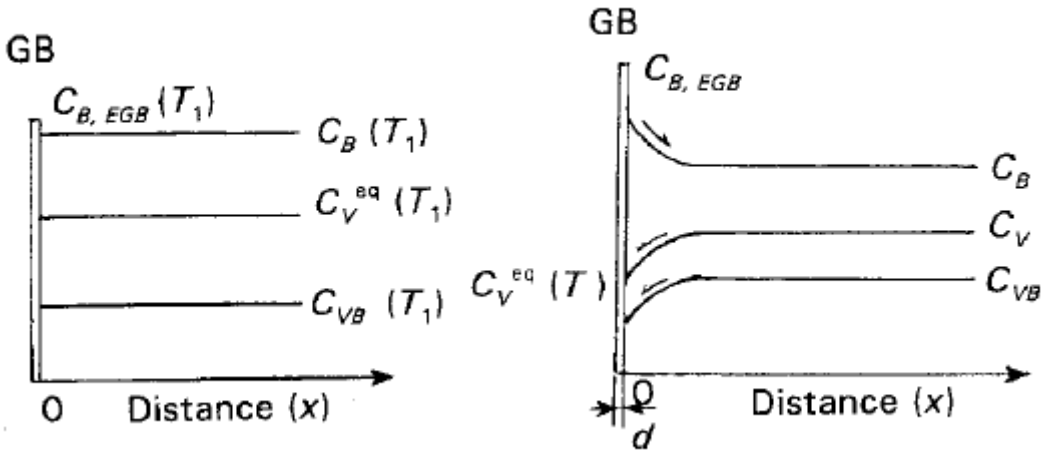

Figure 2.7 Schematic drawing of concentration distribution of vacancies, solutes and vacancy-solute complexes near a GB. (a) At temperature T_1 and (b) quenched to and held at lower temperature T [102].

2.4.2 Thermodynamics

The experimental results indicated that factors influencing GB included the temperature difference between the solid solution temperature and the aging temperature, the cooling rate and the aging time. Among these factors, only the temperature difference is related to the thermodynamics. Faulkner [1] and Xu [3] derived the maximum segregation content at any temperature ($C_m(T)$) using different methods as (see Appendix equation A42)

$$C_m(T) = C_g\left(E_b/E_f\right)exp\left[\frac{\left(E_b - E_f\right)}{kT_0} - \frac{\left(E_b - E_f\right)}{kT}\right] \qquad 2.24$$

where C_g is the concentration of solute in the grain, E_b the binding energy between a vacancy and a solute atom, E_f the formation energy of a vacancy and T_0 the succeeding solution treatment temperature.

2.4.3 Kinetics

According to 2.4.1 there are two fluxes involved in the diffusion, i.e. the complexes to the GB and the backwards diffusion of the solutes. At first, the diffusion process is dominated by the diffusion of the complexes to the GB. At a specific time, the flux of complexes to the GB and of solute to the grain interior equal each other. Segregation has reached its highest level. After that time, the diffusion of the solute to the grain interior dominates. The time is called the critical time t_c. An expression for the critical time was first derivated by Faulkner [1] (see Appendix equation A26)

$$t_c = \frac{r^2 \ln(D_c/D_i)}{\delta(D_c - D_i)} \qquad 2.25$$

where r is the grain radius, δ the critical time constant, and D_c and D_i the diffusion coefficients for complex and solute, respectively.

Experimental evidence observed by Williams [92] was first explained by Xu [103] in Fe-30%Ni(B) using particle tracking autoradiography (PTA). The samples were solution treated at 1250 ºC, quenched into a salt bath at 1050 ºC and held for 3s-80s. The GB concentration of B increases until 11-15s and then decreases. With the development of AES, direct measurement of the GB concentration of B in FeAl alloys annealed at 400 ºC after an air quench was achieved by Gay [104]. A maximum concentration appears at 24h, confirming the existence of a critical time for B in this alloy.

One of the most important GB NES situations is to confirm the NES of P in steel. Briant [105] investigated the GB segregation of P in an HY130 steel aged for different times at 480ºC after water quenching from 650 ºC and found that the GB concentration of P first increased and then decreased with the maximum appearing at 100-400h. The same results were also observed by Misra [106] in a Ni-Cr-Mo-V steel. No reasonable interpretation was available when these articles were published. Xu [107] studied the phenomenon again, calculated the critical time

and concluded that they were due to the NES of P in steel. The NES characteristics of P were also confirmed in a 2.25Mo-1Cr steel by Ding [108], in a 12Cr1MoV steel by Li [109] and in a Cr steel with medium C by Zhang [110]. Briant [111, 112] investigated the segregation of P in 304L steel aged for 100h at 500, 550, 600, 650 and 700ºC after quenching from a solid solution temperature of 1100ºC and found that the maximum NES content appeared at 600ºC for this aging time. However, this could not be rationalized then. Wang [113] calculated the kinetic curves and found that the critical time for 600ºC is about 108h, quite close to the aging time of 100h. With a temperature lower or higher than 600ºC, the critical time deviated from the aging time, resulting in a lower NES content. A similar phenomenon for Mg in a Ni-Cr-Co alloy was also observed and successfully rationalized by Xu [114].

Based on the critical time, NES can be divided into two phases, the segregation phase when the aging time is shorter than the critical time and the desegregation phase when the aging time is longer than the critical time.

Faulkner [2] proposed that the solute distribution along the GB can be described by

$$\frac{\left[C_{gb}(t,x)-C_0\right]}{\left[C_m(T)-C_0\right]}=\mathrm{erfc}(\mathrm{x}/2\sqrt{D_c\mathrm{t}}) \qquad 2.26$$

and

$$\frac{\left[C_{gb}(t,x)-C_0\right]}{\left[C_m(T)-C_0\right]}=\left(\frac{D_c t_c}{D_I t}\right)^{\frac{1}{2}}\exp(-x^2/4D_I t) \qquad 2.27$$

during segregation and desegregation stage, respectively.

Xu and Song [3, 115] also proposed kinetics of NES for both phases without considering the distribution near the GB. For the segregation phase, the GB content can be expressed as (see Appendix A36)

$$\frac{[C_{gb}(t)-C_0]}{[C_m(T)-C_0]}=1-\exp\left(\frac{4D_ct}{\alpha^2\theta^2}\right)\mathrm{erfc}(2\sqrt{D_c}\mathrm{t}/\alpha\theta) \qquad 2.28$$

and

$$C_{gb}(t)=C_g+\frac{[C_{gb}(t_c)-C_g]}{2}\cdot\left\{\mathrm{erf}\left[\frac{\theta}{2\sqrt{D_i(t-t_c)}}\right]-\mathrm{erf}[-\frac{\theta}{2\sqrt{D_i(t-t_c)}}]\right\} \qquad 2.29$$

for the desegregation phase.

Faulkner's theory [2] and Xu's formula [3, 115] did not consider the effect of grain size on the segregation though the critical time depends on the grain size. Wu proposed a model illustrated in figure 2.11 to calculate segregation and desegregation using one formula [4]. The process can be divided into two parts, i.e. complexes diffuse to segregation zone and transfer through the interface B.

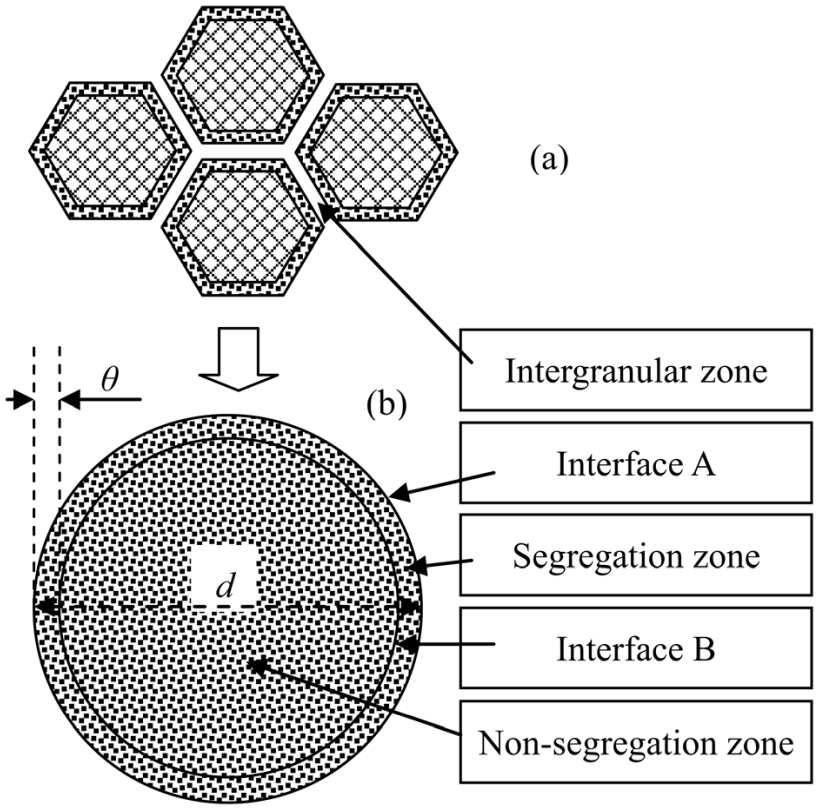

Figure 2.8 Schematic illustration of the simplified structure and morphology of polycrystals [4].

Based on this theory, the segregation kinetics can be described by [4](see appendix A67):

$$C_{gb}(t) = \frac{(k_V - k_C)C_{gb}^i - k_C(\alpha - 1)C_{gb}^i e^{-k_V t} + [k_V(\alpha C_{gb}^0 - C_{gb}^i) - k_C\alpha(C_{gb}^0 - C_{gb}^i)]e^{-k_C}}{(k_V - k_C)[1 + (\alpha - 1)e^{-k_V t}]} \quad 2.30$$

where C_{gb}^i is the transformed solute concentration in the non-segregation zone, C_{gb}^0 the initial concentration and k_V, k_C and α are defined as

$$k_V = 12D_{0V}\exp\left(-\frac{Q_V}{kT}\right)/d^2 \quad 2.31$$

$$k_C = \frac{12(d - 2\theta)D_{0C}\exp\left(-\frac{Q_C}{kT}\right)}{d^3 - (d - 2\theta)^3} \quad 2.32$$

$$\alpha = \exp[Q_f(T_0 - T/kT_0T] \quad 2.33$$

where Q_V and Q_C are the migration energies of the vacancies and complexes respectively and Q_f is the vacancy formation energy.

Based on the critical time equation, the thermodynamic equation and the kinetic equation, kinetic curves can be obtained for different aging temperatures. When the aging time is shorter than the critical time, the NES content is higher at a higher temperature than at a lower temperature. This is due to the higher diffusivity of vacancy-solute complexes at high temperature. In the desegregation phase, however, the NES content at a lower temperature will eventually exceed that at a higher temperature. This kind of temperature dependence is an important characteristic of NES. When aging for a specific time, there exists a temperature at which the critical time is comparable with the aging time, yielding a maximum NES content.

2.4.4 Important factors in NES

(a) Temperature. As NES takes place when the temperature decreases and a concentration gradient of complexes is formed between the GB and grain interior, temperature plays an

important role in determining the segregation level. Thermodynamically, when cooling from T_0 to T, the maximum NES concentration at the GB increases with T_0 and decreases with T (Equation 2.24). Figure 2.8 shows the calculated maximum NES of B in steel when cooling from different temperatures to 500 °C [107]. The NES level increases monotonically with T_0. This is consistent with reported experimental results in Type 316 austenitic stainless steel which showed obvious B segregation when cooling from 1200 °C but not from 1000 °C [92].

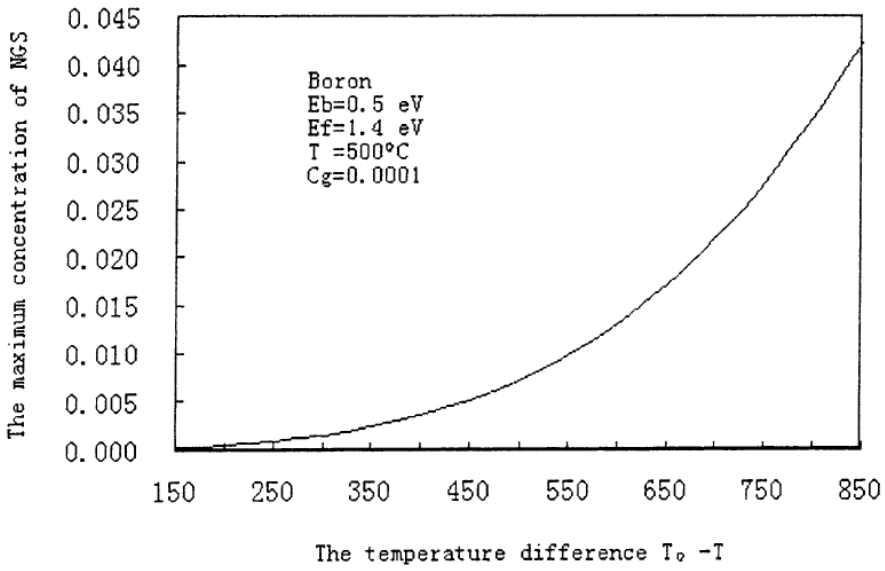

Figure 2.9 The calculated maximum NES concentration of B in steel when cooling from different temperatures to 500 °C [107].

Kinetically, temperature affects the diffusion coefficient and thus the GB concentration. The calculated S content in a Ni-base alloy aged at different temperatures after quenching from 1180 °C is shown in figure 2.9 [116]. At a lower aging temperature, the critical time is longer and the GB concentration during the segregation phase is lower as the diffusion coefficient of the complexes is smaller than that at high temperature.

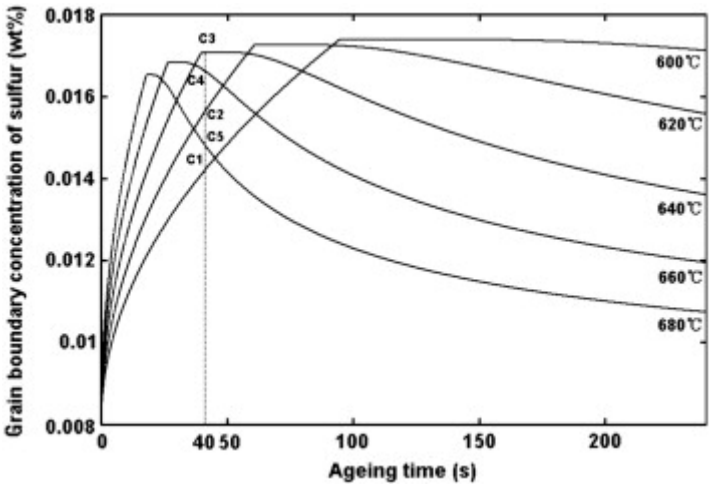

Figure 2.10 The calculated results for the GB concentration of sulphur NES in a Ni-base alloy for aging at 600, 620, 640, 660 and 680 °C after quenching from 1180 °C. The vertical dashed line is for an aging time of 40 s [116].

(b) Binding energy. As the solute migrates via V-P complex diffusion, the binding energy between a solute and a vacancy is another key parameter affecting the segregation level. With too low a binding energy, the complex cannot form. The calculated relation between binding energy and maximum segregation based on equation 2.24 is shown in figure 2.10 [1]. It can be seen that the segregation level is high and does not change too much over a range 0.3-0.6 eV. This is the suitable range for the NES [1, 117]. To best fit of the experimental results indicated that the binding energy between Cr and vacancy should be as high as 0.5 eV [118, 119]. If the binding energy is below 0.2 eV, no segregation of Cr will be observed [120].

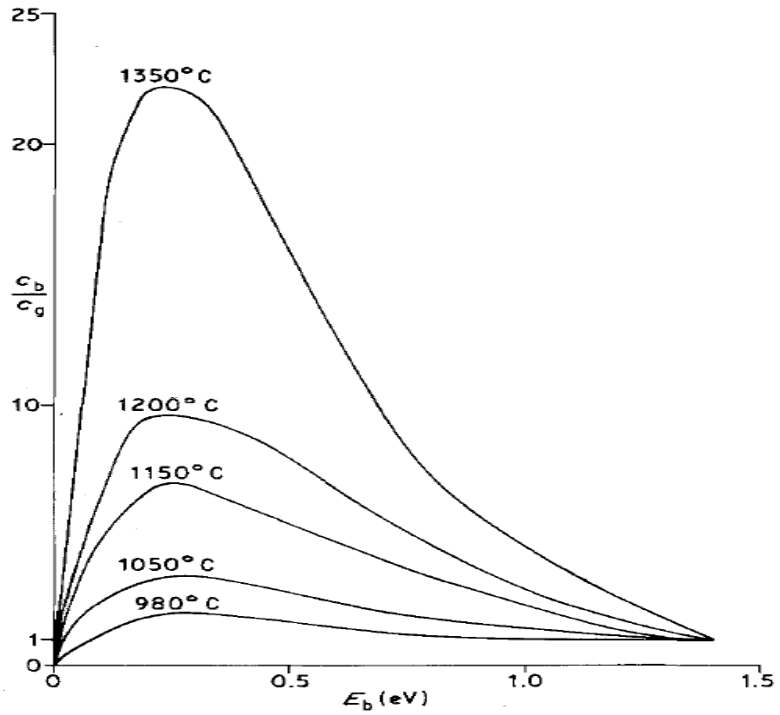

Figure 2.11 Effect of vacancy-impurity binding energy on the NES magnitude when cooling to 750 °C from different solution-treatment temperatures [1].

Several methods have been proposed to calculate the binding energy. Based on elastic strain field arguments, the binding energy can be calculated considering the change of interfacial energy, surface energy and volume when forming V-S complexes [96, 121]. The P-vacancy binding energy in steel and Ni was determined to be 0.33 eV [96], falling in the suitable range for NES [96]. It should be noted here that this method did not consider the electronic effect. More recently, first principles calculations have been widely used to calculate the binding energy [122-128]. The results are consistent with those in [96] and with molecular dynamics simulations [129].

Compared with P, the binding energies between Cr or Mo and vacancies are much smaller. The calculated value of less than 0.1 eV is consistent with the experimental results obtained by muon spectroscopy [130]. With such a low binding energy, NES of Cr or Mo is impossible [120]. However, Cr and Mo were reported to segregate to the grain boundary in both steels and

Ni-base alloys during quenching which was attributed to complex diffusion [118, 119], which is contradictory with the calculations of [96]. The discrepancy between the calculation and experiment is possibly due to the effect of non-metallic elements, such as C, B, N and P. To verify this, samples free of B, C, N and P need to be used.

(c) Misorientation. Segregants occupy the free volume sites which are misorientaion dependent. However, little research has been done on the dependence of GB concentration on misorientaion. Ding [131] found the P contents at grain boundaries in steel were different although the misorientation was not measured. Cr concentration at coincidence site lattice (CSL) In electron-irradiated Fe–15Cr–20Ni alloys, the GB concentration of Ni was shown increasing with tilt angle except for those special CSL GBs, where a local minimum was present [54]. GBs in irradiated 304 stainless steel was found to increase with Σ up to Σ =15. Also, the concentration at CSL boundaries is much higher than for random high angle GBs [132, 133]. However, the diffusion mechanism for irradiation induced NES is different from thermal induced NES. In this project, the dependence of segregation on misorientation will be investigated.

(d) Grain size. Unlike for ES, little has been done on the effect of grain size. NES of B in Type 316 austenitic steel during cooling was investigated using autoradiography [1]. A larger grain size leads to more intense segregation. A similar result has also been reported for P in a 2.25Cr1Mo steel [108]. However, to achieve a larger grain size, a higher solution or austenitization temperature was used. It has been shown that a higher solution temperature also produces a higher segregation level. The effect of grain size cannot be isolated from the effect of temperature.

According to Wu's theory, during the segregation stage, complexes diffuse to a narrow region close to the GB with a thickness of θ. The mass transfer coefficient of the complex at interface B can be calculated as [134]

$$\beta_c = 2D_c/(d - 2\theta) \quad (2.34)$$

With increasing grain size, the mass transfer coefficient of the complex decreases, resulting in a decrease of the GB concentration (figure 2.12). In the desegregation stage, solute diffuses to the grain interior through a vacancy-mediated mechanism. The mass transfer coefficient of the vacancy at interface B is

$$\beta_V = 2D_V/d \quad (2.35)$$

A larger grain size leads to a smaller transfer coefficient and less solute diffuse to the bulk area, resulting in a higher GB concentration. Also, the maximum segregation level relates inversely to the grain size (figure 2.12). However, no direct experimental evidence has been observed. This will be carried out in this project.

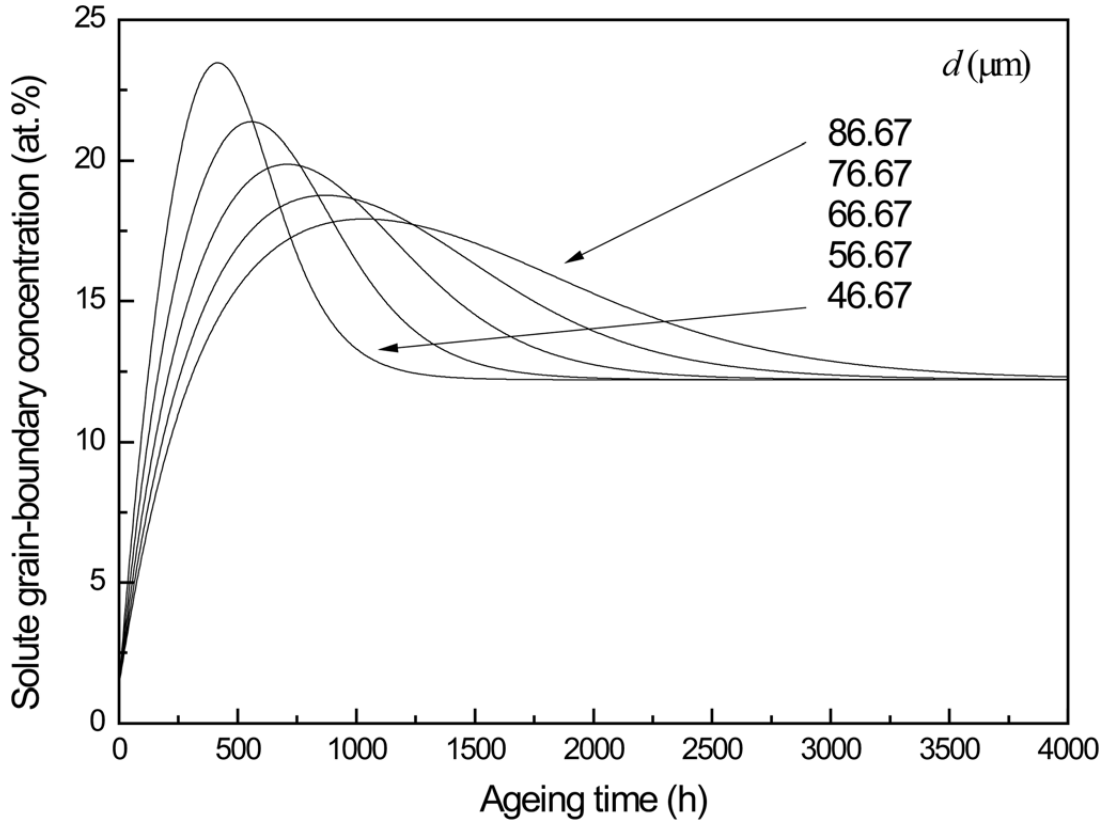

Figure 2.12 Predicted segregation kinetics with different grain size. The largest grain size was obtained by fitting the experimental results [4].

(e) Elemental interaction. Xu extended Guttmann's elemental interaction model to NES [117]. If one of the solute atoms has a binding energy in the range 0.3-0.6 eV and the attractive interaction between solutes is stronger than that between solute and solvent (positive relative interaction coefficient), co-segregation can take place even if the other solute has no segregation tendency [117]. If the relative interaction coefficient is negative, the stronger segregant will inhibit the segregation level of the weaker segregant. In both steels and Ni-based alloys, non-equilibrium co-segregation of Cr or Mo with non-metallic elements such as B, C, N, and P has been widely reported. P and Cr or Mo co-segregation has been reported in 2.25Cr1Mo steel quenched from 1100ºC using EDS due to the attractive interaction between P and Cr or Mo [108]. Similar results have also been observed in an industrial steel [109], 12Cr1MoV steel [21] and Fe-Cr-P alloy [19] by AES. Also, increasing the P concentration

promoted the segregation of Cr [19]. In a Ni-Cr alloy and IN 718, P and Cr or Mo co-segregation was measured by AES and attributed to the strong interaction between P and Cr or Mo [20, 62]. The GB Cr or Mo concentration increased with GB P content (figure 2.13) [22].

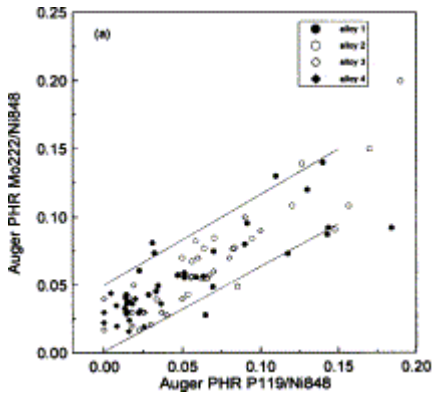

Figure 2.13 Relationship between the Auger peak ratio of P with that for Mo. Alloys 1, 2, 3 and 4 contain different C concentrations [22].

It should be noted here that all the samples studied contained C and/or B and/or N. Cr and Mo can also co-segregate with these three elements. So, the interaction between P and Cr or Mo cannot be isolated. To exclude the effect of other elements, simplified alloys free of C, B and N need to be used and have been in this work.

2.4.5 Application

NES segregation has been used to interpret various mechanical properties, including the intermediate brittleness and temper brittleness.

(a) Intermediate brittleness. It has been observed that Ti alloys [135], Ni-base alloys [136] and Al-Mg alloys [137] suffer from brittleness in the temperature range 0.5-0.8 T_m. Several mechanisms have been proposed to interpret this phenomenon, but no satisfactory explanation obtained. Generally, to conduct a tensile test, the sample was held for at least 10 min before mechanical testing after cooling from the higher solid solution temperature. Also, it took some time for the sample to fracture. That is to say the samples went through the test isothermal time

(TIT) after cooling. This process resulted in NES. So, Xu [138] proposed that intermediate brittleness was due to NES during the mechanical test. At the specific temperature where intermediate brittleness occurred, the critical time was comparable to the TIT. At lower and higher temperature, the critical time deviated from the TIT, and the NES content in the GB decreased. This eventually resulted in an increase of the ductility in both cases.

A slow tensile rate led to a longer TIT, which resulted in the movement of the maximum brittleness temperature (T_{min}) to a lower level. This was verified in an Al-Mg alloy [139]. With a decrease of the tensile rate from 10^{-1} to 10^{-5} s^{-1}, T_{min} also decreased from 380 ºC to 230 ºC. If the sample was held for a long enough time around T_{min}, intermediate brittleness can be eliminated. This is consistent with the experimental results [140].

(b) Reverse temper brittleness

Reverse temper brittleness (RTE) is defined as the embrittlement appearing after heating and slow cooling in the temperature range 350 ºC to 600 ºC in steels. RTE was first interpreted by ES theory [141]. However, no completely satisfactory theory has ever emerged. Xu [3, 107] analysed many experimental results concerning RTE and suggested that NES is the main reason for RTE and that the critical time for NES led to a critical time for RTE. At this critical time, embrittlement reached its maximum. On aging a 12Cr-1Mo-V steel for different times at 540 ºC after quenching from 1050 ºC, it was found that both the maximum NES content and the minimum ductility appeared at around 500 h [90]. Similar results were also observed in a medium-carbon Cr steel [110].

2.5 Analytical methods

2.5.1 Auger electron spectroscopy (AES)

AES was the first method to measure the GB content directly which validated the theory of segregation and led to its rapid development [142]. During the past four decades, AES has

remained the most commonly used technique to investigate segregation. Generally, samples are fractured under high vacuum conditions to expose the GB planes without contamination. AES can be used for all elements except for H and He with its strength lying in determining light elements. The main limitation of AES is that an intergranular fracture mode is needed. The segregation level varies for different GBs: those GBs containing the most amounts of segregant are most brittle [77]. The fracture path will follow these GBs, making the measured results larger than the true average levels. Also, it is difficult to quantify and careful calibration is needed.

2.5.2 Secondary ion mass spectroscopy (SIMS)

Like AES, SIMS is also a surface sensitive technique with a depth resolution down to several nanometres and a high elemental sensitivity of 1 ppb [143]. Also, sample preparation for SIMS is relatively easy and compositional mapping is available now with instrumental development [144]. However, SIMS suffers from a poor lateral resolution (50nm) and the quantitative results are very unreliable even though relative concentrations can be measured within a factor of two.

2.5.3 Atom probe tomography (APT)

The most important characteristic of APT is a high spatial resolution, both laterally and depth-wise [145]. The ultra-high resolution makes it a most useful method to determine GB segregation and extensive usage is expected. However, it is difficult to prepare suitable specimens. The recent development of focussed ion beam (FIB) for preparing tips may improve this situation. Also, it is not suitable for severely brittle samples as they tend to fracture during measurement due to the high mechanical stress imposed on the sample. And, the volume examined is very small.

2.5.4 Energy dispersive spectroscopy (EDS) of X-rays in an electron microscope

EDS is a direct and quantitative method to investigate GB segregation and has been widely used in analytical electron microscopy, including both scanning electron microscopy and transmission electron microscopy. The pioneering work was done by Doig and Flewitt [146], who demonstrated that monolayer-level segregation can be detected in a thin foil. With the development of the field emission gun, the incident probe size can be less than 2 nm. A high spatial resolution can be obtained with an elemental sensitivity of about 0.25 at% [147]. Generally, there are two methods to determine GB segregation in the AEM. The first is to fix the probe on both the GB and the inner grain to generate two spectra. Alternatively, a stepped probe is used along a line perpendicular to the GB to obtain the segregation profile. The fixed probe was adopted by Faulkner [148] to quantify the grain boundary segregation of P in a 2.25Cr-Mo steel and by Vorlicek and Flewitt [149] to determine the segregation layer thickness of P. Stepping the probe along a line was used by Papworth and Williams to investigate the GB segregation of P in a low alloy steel. Another method is to use 2D mapping to collect compositional information from the grain interior and from the GB. This method can be used to detect GB segregation at several GBs at the same time. However, as the total acquisition time is limited by several factors such as stage drift, beam damage and contamination, the acquisition time for individual points is much shorter than for point analysis or a line-scan, resulting in low counts for each point and low analytical sensitivity. This was verified by Papworth and Williams [150] who failed to detect GB segregation of P in a low alloy steel by 2D mapping.

As the GB is quite narrow (several atomic layers), signals from the matrix are also collected by the detector, which resulted in a lower concentration measured. Deconvolution needs to be done as a correction. Several models have been proposed by considering the probe profiles, the width of the segregation layer and the sample thickness [151, 152]. The results indicated the

effect can be neglected when the probe size used is comparable with or less than the thickness of the segregation layer [151].

It can be seen that among the several common methods, EDS on a TEM has the advantages of high precision, high spatial resolution and relatively easy sample preparation and it will be used in this project.

2.6 Aim of this project

The aim of this project is to investigate the NES of P after cooling and aging in model Ni-base alloys. The effect of misorientation angle and grain size will be investigated. Segregation of Cr and Mo in samples with and without P addition will be looked at and the interaction between P and Cr or Mo will be characterised.

Chapter 3. Experimental procedure

3.1 Alloy preparation

3.1.1 Alloy melting

As shown in part 2.1, the effect of P on the mechanical properties is alloy specific. A commercial superalloy is a complex system with more than ten different alloying elements plus impurities and different phase contents. This situation makes it hard to isolate the effect of P as well as the GB segregation characteristics of P. To investigate the segregation behaviour while eliminating the effect of other factors, a simplified alloy system should be used. Further to that, other elements will be added to the system to investigate the interaction between them and P.

Table 3.1 Nominal composition of the alloys used in this project (at%)

Alloy	Ni	Al	Cr	Mo	P
1	Bal.	6			
2	Bal.	6			0.1
3	Bal.	6	6		
4	Bal.	6	6		0.1
5	Bal.	6		2	
6	Bal.	6		2	0.1

The nominal compositions of the alloy studied are listed in table 3.1. Al, Cr and Mo are common elements in superalloys. The basic composition was chosen based on the commercial alloys compositions. Al is mainly used to form γ'-Ni_3Al strengthen phase [5]. A modern superalloy usually contains 6 wt% Al (~12 at%). However, 6 at% is chosen in this project to

produce a single-phase alloy according to the phase diagram shown in figure 3.1. Cr is beneficial for the oxidation resistance and Mo is the main solution strengthening element [5]. However, Cr and Mo promoted the formation of TCP phase, which is detrimental to the creep properties [5]. For second generation superalloys, such as PWA1484, Rene N5, MC2 and TMS-82+ the Cr content is in the range of 4.9-8 wt% and Mo is around 2 wt% [5]. GB segregation of Al and its effect on the segregation of P has not been reported. Cr and Mo segregation and their interaction with P have been reported [148, 149].

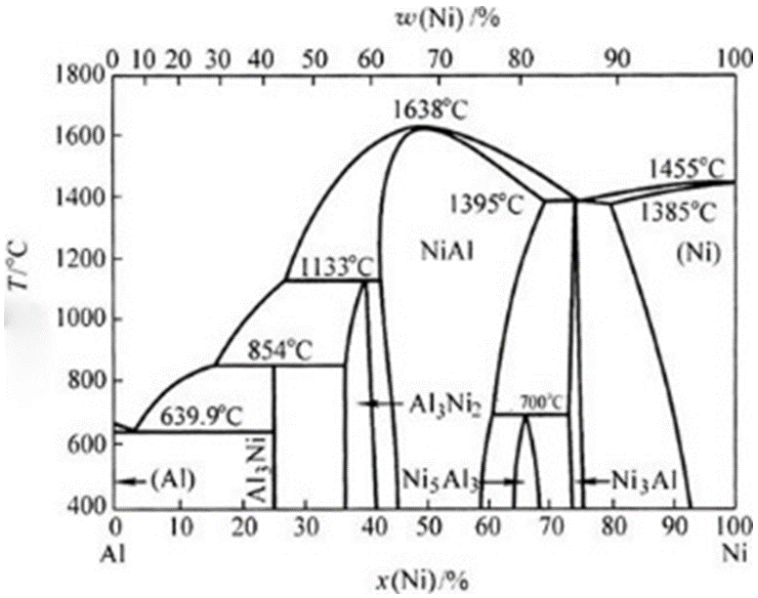

Figure 3.1 Ni-Al binary phase diagram

Raw materials of Ni, Al and Ni_2P with purities of 99.99%, 99.995% and 99.95% respectively were used to produce Ni-Al and Ni-Al-P alloys using arc melting. Ni-Al-Cr/Mo with and without P were prepared by plasma melting. The alloys were re-melted twice to eliminate any cavities and improve the alloy homogeneity.

3.1.2 Solid solution heat treatment

Macro-segregation inevitably existed after casting. To make the sample homogeneous, a solid solution heat treatment is needed. With a high temperature and a long time, the sample oxidation has to be considered. To protect the samples, they were sealed with quartz tubes

under argon. The heat treatment adopted here was 1300ºC for 48h with a heating rate and cooling rate of 1ºC/min.

After heat treatment, microstructure observations were conducted. Samples were cut from the alloys and polished with a final polish by OPS. They were then etched using a solution of 5g $CuSO_4$, 20mL HCl and 100mL H_2O to reveal the GBs.

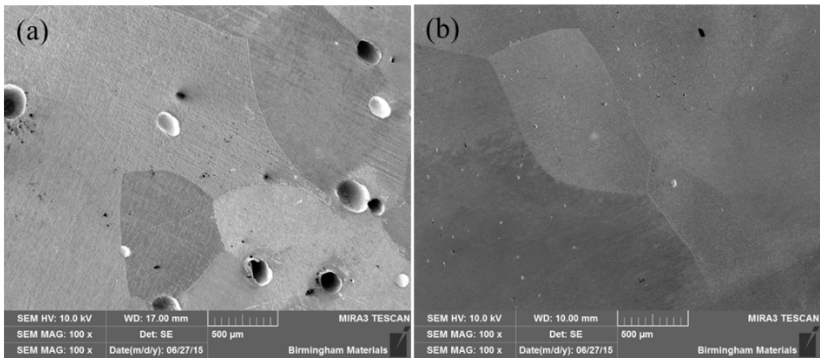

Figure 3.2 Microstructure of the as-heated (a) Ni-Al and (b) Ni-Al-P showing the large grain size in both alloys

Secondary electron images of Ni-Al and Ni-Al-P alloys are shown in figure 3.2. It can be seen that there are some small cavities with diameters of about 150µm in the Ni-Al, but in the Ni-Al-P alloy no cavities were found. Both of the alloys have a large grain size of 500µm to several millimetres. For the Ni-Al-Cr/Mo alloys with and without P, the grain sizes are even larger.

3.1.3 Recrystallization

Problems arise with the large grain size. Firstly, the final TEM samples will contain few GBs or even no GB, which is bad for investigating the GB segregation of P, especially the relationship of P segregation with grain orientation as numbers of variously oriented grains are needed. Moreover, according to the critical time equation, the critical time is proportional to the square of the grain radius. Larger grains require a longer time to reach the maximum GB segregation situation. Based on the thermodynamic parameters, the critical time can be

estimated. For samples with a grain size of about 40μm, the critical time is calculated as about 12h. However, for samples with a grain size of 500μm, the critical time can be as long as 1875h (~2.5 months), which is not easy to reach in practice.

To reduce the grain size, recrystallization was utilized. Samples were first compressed by a strain of about 60% and then annealed at 700 ºC. It has been shown that recrystallization ended after 6 minutes for a sample with a similar composition to ours after experiencing a much larger strain of about 240% by rolling [153]. Due to the smaller strain, a longer time is needed to complete the recrystallization process, so 2h was adopted. Again, the samples were sealed under argon to prevent oxidation.

After annealing at 700 ºC for 2h, the samples were cooled down at different cooling rate, i.e. water quenching, air cooling and furnace cooling, to investigate the effect of cooling rate. Part of the water quenched samples were heat treated at 1000 ºC for 1h, water quenched and aged at 500 ºC for 20min, 2h, 12h and 48h to investigate the effect of aging time on the segregation level.

The reasons to use 700 ºC and 500 ºC are: 1) in the point view of engineering, 700 ºC is the temperature for recrystallization of Ni-base alloys with low solute concentration and 500 ºC is the aging temperature for the precipitates [154]; 2) the temperatures cannot be too high or too low, a high recrystallization temperature results in a large grain size and a low temperature leads to a long recrystallization time and high ES concentration [16]. A high aging temperature resulted in a low NES concentration and a low temperature leads to a low diffusion coefficients [1].

3.2 Microscopy characterization

3.2.1 Optical microscopy

The samples were ground on SiC papers down to 2500 grade and then polished to an OPS finish. All the samples were etched by immersion in a solution of 5g $CuSO_4$, 20mL HCl and 100mL H_2O for 30s to reveal the GBs. The etched samples were observed on a Leica DMRX optical microscope.

3.2.2 Scanning electron microscopy

The samples were ground and polished using the same method as described in 3.2.1. The polished samples were examined in a TESCAN Mira 3 scanning electron microscope equipped with an Oxford EDS system. Point analysis was carried out at 20kV with an acquisition time of 300s, while the dwell time for a line-scan was 120s.

3.2.3 Transmission electron microscopy

TEM foils were prepared by twin-jet polishing using a solution of 5% $HClO_4$ and 95% C_2H_5OH, at a current of 0.05A and a temperature of -25 ºC and characterized using an FEI Talos F200 microscope operated at 200kV. The Super-X EDS system consists of 4 EDS detectors (figure 3.3).

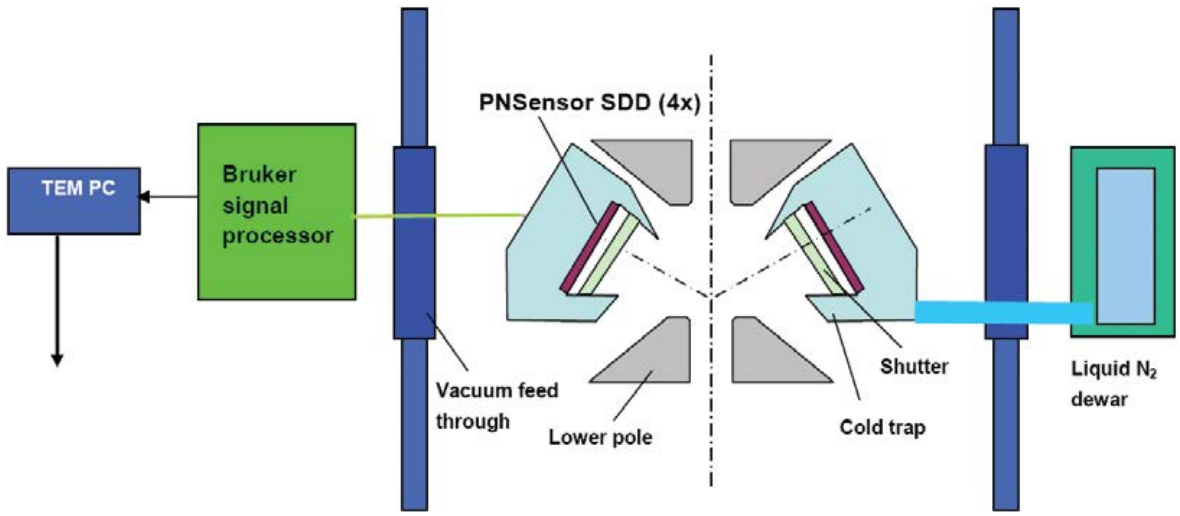

Figure 3.3 Schematic diagram of a cross section view of the Super-X design through the objective lens and specimen. Two of the four X-ray detectors mounted on the cold trap surrounding the specimen are shown [155]

The signal counts were much higher on this system than those acquired on the FEI Tecnai with only one detector. For the same beam current, the count rates on both systems are shown in table 3.2. The input count rate on the Talos is about 8 times higher than that on the Tecnai, while the output count rate is more than 8 times higher than for the Tecnai due to a shorter dead time on the Talos.

Table 3.2 Input and output counts rate on Talos and Tecnai

	Input (kcps)			**Output (kcps)**		
	Talos	Tecnai	ratio	Talos	Tecnai	ratio
250pA	26.6	3.4	**7.8**	25.7	3.0	**8.6**
570pA	59.9	7.4	**8.1**	54.2	5.7	**9.5**
1040pA	122.8	15.4	**8.0**	99.6	9.0	**11.0**

Also, the higher signal can be sustained even with a high tilt angle. It has been shown that the count rate reduces only by 20% when tilting ±25 degrees [155]. This enables us to align the GB without reducing the count rate too much.

The electron beam size used was measured by fitting the intensity profile to a Gaussian function. The full width at half maximum (FWHM) was about 0.73nm (figure 3.4).

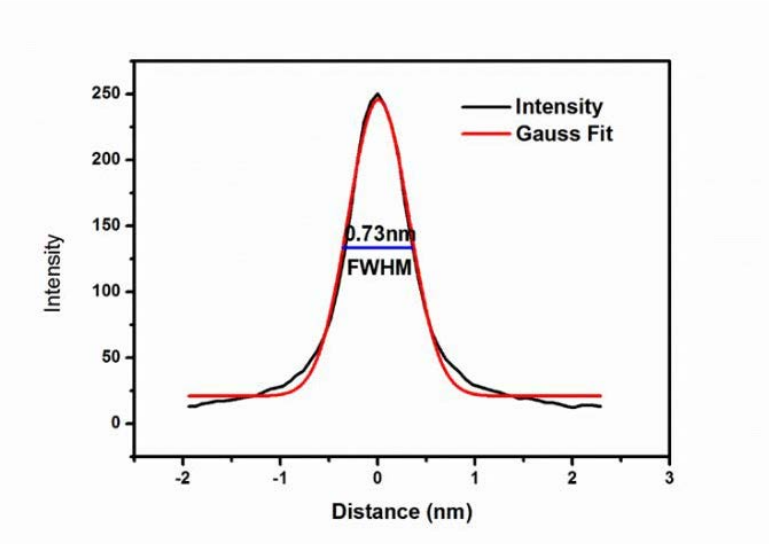

Figure 3.4 Gaussian fit of the probe intensity profile.

Quantification of the spectra were performed using the Cliff-Lorimer method [156], in which the X-ray intensities can be converted to the relative concentration by

$$\frac{C_i}{C_j} = k_{ij}\frac{I_i}{I_j} \qquad 3.1$$

where *C* is the concentration, I the intensity and k the Cliff-Lorimer factor. This is valid only when the film is thin enough that the absorption can be neglected. Normally, the absorption effect needs to be considered. Goldstein proposed a method to correct the absorption effect by multiplying the Cliff-Lorimer factor by a correction factor A_{ij} [157]. According to Beer's law, estimation of A_{ij} requires the measurement of mass-thickness [157]. For example, the Al concentration in the matrix measured without absorption correction is shown in black in figure 3.5. With increasing thickness from 30 nm to 140 nm, the apparent Al concentration determined using a k_{AlNi} factor of 0.6 decreased from 5.3 at% to 3.7 at%, while after absorption correction using the thickness measured by CBED and a density of 7.9 g/cm^3, the Al concentration did not vary too much with thickness. The dependence of the absorption correction coefficients on the thickness were listed in table 3.3.

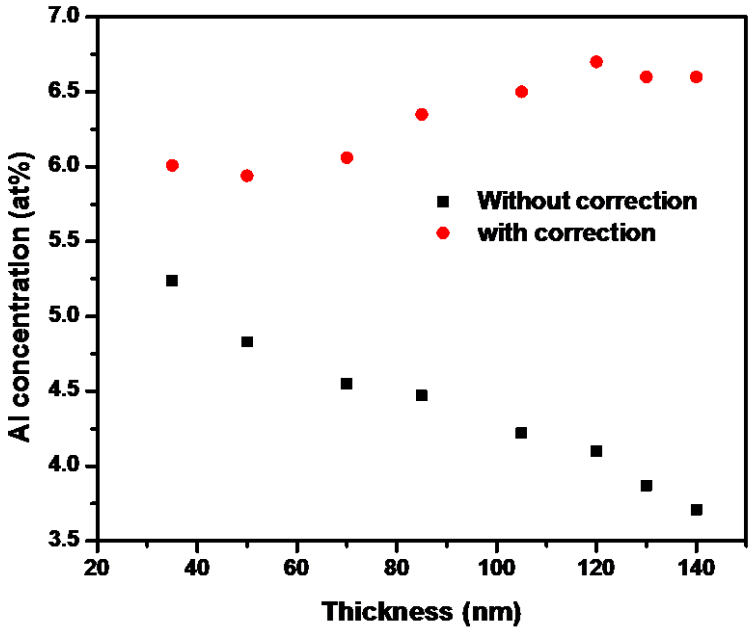

Figure 3.5 Measured Al concentration in the matrix of Ni-6Al alloy with and without absorption correction.

Table 3.3 Absorption correction coefficient of A_{AlNi} used for the quantification.

Thickness (nm)	35	49	70	84	103	120	130	140
coefficient	1.15	1.24	1.35	1.44	1.55	1.66	1.73	1.81

Experimental parameters, such as the probe size which determines the beam current, sample thickness and dwell time affect the measured concentration. This will be discussed further in Chapter 6. In this study, a beam current of 200 pA (corresponding to a probe size of 0.73nm), thickness of 60-100 nm and a dwell time of 1s for line-scans and 10s for point analysis was used.

Chapter 4. Segregation in Ni-Al-P

4.1 Introduction

Even at low content, the effect of P on the mechanical properties of Ni-base alloys is dramatic due to its GB segregation [7, 8, 12]. A knowledge of GB segregation is therefore essential for a deep understanding of the effects of P on nickel-based alloys.

It has been shown that temperature, holding time, cooling rate, elemental interaction, grain size and misorientation all affect the GB segregation [13, 16, 77, 78, 82, 102, 107, 158], of which Grain size and GB misorientation are key parameters for GB engineering. During the past several years these have been a hot topic. By controlling grain size and GB configuration, the mechanical properties can be modified [159, 160]. So, it is quite important to determine the effect of grain size and misorientation on GB segregation. However, all the previous work focused on ES. Little has been done on the relationship between the grain size and GB misorientation and the NES content, particularly compared with their importance. So, detailed research will be conducted in this project to reveal the relationship between grain size and GB misorientaion and NES.

Triple junctions (TJs), as line defects in their own right with specific kinetic and thermodynamic properties, have received more attention recently [161, 162]. They act as fast diffusion paths due to their larger free volume as compared with GBs, which has been confirmed both by diffusion experiments and molecular dynamics modelling [161-166]. TJ serves as the nucleation site during phase transformation because of the removal of interfacial material by forming an embryonic precipitate [161]. With a low mobility, they can exert a drag on the GB motion and slow down the grain growth. Also, they have an effect on the mechanical properties. For example, they have been identified as the nucleation site for cracks during high temperature creep when GB sliding is operating [167]. Though intensive work has been done

on the TJ structure, diffusion and mobility, there has been less focus on TJ segregation compared with its importance, as segregation has been considered to affect the mechanical properties dramatically. Possible reasons are: 1) experimentally, the TJ line needs to be aligned before doing energy dispersive spectrometry (EDS) measurements, which is difficult and sometimes impossible due to the limitation of the tilt angle. Also, the sample needs to be tilted to a specific angle to maximize the X-ray counts the detector received where the TJ may not be well aligned [168]. 2) due to the complicated TJ structure, simulations have only been done on those composed from special GBs, such as Σ3 twin boundaries [169]. In this project, an advanced TEM with four EDS detectors was used to check the segregation of P in Ni-base alloy to TJs made by random GBs. This enables a high count rate even with a high tilt angle.

Holding time and cooling rate are also important as segregation is a dynamic process. For ES and NES, the kinetics are different. ES increases with time, whereas NES displays a critical time when segregation reaches a maximum. A detailed study of the segregation kinetics helps an understanding of the relative contribution of ES and NES during heat treatment. This is also important for optimizing the heat treatment conditions to obtain a certain microstructure and GB composition.

4.2 Experimental results

4.2.1 Microstructure

The alloys used here are Ni-6Al and Ni-6Al-0.1P (at%). The Ni-Al-P alloy composition after solution treatment was measured by SEM-EDS. The sample was plasma cleaned for 20 min. One typical spectrum is shown in figure 4.1 and the measured concentrations from different areas are listed in table 4.1. The measured concentration is quite close to the nominal composition. Also, the sample is homogeneous after solution treatment.

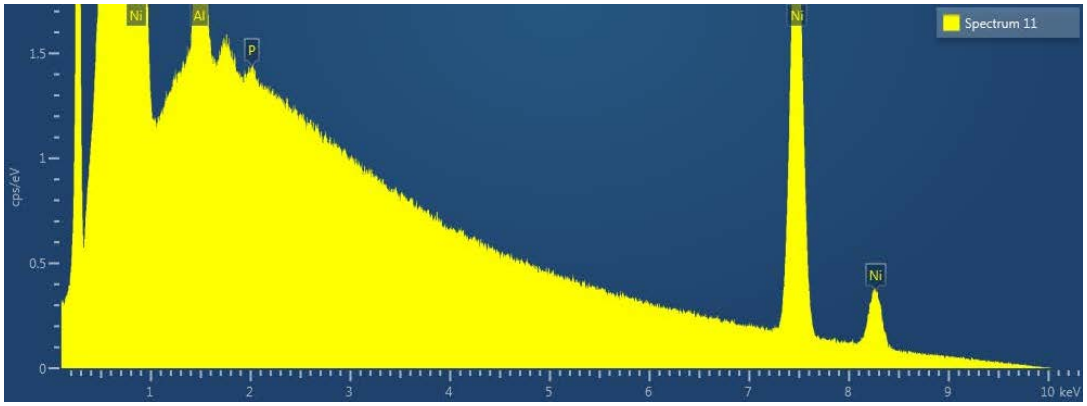

Figure 4.1 A typical spectrum collected from the matrix of the Ni-Al-P alloy after solution treatment.

Table 4.1 Concentration measured from different areas in Ni-Al-P after solution treatment. The standard error were included in the parenthesis (at%).

Spectrum	Al	P	Ni
1	6.67 (0.04)	0.10 (0.02)	93.22 (0.02)
2	6.65	0.10	93.25
3	6.67	0.10	93.23
4	6.70	0.12	93.18
5	6.60	0.11	93.29
6	6.68	0.09	93.23
Average	6.66±0.03	0.10±0.01	93.23±0.04

Figure 4.2 shows the secondary electron SEM images of both samples after recrystallization. The samples were etched by a solution of 5 g $CuSO_4$, 20 mL HCl and 100 mL H_2O. It can be seen that the grain sizes of both samples are typically less than 100 μm.

Figure 4.3 show the electron backscattered diffraction (EBSD) orientation map and the grain size distribution obtained from Ni-Al and Ni-Al-P, respectively. Both alloys were completely recrystallized with a random orientation distribution. The average grain sizes of Ni-Al and Ni-

Al-P alloys are 10.9 μm and 21.2 μm, respectively. The grain size of Ni-Al-P is larger than that of Ni-Al due to the initially larger grain size of Ni-Al-P before recrystallization. Also, the grain sizes are not homogeneous for both alloys. So, during EDS measurements on TEM, only those areas with similar grain size were used and the actual grain size rather than the averaged grain size will be used for the calculation.

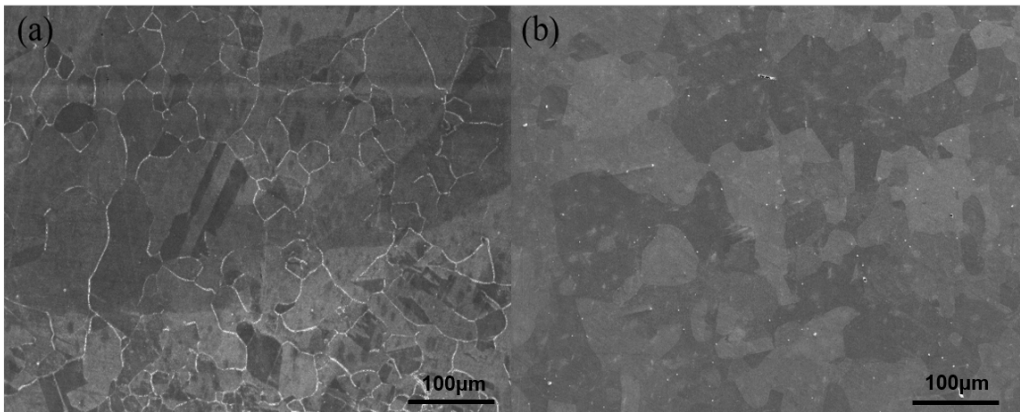

Figure 4.2 Secondary electron SEM images of recrystallized (a) Ni-Al and (b) Ni-Al-P.

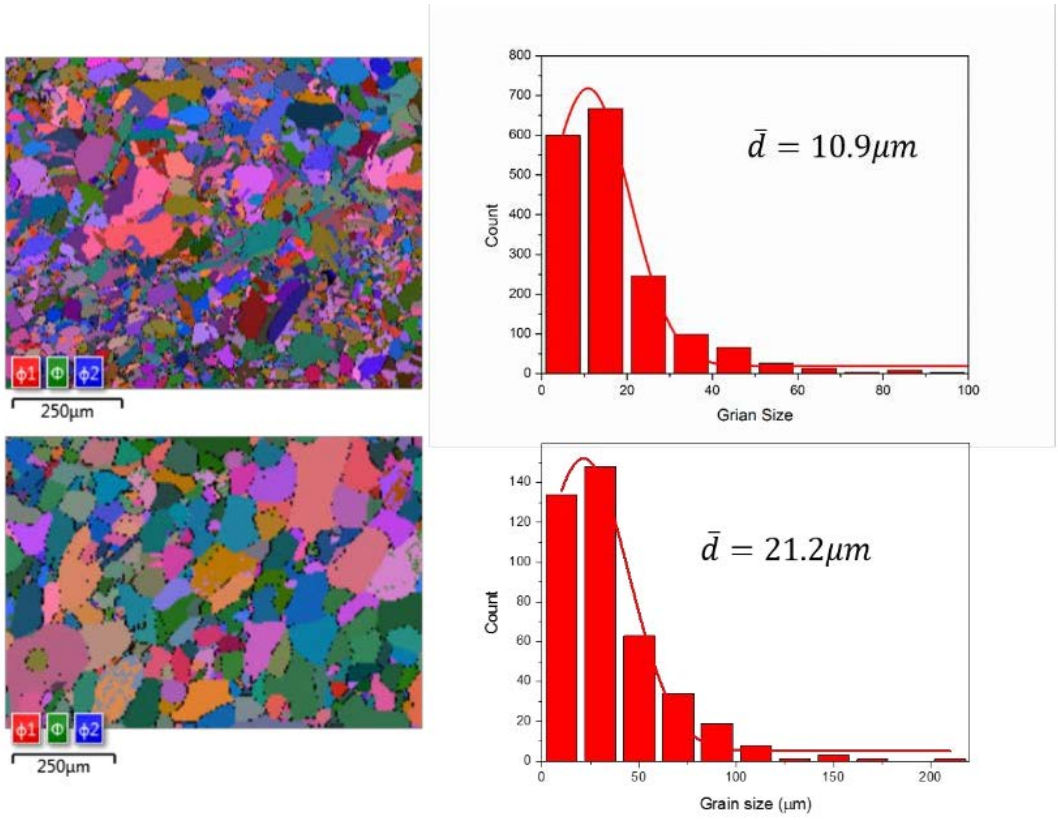

Figure 4.3 EBSD orientation map and grain size distribution of Ni-Al and Ni-Al-P.

The misorientation angle distributions of both samples are shown in figure 4.4. With the addition of P, the fraction of boundaries with a misorientation of about 60º decreases dramatically. According to coincidence site lattice (CSL) theory [81] and considering the maximum permitted deviation angle from the ideal CSL proposed by Brandon [79], these 60º GBs can be regarded as twin boundaries. Research indicates that P lowers the stacking fault energy [80], so why the addition of P reduces the twin boundary fraction remains unclear at this stage.

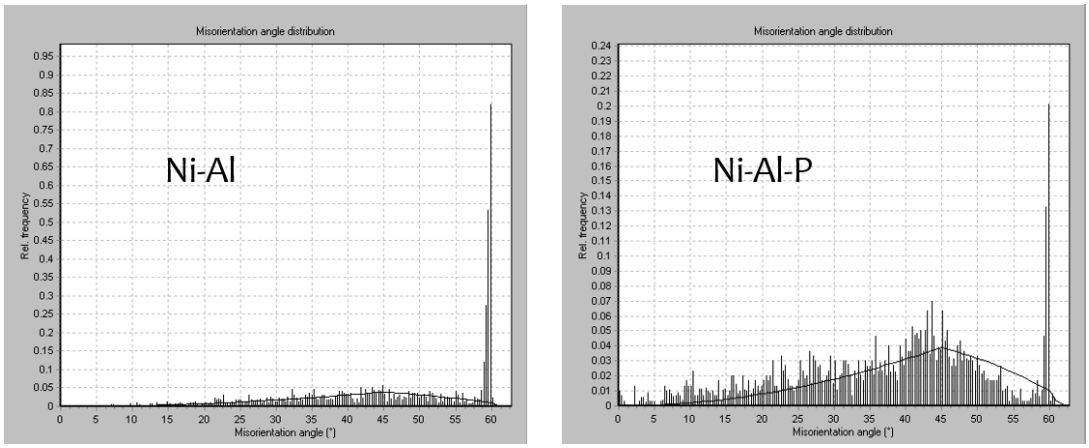

Figure 4.4 Misorientation angle distribution of Ni-Al and Ni-Al-P.

EBSD orientation maps of the samples with different cooling rates from 700 °C after recrystallization are shown in figure 4.5. The averaged grain size is about 40 μm. No obvious effect of the cooling rate on the grain size has been found.

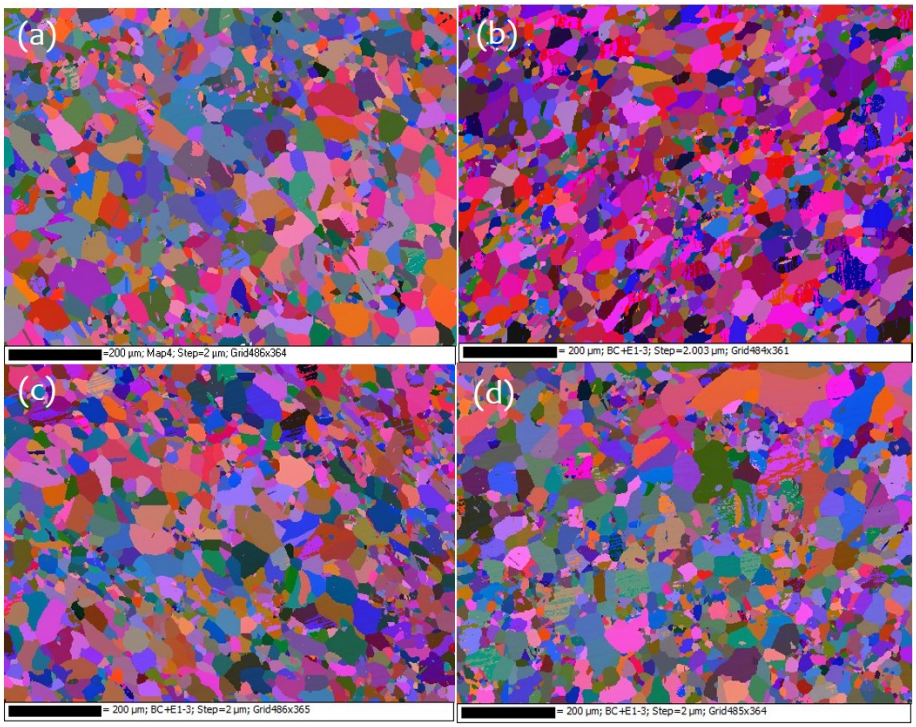

Figure 4.5 EBSD orientation map of Ni-Al-P samples cooled from 700 °C at different rates. (a) water quench, (b) air cooling (c) furnace cooling with door open and (d) furnace cooling with door closed.

Figure 4.6 shows the EBSD orientation map of Ni-Al-P after aging for 48 h at 500 °C. The average grain size is determined to be 140 µm.

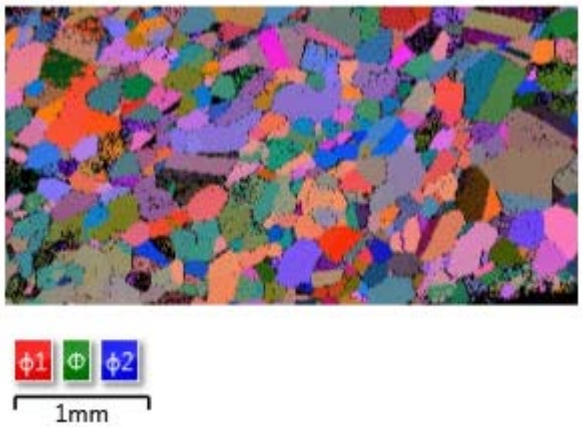

Figure 4.6 EBSD orientation map of Ni-Al-P after aging for 48h at 500 °C

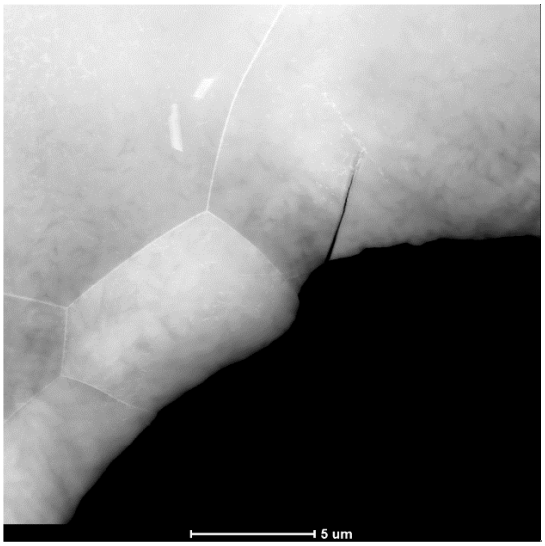

Figure 4.7 HAADF image of Ni-Al-P after water quenching following the recrystallization at 700 °C.

Figure 4.7 shows a TEM HAADF image of Ni-Al-P after water quenching from 700 °C. The sample is fully recrystallized without observable dislocations. Very occasionally, a precipitate with a size of about 300nm is observed in the matrix as shown in figure 4.8. EDS mapping in figure 4.8 indicates it is Al and O rich. Electron diffraction (not shown here) confirms the precipitate is Al_2O_3. This was probably introduced during the alloy melting.

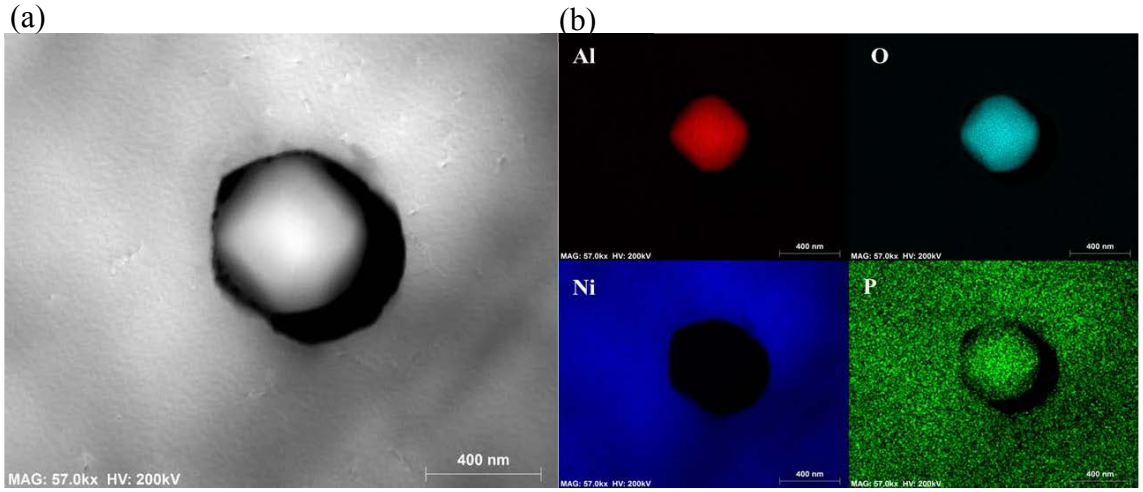

Figure 4.8 (a) HAADF image and (b) EDS maps of a precipitate in Ni-Al-P water quenched from 700 ºC.

4.2.2. GB segregation

Figure 4.9 shows typical GBs analysed in Ni-Al (a) and Ni-Al-P (c). The samples were tilted carefully until the projected GB width reached the minimum (less than 2nm) to achieve GB plane alignment with the incident electron beam. EDS analysis was conducted in spot mode at the GB and in the grain interior and the corresponding spectra are shown in figure 4.9 (b & d). In Ni-Al (figure 4.9b), there is no obvious difference between the spectra at the GB and in the grain interior. This is consistent with the line-scan results (not shown). In Ni-Al-P (figure 4.9d), an obvious peak from P exists in the spectrum obtained at the GB. It was much weaker in the grain interior, indicating the existence of GB P segregation. This is in agreement with the line-scan and mapping results shown in figure 4.10. Ni and Al are depleted at the GB, possibly due to the site competition [62]. It can be seen that the concentration along a GB does not vary very much. Also, the segregation thickness is about 10nm, which is in agreement with [170]. It was found there that the holding temperature, cooling rate and vacancy-solute binding energy strongly affected the segregation thickness. A higher holding temperature, lower cooling rate and smaller binding energy resulted in a wider segregation layer [118, 119].

Deconvolution based on the method described in [151] has been performed. Assuming a segregation layer of 2nm and a probe size of 0.73nm, the calculated concentration (C_{cal}) is slightly larger than the measured one (C_{meas}) with a relationship of $C_{cal} = 1.0012 C_{meas}$. The difference is even smaller than the standard error. The reason is a top-hat profile was assumed in [151] and the probe size is smaller than the thickness of the segregation layer. So this effect was neglected in this study.

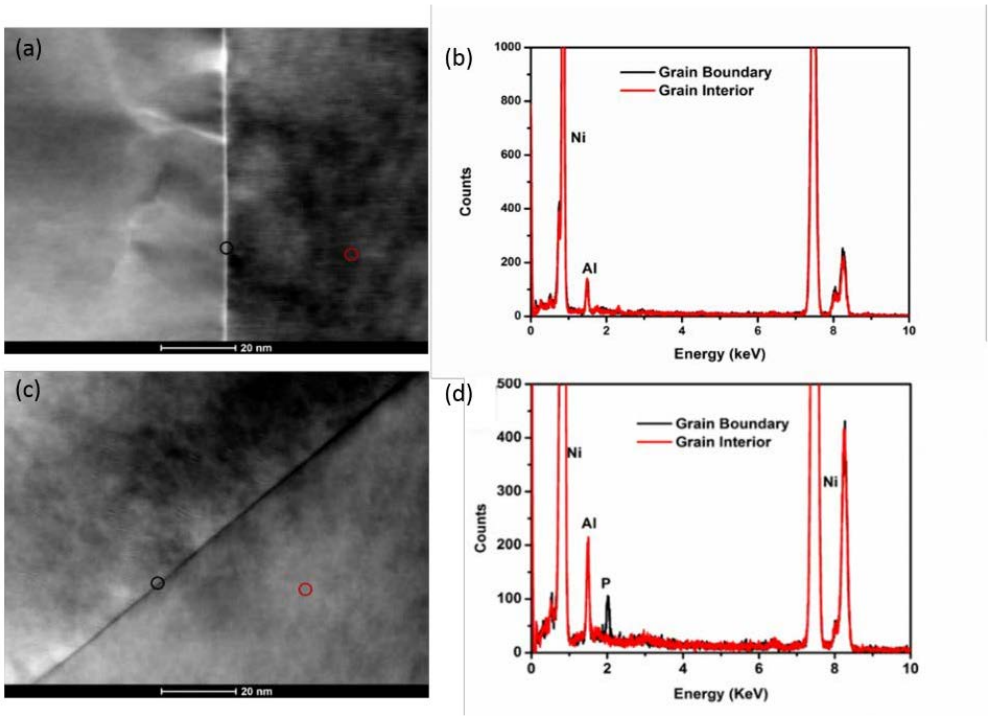

Figure 4.9 (a) (c) STEM-HAADF images of typical GBs and (b) (d) EDS spectra obtained from a GB and the grain interior in Ni-Al (a&b) and Ni-Al-P (c&d) water-quenched from 700 ºC.

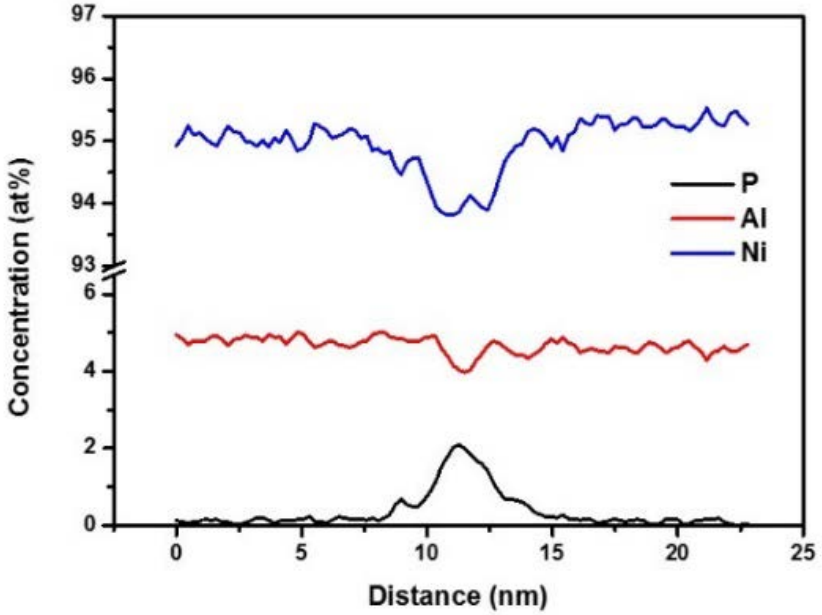

Figure 4.10 Line-scan profiles across the GB shown in figure 4.9 (c) for Ni-Al-P water-quenched from 700 ºC.

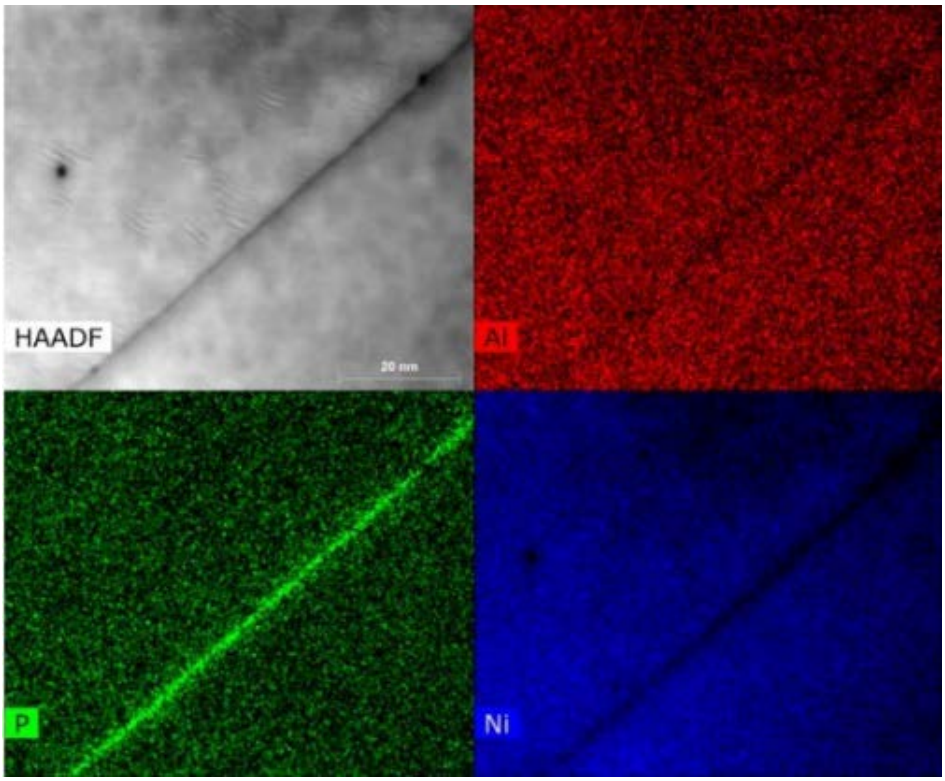

Figure 4.11 EDS maps of the GB shown in figure 4.9 (c) for Ni-Al-P water quenched from 700 ºC.

4.2.3 Effect of misorientation on the segregation concentration

To investigate the effect of GB misorientation on segregation, the misorientation angle is measured by first calculating the rotation matrix. There are several methods to obtain the rotation matrix [171-174]. Among these methods, the one proposed by Liu et al. [172] is relatively easy to operate. Only three different diffraction patterns from each grain are needed. In this work, a similar method to Liu et al. [172] but with a different coordination system was used. In their paper [172], they used [100], [010] and [001] to form the rotation matrix. In this work, the axes with corresponding (α, β) tilt angles of (0°, 0°), (0°, 90°) and (90°, 90°) which can be calculated from the obtained diffraction patterns were used. This method avoids the calculation of the angle when [100], [010] or [001] were parallel to the beam direction and also reduces the matrix calculations involved. Figure 4.12 shows an example of a GB and the corresponding diffraction patterns obtained from each grain. Then the rotation matrix of each

grain can be calculated as R_1 and R_2. The rotation matrix can be derived by $R=R_2*R_1^{-1}$. The misorientation angle can be deduced by the trace of R as $\theta=\arccos(\frac{tr(R)-1}{2})$. It should be noted here that the symmetry of the cubic structure should be considered. 24 equivalent combinations of misorientation angle and rotation axis could be obtained. The one with the smallest misorientation angle was adopted.

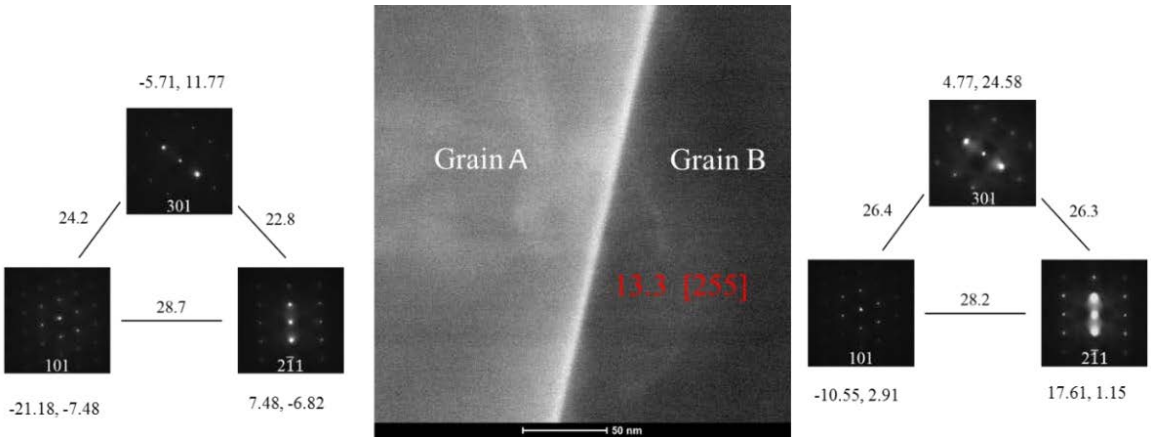

Figure 4.12 HAADF image of a low angle GB (13.3º) in Ni-Al-P and corresponding SAD patterns together with the tilt angle and the angles between two zone axes.

To verify the accuracy of this method, 10 randomly selected GBs were characterised both by SAD and transmission Kikuchi diffraction (TKD). For TKD, orientation determination is based on the calculation of the orientation of the corresponding crystal lattice with respect to a reference frame. Normally a sample reference frame is used and a sequence of rotations is applied to bring the sample's frame into coincidence with the crystal lattice frame. More details can be found in [175]. The results are shown in figure 4.13. It can be seen that the difference between SAD and TKD is less than 1°, indicating a high accuracy for this method. Using electron diffraction in a TEM enables the study of GB at the thickness much greater than that possible in a TKD.

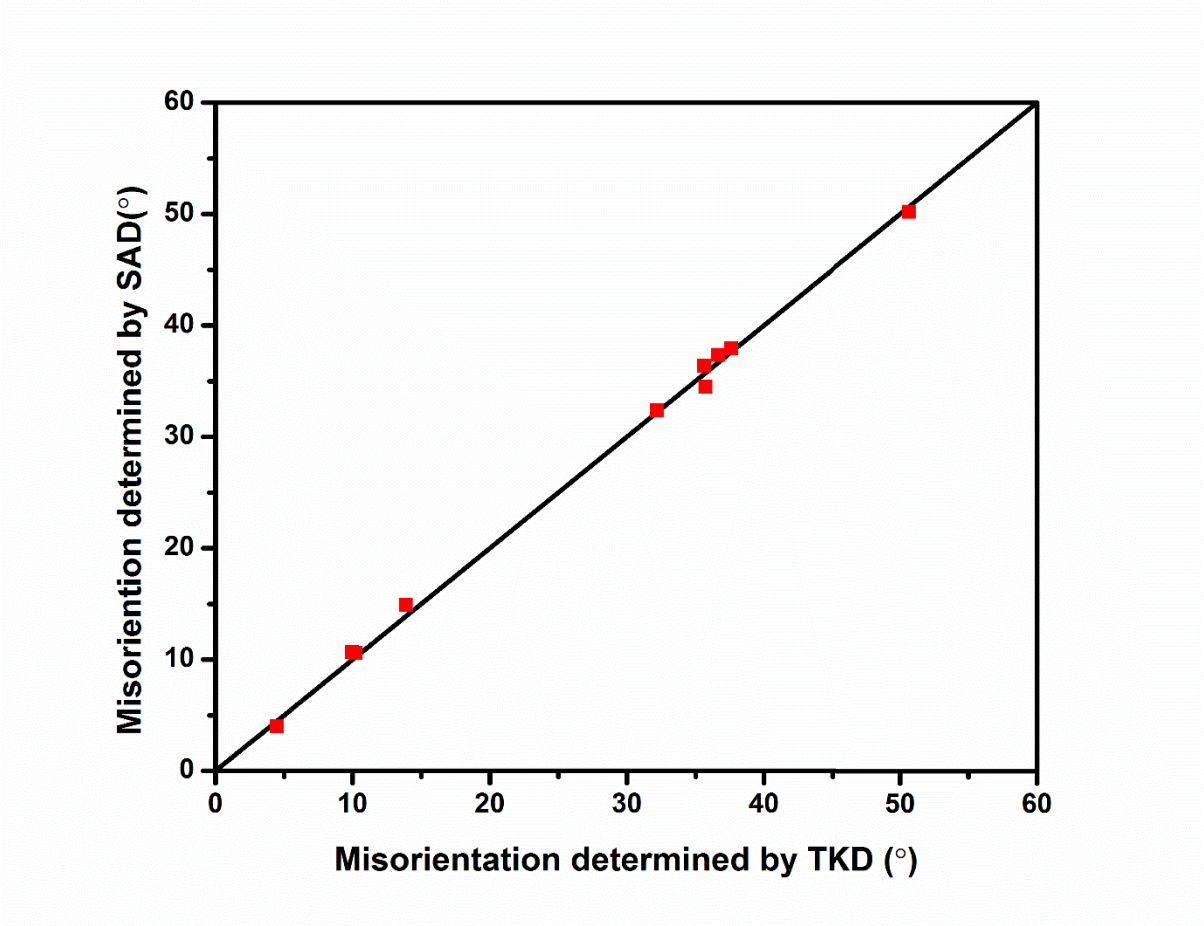

Figure 4.13 Comparison of the misorientation angles measured by SAD and TKD from 10 randomly selected GBs

Figure 4.14 shows the profiles obtained from GBs in Ni-Al-P alloy water-quenched from 700 º C with low misorientation angle (13º), high angle (45º) and twin boundary (60º). The high angle GB concentration is much higher than that of the low angle GB, while no segregation to the twin boundary was detected.

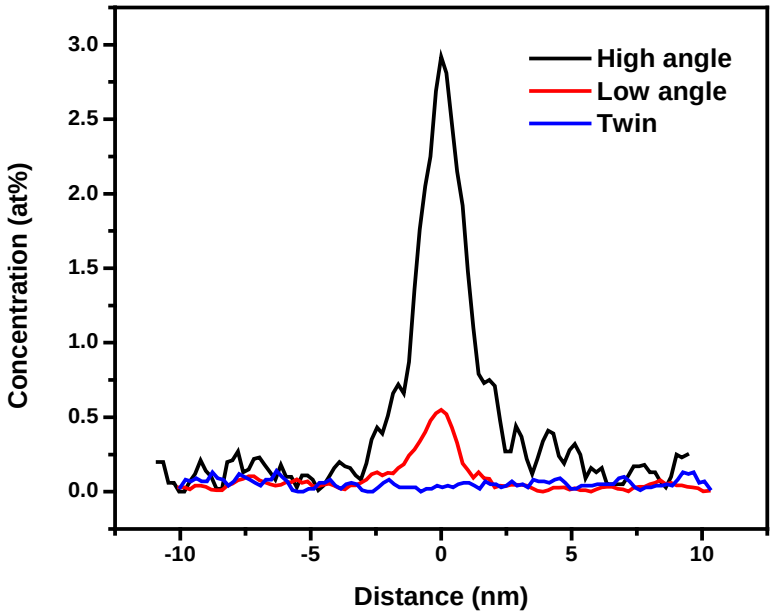

Figure 4.14 P profiles obtained from high angle GB, low angle GB and twin boundary in Ni-Al-P water-quenched from 700 ºC.

At least four point analyses were made from each GB. The detailed relationship between the misorientation and P concentration at GBs in Ni-Al-P water quenched from 700 ºC is shown in figure 4.15. With increasing misorientation, the P concentration increased until about 45°. A further increase of the misorientaion angle results in a decline in the segregation level. For Σ3 twin boundary, no obvious segregation was detected.

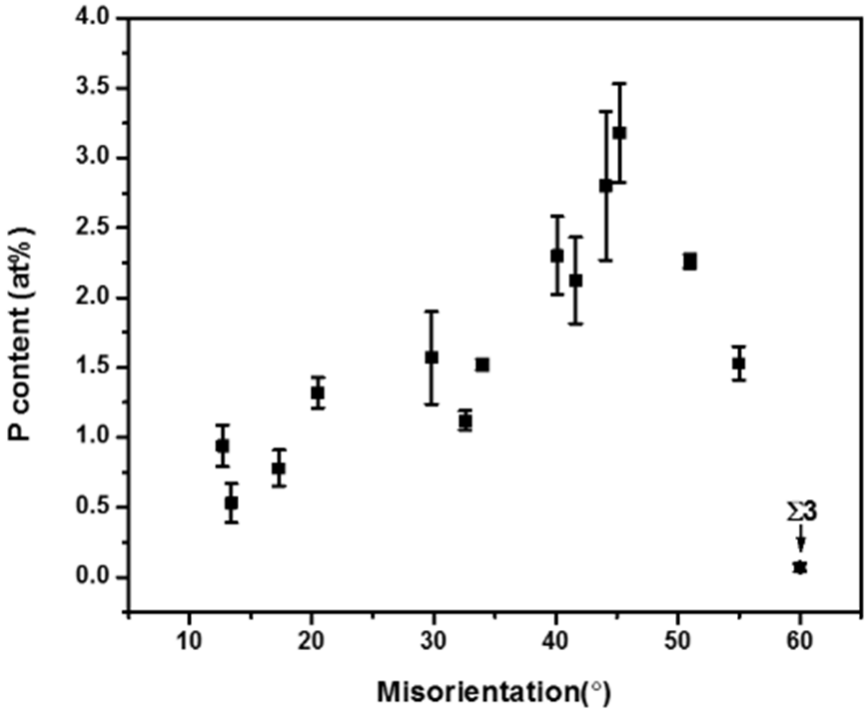

Figure 4.15 Measured effect of misorientation angle on the averaged grain boundary concentration of P in Ni-Al-P water quenched from 700 ºC.

4.2.4 TJ segregation in Ni-Al-P

As the GB concentration is misorientation angle dependent, different segregation levels are expected at GBs close to a triple junction. It is of interest to investigate the composition at triple junctions.

Figures 4.16 (a&b) show HAADF images of two TJs in Ni-Al-P water-quenched from 700 ºC where in each case all 3 associated GBs were tilted to align with the electron beam. The misorientation angles associated with the individual GBs (varing between 32 and 55 degrees) were determined and are listed in table 4.2. EDS Spectra collected from the TJs and the grain interior next to the TJs are shown in Figures 4.16 (c&d). Obviously high P peaks can be seen in the spectra collected from the TJ but not in those from the grain interior, indicating

segregation of P to the TJ. This is more obvious in the line-scan results shown in Figures 4.16 (e&f). The P concentrations are 2.71 at% and 4.80 at% for TJ-I and TJ-II, respectively.

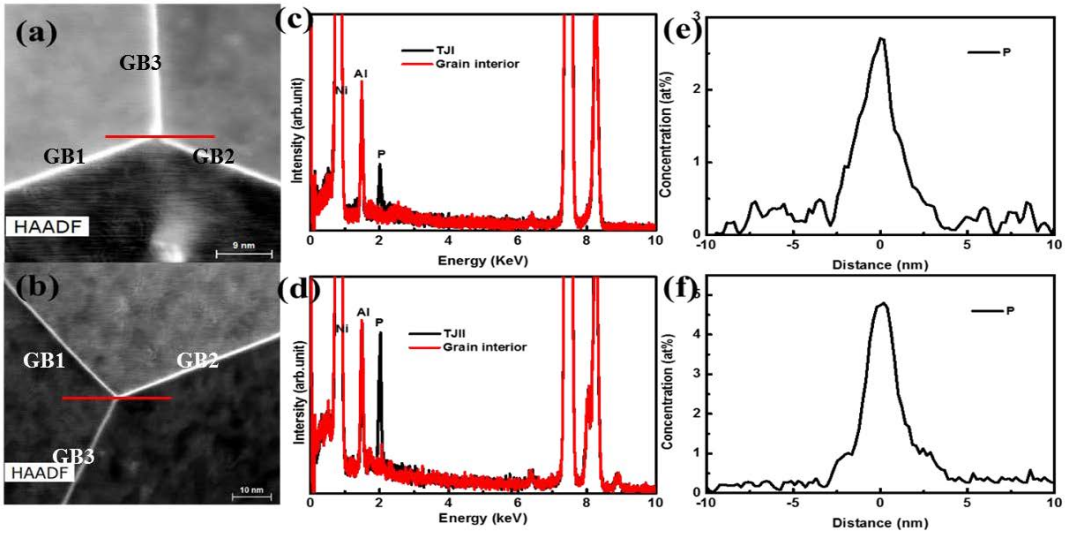

Figure 4.16 (a-b) HAADF image of TJ-I and TJ-II, (c-d) spectra collected from the TJs and the grain interiors and (e-f) P concentration profiles obtained from the line-scan across TJ-I and TJ-II as shown in (a-b).

Table 4.2 The misorientation angles associated with each GB and the P concentration measured from each GB, TJ and matrix in a Ni-Al-P sample water quenched from 700 ºC.

TJ	GB	Misorientation angle (°)	GB concentration (at%)	TJ concentration (at%)	Matrix concentration (at%)
TJ-I	GB1	40.8	4.01	2.71	0.09
	GB2	42.0	3.89		
	GB3	53.2	1.78		
TJ-II	GB1	43.9	4.12	4.80	0.09
	GB2	32.7	3.25		
	GB3	55.3	1.59		

Figure 4.17 shows EDS elemental maps obtained from the two TJs. GB and TJ segregation of P are obvious. As shown in table 4.2, the P concentrations at different GBs are different in that GB3 has an obviously lower value of segregation than GB1 and GB2, in both cases. This is shown more clearly in figure 4.18 which presents the spectra collected from the TJs, GBs and grain interiors. The P concentrations at GBs with misorientation angles of 40-44 º (i.e. GB1 and GB2 associated with TJ-I and GB1 associated with TJ-II) are higher than that at GBs with misorientation angles of 33º, 53º and 55º. This is consistent with the results shown in figure 4.15.

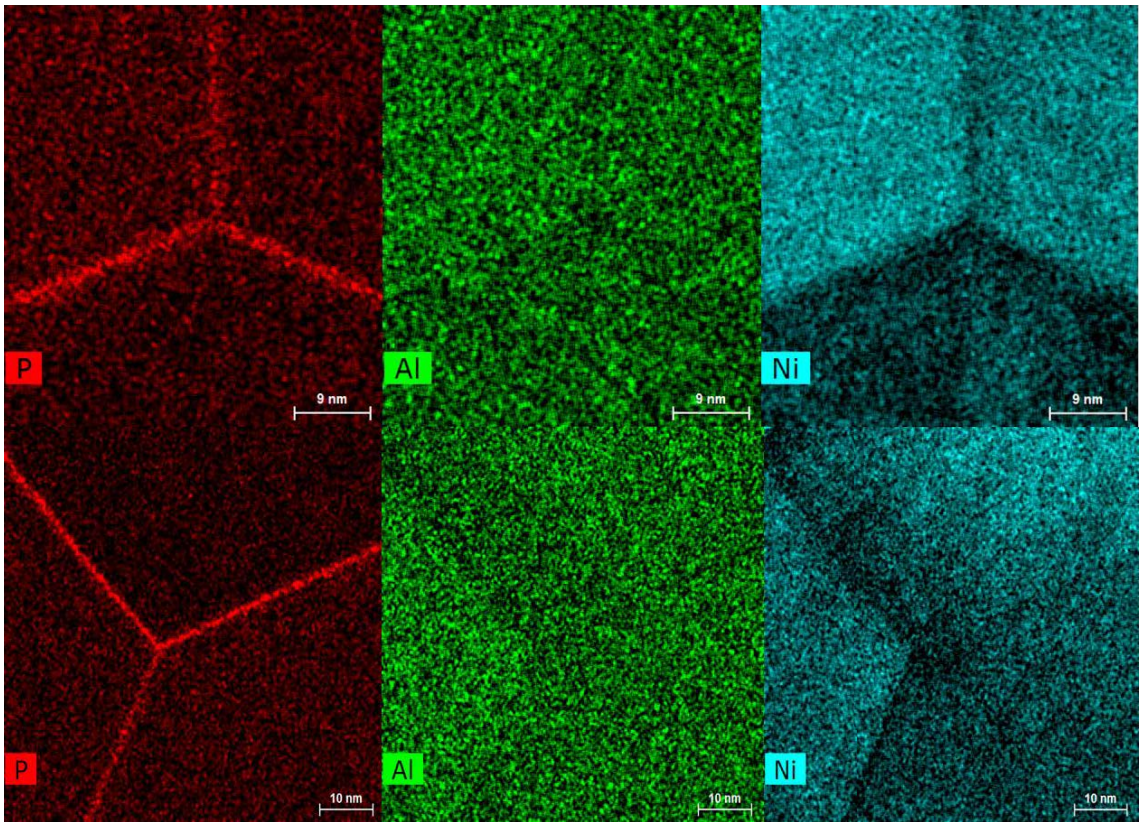

Figure 4.17 EDS elemental mapping of TJ-I (upper) and TJ-II (lower)

Figure 4.18 also shows that the P concentration at TJ-I is higher than that at GB3 but lower than that at GB1 and GB2, while the P concentration at TJ-II is higher than all the constituent GBs, consistent with the mapping results in figure 4.17.

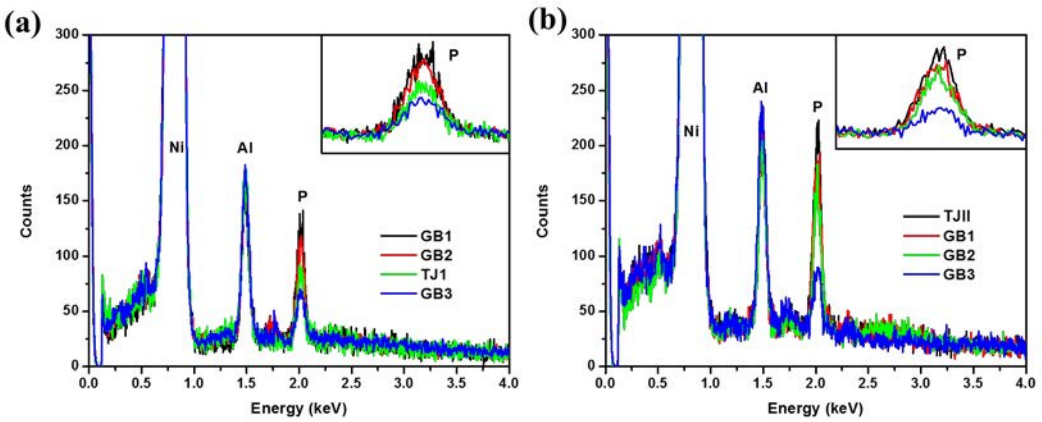

Figure 4.18 Comparison of the spectra collected from (a) TJ-I and (b) TJ-II and constituent GBs shown in figure 4.16.

In the above measurements, the P concentrations at the GBs were measured from positions located at least a few hundred nanometres away from the TJs. The P concentrations along the GBs towards TJ-I were also measured and the results are shown in figure 4.19. While the concentration of P at TJ-I is about 2.71 at%, the concentration of P increased to about 3.89 at% over a distance of about 100 nm from TJ-I along GB2. The concentration of P decreased from 2.71 at% at TJ-I to about 1.78 at% over a distance of about 40 nm along GB3. The P concentration profile along GB1 is characterized by a sharp increase to about 4.01 at% within 5 nm from TJ-I.

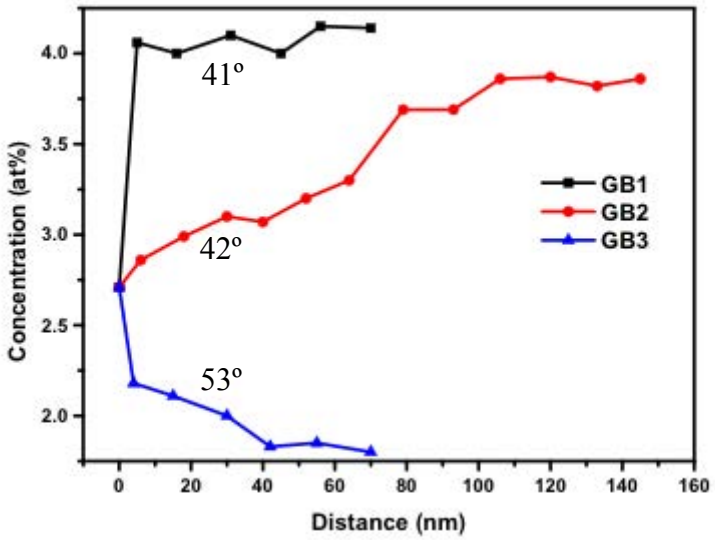

Figure 4.19 P concentration profile at the GB measured versus distance from TJ-I along GBs with different misorientation angle (shown in the image).

4.2.5 Effect of grain size

TEM samples with two different grain sizes were prepared to investigate the effect of the grain size on GB P segregation in Ni-Al-P water quenched from 700 ºC. Figure 4.20 shows secondary electron images of each sample. It can been seen that the grain size of sample A (~60 μm) is much larger than that of sample B (~40 μm).

Figure 4.21 illustrates the P concentration profile obtained from GBs with a similar misorientation angle from each sample. The GB concentration from sample A with a larger grain size is much lower than that from sample B.

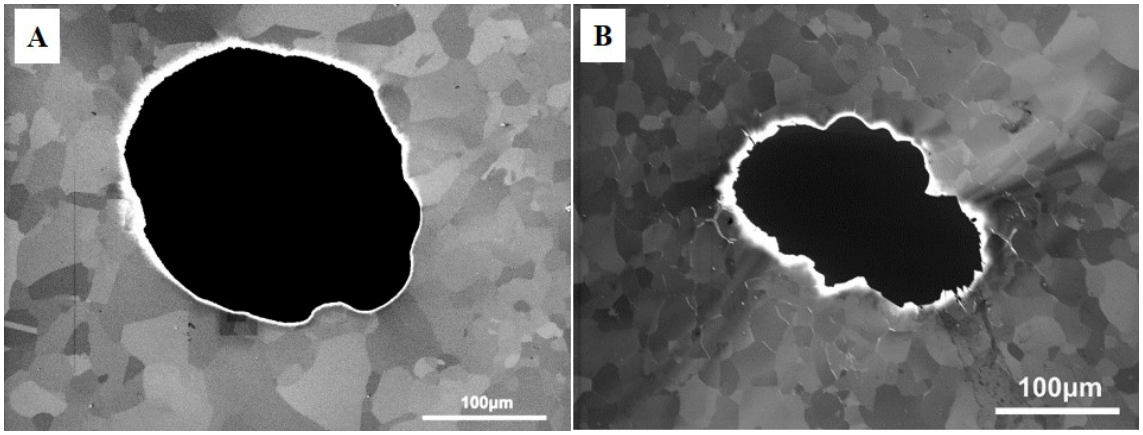

Figure 4.20 Secondary electron images of two samples with different grain sizes in Ni-Al-P water quenched from 700 ºC.

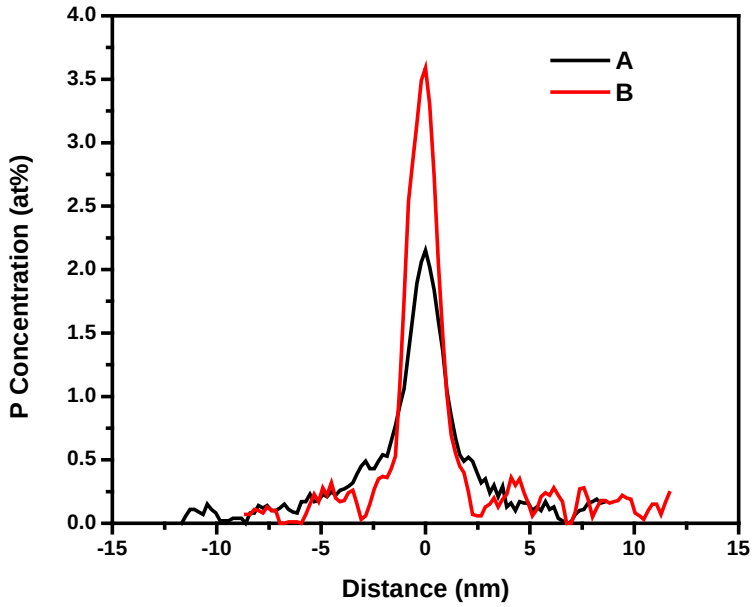

Figure 4.21 P profiles collected across two GBs with similar misorientation angles of 33º from sample A (of larger grain size) and B (of smaller grain size)

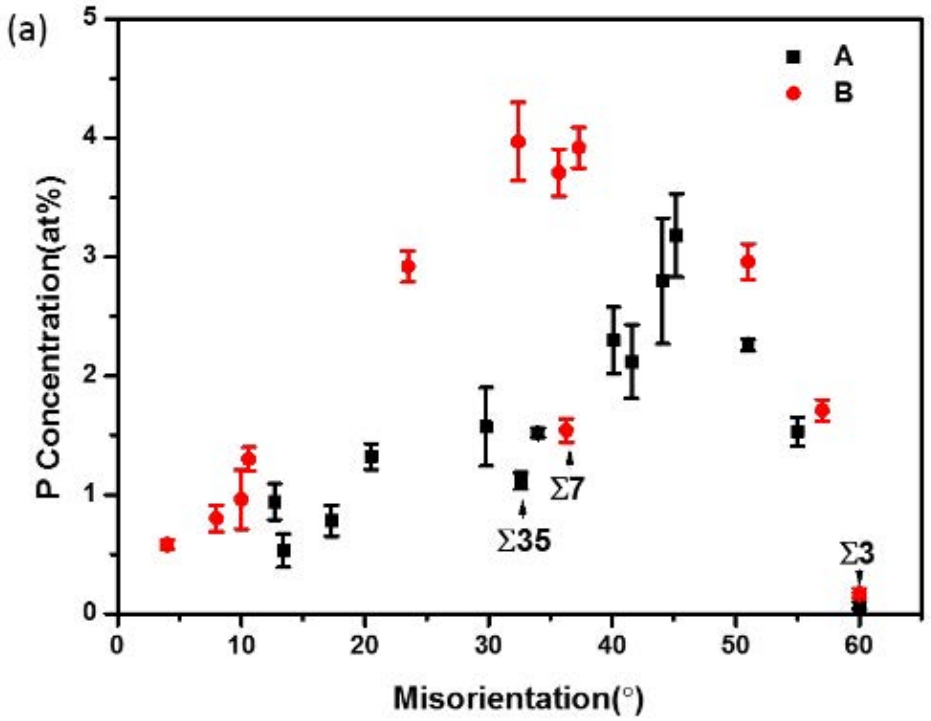

Figure 4.22 GB concentration versus GB misorientation angles in the Ni-Al-P alloy water quenching from 700 ºC showing the effect of grain size. The grain size of sample A is larger than sample B.

The P GB concentrations measured in both samples are shown as a function of misorientation in figure 4.22. The GB content of P in sample B increases with increasing misorientation angle until 40° and then decreases. The special GBs with Σ3 and Σ7 are both low. This is consistent with the results shown in figure 4.15. Also, the GB concentrations of P in sample B is always higher than for sample A with the larger grain size.

4.2.6 Effect of cooling rate and aging time

The cooling rates for water quenching, air cooling, furnace cooling with open door and furnace cooling from 700 °C are estimated to be 200 ºC/s, 10 ºC /s, 0.5 ºC /s and 0.1 ºC /s, respectively. The effect of cooling rate on the GB concentration of P is illustrated in figure

4.23. With a cooling rate of 0.5 °C /s, the concentration is the highest. A quicker or slower cooling will result in a lower P concentration at the GB.

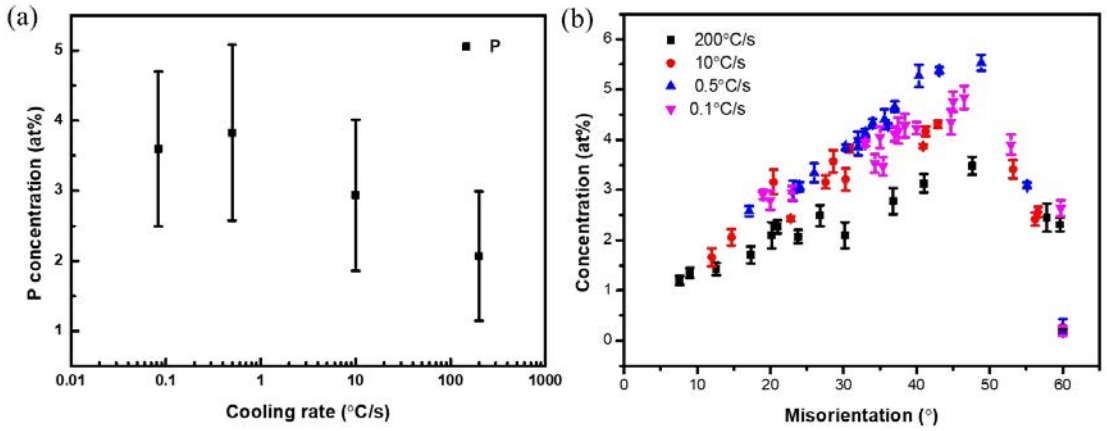

Figure 4.23 (a) Effect of cooling rate from 700 °C on the GB concentration of P and (b) GB P concentration versus misorientation showing the effect of cooling rate on the GB concentration of P

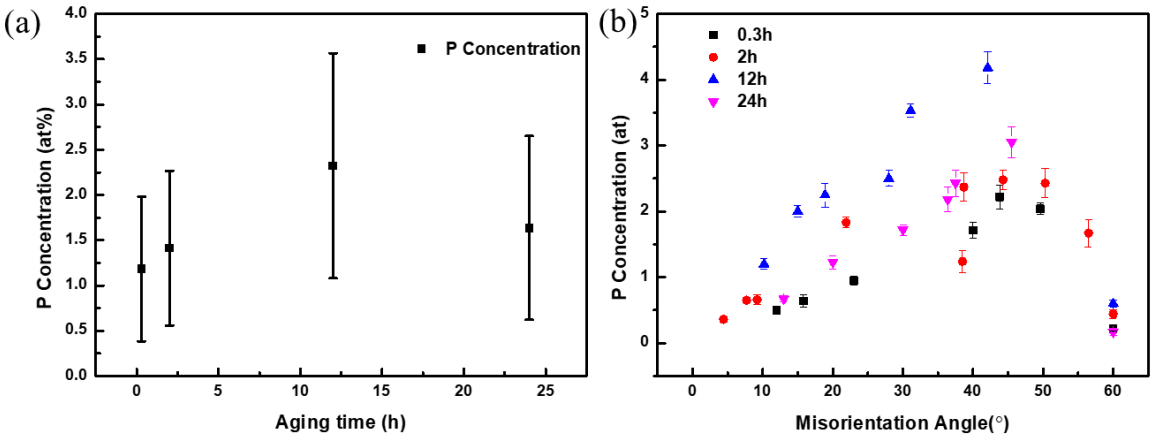

Figure 4.24 (a)Effect of aging time at 500 °C on the GB concentration of P and (b) GB P concentration versus misorientation showing the effect of aging time at 500 °C on the GB concentration of P

Following a water quench from 1000 °C, the aging time dependence at 500 °C of the GB concentration of P is shown in figure 4.24. It can be seen that the GB concentration of P increases with aging time until 12h. A further increase of aging time leads to a reduction in the P concentration.

4.3 Discussion and analysis

4.3.1 ES and NES

For a quenched sample, the segregation is developed during high temperature holding or quenching because segregation at room temperature can be neglected due to the low diffusion rate (see below). However, the diffusion mechanisms during these two stages are different. On holding at high temperature, ES takes place. P diffuses to the GB through a vacancy-mediated mechanism. The driving force is the energy difference between two states in which P is either in the grain interior or at the GB [16]. In both states, lattice distortions are induced by P. However, the distortion is smaller at the GB due to the free volume of the GB. For NES during quenching, P diffuses to the GB via P-vacancy complexes. At high temperature, the concentrations of vacancies (V), solute atoms (P) and complexes (C) are in equilibrium. During cooling or aging, a new equilibrium between V, P and C is set up at the GB with a lower concentration of the complexes as GBs are vacancy sinks. In the grain interior, the concentration of vacancies remains and the concentration of complexes increases according to equation 2.21. This results in a concentration gradient of the complexes and acts as the driving force for P to segregate to the GB. Complexes decompose at the GB, resulting in a pileup of P at GB [107]. At the same time, P back-diffuses to the grain interior via vacancies due to the P gradient between the GB and the grain interior. At first, diffusion of the complexes dominates. After a particular time, diffusion of P to the grain interior dominates. This particular time is called the critical time at which the segregation concentration reaches the maximum [107].

The critical time can be calculated as [1, 3] (see Appendix A26 and equation 2.25)

$$t_c = \frac{r^2 \ln(D_c/D_i)}{\delta(D_c - D_i)} \quad 4.1$$

where r is the grain radius, δ the critical time constant, and D_c and D_i the diffusion coefficients for complex and solute, respectively.

Table 4. 3 Parameters used in the calculation of the critical time [68].

Self-diffusion coefficient of Ni, m^2s^{-1}	1.27×10^{-4}exp(-2.9 eV/kT)
Vacancy formation energy, eV	1.5
Diffusion coefficient of P in Ni, m^2s^{-1}	1×10^{-8}exp(-1.78 eV/kT)
Diffusion coefficient of complexes, m^2s^{-1}	4.23×10^{-5}exp(-1.4 eV/kT)
Critical time constant δ	47
P-vacancy binding energy, eV	0.33
P matrix concentration, at%	0.1
Grain size, μm	40

Calculated using the parameters list in table 4.3 [68], the critical time is about 12.8s and 5.9×10^{17}s at 700 ˚C and room temperature, respectively. That is why the segregation at room temperature can be neglected.

During quenching, another parameter called the effective time is used to characterize the segregation. By dividing the cooling curve into n steps each with a holding time of t_j at temperature of T_j, the effective time equivalent to holding at T_i can be calculated by assuming that the diffusion distance during the j^{th} step is the same as holding at T_i for t_e^j, where

$$D_c(T_i)t_e^j = D_c(T_j)t_j \quad (4.2)$$

Then the effective time can be calculated by summing the t_e^j as [103]

$$t_e = \sum_{j=1}^{n} t_j \exp(-E_A(T_i - T_j)/kT_iT_j) \quad (4.3)$$

where E_A is the activation energy of the complex diffusion. Calculation of t_e requires the quench rate value, which is not available. However, as discussed in Ref. [118], the temperature as a function of cooling time may be approximated by

$$T = T_0 \exp(-\phi t) \quad (4.4)$$

where ϕ is the cooling rate parameter, which is $1s^{-1}$ for water quenching and small samples [118].

By using the effective time, the non-isothermal process can be made equivalent to an isothermal process. The effective time correspond to 450 ˚C was calculated as 17.98s on cooling from 700 ˚C, which means that the GB segregation developed during cooling process is equal to that developed during a holding time of 17.98s at 450 ˚C. It should be noted here that the contribution from each step is quite different as the diffusion coefficient is different. Figure 4.25 shows the effective time of each step with a holding time of t_j at temperature of T_j and the total effective time by temperature T. It can be seen that the effective time decreases with temperature. Below 450 ˚C, the effective time at each step can be neglected.

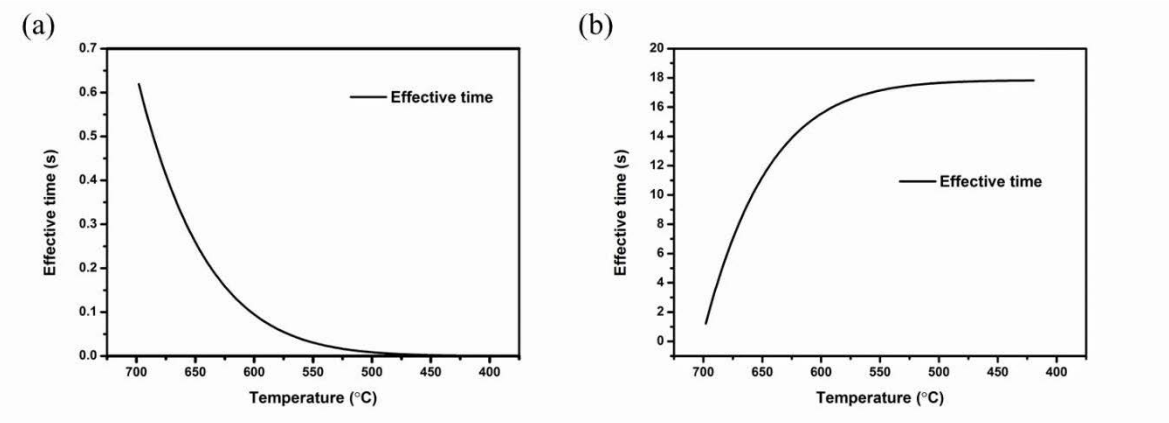

Figure 4.25 (a) The effective time of each step and (b) the total effective time at different temperatures corresponding to 450 ˚C when water quenched from 700 ˚C. The holding time for each step is 0.002s

If neglecting the NES process during the aging at room temperature, the measured concentration of P at GB can be attributed to the combination of ES when holding at high temperature and NES during quenching.

The maximum ES concentration can be calculated by [16] (see equation 2.5)

$$\frac{C_{gb}^{m}}{1-C_{gb}^{m}} = \frac{C_0}{1-C_0}\exp\left(-\frac{\Delta G}{RT}\right) \qquad 4.5$$

Where C_0 is the bulk concentration (0.1 at%) and ΔG is the segregation energy. No available data has been found for the segregation energy of P in Ni. According to the results in section 4.2.6, the P concentration aged at 500 ˚C for 24h is only less than 1.5 at%. The time to reach 90% ES concentration can be estimated as 19h [176]. This means ES has been reached. Using 1.5 at%, the segregation free energy can be calculated as -17.4kJ/mol. Then the maximum ES concentration at 700 ˚C can be calculated as 0.86 at%, which is small enough and can be neglected. Another reason that ES was not considered is the low diffusion coefficient of P via

vacancy. Using the parameters list in table 4.3, the diffusion coefficient of P via vacancy can be calculated and is 6 orders lower than that of P via complexes.

NES during quenching can be calculated by considering the iso-thermal kinetics and the effective time. When annealing at temperature T, the GB concentration at the segregation stage, $C_{bs}(t)$, is given by [3, 115] (see equation 2.28)

$$\frac{C_{bs}(t)-C_g}{C_b^m(T)-C_g}=1-\exp\left(\frac{4D_ct}{\alpha^2\theta^2}\right)\mathrm{erfc}\left(\frac{2\sqrt{D_ct}}{\alpha\theta}\right) \tag{4.5}$$

where $C_b^m(T)$ is the maximum NES level during cooling from T_0 to T, C_g the bulk concentration and α is the NES ratio, given by $C_b^m(T)/C_g$, θ is the segregation width, 10nm in this work. At the desegregation stage, P diffuses from the GB to the bulk via vacancies. So the GB concentration at the desegregation stage can be written as [3, 115] (see Appendix A36 and equation 2.29)

$$C_{bd}(t)=C_g+\left\{\frac{\left[C_{bs}(t_c)-C_g\right]}{2}\right\}*\left\{\mathrm{erf}\left[\frac{\theta}{\sqrt{16D_i(t-t_c)}}\right]-\mathrm{erf}\left[-\frac{\theta}{\sqrt{16D_i(t-t_c)}}\right]\right\} \tag{4.6}$$

$C_b^m(T)$ after cooling from T_0 to T_L can be calculated by (see Appendix A42 and equation 2.24)

$$C_b^m(\mathrm{T})=C_g\frac{E_b^{vs}}{E_f^v}\exp\left(\frac{E_b^{vs}-E_f^v}{kT_0}-\frac{E_b^{vs}-E_f^v}{kT_i}\right) \tag{4.7}$$

where E_b^{vs} is the binding energy of the vacancy to the solute P and E_f^v is the vacancy formation energy. According to [148], an appropriate T_i should be chosen rather than room temperature because diffusion can be neglected below a certain temperature. For example, 580 ˚C was chosen when calculating the NES of P in a 2.25Cr-1Mo steel in [148], while 450 ˚C was used to calculate the NES of B in a Fe-30Ni% alloy, Al in Inconel 600, Cr in 2.25Cr-1Mo steel and

Sn in 2.25Cr-1Mo-0.08Sn in [115]. As stated in [148], the calculated result is sensitive to the chosen temperature below which the diffusion can be neglected. Three different temperatures were chosen for the calculation: 400 ˚C, 450 ˚C and 500 ˚C. Using the parameter list in table 4.3, the concentrations were calculated and are compared with the experimental results in table 4.4. When the chosen temperature T_i increases from 400 to 500 ˚C, the maximum NES level decreases dramatically, as well as the theoretical concentration of P during quenching. The calculated results are consistent with experimental results, especially when the temperature T_h is chosen to be 450 ˚C.

Table 4.4 Calculated and experimental P concentrations after water quenching

Temperature T_h, ˚C	400	450	500
$C_b^m(T_h)$, at%	11.00	2.73	0.81
$C_b(t_e)$ (cal.), at%	5.08	2.19	0.76
$C_b(t_e)$ (exp.), at%	1.71±0.98		

According to [107], equation 4.7 is based on an assumption that the concentration of the complex in the grain interior remained consistent during cooling and thus the equilibrium concentration of the complex at the GB is equal to that in the grain interior at high temperature. However, a calculation of the concentration of the complex in section 2.4.1 indicated that the complex concentration at low temperature is much lower than that at high temperature. Also, the complex concentration decreases with decreasing temperature. So, the assumption made in [107] would overestimate solute concentration at the GB, especially for low temperature.

Though accurate decoupling the ES and NES is not possible in this work, the calculated diffusion coefficients of P and of the complexes indicate that the diffusion of the complexes is much quicker than that of P via vacancies, meaning that NES made the dominant contribution

to the measured concentration. Another piece of evidence of the dominant NES is the segregation width, which is about 10nm. Due to the different mechanisms of ES and NES, the resultant segregation profiles are also different in each case. For ES, the driving force is the energy difference when the solute atom locates in the matrix or at the GB. Only when the solute atom takes the GB site, which is several atomic layers thick, can the system energy be reduced. So the segregation profile is very narrow with a top-hat shape [177]. For NES, the driving force is the concentration gradient of the complex. Thus a broader profile is expected. Though the measured profile will be wider than the theoretical profile due to beam broadening, Monte Carlo simulation shows that the full width at tenth maximum of the probe profile in the exit surface is less than 2nm. This will not produce a measured profile with a width of about 10nm, which is the typical width of the GB segregation measured. This means that NES dominates the segregation process although ES may also exist.

There are two methods to decouple accurately ES from NES. One is in-situ heating, which has received increasing attention during the past several years due to the development of in-situ instruments [178]. The other is via minimizing the effective time by changing the cooling rate. If the cooling rate is high enough, the effective time will be small enough to be neglected. Then the measured results can be attributed to ES [102].

4.3.2 Effect of misorientation

The difference arises from the different GB configurations. With increasing misorientation, the GB becomes more irregular. More available sites can be supplied for P to segregate to [179]. By atomistic molecular dynamics simulation, the GB free volume has been found to increase with misorientation angle until 50°, and then to decrease (figure 2.3) [55]. This is consistent with the results by first-principle calculations [56]. However, some special GBs like twin boundaries are exceptional. These GBs are much more regular than normal large angle GBs and the number of available sites for P to occupy is much smaller than for a random large angle

GB. This results in a lower GB concentration of P. This is consistent with the results reported in [54].

4.3.3 TJ segregation

To the author's best knowledge, Yin et al [180] reported the first experimental measurement of TJ chemical composition, performed using EDS on a nano-crystalline Cu sample. While their experiment clearly showed the segregation of Bi to the GB and TJ, no experimental details about the alignment of the GBs and the TJ with the electron beam were given. As mentioned earlier the alignment of a TJ with the electron beam in a nano-crystalline sample is practically very difficult. Based on a purposely prepared tricrystal foil, Sorbello et al [168] observed the segregation of impurity elements (P and Sn) to a TJ after tilting one of the three GBs to an edge on condition. More recently, 3D atom probe studies [181-183] have reported the segregation of Bi to the TJs in Ni and C segregation to TJs in steel. Molecular dynamics and Monte Carlo simulations indicated that Mg segregated to TJs in Al and resulted in the formation of nuclei of an ordered phase [184]. Due to the existence of free volume at the TJ, it can serve as a vacancy sink, just like a GB and a surface [185]. In the present work, it is likely that the fast cooling during the water quench from 700 °C led to vacancy annihilation at the TJ and hence to a concentration gradient between the grain interior and the TJ. The subsequent diffusion of the solute-vacancy complexes to the TJ thus led to the observed TJ segregation. As suggested in [180], the different TJ concentrations measured can be attributed to the structural differences between the TJs which are dependent on the misorientation angles and planes of the constituent grain boundaries. A quantitative relationship is currently not available and also out of the scope of the current thesis, due to the complexity of the TJ structure. The number of degrees of freedom needed to describe a TJ and the constituent grain boundaries suggest that misorientation is, but not the sole parameter that one should consider in defining the structure and therefore understanding the chemical segregation to a TJ.

It is generally agreed that a TJ has a larger free volume and therefore a faster diffusion path than the constituent GBs. For instance, the TJ diffusion coefficients of Ni in Cu [181-183], Zn in Al [58] and Ge in Si [164] are 2-3 orders of magnitude higher than the corresponding GB diffusion coefficients. Molecular dynamics simulation [163] has also confirmed that TJ segregation would be expected to be larger due to the large free volume. This is consistent with the experimental results of Bi in Cu where the Bi concentration at TJ was higher than those at both a special GB and at random large angle GBs [180]. Monte Carlo simulation results also indicate that Pd segregated to the TJ more than to special GBs [186]. According to this, one would expect that the P concentration at TJs should always be higher than that at GBs. However, this contradicts the current results which show that the P concentration at the TJ can be lower than that at the constituent grain boundaries (cf. 2.71 at% at TJ-1 versus 4.01 at% at GB1 and 3.89 at% at GB2). This suggests that the free volume is not the only factor that determines the TJ segregation level. Although the electron probe size is small (0.73 nm), the electron beam spreading within the specimen may lead to an underestimate of the segregation level, but in fact the higher P concentration at TJ-2 than that at all three constituent GBs implies that the P segregation measurement at the TJ cannot be controlled by electron beam spreading.

Using Monte Carlo simulation, the segregation of Y in Mg to a TJ composed of 2 twin boundaries and 1 random high angle GB was investigated [169]. It was found that the Y concentration at the TJ is composition dependent and can be lower than for a random high angle GB and even a twin boundary although the average free volume of TJ was always higher than that of the other GBs. Some of the fee volume cannot serve as segregation sites due to a large anisotropic factor [169]. In addition the anisotropic factor of the free volume, the shortest interatomic distance and coordination number of Mg at the TJ were regarded as secondary factors affecting the Y segregation. The simulation results suggested that high free volume,

small anisotropic factor, large nearest atomic neighbour distance and high coordination number enhance the segregation level [169].

Another possible reason that TJ concentration is not necessarily higher than GBs can be explained by the binding energy and the activation energy of vacancy diffusion. As discussed in [107], vacancy annihilation at a GB results in a gradient of the complex and the enrichment of solutes at a GB. Vacancy annihilation depends on diffusion along the GB [187]. If the vacancy migration energy is small, the vacancy will find an interstitial site and annihilate. So, GB diffusion of vacancies plays a key role in determining the segregation level [185]. Using molecular statics modelling along with the nudged elastic band method, the binding energy between a vacancy and the GB and the activation energy of vacancy diffusion at several TJs in Al, Cu and Ni were calculated [185]. Due to a large binding energy with the TJ of up to 1.2 eV, the activation energy of vacancy diffusion at TJ in Ni was found to be larger than that in Al and Cu, within the range 2.26 eV to 2.57 eV. This can be higher than the activation energy of vacancy diffusion along GBs. For example, the activation energy of vacancy diffusion determined using molecular statics based on embedded-atom-method potentials was below 1.8 eV along Σ5 (210) boundaries in Ni [188], which is consistent with other calculations for Σ5 (1.5 eV), Σ11 (1.8 eV) and Σ37 (1.7 eV) GBs [59]. Therefore, the higher activation energy for vacancy diffusion contributes to a lower mobility of the vacancy along the TJ and eventually a lower TJ segregation level compared with that at the GBs. Therefore the relative segregation level at TJ with regard to that at the constituent GBs has a contribution from both the structural parameters such as the free volume, anisotropic factor, atomic distance, coordination number and also the atomic diffusion characteristics including the binding energy and activation energy.

As shown in figure 4.19, the P concentration on GBs varies with distance from the TJ. Similar observations have been reported where the Bi concentration along the GB varies within a

distance of 5 nm to 80 nm from a TJ in Cu [15]. Two possible reasons have been proposed regarding the interplay between a TJ and its constituent GBs [180]. If the sample is in equilibrium, the concentration gradient can be attributed to the decaying strain field of the TJ at the constituent GBs [189] which may alter the GB structure, especially the size and/or the geometry of the free volume available for the segregation. If the sample is in a non-equilibrium state such as is the case in the current study, the concentration gradient may result from the diffusion of solute atoms from the TJ to the constituent GBs or in the reverse direction, depending on the structural characteristics and atomistic diffusion characteristics.

4.3.4 Effect of grain size

This can be interpreted via the critical time and effective time. As the critical time is proportional to the square of the radius, it is much higher for sample A with larger grain size than for sample B. While for effective time, it only depended on the initial temperature, final temperature and the cooling rate. The effective times for both samples were the same, as they experienced the same process. According to the calculated results in section 4.3.2, the effective time is smaller than the critical time.

According to Faulkner's theory [1, 2], the maximum segregation does not depend on the grain size. Larger grain has longer critical time. The effect of grain size can be illustrated in figure 4.26. At the effective time te which is smaller than the critical time tc, the concentration for grain size A (larger) is lower than that for grain size B. However, the underlying mechanism is not clear as the diffusion coefficient and diffusion time thus the diffusion distance are the same for smaller and larger grain size.

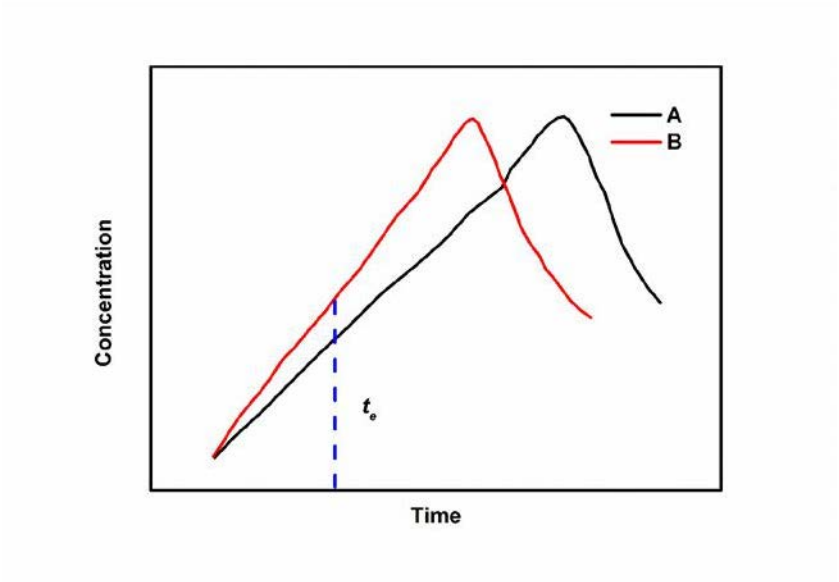

Figure 4.26 Calculated grain size effect on the grain boundary concentration based on equation 4.5 and 4.6. A and B represent different grain sizes and A>B. t_e is the effective time during quenching from 700 ˚C.

Based on Wu's model [4], the diagram of the P concentration profile with time for different grain sizes (A>B>C>D>E) is shown in figure 4.27. It can be seen that with decreasing grain size, the concentration peak shifts to the left. Also, the maximum concentration decreases with grain size. At the effective time t_e, the GB concentration increased with decreasing grain size until C where the critical time for C is equal to the effective time and the concentration difference reaches a maximum. A further decrease of grain size would result in a decrease of the GB concentration as the effective time exceeds the critical time. The critical grain size corresponding to a maximum GB concentration can be calculated by equating the effective time and the critical time. For example, it is about 6 μm when quenched into water from 700 ˚C.

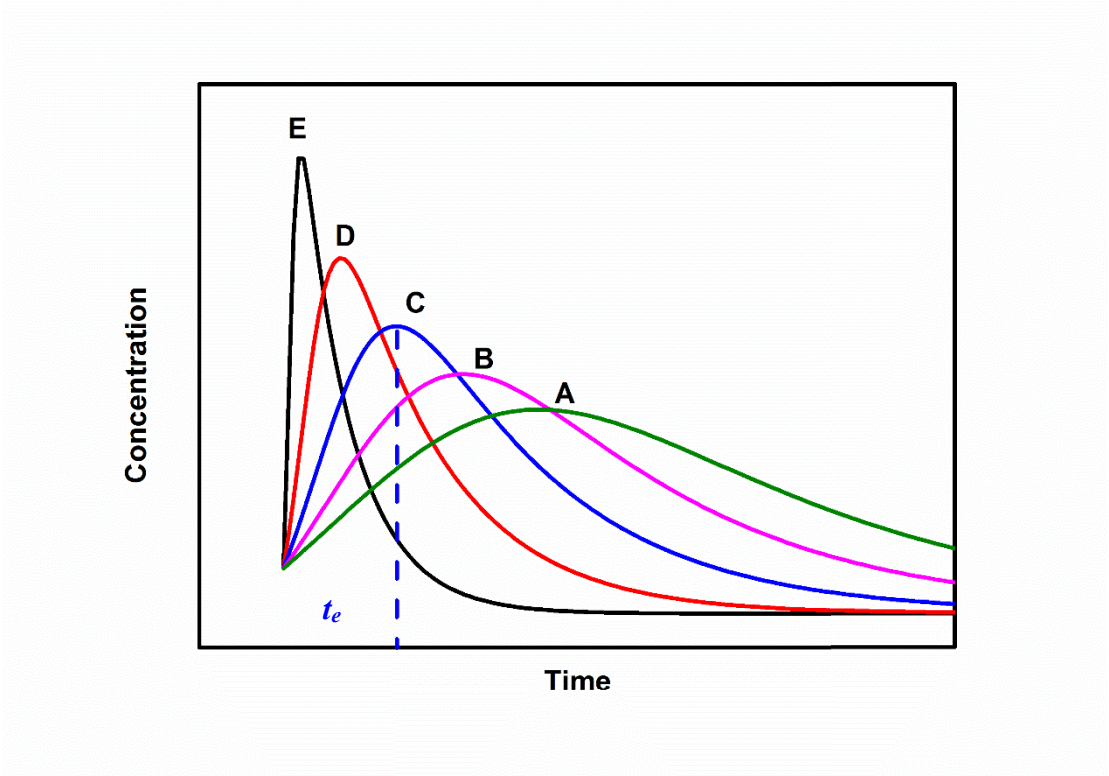

Figure 4.27 Calculated grain size effect on the grain boundary concentration based on Wu's theory [4]. A, B, C, D and E represent different grain sizes and A>B>C>D>E. t_e is the effective time during quenching from 700 ˚C.

It was found in section 4.2.6 (figure 4.23 and 4.24) that the segregation level during cooling from 1000 ℃ is lower than that from 700 ˚C. The reason is also due to the size effect. The grain size of the sample cooling from 1000 ℃ is much larger than that from 700 ℃, resulting in a lower segregation according to [4].

A critical grain size exists for each specific set of conditions, i.e. holding temperature, cooling rate or aging time. Under these conditions, the P concentration at the GB increases with grain size until the grain size equals the critical grain size and then it decreases. This is caused by the critical time and is therefore a characteristic of NES. For ES, this is quite different. According to equation 2.13, the condition $C_0 \gg \frac{3\theta}{2\bar{R}} C_{gb}$ is met in this work. This means that grain size has

no effect on the segregation level if ES is the dominant mechanism, which is inconsistent with the experimental results. Thus a NES dominant mechanism is again confirmed.

4.3.5 Effect of cooling rate and aging time

Based on the theory in section 4.3.1, the effective times corresponding to 700 ˚C during cooling can be calculated as 0.26s, 5.2s, 104s and 622s for water quenching, air cooling, furnace cooling with the door open and furnace cooling, respectively. Then the cooling rate dependence can be replotted as the relationship between effective time and GB concentration, as shown in figure 4.28. The critical time at 700 ˚C is 133s, which is quite close to our experimental result.

Based on the parameters used in section 4.3.1, the temperature below which diffusion of the complex can be neglected is chosen to be 450 °C. Then the segregation profile can be calculated using the parameters in table 4.3. The calculated results are shown in figure 4.29 and are compared with the experimental results.

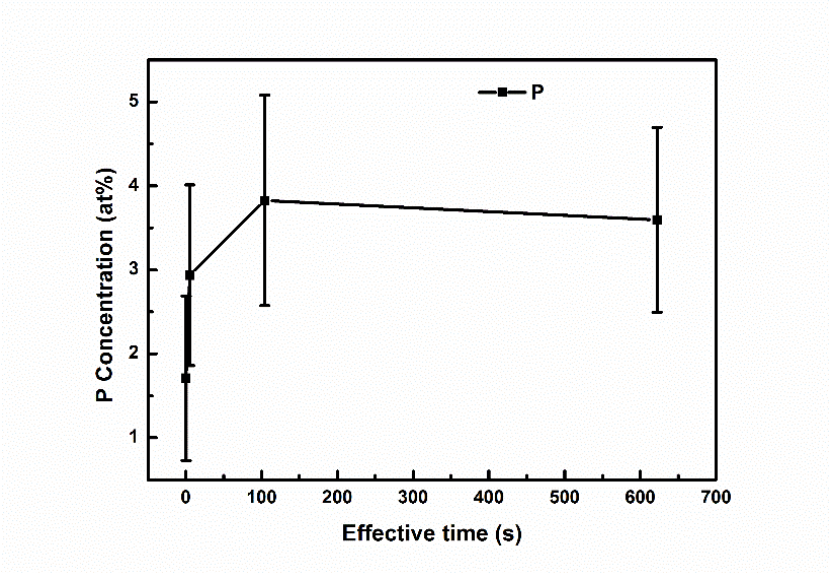

Figure 4.28 GB P concentration dependence on the effective time cooling from 700 ˚C at different rates

From figure 4.29 it can be seen that the calculated concentration during segregation is slightly smaller than the experimental results, while it is much lower during the desegregation stage. This indicates an overestimation of the diffusion coefficient of P via vacancies in Ni as it is the dominant process during desegregation.

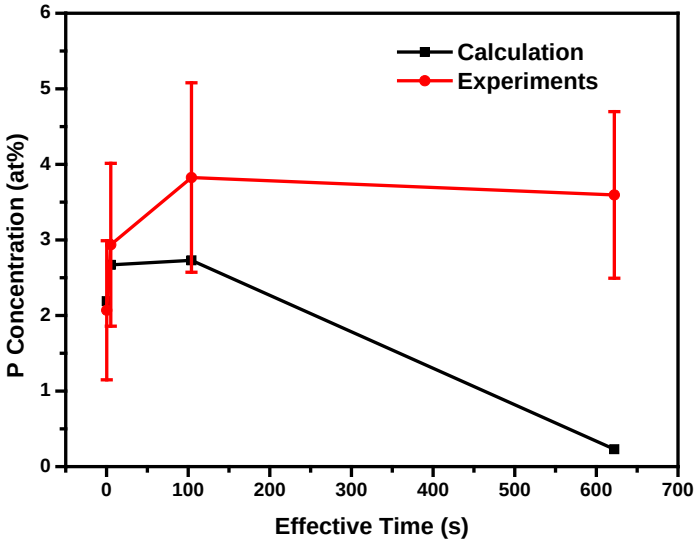

Figure 4.29 Comparison of the calculated and experimental GB P concentration during cooling from 700 ˚C at different rates

Another problem of Faulkner's [1, 2] and Xu's theory [115] is that the grain size is not taken into consideration. Our experiments clearly indicate that smaller grain size leads to higher segregation when the effective time is smaller than the critical time. Also, the segregation kinetics measured during cooling and aging demonstrate that the maximum segregation level is grain size dependent. Wu [4] considers the effect of grain size by dividing the segregation process into two steps, i.e. the diffusion of the complexes towards the enriched region close to the GB and the mass transfer at the interface between the segregation region and the grain interior (figure 2.11). Smaller grains have larger transfer coefficient and thus higher segregation levels at the segregation stage, while in the desegregation stage, more solute

diffuses to the inner grain due to the higher transfer coefficient in smaller grains, resulting in a lower grain boundary concentration. Based on this theory, the segregation kinetics can be described by (see Appendix A67) [4]:

$$C_{gb}(t) = \frac{(k_V - k_C)C_{gb}^i - k_C(\alpha - 1)C_{gb}^i e^{-k_V t} + [k_V(\alpha C_{gb}^0 - C_{gb}^i) - k_C\alpha(C_{gb}^0 - C_{gb}^i)]e^{-k_C}}{(k_V - k_C)[1 + (\alpha - 1)e^{-k_V t}]} \quad 4.8$$

where C_{gb}^i is the transformed solute concentration in the non-segregation zone, C_{gb}^0 the initial concentration and k_V, k_C and α are defined as [4]

$$k_V = 12D_{0V}\exp\left(-\frac{Q_V}{kT}\right)/d^2 \quad 4.9$$

$$k_C = \frac{12(d - 2\theta)D_{0C}\exp\left(-\frac{Q_C}{kT}\right)}{d^3 - (d - 2\theta)^3} \quad 4.10$$

$$\alpha = \exp[Q_f(T_0 - T/kT_0T] \quad 4.11$$

where Q_V and Q_C are the migration energies of the vacancies and complexes respectively and Q_f is the vacancy formation energy.

This formula is used to fit the experimental results obtained from the aged samples using the method described in [4] and the results are shown in figure 4.30. By assuming that the pre-exponential constant for both vacancy and complex diffusion is $5\text{x}10^{-5}$ m^2s^{-1} [2], the migration energies of vacancy and complex can be derived from k_V and k_c as 1.34 eV and 1.9 eV, respectively. This is consistent with the results of P in CrMo steel and low carbon steel [2]. By fitting the experimental data in ref. [109, 190, 191], the migration energies of the vacancy and complex are determined as 1.24-1.80 eV and 1.91-2.17 eV [4].

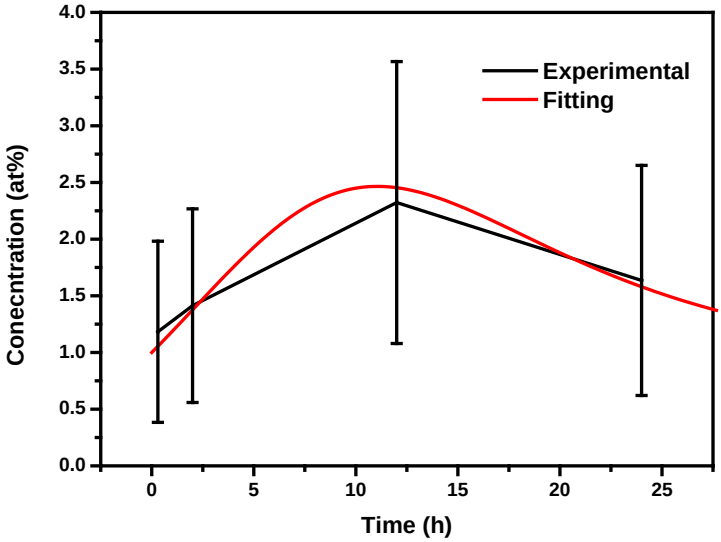

Figure 4.30 Experimental and fitted GB concentration of P during aging at 500 °C after water-quenched from 1000 ℃.

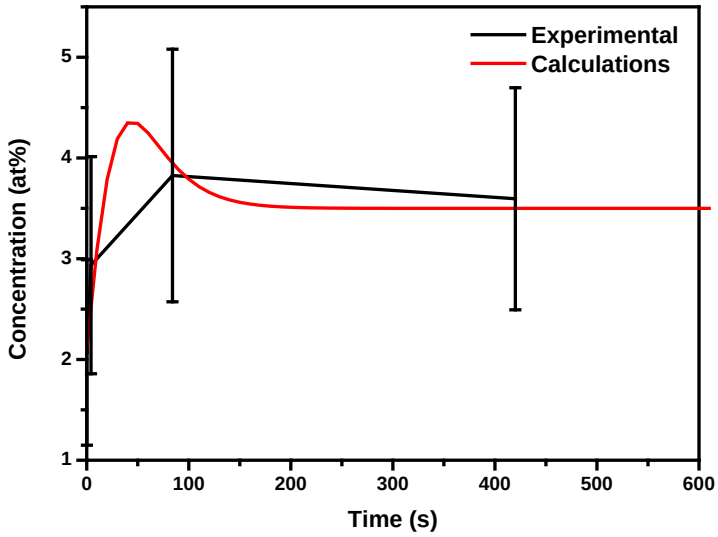

Figure 4.31 Experimental and calculated GB concentration of P during cooling from 700 ℃ using the fitted parameters.

Using the parameters obtained, the kinetic profile during cooling can be calculated and compared with the experimental results as shown in figure 4.31. It should be noted here that

the effective time is calculated again using the fitted parameters. A very good agreement between the experimental results and calculations validates the theory proposed by Wu [4].

Research indicates that the effect of P on the mechanical properties is concentration dependent. A higher P concentration at the GB increases the nucleation rate of GB carbides, leading to finer and more evenly distributed carbides compared with at a lower P concentration. This is beneficial for the stress-rupture properties. A further increase in P concentration results in the formation of large blocks of carbides or ellipsoids and a reduction of the stress-rupture life [12]. P retards the diffusion of oxygen along GBs and protects the GB from oxidation, eventually improving the creep life. But if the GB concentration of P is in excess, the cohesive strength of the GB will become lower, leading to a reduction of the creep properties [8]. First-principles calculations also indicate that there exists an optimum concentration for P segregation in the GB region when the P-segregated GB can be even as strong as a clean GB [26]. As discussed above, the factors affecting the GB concentration of P include holding temperature, cooling rate, aging temperature and grain size. By altering these parameters, it is possible to derive an optimum GB concentration for the P.

4.4 Conclusions

1. GB segregation of P after cooling or aging was detected at small and large angle GBs using STEM-EDS. Comparisons of the diffusion coefficients of P via vacancies and complexes indicate the enrichment at GB is mainly caused by NES. The GB P concentration is higher in boundaries with larger misorientation and no segregation to twin boundaries has been observed. This is caused by the larger excess free volume at high angle GBs than in low angle GBs.

3. Triple junction segregation was observed. However, the concentration at a triple junction can be lower than at GBs. A concentration gradient along the GB near the triple junction existed on the GBs with a width of 5-100nm.

4. When the effective time is smaller than the critical time, the GB concentration of P decreases with increasing grain size. Based on a theoretical analysis, a critical grain size of 6 μm is expected during quenching from 700 ºC.

5. A critical cooling rate corresponding to furnace cooling with the door open exists when the GB concentration reaches a maximum. This is consistent with the calculations.

6. When aging at 500 ºC, the GB segregation increased until 12h and then decreased. The calculation of the critical time based on NES agreed well with the experimental results.

7. The calculated profile during cooling from 700 ºC at different rates deviated from the experimental results, especially during the desegregation stage. The calculated concentration is much lower than the experimental results, indicating an overestimate of the solute diffusion coefficient.

Chapter 5 Interaction between P and Cr/Mo

5.1 Introduction

In the work reported in the last chapter, a very simple ternary alloy Ni-6Al-0.1P was used to investigate the GB segregation of P. Modern superalloys contain more than ten kinds of alloying elements, among which Cr is mainly used to improve the oxidation resistance and Mo is beneficial to strength by forming precipitates. In such a complex system, the effect of inter-elemental interaction on segregation is quite important. There are many experimental results on the ES or NES of Cr and Mo in steel and Ni-base alloys with or without P. Segregation of Cr/Mo in steel and Ni alloys has been attributed to Cr/Mo-vacancy complex diffusion (NES), vacancy-mediated diffusion (ES) and an interaction with C/B/N/P (NES and ES). However, all previous studies were on samples containing C which makes the mechanisms validation impossible. In this chapter, we will measure the GB segregation behaviour in Ni-Al-Cr/Mo with and without P but free from C/B/N. All three mechanisms will be discussed in the context of the results.

5.2 Experimental results

5.2.1 Microstructure

The alloys used in this study are Ni-6Al-6Cr, Ni-6Al-6Cr-0.1P, Ni-6Al-2Mo and Ni-6Al-2Mo-0.1P (at%) prepared by plasma melting. After solid solution heat treatment at 1300 °C for 48 h, sample homogeneity was checked via line-scans over a large area. The SEM images and corresponding EDX profiles for Ni-Al-Cr and Ni-Al-Mo are shown in figure 5.1 and figure 5.2, respectively. No macro-segregation has been observed in either sample. Similar results were obtained for the samples with P addition but are not shown here.

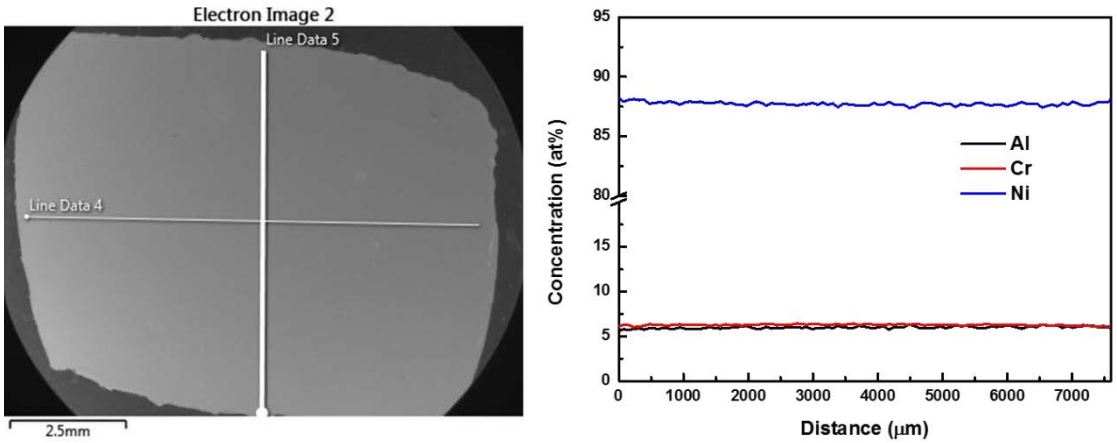

Figure 5.1 SEM image and corresponding profiles (line 5) of Ni-Al-Cr concentrations after solution heat treatment

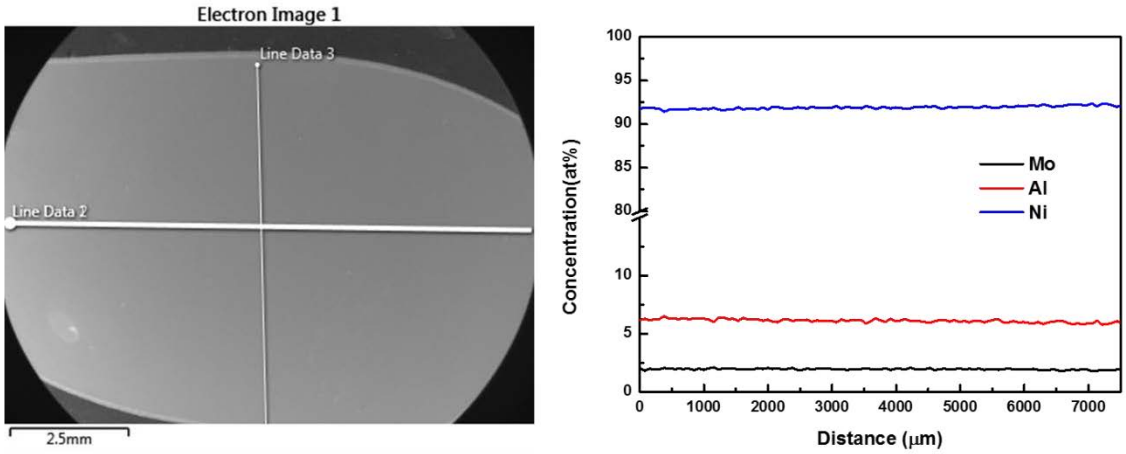

Figure 5.2 SEM image and corresponding profiles (line 3) of Ni-Al-Mo concentrations after solution heat treatment

Alloy compositions were measured by point analysis. Spectra from each of Ni-Al-Cr-P and Ni-Al-Mo-P are shown in figure 5.3 and figure 5.4, respectively. A small but obvious P peak appears in both spectra. The compositions derived from each spectrum and an averaged one are listed in table 5.1 and table 5.2. The standard errors σ are included in red in parentheses. The measured results are close to the nominal compositions for both alloys.

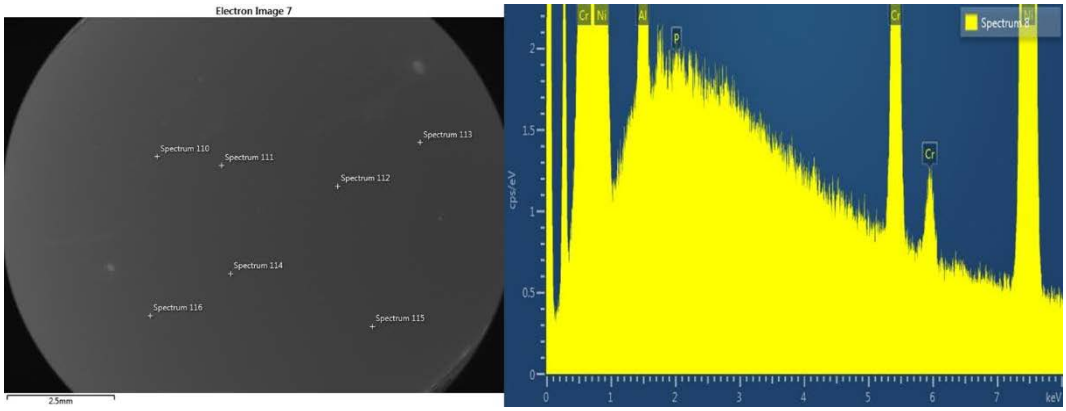

Figure 5.3 SEM image of Ni-Al-Cr-P showing the positions of the point analyse and one of the spectra showing a weak P peak

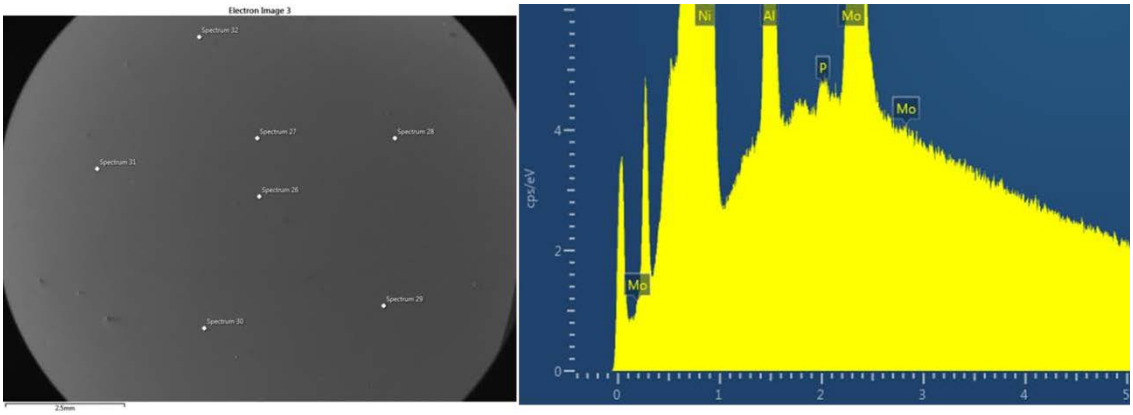

Figure 5.4 SEM image of Ni-Al-Mo-P showing the positions of the point analyse and one of the spectra showing a weak P peak

Table 5.1 Compositions (at%) measured from each point and the averaged results in Ni-Al-Cr-P after solid solution heat treatment

Spectrum Label	Al	P	Ni	Cr
Spec 110	6.13(0.04)	0.09(0.02)	87.54(0.05)	6.24(0.04)
Spec 111	6.02	0.14	87.66	6.18
Spec 112	6.07	0.11	87.57	6.25
Spec 113	6.06	0.14	87.57	6.22

Spec 114	6.00	0.13	87.66	6.20
Spec 115	5.99	0.12	87.75	6.14
Spec 116	5.94	0.10	87.70	6.25
Average	6.03±0.06	0.12±0.02	87.64±0.08	6.21±0.04

Table 5.2 Compositions (at%) measured from each point and the averaged results in Ni-Al-Mo-P after solid solution heat treatment

Spectrum Label	Al	P	Ni	Mo
Spec 26	6.11(0.04)	0.10(0.02)	91.81(0.05)	1.99(0.03)
Spec 27	6.11	0.10	91.74	2.05
Spec 28	6.06	0.10	91.84	2.00
Spec 29	6.07	0.13	91.83	1.97
Spec 30	5.96	0.12	91.89	2.03
Spec 31	5.96	0.13	91.95	1.97
Spec 32	5.88	0.11	92.04	1.96
Average	6.02±0.09	0.11±0.01	91.87±0.10	2.00±0.03

EBSD orientation maps of the Ni-Al-Cr and Ni-Al-Mo specimens after annealing at 700 °C for 2 h are shown in figure 5.5. It can be seen from figure 5.5 that Ni-Al-Cr is fully recrystallized. For Ni-Al-Mo, the whole area is from one grain and the colour varies due to the large strain. This indicates the sample is not recrystallized. A STEM-HAADF image of Ni-Al-Mo annealed at 700 °C for 2 h (figure 5.6) shows that the dislocation density is very high, meaning that the recrystallization is not completed. The retardation effect of Mo on the recrystallization of steel due to solute drag has been reported [192]. With Mo concentration increasing from 0.18 to 0.38

wt% in a low alloy steel, the time corresponding to half recrystallization at 850 °C increased from 75 s to 216 s [192].

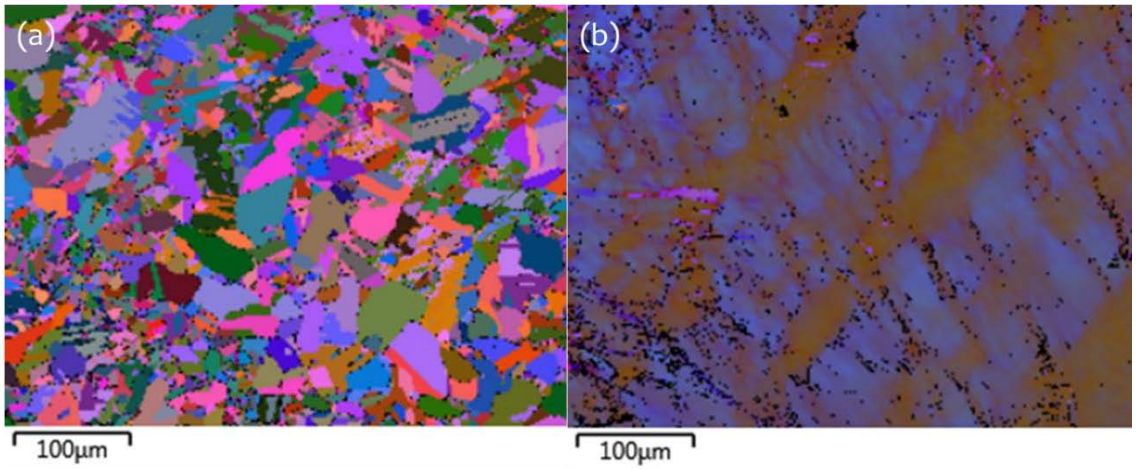

Figure 5.5 EBSD orientation maps after 2 h at 700 °C of (a) Ni-Al-Cr and (b) Ni-Al-Mo.

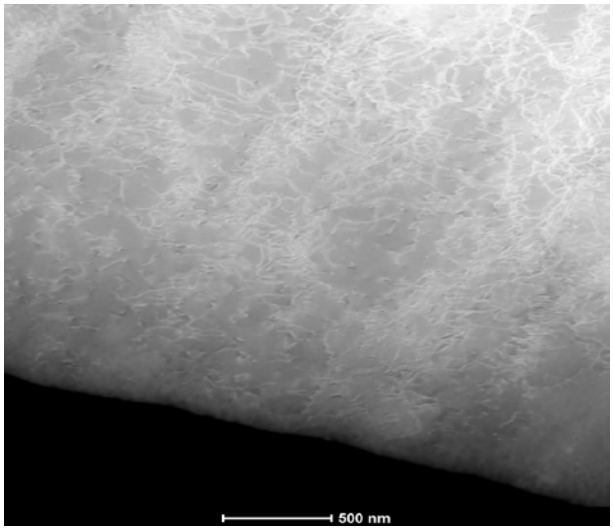

Figure 5.6 HAADF image obtained from Ni-Al-Mo after 2 h at 700 °C showing high density of dislocations.

The microstructures of Ni-Al-Mo after annealing at 700 °C for different times are shown in figure 5.7. Only after 8h the sample became fully recrystallized. So, 8 h has been used as the recrystallization time.

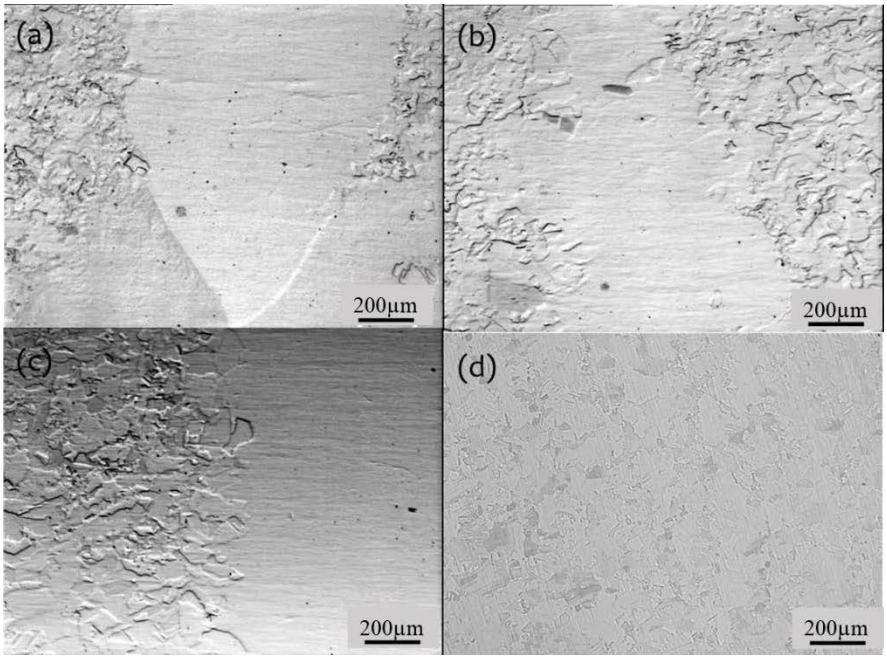

Figure 5.7 Optical micrograph showing the microstructure of Ni-Al-Mo after annealing for (1) 1 h, (b) 2 h, (c) 4 h and (d) 8 h at 700 °C.

5.2.2 Segregation of Cr/Mo in Ni-Al-Cr/Mo

The line-scan profiles across GBs in Ni-Al-Cr and Ni-Al-Mo water quenched from 700 °C are shown in figure 5.8 and figure 5.9, respectively. It is obvious that Cr and Mo are not enriched at the GBs. The same results were observed in samples air or furnace cooled from 700 °C.

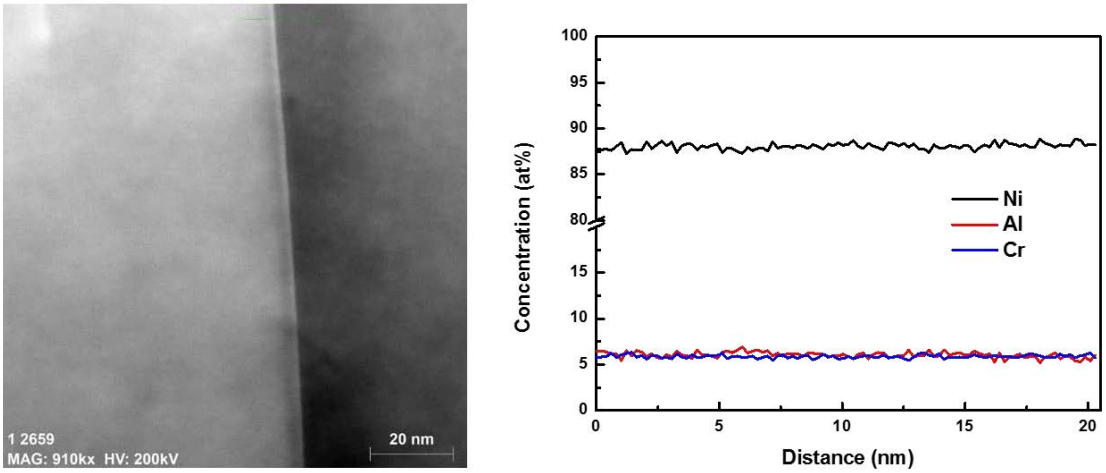

Figure 5.8 HAADF image of a typical GB (28.6º) in Ni-Al-Cr water quenched from 700 ºC and the corresponding line-scans

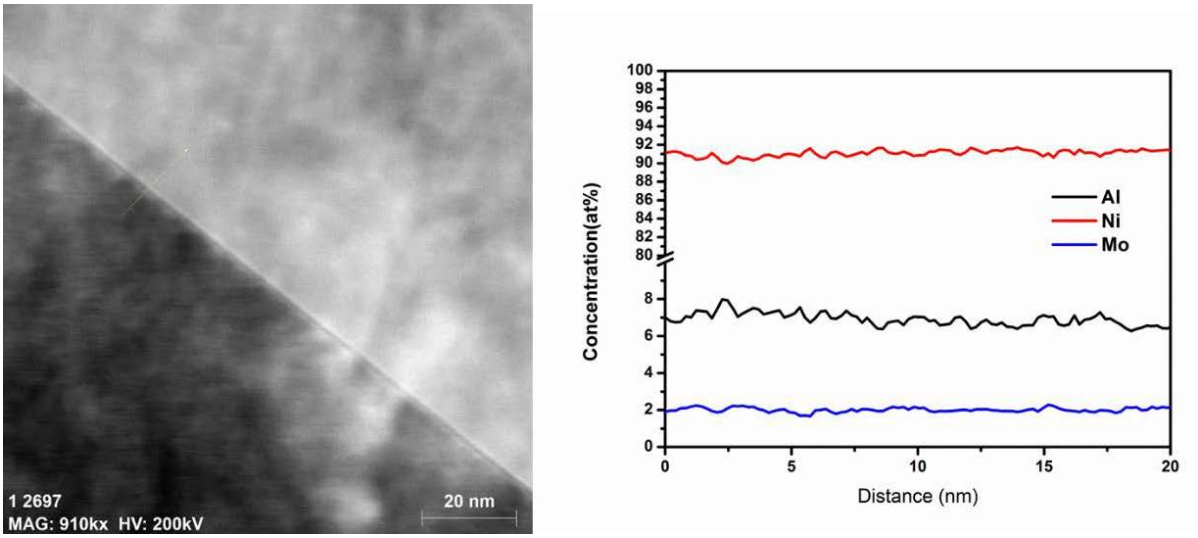

Figure 5.9 HAADF image of a typical GB (35.2º) in Ni-Al-Mo water-quenched from 700 ºC and the corresponding line-scans

It has been shown that the GB segregation level increases with the temperature at which the sample was held and that there is a critical temperature below which no segregation will be detected [118, 119]. So, a higher temperature of 1200 °C was used for the recrystallization heat treatment, following by different cooling rates. For both alloys and with different cooling rates (water quenching, air cooling and furnace cooling), no segregation of Cr and Mo was observed (figures 5.10-11).

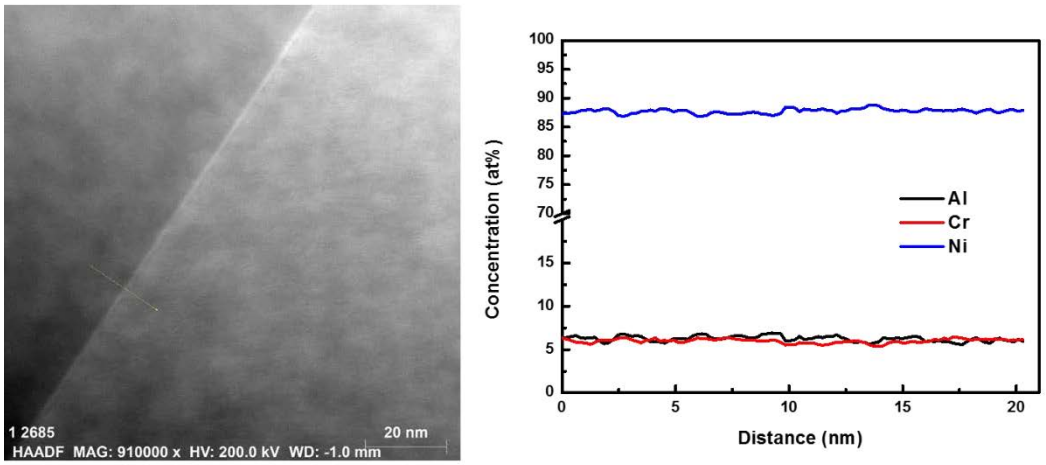

Figure 5.10 HAADF image of Ni-Al-Cr air-cooled from 1200 °C and corresponding line-scans cross the GB (37.4º).

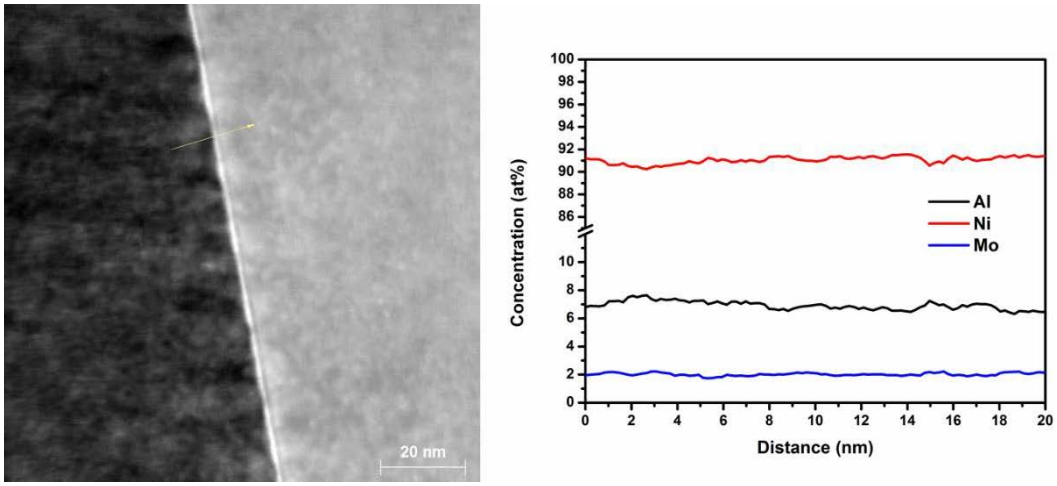

Figure 5.11 HAADF image of Ni-Al-Mo air-cooled from 1200 °C and corresponding line-scans cross the GB (48.1º)

The results are inconsistent with previous results, which showed that Cr/Mo segregated to the GBs of steel and Ni alloys during cooling [118, 119, 149, 158]. Possible reasons for this will be discussed in section 5.3.1.

5.2.3 Segregation of P and Cr/Mo in Ni-Al-P-Cr/Mo

A GB line-scan from Ni-Al-Cr-P water quenched from 700 °C is shown in figure 5.12. P was enriched at the GB while Cr was depleted. This is consistent with the elemental mapping shown in figure 5.13. In the samples which were cooled from 700 °C at different cooling rates and in the samples aged at 500 °C for different times, enrichment of P and depletion of Cr at the GBs were also observed.

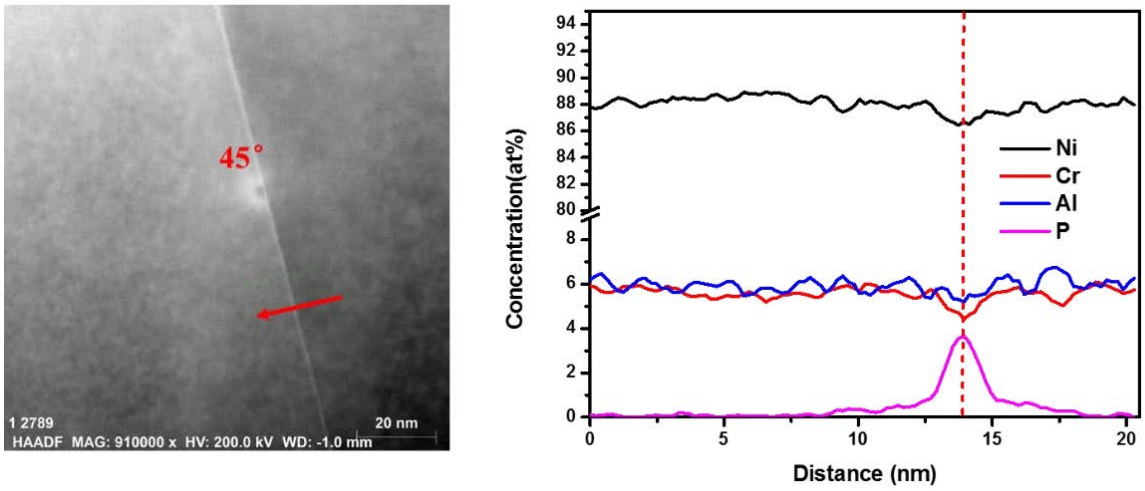

Figure 5.12 HAADF image obtained from a typical GB in Ni-Al-Cr-P water-quenched from 700 ºC and the corresponding line-scan carried out along the red arrow in the HAADF image.

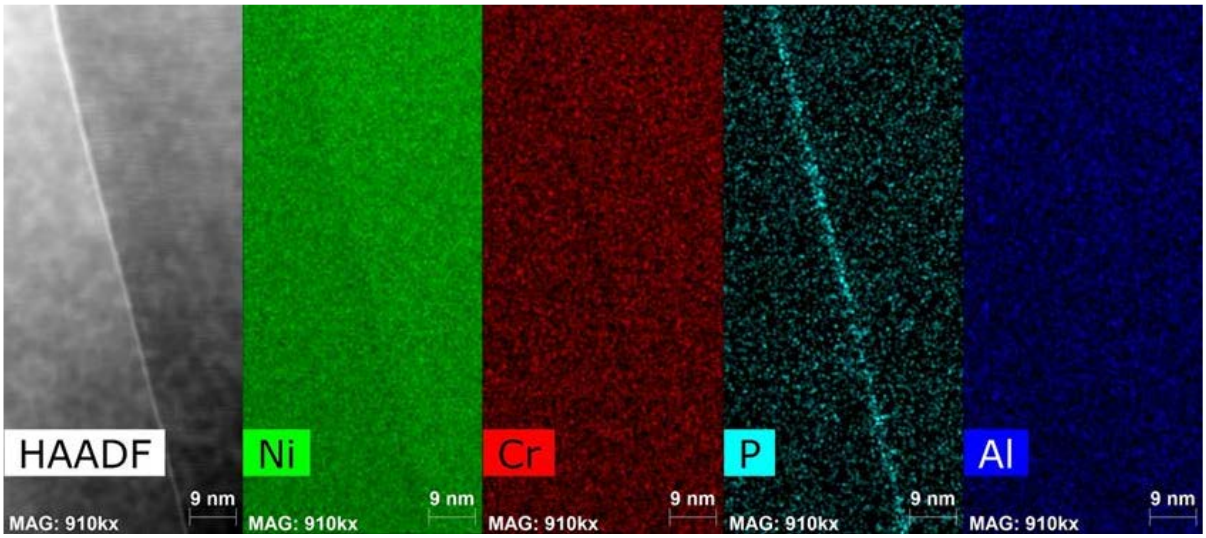

Figure 5.13 Elemental maps collected from the same GB shown in figure 5.12

Point analyses from Ni-Al-Cr-P water-quenched from 700 ºC were performed and the measured concentrations at the GB and in the matrix are listed in table 5.3. The GB P concentration was much higher than that in the matrix, while Al, Cr and Ni are depleted.

Table 5.3 Measured concentration (at%) at GB and matrix in Ni-Al-Cr-P water-quenched from 700 ºC.

Spectrum	Al	P	Cr	Ni
Matrix	5.88	0.02	5.79	88.31
	6.12	0	5.98	87.89
	6.17	0.31	5.93	87.59
	5.96	0.36	5.64	88.04
Average	6.03±0.14	0.17±0.19	5.84±0.15	87.96±0.30
GB	5.87	3.56	4.91	85.66
	5.49	3.7	4.82	85.98
	5.37	3.5	5	86.13
	5.64	3.17	5.12	86.07
Average	5.59±0.22	3.48±0.22	4.96±0.13	85.96±0.21

Similar to Ni-Al-Cr-P alloy, the GB line-scans from Ni-Al-Mo-P (figure 5.14) indicated that P segregated to the GB, while Mo was depleted at the GB. According to the elemental mapping, it is not very obvious that Mo desegregated from the GB (figure 5.15). This is possibly due to the low concentration of Mo and the small difference in concentration between the GB and the matrix. Mo depletion could, however, be confirmed by point analysis, as listed in table 5.4. The concentration difference of Mo between GB and matrix is less than 0.5 at%.

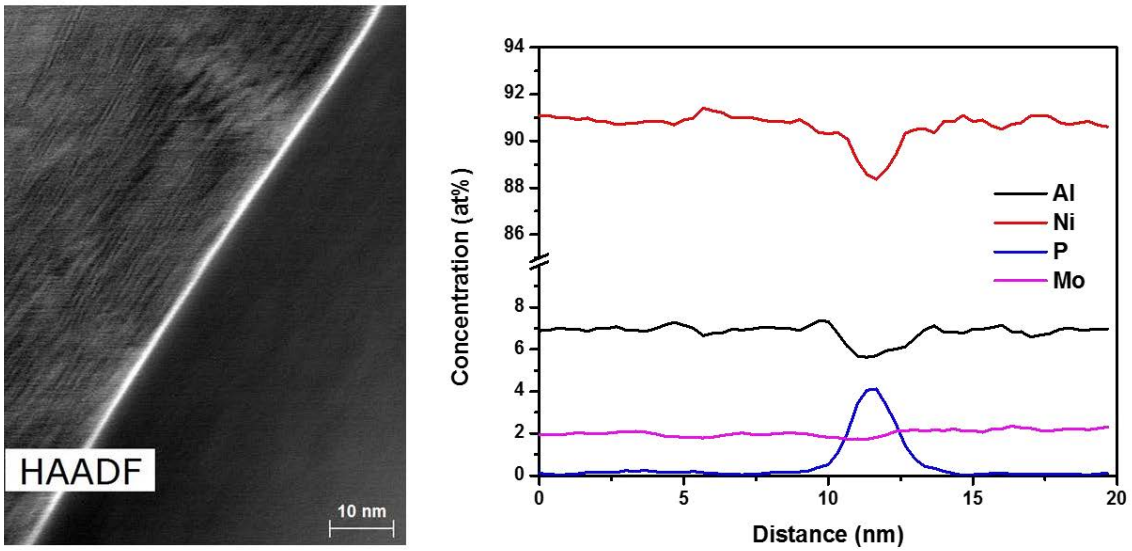

Figure 5.14 HAADF image of a typical GB in Ni-Al-Mo-P water-quenched from 700 ºC and the corresponding line-scan.

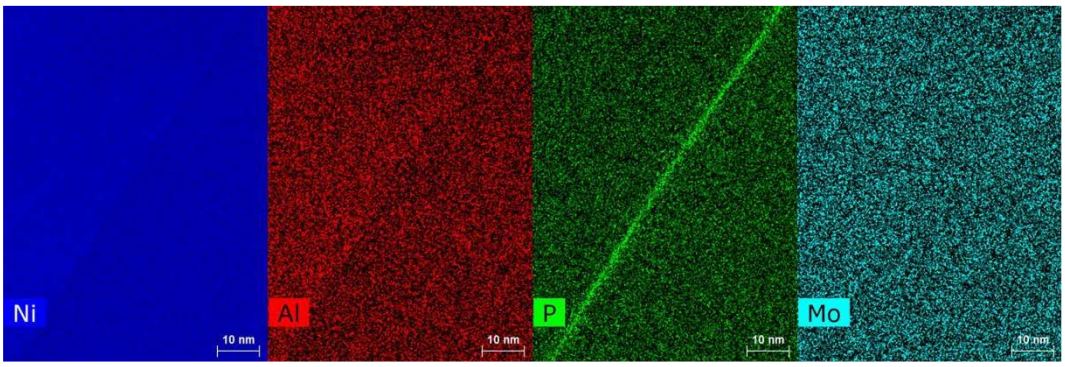

Figure 5.15 Elemental maps collected from the same GB as shown in figure 5.14.

Table 5.4 Measured concentrations (at%) at the GB and in the matrix in Ni-Al-Mo-P water-quenched from 700 ºC.

Spectrum	Al	P	Mo	Ni
Matrix	6.37	0.09	2.08	91.45
	6.19	0.07	1.95	91.78
	6.38	0.07	2.11	91.44
	6.19	0.10	1.98	91.73

Average	6.28±0.11	0.09±0.02	2.03±0.08	91.60±0.18
GB	5.06	4.17	1.72	89.05
	5.24	4.16	1.79	88.81
	5.12	4.23	1.75	88.80
	5.35	3.94	1.83	88.93
Average	5.19±0.13	4.13±0.13	1.77±0.05	88.91±0.12

Similarly to Ni-Al-P, triple junction segregation of P in Ni-Al-Cr and Ni-Al-Mo has also been observed and is shown in figure 5.16 and figure 5.17, respectively.

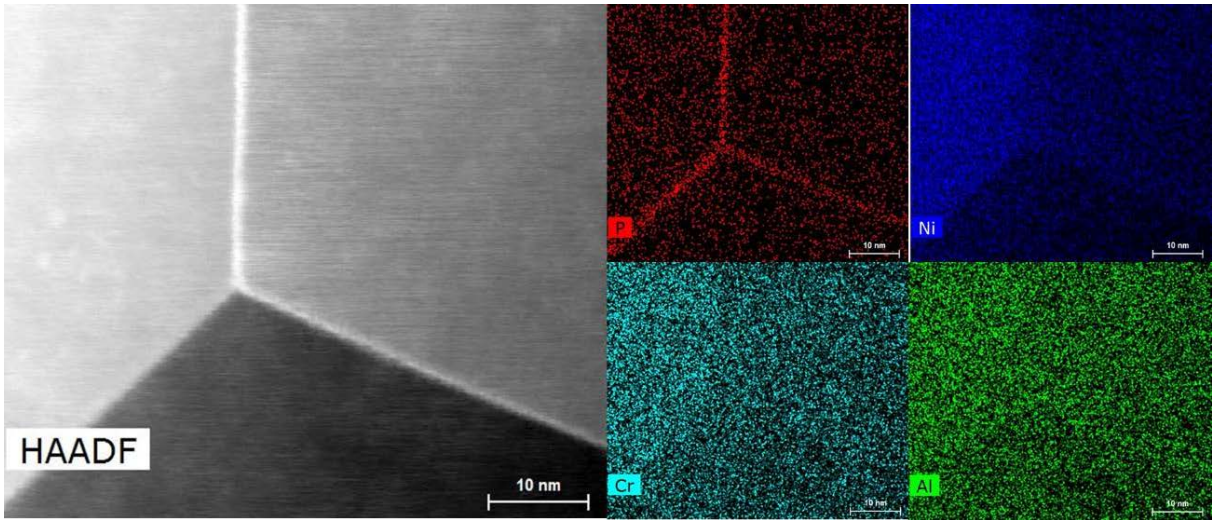

Figure 5.16 HAADF image of a TJ and corresponding elemental maps in Ni-Al-Cr-P water-quenched from 700 ºC

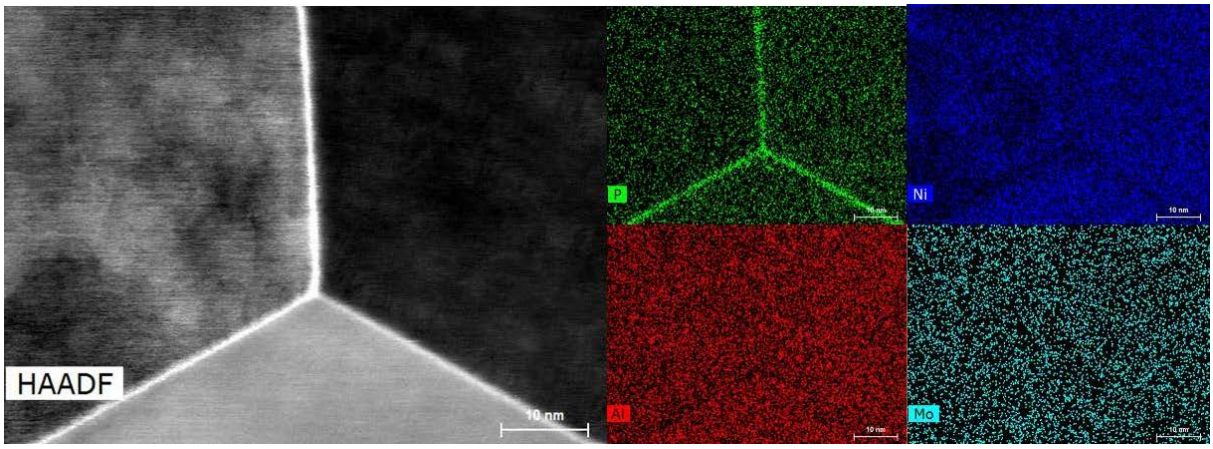

Figure 5.17 HAADF image of a TJ and corresponding elemental maps in Ni-Al-Mo-P water-quenched from 700 ºC

The relationship between the GB Cr and Mo concentrations at the GB and the P concentration at the GB From Ni-Al-Cr-P and Ni-Al-Mo-P cooled from 700 ºC at different rate is shown in figure 5.18 and figure 5.19, respectively. With increasing P concentration, the Cr and Mo concentration decreased. Linear least squares fitting shows that the relationship between the P and the Cr/Mo concentration at the GB is

$$C_{Cr}^{GB} = (5.90 \pm 0.08) - (0.35 \pm 0.02) * C_P^{GB}$$

$$C_{Mo}^{GB} = (2.13 \pm 0.03) - (0.08 \pm 0.01) * C_P^{GB}$$

The fitting parameters R^2 for Cr and Mo is 0.91 and 0.95, indicating a good fitting. This is contradictory to previous results which indicated that P and Cr or Mo co-segregated to the GB. P and Cr or Mo co-segregation has been reported in 2.25Cr1Mo steel quenched from 1100 ºC using EDS and interpreted as being due to an attractive interaction between P and Cr or Mo [108]. Similar results have also been observed in an industrial steel [109], 12Cr1MoV steel [21] and Fe-Cr-P alloy [19] by AES. Also, increasing the P concentration promoted the segregation of Cr [19]. In a Ni-Cr alloy and IN 718, P and Cr or Mo co-segregation was measured by AES and attributed to the strong interaction between P and Cr or Mo [20, 62]. Possible reasons for the differences from my results will be discussed in section 5.3.2.

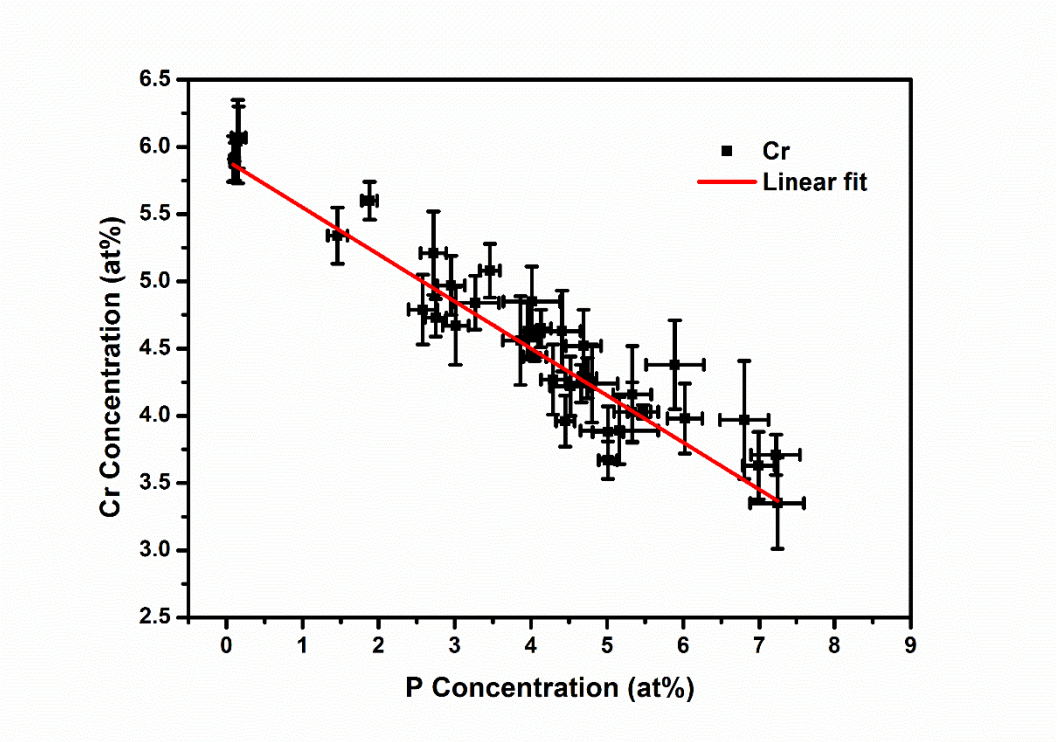

Figure 5.18 Dependence of GB Cr concentration on the GB P concentration in Ni-Al-Cr-P cooled from 700 ºC at different rate (water quenching, air cooling, furnace cooling)

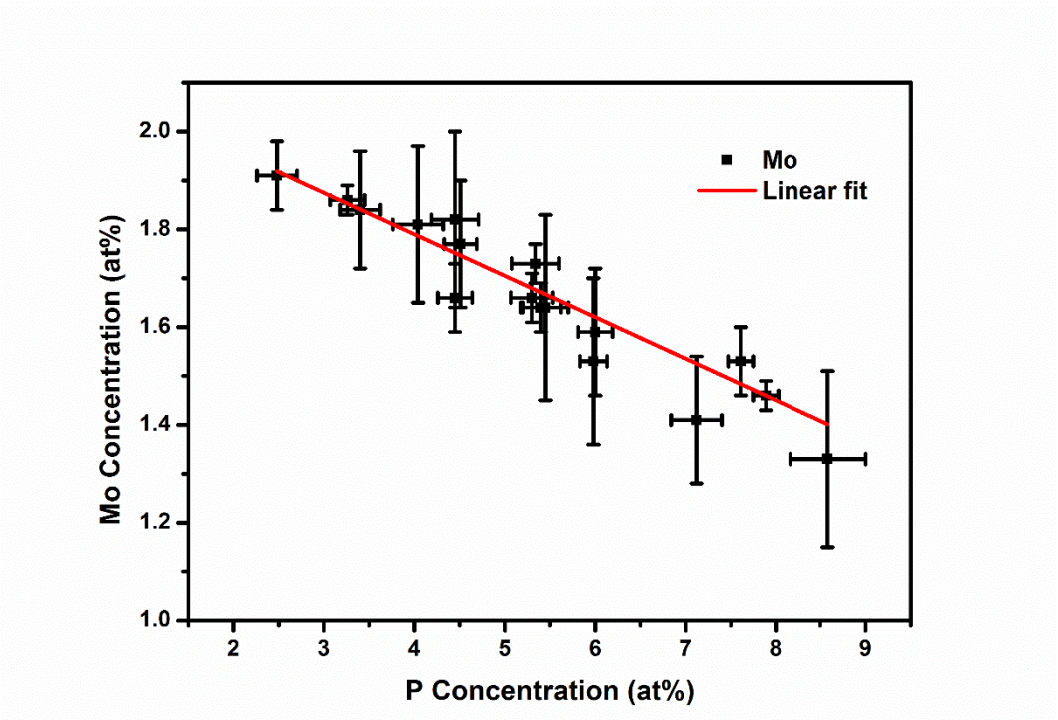

Figure 5.19 Dependence of GB Mo concentration on the GB P concentration in Ni-Al-Mo-P cooled from 700 ºC at different rate (water quenching, air cooling, furnace cooling)

The GB concentrations of P during cooling from 700 ºC with different cooling rates in Ni-Al-Cr-P were measured and are shown in figure 5.20. A critical cooling rate existed where the GB concentration reached a maximum. A higher or lower cooling rate led to a reduction in the GB P concentration. This indicated that P diffused to the GB via non-equilibrium segregation, consistent with the results in Ni-Al-P. Compared with Ni-Al-P, the critical cooling rate is smaller. This means the critical time is larger than that of Ni-Al-P (figure 5.20). The reason is that the grain size of Ni-Al-Cr-P is much larger than for Ni-Al-P and the critical time is proportional to the square of the grain size.

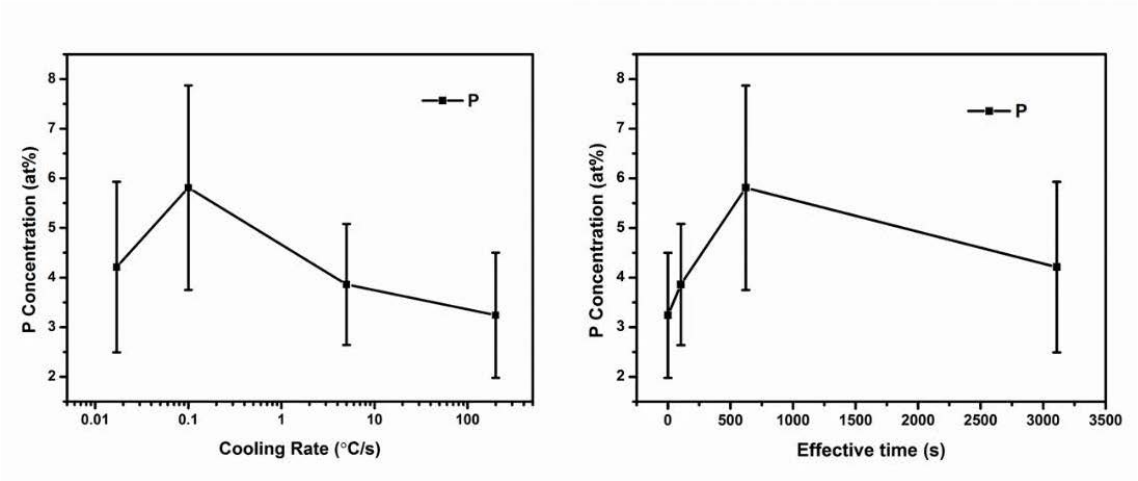

Figure 5.20 Effect of cooling rate and the calculated effective time on the GB P concentration in Ni-Al-Cr-P

The experimental results were fitted based on Wu's theory (Equation 4.8) [4] (figure 5.21). The parameters obtained are quite close to those for Ni-Al-P, with a slightly higher complex diffusion migration energy.

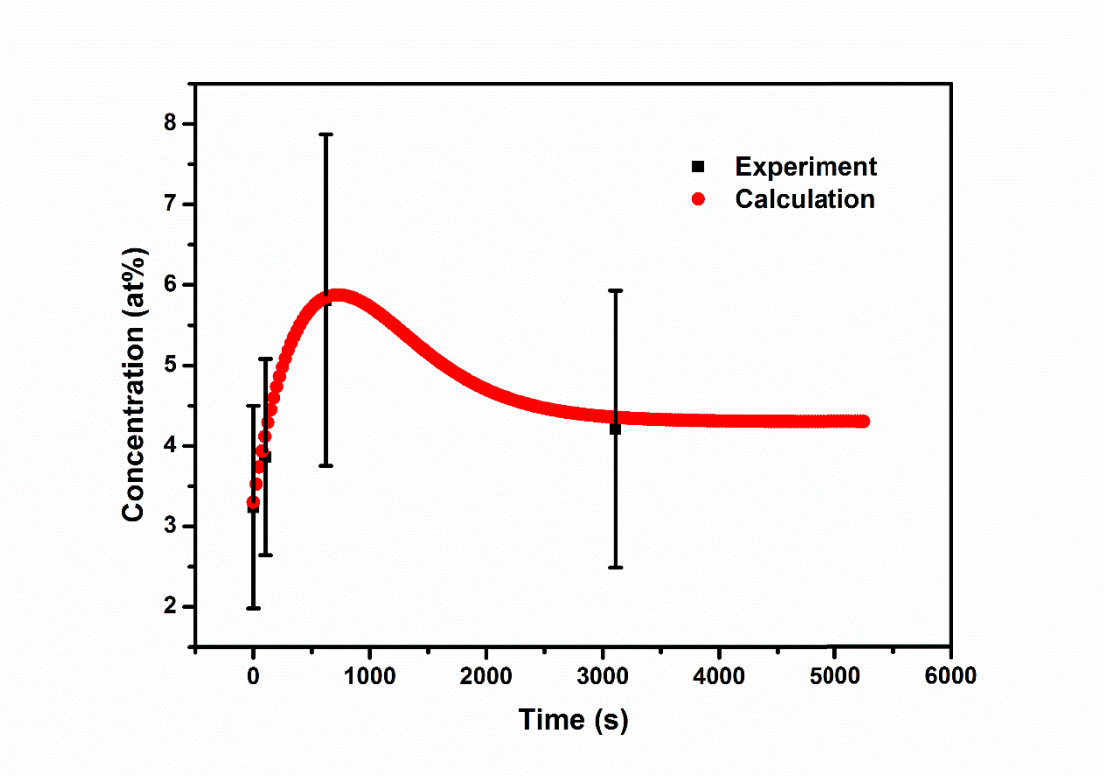

Figure 5.21 Comparison of the calculated and experimental P concentration at the GB in Ni-Al-Cr-P alloy versus the effective time during cooling from 700 ºC at different rate (water quenching, air cooling, furnace cooling)

5.3 Discussion and analysis

5.3.1 Segregation of Cr/Mo

Cr segregation to GBs has been widely observed in steels and Ni alloys. Possible mechanisms proposed are summarised as below.

1) Cr-vacancy complex diffusion (NES). Cr NES in a 2.25Cr1Mo steel after quenching from 1050 ºC and 1150 ºC was observed using EDS [116]. As shown in Chapter 4, the solute-vacancy binding energy affects the segregation level as the solute-vacancy binding must be strong enough to diffuse as a complex. Based on an analysis of the Cr-vacancy complex diffusion, it was found that the binding energy between Cr and vacancy should be ~0.5 eV to achieve the measured segregation level [118]. This was

further confirmed in the same alloy water-quenched and in type 316 steel argon gas-quenched from 950-1150 ºC [119]. In 304 stainless steel, the GB concentration of Cr after cooling from 1100 ºC at different cooling rates was measured using EDS and compared with calculations [170]. It was found that a binding energy between Cr and vacancy below 0.2 eV led to trivial segregation and a best fit of the experimental results indicates the binding energy should be 0.5 eV [170], which is consistent with the results in [118, 119]. However, the binding energy of 0.5 eV required for the segregation is much greater than expected. Using a strain analytical approach based on the lattice energy change by forming the complex configuration from an isolated point defect and solute atom [96], the binding energies of Cr to a vacancy in α-Fe and γ-Fe are predicted to be 0.12 eV and 0.036 eV respectively [99]. It should be noted here that these calculations based on a dilute alloy system. When the concentration exceeds 1%, the binding energy needs to be re-calculated. A molecular dynamics simulation using an embedded-atom method (EAM) interatomic potential in Fe-10%Cr produces a binding energy of 0.010-0.082 eV, depending on the exact method utilized [129]. This is consistent with first principles ab initio calculations of 0.007 eV [124], 0.03 eV [122], 0.04 eV [128], 0.05 eV [125-127] and 0.057 eV [123]. Experimental results using muon spectroscopy also indicated that the binding energy was smaller than 0.1 eV [130]. Even a slightly repulsive binding energy of -0.03 eV between Cr and vacancy in α-Fe has been obtained using the dimer and the nudged elastic-band methods [193]. The weak interaction between Cr and vacancies indicates that a Cr-vacancy complex is unlikely to be the main mechanism for the transport of Cr under normal experimental conditions. This is consistent with the experimental results that no segregation of Cr has been detected by atom probe tomography of Mo-free steel or a low carbon steel quenched from 970 ºC [194, 195].

The Cr-vacancy binding energy in Ni has also been calculated using different methods. Based on strain field arguments, the binding energy in Ni was calculated as 0.1 eV [96]. First principles calculations indicated a repulsive interaction of about -0.05 eV between Cr and a vacancy [196-198]. The very low or even repulsive binding energy indicates that Cr-vacancy complex formation and diffusion in Ni is energetically unfavourable.

2) Interaction with other elements (ES and NES). A second solute species, like C, B, N and P may also be present and interact with the Cr, affecting the segregation [170]. C-Cr co-segregation in 304 stainless steel aged at 500 ºC for 0.5 h (before carbide nucleation) after water quenching from 1000 ºC has been confirmed via APT [199]. Using EDS, segregation of Cr and formation of a GB chromium-rich carbide was observed in a 2.25Cr1Mo steel cooled from 1000 and 1100 ºC at different rates [149]. A similar phenomenon has also been observed in Ni-based Alloy 690 aged at 700 ºC after quenching from 1000 ºC [199, 200], in 617B alloy aged at 700 ºC after quenching from 1175 ºC [201], in a 700 ºC aged Ni-19Cr-9Fe alloy [120] using APT, and in Ni-base alloy 182 quenched from 1200 ºC and measured by AES [202]. At the beginning of aging, C diffused to the GB and then Cr migrated to the GB due to the attraction of the C [199]. The attractive interaction between C and Cr has been confirmed by first principles calculation [127, 203]. This interaction resulted in the co-segregation of C and Cr. When the C and Cr concentrations are high enough, carbides start to nucleate and grow at the GB, leading to the decrease or depletion of Cr at the GB [204-206].

   A B-Cr interaction in steel has not been observed. However, B is reported to have a larger segregation tendency than C and to compete with C for the GB segregation sites [199, 207]. B additions thus may reduce the segregation level of C and lead indirectly to a decrease in the Cr segregation. That is probably another reason why no Cr segregation has been observed in low carbon steel and Mo-free steel with B additions

[194, 195]. Different from steels, a B-Cr interaction was detected in a Ni-base alloy. GB chromium boride together with GB segregation of B and Cr were observed by APT in N18 alloy [145]. This is consistent with the EDS results from Nimonic PE16 alloy [204] and from Rene 80 alloy [208]. It was suggested that the segregation of B is via the migration of B-solute-vacancy complexes rather than B-vacancy complexes as models based on the latter did not match the measured B segregation level [204].

P and Cr co-segregation have been reported in 2.25Cr1Mo steel quenched from 1100 ºC using EDS [108] and in an industrial steel [109] and Fe-Cr-P alloy [19] by AES. Also, increasing the P concentration promoted the segregation level of Cr [19]. In Ni-Cr and Ni-Cr-Mn alloys, P-Cr co-segregation was measured by AES and attributed to the strong interaction between P and Cr [20].

N and Cr co-segregation has been observed by AES in low alloy steels [209, 210] and Ni-Cr-Mo-V steel [106]. It was found that the segregation patterns of Cr and N are similar, while P and Cr had different critical times of GB segregation [106] [209, 210], indicating that N rather than P co-segregated to the GB with Cr. Co-segregation of Cr and N to the free surface have also been reported in several steels [211-213]. In Ni-base Hastelloy C-276, Cr-N co-segregation to a free surface was confirmed by AES [214].

It should be noted that all samples studied for the interaction between B/N/P and Cr contain C. So, the effect of C on the segregation should be excluded. This is possible by an analysis of the interaction coefficient, as will be discussed in section 5.3.2. Compared with the first posited mechanism of Cr-vacancy complex diffusion, which required a larger binding energy than expected, segregation caused by interaction with C/B/N/P seems more reasonable and can be used to explain most of the segregation behaviour of Cr in steel, as all the studied steels contain C or/and P.

3) Diffusion via vacancies (ES). This has been observed in samples which had been aged for a long time. Using EDS, GB segregation of Cr was detected in 2.25Cr1Mo steel aged at 520 ºC for up to 210 h [215]. Cr has been demonstrated to be a fast diffuser in iron, with its diffusion coefficient dependent on the concentration [216, 217]. First principles calculations also indicated a lower migration energy for Cr via a vacancy mechanism in Fe [193]. In Ni-base alloy IN 718 aged at 560 ºC for up to 216 h, the segregation level of Cr measured by EDS is much lower than that in a 2.25Cr1Mo steel [215, 218]. This is consistent with the results from APT on the same alloy which was held at 600 ºC for at least 10000 h [219]. A possible reason is that the diffusion coefficient of Cr in Ni is lower than that in Fe [57, 220]. It should be noted that the C concentration in 2.25Cr1Mo steel is 4-6 times higher than in IN 718 and C may promote the segregation of Cr due to the attractive interaction between C and Cr. P was also present in both alloys. So the ES mechanism cannot be validated due to the C and P presence. By analysing the dependence of the ES free energy of Cr on the P concentration at the GB in low-Mo, 12Cr steel, the ES free energy of Cr without P was obtained as -0.4 kJ/mol [221]. This small, negative value indicates that Cr does not segregate to GBs in Fe without the addition of P. The segregation observed is due to the interaction between Cr and P.

   Compared with Fe, no available data for the ES free energy was found in Ni alloys. To verify this, Ni-6Al-6Cr alloy free of C and P was aged at 700 ºC for up to 200 h and quenched into water. Figure 5.22 is the HAADF image and corresponding profile across a GB in the sample aged for 200 h. It is obvious that no Cr segregation was detected. This indicates that the ES free energy of Cr is too small to generate GB segregation of Cr, consistent with the calculations in [221]. The segregation of Cr mentioned in the

literature was more probably due to the interaction of Cr with other elements, such as P and C.

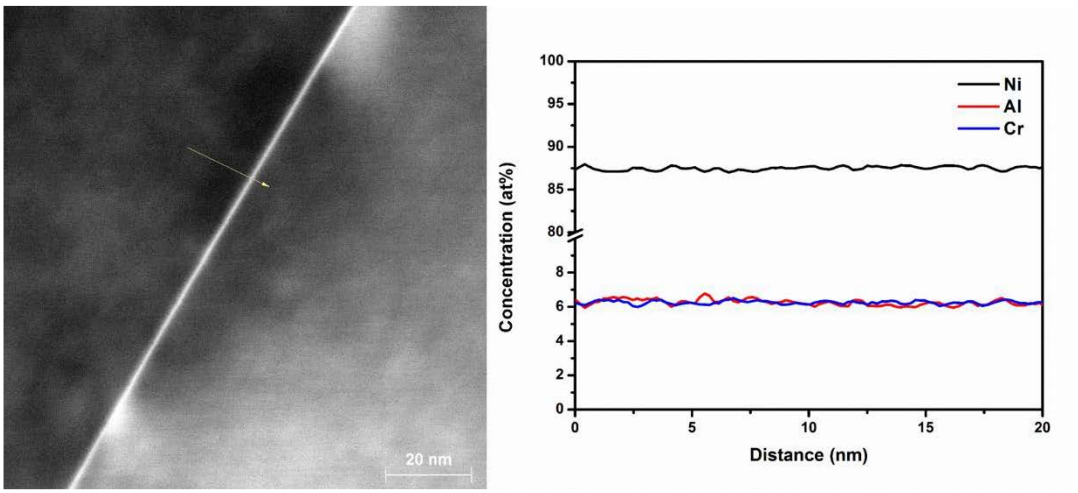

Figure 5.22 HAADF image and line-scan profile of the Ni-Al-Cr aged at 700 ºC for 200 h followed by water-quenching

Based on the above discussion, the absence of GB segregation of Cr during cooling from 700 ºC and 1200 ºC, and the aging at 500 ºC for up to 48 h can be attributed to the low binding energy between Cr and vacancies, the absence of B, C and P which can attract Cr to the GB and a low segregation free energy of Cr via an ES mechanism.

Similar to Cr, the GB segregation of Mo has also been investigated in steels and Ni-base alloys and possible mechanisms are:

1. Solute-vacancy complex diffusion (NES). Mo segregation was measured using EDS in a 2.25Cr1Mo steel with P or Sn additions after cooling [149]. This is consistent with the results in the same alloy in [158]. A Mo-vacancy complex diffusion mechanism was proposed as the binding energy calculated based on the strain field analysis was 0.38 eV and 0.43 eV in ferritic and austenitic steel matrices, respectively [96]. This is comparable with the P-vacancy binding energies of 0.36 eV and 0.41 eV, and much larger than those of Cr of 0.12 eV and 0.036 eV [96]. The binding energy falls into the

range 0.3-0.6 eV suggested by Xu [117], which is suitable for the occurrence of NES. A first principles calculation also indicated that the Mo-vacancy binding energy in bcc Fe is 0.33 eV, similar to 0.36 eV for P [125]. However, these results of the Mo-vacancy binding energy are much larger than other first principles calculations, such as 0.08 eV [122], 0.09 eV [222] 0.10 eV [128] and 0.17 eV [223]. The difference between different calculations makes it hard to determine whether Mo-vacancy diffusion plays a key role during cooling. Compared with iron, the binding energy of Mo to vacancies in Ni is much smaller. Using first principles calculations, the binding energy was determined to be 0.01 eV [224], which is consistent with the calculated results in [198]. Such a low binding energy makes the formation and diffusion of Mo-vacancy complexes unlikely.

2. Interaction with other elements (ES and NES). B-Mo segregation and the formation of Mo boride at GBs was observed using 1-D atom probe in a 316L steel during cooling [225]. A similar phenomenon has also been reported in a quenched low-carbon steel using APT [194]. Using ES theory, the measured segregation of B and Mo by APT in low carbon steel and its dependence on cooling rate was explained [226]. However, this contradicts previous results which indicated that B segregation during cooling is of non-equilibrium type [194, 195, 225, 227, 228]. Also, the measured segregation profile indicates that the width of the segregation zone is several nano-metres, falling into the range of NES and much larger than the ES of several atomic layers. In Ni-base superalloy 617B water-quenched from 1175 ºC, GB segregation of B and Mo was detected [201], which is consistent with the results for Astroloy [228], N18 [145] and HAYNES 242 [229]. It was found that the segregation level of B and Mo in PE16 increases with the solution treatment temperature and depends on the cooling rate, which is a characteristic of NES [204]. Also, the GB concentration of Mo increases with B, indicating a synergistic segregation of B and Mo [204].

P-Mo co-segregation in a 2.25Cr1Mo steel during quenching and tempering was measured using EDS [108]. Using AES, the co-segregation of P and Mo was measured in 2.25Cr1Mo and 12Cr1MoV steels [21]. The GB concentration of P increases with the Mo content at the GB [21]. Similar results have also been observed for both ES and NES in steels [109, 158, 230]. In Ni-base alloy IN718, P-Mo co-segregation was observed by AES [22, 37]. The GB P concentration increases with that of GB Mo.

Using AES, the co-segregation to a free surface of Fe-3.5Mo-N alloys was reported and the calculated interaction coefficient between N and Mo is very close [231, 232]. Similar to Cr, all the samples studied here for the interaction between Mo and P/B contain C. So, the effect of C on the GB segregation of Mo should be excluded. This is possible by analysis of the interaction coefficient, as will be discussed in section 5.3.2.

3. Diffusion via vacancies (ES). This was observed in samples subjected to long term aging. Using EDS, the segregation of Mo was measured in a 2.25Cr1Mo steel aged at 520 ºC for up to 210 h [215]. Similar results have also been reported for Ni-base 718 alloy aged at 560 ºC for up to 216 h [218] or in service at 600 ºC for more than 10000 h [219]. The segregation level of Mo in 718 alloy is more or less the same as that in 2.25Cr1Mo steel [215], although the temperature is higher and the nominal concentration is higher in the 718 alloy. A possible reason is that the diffusion coefficient of Mo via a vacancy mediated mechanism is about 2 orders lower in Ni than in Fe [233-235]. It should be noted here that all these samples contained C and P or B, which may induce Mo segregation by attraction. By fitting the experimental data from a 2.6Cr-0.7Mo-0.3V steel, the intrinsic segregation energy of Mo, ΔG_{Mo}^{0}, was determined as 20-22 kJ/mol [236, 237]. However, this is much larger than the 0.1 kJ/mol in 12Cr1Mo and 2.25Cr1Mo steel [221] as the interaction coefficient of P and Mo estimated in [221] is much larger than that in [236, 237].ıA range of 8.8-11.8 kJ

/mol was obtained from several Fe-Mo-P alloys [238], which is between the results reported in [221] and those in [236, 237].

Compared with Fe, no data were found for Ni alloys. To verify whether Mo segregation during long term aging is caused by the diffusion of Mo via vacancies or the interaction between Mo and C, B or P, a Ni-Al-Mo sample was aged at 700 ºC for up to 200 h followed by water quenching to check whether Mo segregation develops during this stage. Figure 5.23 shows the HAADF image and corresponding profile across the GB in the samples aged for 200 h. Slight Mo segregation was detected. It is consistent with the elemental maps shown in figure 5.24. Similar results have also been observed in a sample aged for 50 h. The segregation width is less than 2 nm, indicating ES. This is different from the results for Cr which was not enriched at the GB. Possible reasons are a higher diffusion coefficient or a higher segregation energy of Mo than for Cr. By first principles calculations, the diffusion coefficients of Cr and Mo have been shown to be very close at 700 ºC [239, 240]. This indicates that the segregation energy of Mo is probably higher than that of Cr, consistent with the calculation in [238]. Also, the segregation level of Mo in this study is much lower than that reported in [218]. This means that an elemental interaction between C/P and Mo rather than vacancy mediated diffusion of Mo is the main segregation mechanism in those reported in the literature [218].

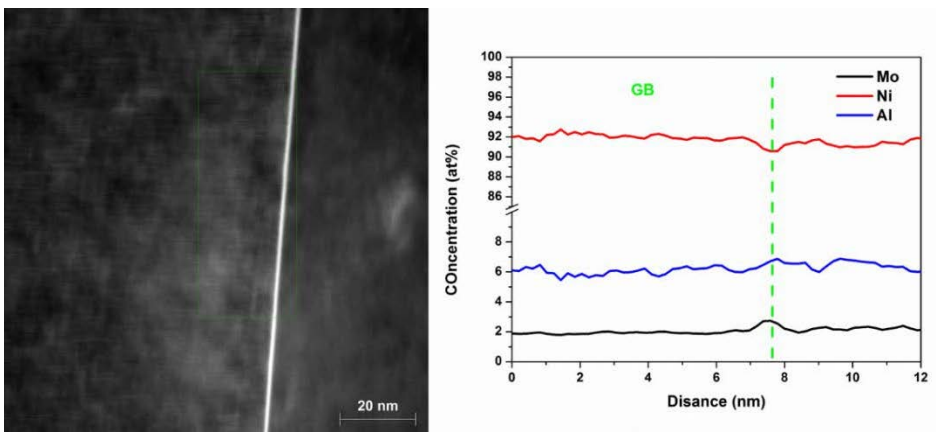

Figure 5.23 HAADF image and profile of Ni-Al-Mo aged at 700 ºC for 200 h followed by water-quenching

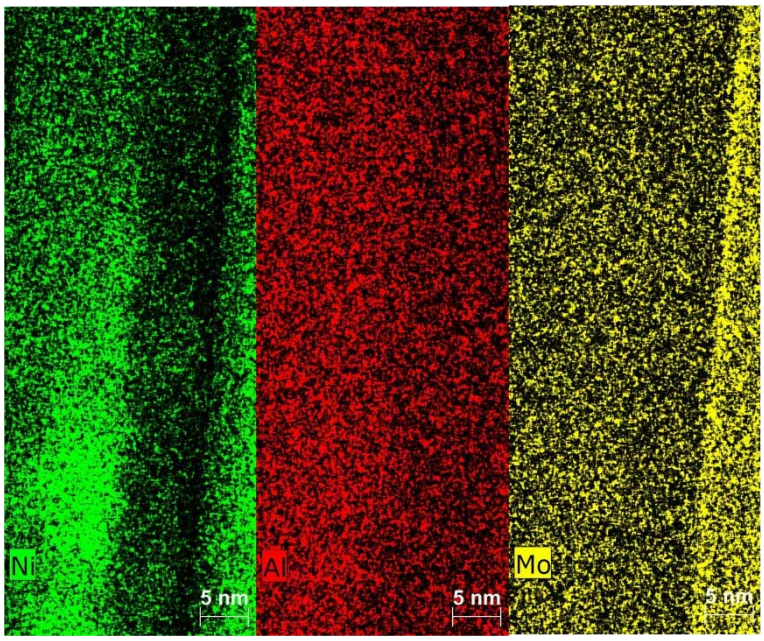

Figure 5.24 Elemental maps of Ni, Al and Mo obtained from the area shown in figure 5.23

Based on the above discussion, it can be concluded that a low binding energy between Mo and vacancies, absence of a synergistic effect with minor elements like B, C and P and a low diffusion coefficient resulted in no GB segregation of Mo being detected after cooling from 700 °C and 1200 °C.

5.3.2 Effect of P on Cr/Mo

This can be divided into elemental interaction (attractive or repulsive) and site competition.

It has been shown that the segregation of impurities (S and As) can be promoted by the addition of transitional metal Ce in a Ni-Cr-Mo steel [241]. This is consistent with previous results which showed that alloying elements e.g. La and Ce were necessary for the embrittlement of steels by impurities e.g. P and As [242]. This indicates that an interaction between these two categories of atoms, i.e. impurities and transition metals, exists. A co-segregation model was first proposed by Guttman [62] to explain the interaction between metallic alloying elements

and non-metallic impurities during ES. This model considers the GB as a homogeneous bi-dimensional phase ∅, in which all the thermodynamic parameters can be defined, similar to a bulk phase. During diffusion, a thermodynamic equilibrium between the bulk phase and ∅ is established, i.e. the chemical potentials of each element in both phases are the same.

According to the model, the segregation energy in a ternary solution with impurity I and transition metal M in solvent S can be calculated as [62] (see Appendix A54 and A55)

$$\Delta G_I = \Delta G_I^0 + \alpha'_{MI} N_M^{\emptyset} \quad 5.1$$

$$\Delta G_M = \Delta G_M^0 + \alpha'_{MI} N_I^{\emptyset} \quad 5.2$$

where α'_{MI} is the relative interaction coefficient between M and I and $N_I^{\emptyset}$ and $N_M^{\emptyset}$ are the concentrations of the impurity and metal at the GB, respectively. α'_{MI} can be calculated by [62] (see Appendix A57 and equation 2.8)

$$\alpha'_{MI} = \alpha_{MI} - \alpha_{MS} - \alpha_{IS} \quad 5.3$$

where α_{MI}, α_{MS} and α_{IS} are the intrinsic interaction coefficients between M and I, M and S and I and S, respectively. Normally, the interaction between M and S is weak and can be neglected [243, 244].

A positive α'_{MI} indicates that an attractive interaction between the solute M and I compared with I and S results when balancing all the interactions. This will lead to the enhanced segregation of each other. Even when M did not segregate to the GB in the binary S+M system, addition of a slightly GB segregated element I resulted in the segregation of M, and in turn enhanced I segregation. If α'_{MI} is negative, stronger segregating elements will cause the desegregation of weaker segregating elements, even when both I and M are not very GB active. An attractive interaction between C and Cr and a repulsive interaction between C and Si have been observed in liquid Fe [245].

Xu [117] extended Guttmann's equilibrium co-segregation model to NES by assuming the thermodynamic equilibrium between bulk phase and GB 2-D phase is still valid during the whole diffusion process, i.e. both the segregation and desegregation stages. This is reasonable as thermodynamic equilibrium is only concerned with short range diffusion and in a small region close to the GB [117]. Based on this assumption, co-segregation of M and I can take place when one of the binding energies between M or I and vacancies fall in the range 0.3-0.6 eV and the relative interaction coefficient α'_{MI} is positive. If α'_{MI} is negative, elements with a stronger segregation tendency will discourage the segregation of those with a lower segregation tendency.

The above discussion indicates the importance of the interaction coefficient between solute and solvent atoms. There were some interaction coefficient measurements. Using the slag/metal equilibration technique, the interaction parameter between P and Cr in Fe-Cr-P alloys with a Cr concentration lower than 20 wt% was measured to be 0 in the range 1350 °C -1450 °C [246]. This is close to the previous results of -0.0386 [247], -0.0366 [248], and -0.085 [249] at 1300 °C in similar alloys using the same method. Thermodynamic calculation indicates that the interaction parameter between P and Cr is positive and decreases with temperature over the range 1420-1620 ºC [250], which is different from the results in [246]. All these experiments were done in liquid alloys at high temperature and the interaction parameter should be different from that in the solid state. For example, the interaction coefficients for P-Ni and P-Mn in the liquid are close to 0, much smaller than that in the solid [221]. So it is not safe to use these data to do a quantitative analysis in solids [221]. By analysing previous experimental data, the relative interaction coefficient between P and Cr/Mo was calculated based on Guttmann's model [221]. The relative P-Cr interaction coefficient, α'_{PCr}, in 12Cr steels was obtained as 68.4±9.6 kJ/mol [221, 251, 252]. This is much higher than the 2-5 kJ/mol obtained from a low alloy Cr steel [253]. The positive value indicates that P can co-segregate with Cr to the GBs in

Fe. Also, the interaction coefficient is dependent on the concentration of Cr. Increasing Cr concentration leads to a decreasing coefficient [221]. Fitting the experimental data in Fe-1.2at%Mo-P and Fe-0.3at%Mo-P [250], the relative interaction coefficients between P and Mo, α'_{PMo}, were determined as 177 kJ/mol [221] and 150±26 kJ/mol [251, 252] respectively. Using the data for 12Cr-Mo [254] and a 2.25Cr1Mo steel [255], α'_{PMo} was determined to be 125 kJ/mol [221]. This is much higher than the 19.7 kJ/mol for a 2.6Cr-0.7Mo-0.3V steel [237]. The possible reason is the neglect of the interaction of Mo with other elements, such as C, when fitting the experimental data. The relative interaction coefficient can be over or under estimated depending on the relative interaction coefficient of Mo with other elements. If the value is positive, then the contributions from other elements were also attributed to P. This results in an overestimation of α'_{PMo} and *vice versa*. Though the values of α'_{PMo} are quite different in different alloy systems, positive α'_{PMo} and co-segregation of P and Mo are expected in Fe. Compared with Fe, experimental data on the segregation of P and Cr/Mo in Ni-base alloys are limited. Also, it can be expected that the estimated value is alloy dependent due to the addition of C and/or B. It was proposed by Guttmann [62] that the interaction coefficient between elements *i* and *j* can be roughly estimated using the standard enthalpy of formation of the stable phase containing *i* and *j* at 25 ºC

$$\alpha_{ij} = -\Delta H^0_{ij}/N_i N_j \qquad 5.4$$

where N_i and N_j are atomic percent in the phases formed by *i* and *j*, respectively.

P and Cr/Fe/Mo/Ni can form different types of phosphides. For example, P and Cr can form Cr_3P, Cr_2P, $Cr_{12}P_7$, CrP, CrP_2 and CrP_4. P and Fe can form Fe_3P, Fe_2P, FeP, FeP_2 and FeP_4. P and Mo can form Mo_3P, Mo_4P_3, MoP, MoP_2 and Mo_2P_5. P and Ni can form Ni_3P, Ni_2P, NiP, NiP_2 and NiP_3. The standard enthalpies of formation of M_xP_y (where M=Fe, Cr and Ni) have been measured and were reviewed in [256]. Here we only consider M_3P as this is the most

general form [257]. The measured standard enthalpies of formation of Fe_3P, Cr_3P and Ni_3P were in the range -128 to -200 kJ/mol, -93 to -183 kJ/mol and -140 to -337 kJ/mol, respectively. These data were combined with the heat capacities and entropies to generate enthalpies. The standard enthalpies of formation of Fe_3P and Cr_3P were determined as -143 kJ/mol and -163 kJ/mol [256]. The relative interaction coefficient of Cr and P in Fe, α'_{PCr}, can be calculated as 107 kJ/mol by equations 5.3 and 5.4. By fitting the solubility profile of P for different Cr concentrations, the formation enthalpy of Cr_3P can be obtained and α'_{PCr} determined using the fitted enthalpy as 100 kJ/mol [257], close to our calculated results of 107 kJ/mol. This means P and Cr can co-segregate to the GB in Fe, which is consistent with the results in [221, 251-253]. For Ni_3P, no assessment was done in [256] so the averaged value of -194 kJ/mol was used. α'_{PCr} in Ni can then be determined as -171 kJ/mol by equations 5.3 and 5.4. The negative value indicates that P and Cr co-segregation cannot happen in a Ni alloy. Rather, this repulsive interaction will lead to the desegregation of Cr according to [62, 117]. This is consistent with our experimental results. Experimental data for the standard formation enthalpy of Mo_3P are very rare. So it is difficult to calculate the relative interaction coefficient of Mo and P, α'_{PMo}, in both Fe and Ni. However, α'_{PMo} in steel can be obtained by fitting the solubility of P to be 176 kJ/mol [257]. This is consistent with previous results [221, 251, 252], indicating that Mo can co-segregate to the GB with P in Fe. Also, the standard formation enthalpy of Mo_3P can be calculated to be -176 kJ/mol. The relative interaction coefficient of Mo and P, α'_{PMo}, in Ni can then be determined to be -85.3 kJ/mol. The negative α'_{PMo} in Ni alloy indicates that Mo will deplete at the GB, consistent with our experimental results.

Based on the above discussion, segregation of Cr and Mo in Ni alloys during long term aging cannot be attributed to an interaction between P and Cr/Mo. To further confirm the relative repulsive interaction between P and Cr/Mo in Ni, Ni-Al-Cr-P and Ni-Al-Mo-P were aged at

700 ºC for 200 h following by water-quenching. Figures 25-28 are the corresponding line-scans and elemental maps.

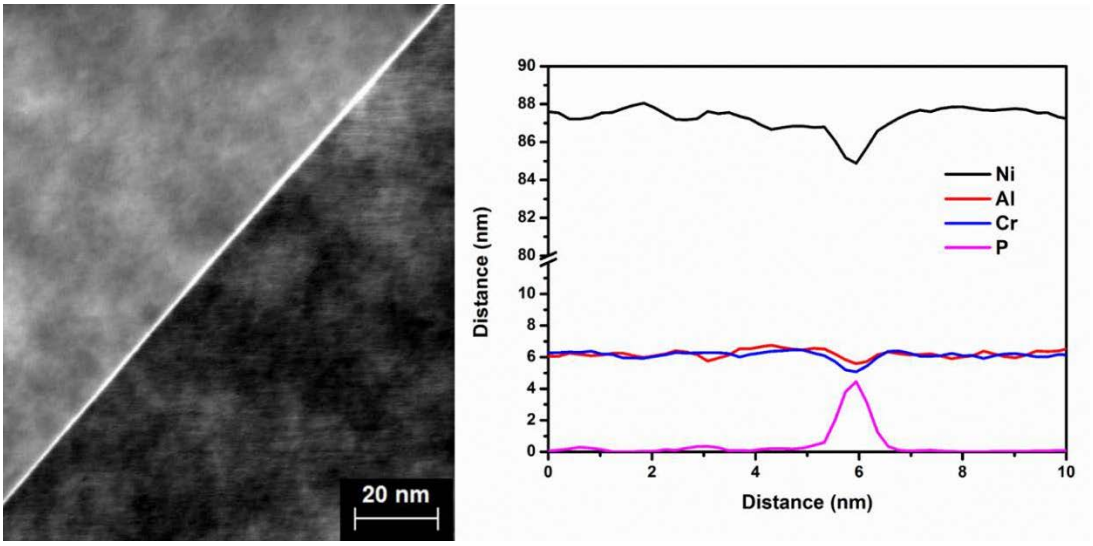

Figure 5.25 HAADF image and corresponding line-scans of Ni-Al-Cr-P aged at 700 ºC for 200h followed by water-quenching.

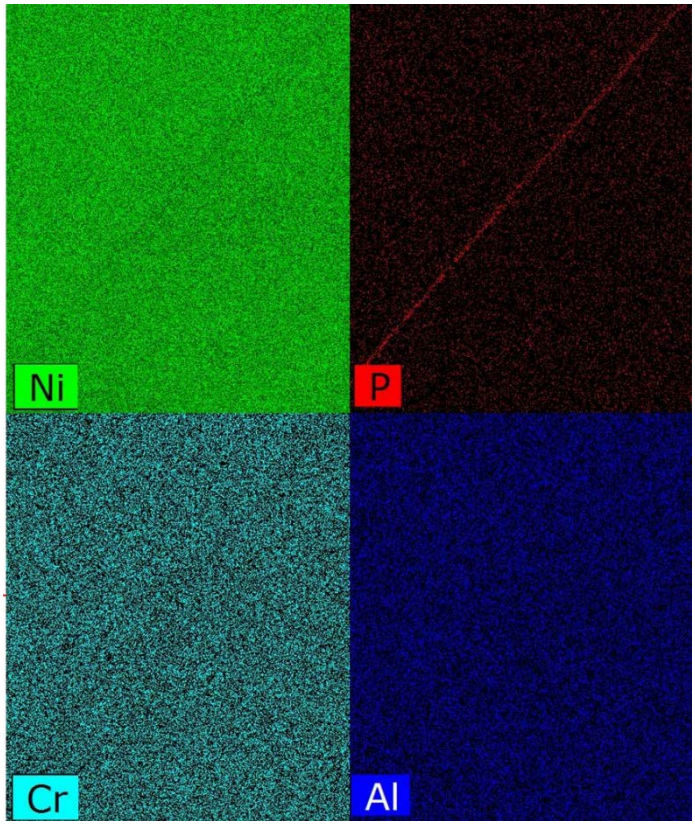

Figure 5.26 Elemental maps of Ni, P, Cr and Al obtained from the area shown in figure 5.25

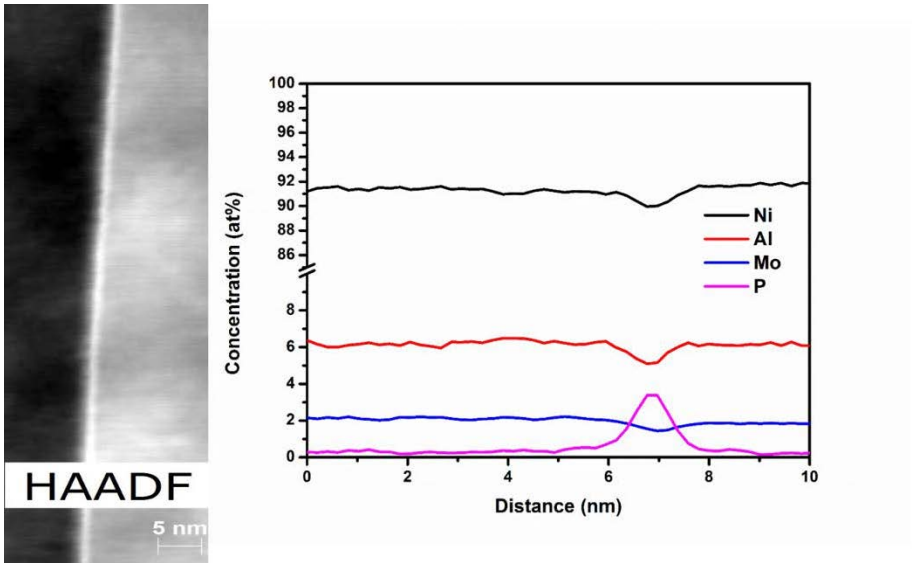

Figure 5.27 HAADF image and line-scans of Ni-Al-Mo-P aged at 700 ºC for 200h followed by a water quench.

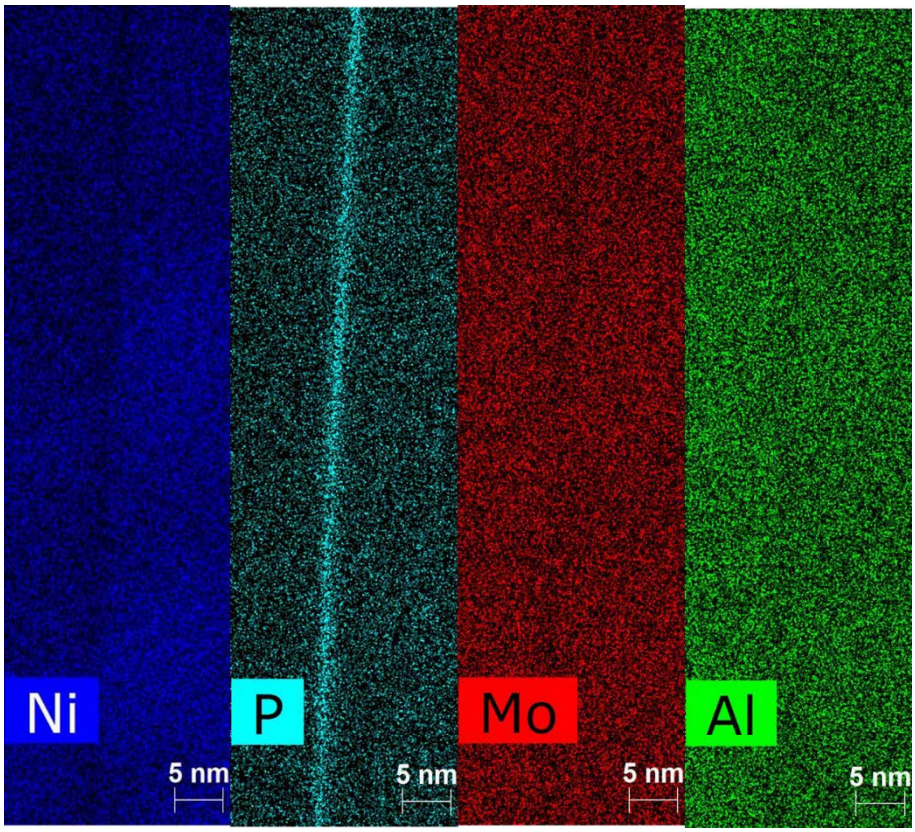

Figure 5.28 Elemental maps of Ni, P, Mo and Al obtained from the area shown in figure 5.27

It can clearly be seen that P segregated to the GB, while Cr and Mo are depleted at the GB. Also, the segregation width is less than 2 nm, which is typical of ES. The depletion of Cr and Mo during ES is consistent with our NES experiments, confirming that α'_{PMo} and α'_{PCr} in Ni alloys are both negative.

By NES and long term aging experiments, it has been confirmed that the main mechanism of Cr/Mo depletion in Ni alloys is due to the interaction between Cr/Mo and P as both α'_{PMo} and α'_{PCr} in Ni alloys are negative. According to the discussion in section 5.3.1, the mechanism of Cr/Mo enrichment at the GB reported in the references is the interaction between Cr/Mo and C/B/N. To validate this, the relative interaction coefficients between C/B/N and Cr/Mo/Fe/Ni need to be determined. The standard formation enthalpy of Cr/Mo carbides, borides and nitrides are more negative than those of Fe/Ni carbides, borides and nitrides (tables 5.5-5.7). This results in a positive relative interaction coefficient according to equations 5.3 and 5.4 and thus co-segregation of Cr/Mo with C/B/N in both Ni and Fe alloys, consistent with the experimental results listed in section 5.3.1.

Table 5.5 Standard formation enthalpy of Cr/Mo/Fe/Ni carbides (unit: kJ/mol) [258]

Carbides	Cr_3C_2	Cr_7C_3	$Cr_{23}C_6$	MoC	Mo_2C	Fe_3C	Ni_3C
$-\Delta H_f^o$	94.1	208.1	396.2	28.5	49.8	-24.7	-37.7

Table 5.6 Standard formation enthalpy of Cr/Mo/Fe/Ni borides (unit: kJ/mol) [258]

Borides	CrB	CrB_2	MoB	Mo_2B	FeB	Fe_2B	NiB	Ni_2B	Ni_3B
$-\Delta H_f^o$	75.3	119.2	123.8	132.2	59.4	55.6	46.4	63.7	88.9

Table 5.7 Standard formation enthalpy of Cr/Mo/Fe/Ni nitrides (unit: kJ/mol) [258]

Nitrides	CrN	Cr_2N	Mo_2N	Fe_2N	Fe_4N	Ni_3N
$-\Delta H_f^o$	117.2	125.5	81.6	3.8	11.7	-0.8 [65]

If more than one non-metallic element is present in the alloys, the systems become more complex as the interaction between different non-metallic elements, as well as the interaction between non-metallic elements and metal elements need to be considered. For example, C-B interaction has been reported [199, 207] and may affect the segregation behaviour of Cr in steel [194, 195].

Another possible reason causing the depletion of Cr/Mo at the GB is site competition. The available sites at the GB for the segregants to take are limited. If several elements have the tendency to segregate to the GB, they compete for the limited sites. Elements with higher segregation tendency occupy preferentially the available sites, preventing other elements from segregating [259].

Although site competition has been widely invoked to explain the antagonistic segregation behaviour, especially of different non-metallic elements, such as C and P [19, 80, 260], P and N [79] and S and C [261], it is hard to distinguish from repulsive interactions. For example, the site competition behaviour between C and P reported in [19, 80] can also be explained based on the strong repulsive interaction between C and P [251], which has been confirmed by first principle calculations [127]. The difference is, the former set all the relative interaction coefficients equal to zero and use ΔS_i^o as an adjustable parameter, whereas the latter choose the reverse. Validation of both approaches requires accurate measurements or theoretical assessments of the coefficients. Despite the difficulties, general rules of site competition have

been proposed [259]. Firstly, segregated atoms need to take the same sites at the GB. Secondly, site competition effects should only matter when the GB concentration is high enough. In our case of P and Cr/Mo in Ni, both P and Cr/Mo are substitutional in the matrix and they are expected to take the same sites at the GB. However, the antagonistic segregation behaviour between P and Cr/Mo happened under all conditions, even with a low concentration at the GB. This indicates that site competition is unlikely to be the main mechanism causing the depletion of Cr/Mo at the GB.

5.4 Conclusions

1. Cr and Mo segregation in Ni-Al-Cr and Ni-Al-Mo during cooling from 700 ºC and 1200 ºC with different cooling rates and following aging at 500 ºC for up to 48 h was not observed due to the low binding energy between Cr/Mo and vacancies.

2. In Ni-Al-Cr and Ni-Al-Mo alloys aged at 700 ºC for up to 200 h, Cr does not segregate to the GB as the segregation energy of Cr is close to 0, while Mo segregates slightly to the GB after due to the low but positive segregation energy of Mo.

3. In Ni-Al-Cr-P and Ni-Al-Mo-P cooled from 700 ºC at different rates or aged at 500 ºC for up to 48 h, P segregated to the GB, while Cr and Mo were depleted at the GB. Also, the Cr/Mo concentration increases with decreasing P concentration at the GB. This is inconsistent with previous results which showed that P and Cr/Mo co-segregated to the GB in steels and Ni alloys.

4. In Ni-Al-Cr-P and Ni-Al-Mo-P aged at 700 ºC for up to 200 h, P segregated to the GB while Cr and Mo were depleted.

5. The relative interaction coefficients between P and Cr/Mo in Ni, α'_{PMo} and α'_{PCr}, were calculated based on Guttmann's theory. Negative α'_{PMo} and α'_{PCr} indicated a relative repulsive interaction between P and Cr/Mo and the desegregation of Cr/Mo caused by P segregation. Also, the calculated relative interaction coefficients between C/B/N and Cr/Mo in Ni are all

positive meaning that Cr/Mo can co-segregate to the GB with C/B/N. This is possibly the main mechanism to account for the Cr/Mo segregation reported in the literature as all the samples studied previously contained C and/or B/N.

Chapter 6. Effect of experimental parameters on chemical analyse

6.1. Introduction

TEM-EDS has been widely used in chemical analysis, especially for small scale features such as nanoparticles and GBs, due to its higher spatial resolution which derives from the higher acceleration voltage and thinner samples in a TEM as compared with those in an SEM [218, 262]. It has been shown that some experimental factors affect the chemical analysis results dramatically. Generally these effects can be divided into two categories: interaction volume (probe size and beam broadening) and beam damage. When measuring GB segregation, a larger probe size leads to a higher statistical accuracy by increasing the signals, although a broader segregation profile with a lower peak value is obtained [263, 264]. Beam spreading during electron transmission through the thin foil has been regarded as the primary factor limiting the spatial resolution [265]. Therefore, many theoretical analyse and experiments have been performed. Based on single scattering theory, an equation defining the beam broadening (b) was first proposed by Goldstein [266] and then modified by Reed [267] as follows:

$$\mathrm{b(cm)} = 7.21 \times 10^5 \times (\frac{\bar{Z}}{E_0}) \times (\frac{\rho}{\bar{A}})^{1/2} \times t^{3/2} \qquad (6.1)$$

where Z is atomic number, E_0 the incident energy, ρ the density, A the atomic weight and t the foil thickness. Monte Carlo simulation has also been performed by considering the effect of backscattering, multiple scattering and inelastic scattering [268] which gave results smaller than those calculated by Equation 6.1 in several materials with specimen thickness larger than 100 nm [268]. Experimental results obtained by measuring the difference between the 90% probe size at the bottom and top surfaces were consistent with Monte Carlo calculations in medium thickness foils [269-272]. However, recent experimental results indicated that beam broadening was smaller than the predicted value, especially when the sample thickness is less

than 200 nm [273]. On the other hand, beam damage has been demonstrated as a factor that affected chemical analysis results [274-276]. Electron-beam-induced surface sputtering and bulk displacement have been widely reported. Theoretical calculations have also been conducted to quantity this effect [277]. The threshold energy for both surface sputtering and bulk displacement and the corresponding cross section have been calculated for elements with atomic number up to 92 and for an acceleration energy of 0.1-1.5 MeV [277]. The threshold energy for surface sputtering is much lower than that of bulk displacement. When using an acceleration of 200 keV which is quite common nowadays, most elements can be sputtered on the surface, while only a few can be displaced with the bulk [277]. Also, the cross-sections for different elements are different, resulting in preferential surface sputtering or bulk displacement and eventually local concentration alteration. Even though both the effects of interaction volume and beam damage have been widely researched, it is still unknown which is the dominant factor.

6.2. Experimental procedure

An alloy with the nominal composition of Ni-6Al-0.1P (at%) was prepared by arc melting and solution heat treated at 1300 °C for 48 hours, compressed by 60% and subsequently heat-treated at 700 °C for 2 h followed by water-quenching. TEM samples were prepared by twin jet polishing using a solution of 5% perchloric acid in ethanol at a current of 50 mA and a temperature of -20 °C. Chemical analysis was carried out across a GB (figure 6.1a) on an FEI Talos F200X with four SDDs. The GB was carefully tilted to make sure its projection width was smaller than 2 nm (figure 6.1b). Various beam currents, acquisition times and thicknesses were used to verify their effect on chemical analysis. At region 1, beam currents of 100 pA, 200 pA, 500 pA and 1000 pA were used for the line-scans with an acquisition time of 1 s for each point. At region 2, the acquisition time was changed from 0.5 s, 1 s, 2 s to 4 s for each point with the same beam current of 200 pA. Regions 1, 2, 3, 4 at distances of 0.45, 1.1, 4.5

and 8 μm from the edge were used with an acquisition time of 1 s and beam current of 200 pA. Thickness measurements were conducted on a JEOL-2100 using convergent beam electron diffraction (CBED) and a **g** of (113). EDS data were processed by Bruker Esprit using the Cliff-Lorimer method [156]. Absorption was corrected by using sample thickness and density because this has been found to affect chemical analysis results, especially for low energy X-rays in high atomic number materials [278].

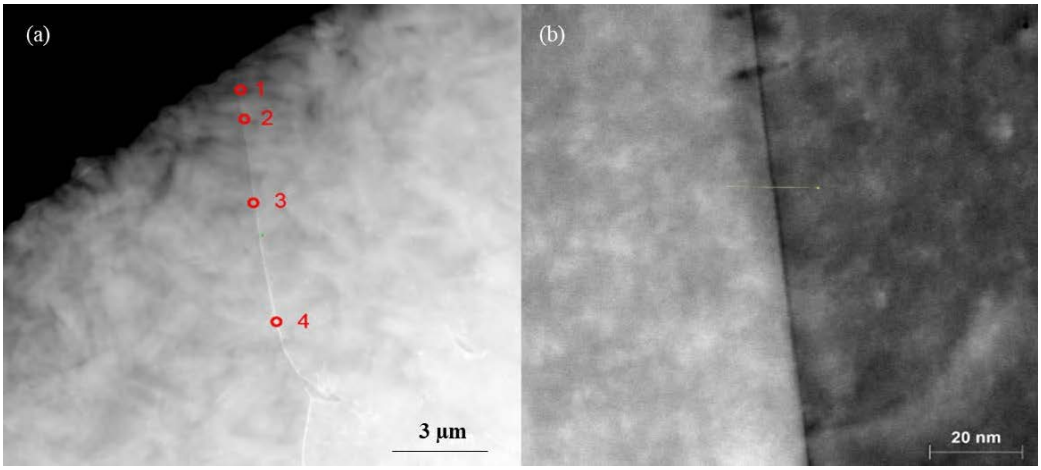

Figure 6.1 (a) HAADF image of the GB in Ni-Al-P alloy showing the regions to perform the analyses and (b) magnified HAADF image of the GB

6.3. Results and discussion

6.3.1 Effect of acquisition time

The effect of acquisition time on the P concentration profile measured is shown in figure 6.2. With increasing acquisition time from 0.5 s to 4 s, the P concentration at the GB declined by more than 50%. As the beam current and the foil thickness are identical for each measurement, the effect of initial probe size and beam broadening can be neglected. The effect of acquisition time can be attributed to beam damage. With increasing acquisition time, beam damage became much more serious (figure 6.2c). When using 0.5 s, beam damage can barely be seen. Dark area caused by surface sputtering can clearly be seen after the line-scan when the acquisition

time increased to 4 s. This is not contamination as the contrast of the contamination would be bright. All three elements (Ni, Al and P) can be sputtered by the electron beam as the threshold energies for Al, P and Ni to be sputtered are 41 keV, 47 keV and 108 keV, respectively, smaller than the incident energy [277]. For bulk displacement, the threshold energies for Al, P and Ni are 148 keV, 167 keV and 355 keV, indicating that only Al and P can be displaced [19]. Though all three elements can be affected by beam damage, the cross sections for surface sputtering and bulk displacement are different (table 6.1) [277]. It should be noted that the cross section list in table 6.1 is for pure elements. Depending on the chemical state, this will be different for different systems. For example, the cross sections of Ni, Al in pure elements and Ni_3Al are different [275]. However, no matter whether pure elements or not, the cross section for Al is larger than that for Ni. So, it is reasonable to use the data for pure elements in this study. The total cross section for P is the largest, followed by Al and Ni. The decrease of apparent P concentration at the grain boundary was due to its large cross section, because more P atoms are sputtered or displaced than Al and Ni. The measured Al concentration at grain boundary is expected to decrease with increasing acquisition time due to its total cross section being larger than the average cross section of Al, P and Ni in Ni-6Al-0.1P. This is consistent with the experimental results (figure 6.2b).

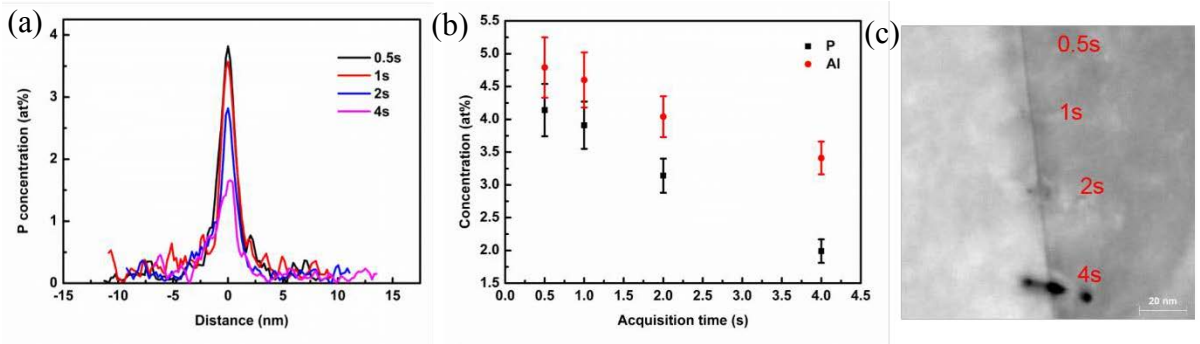

Figure 6.2 (a) Line-scans for P with different times, (b) effect of acquisition time on GB concentration of P and Al and (c) beam damages by the electrons with different acquisition times

Table 6.1 Surface sputtering (σ_{ss}), bulk displacement (σ_{bd}) and total (σ_{tot}) cross sections of Al, P and Ni with an electron acceleration voltage of 200 kV [277]

	Al	P	Ni
σ_{ss} (barns)	383.75	424.67	344.26
σ_{bd} (barns)	24.55	16.98	-
σ_{tot} (barns)	408.30	441.65	344.26

In this section, only beam damage was considered, while the effect of interaction volume was neglected because it was same for each scan. However, both of these two factors should be considered under some circumstances such as different beam current or foil thickness. This will be discussed in the following section.

6.3.2 Effect of beam current

The effect of beam current on the P concentration profile is shown in figure 6.3a. As the beam current increased from 100 pA to 1000 pA, the measured grain boundary P concentration decreased by more than 50%. As the foil thicknesses were the same for these scans, the effect of beam broadening was the same in each case. The possible reasons are probe size and/or beam damage.

The probe size was measured by fitting the intensity distribution to a Gaussian expression. The full width at half maximum (FWHM) was used as the probe size and is shown in figure 6.3b. The probe size increased with beam current, as expected. When the probe size increased, the interaction volume also increased, resulting in the true concentration profile being folded with the beam profile and a decrease in the maximum concentration measured. On the other hand,

beam damage also became more serious with increasing beam current (figure 6.3c). This can also lower the measured grain boundary P content as shown in section 6.3.2.

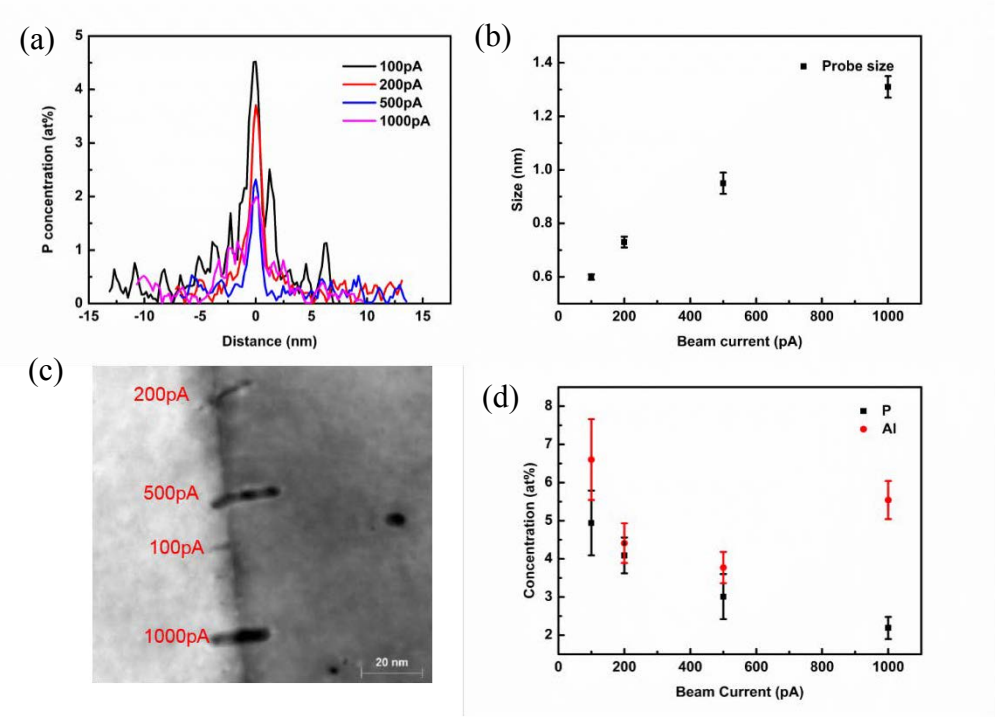

Figure 6.3(a) line-scan profiles of P with different beam current, (b) measured probe size for different currents, (c) beam damage and (d) effect of beam current on P and Al content at the GB.

To verify which is the dominant factor, the measured concentration of Al at the grain boundary can be monitored. If interaction volume is the dominant factor, the measured Al content should increase as more signal from the bulk area where the Al concentration was higher is collected. If beam damage is the dominant factor, the concentration of Al should decrease as shown in section 6.3.1. The measured Al concentration is shown in figure 6.3d. It can be seen that the measured Al concentration at the grain boundary decreased with increasing beam current up to 500 pA. When the beam current increased to 1000 pA, the Al content increased dramatically though remaining smaller than that at 100 pA. This indicated that initially beam damage rather

than interaction volume is the dominant factor. Subsequently, the effect of interaction volume took over when the beam current rose to above 500 pA.

From figure 6.3b it can be seen that the probe size is less than 1nm when the beam current is smaller than 500 pA. This is comparable with the projected GB width. Within this range, the effect of probe size is not profound. At 1000 pA, the probe size is about 1.31 nm, which is broader than the projected GB width, resulting in more signal from the bulk. This leads to a decrease in P concentration and an increase of Al concentration as compared with the situation at 500 pA.

6.3.3 Effect of thickness

Foil thickness was measured by convergent beam electron diffraction (CBED). Figure 6.4a shows a CBED pattern taken at position 4 using a 113 **g** which is large enough to avoid systematic row interactions. Fig. 4b shows the measured results and the corresponding linear fit which corresponds to a thickness of 151 nm. The measured extinction distance ξ_g of 62 nm is close to the 67 nm reported in [279]. The effect of foil thickness on the measured P concentration profile is shown in figure 6.5a. With thickness increasing from 30 nm to 130 nm, the P concentration decreased by about 40%. Just as in section 6.3.2, this can be attributed to beam broadening or beam damage. Beam broadening would lead to an increase in Al concentration as more signal from the bulk area would be collected, while beam damage would result in a decline in the Al concentration, just as in section 6.3.1. The measured Al content increased with increasing thickness (figure 6.5b). This indicated that beam broadening rather than beam damage is the dominant factor. This can be verified by measuring the Al concentration in the matrix as beam broadening, unlike beam damage, would not cause a concentration variation. The result is shown in figure 5c. With increasing thickness, the Al concentration remained almost constant, which agrees with the results of Jiang [280].

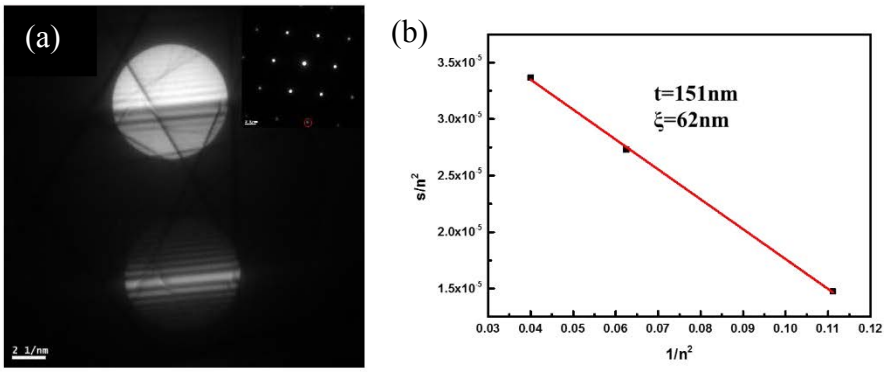

Figure 6.4 (a) CBED taken from position 4 and (b) measured thickness and extinction distance.

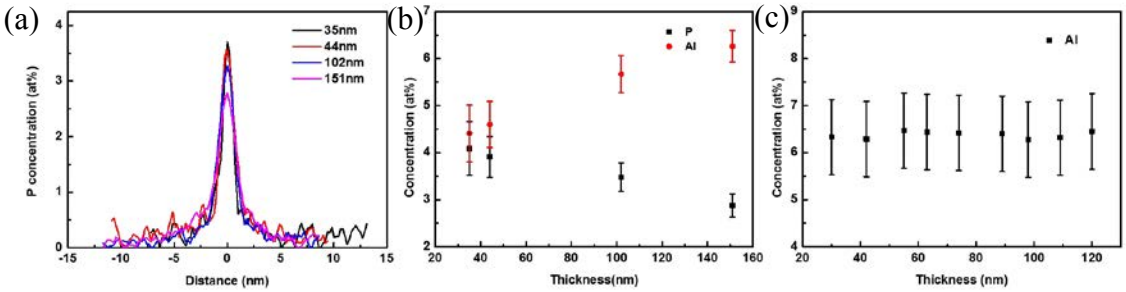

Figure 6.5(a) Line-scans for P for different specimen thicknesses, (b) effect of thickness on the GB concentration of Al and P, and (c) effect of thickness on the Al concentration in the matrix

6.3.4 Concentration, accuracy and counts

Figure 6.6 shows all of the data obtained under different conditions and the corresponding relative errors. With increasing counts, both the measured P concentration at the GB and the relative error decreased except with a beam current of 1000 pA. The counts are only about 5200, which is even smaller than those for 500 pA. At first, the counts were about 18000, which is normal for a larger beam current. However, the count rate dropped very quickly to 5200. This was caused by the serious beam damage.

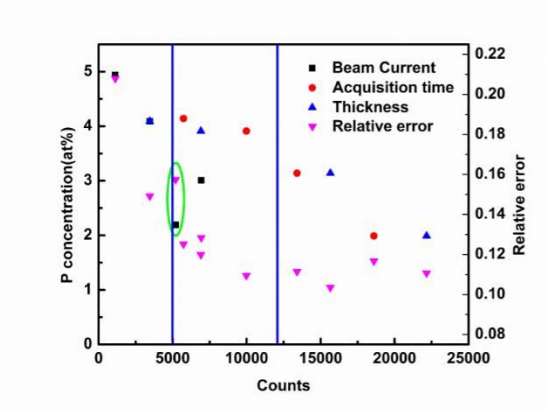

Figure 6.6 Relationship between counts and GB concentration of P and relative error

Higher counts are needed when performing EDS analysis to improve the accuracy. However, higher counts resulted in more serious beam damage and/or beam broadening which resulted in a decrease in the measured P concentration. On the other hand, if the counts are too low, a large statistical error is obtained. So an optimized condition exists which compromises between the measured concentration and the statistic error. In this study, the optimized counts were determined as between 5000 and 12000. It should be noted here that optimum results could not be obtained by controlling the counts only. For example, a shorter acquisition time can be used to collect optimum counts on a thicker specimen. However, this will result in a lower P concentration at the grain boundary because of the beam broadening. This is similar for beam current. A larger beam current with a shorter acquisition time results in a decrease of the P concentration due to the larger probe size. So the optimum experimental conditions should be a compromise between beam current, acquisition time and specimen thickness. According to figure 6.6, the optimum conditions correspond to a beam current of 200-700 pA, acquisition time per point of 0.5-1.5 s and specimen thickness of 40-80 nm.

6.4. Conclusions

The effect of acquisition time per point, beam current and specimen thickness on the measured P and Al concentrations at a GB were investigated using STEM-EDS. With increasing acquisition time, beam current and specimen thickness, the measured P concentration decreased. Possible reasons including the interaction volume and beam damage were considered. Beam damage rather than interaction volume was the dominant factor for long acquisition time and high beam current, while interaction volume was the dominant factor for large specimen thickness. The optimum number of the counts are suggested to lie between 5,000 and 12,000. This can be achieved using a beam current of 200-700 pA, acquisition time per point of 0.5-1 s and specimen thickness of 40-80 nm.

Chapter 7. Conclusions and future work

7.1 Conclusions

STEM-EDS has been employed to measure the GB segregation of P and/or Cr/Mo in Ni-base alloys. The following conclusions can be drawn.

1. P segregated to the GB of Ni alloys during the cooling process and the following aging stage with a NES pattern driven by the concentration gradient of the P-vacancy complexes. The segregation width is about several nanometres.
2. The segregation level of P is misorientation angle dependent. With increasing misorientation angle, the segregation increased until about 45°. A further increase resulted in the reduction of the segregation. The segregation at special CSL GBs were much lower than that at random high angle GBs. No segregation was detected at the twin boundary. Possible reason of this misorientaion angle dependent segregation is the dependence of the GB free volume on the misorientation angle.
3. Triple junction segregation was observed but could be higher or lower than the constitution grain boundaries. At the grain boundary close to the triple junction, a concentration gradient existed within a range of several to 100 nanometres.
4. When the effective time is shorter than the critical time, the concentration increased with decreasing grain size. This can be interpreted based on Wu's theory, in which the mass transfer coefficient is inversely proportional to the grain size.
5. A critical time existed during cooling and aging when the P concentration at the GB reached maximum. Shorter or longer time led to a decline of the P concentration. This is due to the competition of the two fluxes, i.e. P-vacancy complexes diffusion to the grain boundary and the P diffusion to the grain interior. Calculated results considering the grain size effect were quite close to the experimental results.

6. In Ni-Al-Cr/Mo alloys, no segregation of Cr/Mo has been observed during cooling after short time annealing and following aging process. Mo slightly segregated to the GBs after long term aging (200h) while no segregation of Cr has been observed. It is hard for Cr/Mo to form complexes with vacancy as the binding energy between Cr/Mo and vacancy in Ni is lower than 0.1 eV.
7. In Ni-Al-Cr/Mo-P alloys, P segregated to the grain boundary while Cr/Mo were depleted at the grain boundary. Dependence of Cr/Mo concentration on the P concentration can be fitted as

$$C_{Cr}^{GB} = (5.90 \pm 0.08) - (0.35 \pm 0.02) * C_P^{GB}$$

$$C_{Mo}^{GB} = (2.13 \pm 0.03) - (0.08 \pm 0.01) * C_P^{GB}$$

8. Depletion of Cr/Mo can be attributed to the negative relative interaction coefficients between P and Cr/Mo in Ni. This is consistent with the calculations based on the standard formation enthalpy of Cr/Mo phosphides.

7.2 Future work

1. The effect of P on the mechanical properties is alloy specific as the influence is indirect through its effect on other microstructures, such as grain boundary precipitates and grain boundary segregation of other elements. A simplified alloy needs to be used to exclude the effect of other factors. Though calculations indicated that P segregation affected the grain boundary cohesion, no experimental evidence has been reported. Also, the segregation level at each grain boundary is different. Mechanical test on bulk samples only showed the averaged effect. Effect of P on single grain boundary needs to be investigated. In-situ mechanical test in SEM and TEM supplies such a way and some work has been done on other alloys.

2. The effect of grain size on the segregation has been confirmed when the effective time is smaller than the critical time. According to Wu's theory, there is a critical grain size when the segregation reached to maximum. This needs to be further confirmed. By annealing at high temperature for different time, the grain size can be modified.
3. Triple junction segregation. It has been a debate for long time that whether the TJ energy is higher or lower than the constituent GBs. Direct experimental evidence is rarely reported, our results provided a way to investigate this debate as the segregation is shown depending on the free volume, which can be related to the energy.
4. The results on the elemental interaction are different with the literatures, which is possibly due to the interaction between C and Cr/Mo as all the samples studied contained C. However, no experimental results have been carried out. To verify this, samples contain C and Cr/Mo need to be used.

Appendix I: equation derivation

1. ES thermodynamics (Equation 2.5)

Consider a system with N lattice sites occupied by Q solute atoms and n GB sites occupied by q solute atoms. Let the distortion energies when a solute atom occupies the lattice site or the GB site be E and e, respectively. The Gibbs free energy can then be determined

$$\mathrm{G} = \mathrm{qe} + \mathrm{QE} - \mathrm{kT}\{lnN!\,n! - \ln(N-Q)\,!\,Q!\,(n-q)!\,q!\} \quad \text{A1}$$

Equilibrium is when G is at a minimum, i.e.

$$\frac{\partial G}{\partial q} = 0 \quad \text{A2}$$

Using the approximation

$$\mathrm{lnx!} = \mathrm{xlnx} - \mathrm{x} \quad \text{A3}$$

and

$$\mathrm{Q} + \mathrm{q} = \mathrm{constant} \quad \text{A4}$$

we find

$$\frac{q}{n-q} = \frac{Q}{N-Q}\exp(\frac{E-e}{kT}) \quad \text{A5}$$

The equilibrium concentration at the GB and inside the grain can be written as

$$C_{gb}^{m} = \frac{q}{n} \quad \text{A6}$$

$$C_0 = \frac{Q}{N} \quad \text{A7}$$

Combining A5, A6 and A7,

$$\frac{C_{gb}^m}{1-C_{gb}^m}=\frac{C_0}{1-C_0}\exp\left(\frac{Q}{RT}\right) \qquad \text{A8}$$

2. ES kinetics (Equation 2.9)

Suppose the initial and equilibrium concentrations at the GB are $C_{gb}(0)$ and $C_{gb}(\infty)$. The ratios of the two GB concentrations to that in the grain interior (C_1) are α_1 and α_2. As the boundary is too thin, the diffusion process can be simplified as diffusion in two half-infinite crystals with uniform solute contents. The diffusion equation is

$$D\frac{\partial^2 C}{\partial x^2}=\frac{\partial C}{\partial t} \qquad \text{A9}$$

At any time t, the concentration in the grain close to the GB is C=$C_{gb}(\infty)/\alpha_2$. The interface condition is

$$D\left(\frac{\partial C}{\partial x}\right)_{x=0}=\frac{\theta}{2}\left(\frac{\partial C_{gb}}{\partial x}\right)=\frac{\alpha_2\theta}{2}\left(\frac{\partial C}{\partial t}\right)_{x=0} \qquad \text{A10}$$

where θ is the GB thickness. Equation A9 can be simplified by a Laplace transform, putting

$$\bar{C}=\int_0^\infty e^{-pt}C\,dt \qquad \text{A11}$$

Equation A9 becomes

$$\frac{\partial^2 \bar{C}}{\partial x^2}-q^2\bar{C}=-\frac{C_1}{D} \qquad \text{A12}$$

where $q^2=p/D$. This equation has two solution in the form of e^{-qx} and e^{qx}. The former is chosen to keep $\bar{C}$ bounded. Then

$$\bar{C}=Me^{-qx}+\frac{C_1}{p} \qquad \text{A13}$$

Equation A10 can also be simplified by Laplace transform

$$\mathrm{D}\left(\frac{\partial \bar{C}}{\partial x}\right)_{x=0} = \frac{\alpha_2\theta}{2}\left(p\bar{C} - \frac{\alpha_1}{\alpha_2}C_1\right) \quad \text{A14}$$

Inserting A13 into A14 gives

$$\mathrm{M} = \frac{(\alpha_1 - \alpha_2)C_1\theta}{Dq(\alpha_2 q\theta + 2)} \quad \text{A15}$$

Replacing A15 in A13

$$\bar{\mathrm{C}} = \frac{C_1\left(\frac{\alpha_1}{\alpha_2} - 1\right)e^{-qx}}{Dq\left(q + \frac{2}{\alpha_2\theta}\right)} + \frac{C_1}{p} \quad \text{A16}$$

From Tables of Laplace transforms,

$$\mathrm{C} = C_1 - C_1\left(1 - \frac{\alpha_1}{\alpha_2}\right)exp\left(\frac{2x}{\alpha_2\theta} + \frac{4Dt}{\alpha_2^2\theta^2}\right)erfc\left(\frac{x}{2\sqrt{Dt}} + \frac{2\sqrt{Dt}}{\alpha_2\theta}\right) \quad \text{A17}$$

Putting x=0 gives the grain concentration in contact with the GB and the GB concentration can be obtained by multiplying C by α_2

$$\frac{C_{gb}(t) - C_{gb}(0)}{C_{gb}(\infty) - C_{gb}(0)} = 1 - exp\left(\frac{4Dt}{\alpha^2\theta^2}\right)\mathrm{erfc}\left(\frac{2\sqrt{Dt}}{\alpha\theta}\right) \quad \text{A18}$$

3. Critical time (Equation 2.25)

Assuming the reduction rate of the complexes is proportional to their concentration during diffusion, i.e.

$$-\frac{\partial C_c}{\partial t} = kC_c \quad \text{A19}$$

the time dependent concentration can be obtained as

$$\frac{C_c}{C_c^0} = e^{-kt} = e^{-\frac{t}{\tau_c}} \quad \text{A20}$$

where τ_c is the time when the concentration of the complexes inside the grain and at the GB are in equilibrium, i.e. no net flux. The diffusion distance is then half the grain size d

$$D_c\tau_c = \frac{\delta_c d^2}{4} \quad \text{A21}$$

Then

$$\frac{C_c}{C_c^0} = e^{-\frac{4D_c t}{\delta_c d^2}} \quad \text{A22}$$

At the GB, the change rate of the solute concentration can be written as

$$\frac{\partial C_i}{\partial t} = k(C_{max} - C_i) \quad \text{A23}$$

where C_{max} is the maximum permissible solute concentration at the GB, the time dependent solute concentration at the GB can be obtained as

$$C_i = C_{max}(1 - e^{-\frac{4D_i t}{\delta_i d^2}}) \quad \text{A24}$$

At the critical time, the change rates of the complexes and solute are equal:

$$\frac{\partial C_c}{\partial t}|_{t=t_c} = -\frac{\partial C_i}{\partial t}|_{t=t_c} \quad \text{A25}$$

Combining A22, A24 and A25 we can get

$$t_c = \frac{d^2 \ln(D_c/D_i)}{4\delta(D_c - D_i)} \quad \text{A26}$$

4. NES kinetics during segregation phase (Equation 2.26)

Equation 2.26 can be obtained using the same method as equation for 2.9 because it can also be simplified to diffusion in two half-infinite crystals with uniform solute contents. The difference is the diffusion coefficient. For ES, it is the diffusion coefficient of the solute, while it is the diffusion coefficient of the complex for NES.

5. NES kinetics during de-segregation phase (Equation 2.27)

The Gauss solution of the diffusion equation is

$$C(x) = \frac{S(0)}{2\sqrt{\pi D_i t}}\, exp\left(-\frac{x^2}{4D_i t}\right) \quad \text{A27}$$

where $S(0)$ is the amount of the solute at x=0 and t=0. Gauss solution describes a diffusion process that solutes are concentrated in an infinitesimal region at beginning. The situation here is the solutes are concentrated in an infinite region at the beginning. This infinite region can be divided into infinitesimal parts and the solution can be obtained by summing all the Gauss solutions from each infinitesimal part. By an integral of equation A27, the solution can be obtained as

$$C(x,t) = A + Berf(\frac{x}{2\sqrt{D_i t}}) \quad \text{A28}$$

where A and B are constant. For the desegregation, two error solutions are used considering the diffusion from both sides of the GB. The solution can be written as

$$C(x,t) = A + Berf\left(\frac{x+\frac{d}{2}}{2\sqrt{D_i(t-t_c)}}\right) + Cerf(\frac{x-\frac{d}{2}}{2\sqrt{D_i(t-t_c)}}) \quad \text{A29}$$

where A, B and C are constant. At the beginning of the desegregation, t=t_c the following conditions should be met

$$x \ll -\frac{d}{2}, C(x,t) = A + Berf(-\infty) + C(-\infty) = A - B - C = C_g \quad \text{A30}$$

$$x = 0, C(x,t) = A + Berf(\infty) + C(-\infty) = A + B - C = C_{gb}(t_c) \quad \text{A31}$$

$$x \gg \frac{d}{2}, C(x,t) = A + Berf(\infty) + C(\infty) = A + B + C = C_g \quad \text{A32}$$

Combining A30, A31 and A32, A, B and C can be obtained as

$$A = C_g \quad \text{A33}$$

$$B = \frac{1}{2}\left[C_{gb}(t_c) - C_g\right] \quad \text{A34}$$

$$C = -\frac{1}{2}\left[C_{gb}(t_c) - C_g\right] \quad \text{A35}$$

Substituting A, B and C into A29 and let x=0, the GB concentration during desegregation can be obtained as

$$C_{gb}(t) = C_g + \frac{\left[C_{gb}(t_c) - C_g\right]}{2} \cdot \left\{\text{erf}\left[\frac{\theta}{2\sqrt{D_i(t - t_c)}}\right] - \text{erf}[-\frac{\theta}{2\sqrt{D_i(t - t_c)}}]\right\} \quad \text{A36}$$

6. NES thermodynamics (Equation 2.24)

Considering a situation from a high temperature T_0 to a low temperature T. At temperature T_0, the concentration of the vacancies and complexes can be calculated by

$$[\text{V}] = k_V \exp(-\frac{E_f}{kT_0}) \quad \text{A37}$$

$$[\text{C}] = k_C[\text{V}][\text{I}]\exp(\frac{E_b}{kT_0}) \quad \text{A38}$$

where k_V and k_C are constant. Substituting A36 into A37, the concentration of the complexes at T_0 is

$$[\text{C}] = k_C k_V[\text{I}]\exp(\frac{E_b - E_f}{kT_0}) \quad \text{A39}$$

Similarly, the concentration of the complexes at temperature T is

$$[\text{C}] = k_C k_V[\text{I}]\exp(\frac{E_b - E_f}{kT}) \quad \text{A40}$$

The magnitude of the segregation can be indicated by the ratio of the excess concentration at T_0 to that at T

$$\frac{[I]_{gb}}{[I]_g} = \frac{([\text{C}]/[\text{I}])_{T_0}}{([\text{C}]/[\text{I}])_T} = \exp\left(\frac{E_b - E_f}{kT} - \frac{E_b - E_f}{kT_0}\right) \quad \text{A41}$$

Eq. A41 suggests that the GB segregation level will monotonously increase with a decreasing E_b, which is clearly wrong. So, a correction term must be included, in which $[I]_{gb}$ is relative E_b (generally smaller than E_f). Therefore, E_b/E_f is added to Eq. A41 to give Eq. A42

$$[I]_{gb} = [I]_g(E_b/E_f)exp\left[\frac{(E_b - E_f)}{kT_0} - \frac{(E_b - E_f)}{kT}\right] \quad \text{A42}$$

(An equivalent description of this theory is that a new equilibrium is set up at the grain boundary at temperature T with a complex concentration of $[\mathrm{C}]_{T_0}$. This is not correct as the concentration will be lower than that and the concentration of the solute is thus overestimated.)

7. ES free energy (Equation 2.7)

Consider the grain boundary as a bidimentional phase ϕ where all the thermodynamical quantities can be defined just like in the bulk phase B, such as the atomic concentrations N_j^{ϕ}, the activities $a_j^{\phi} = f_j^{\phi} N_j^{\phi}$, the chemical potentials μ_j^{ϕ} for species j. The equilibrium condition is

$$\mu_j^{\phi} = \mu_j^{B} \quad \text{A43}$$

The intergranular layer cannot be considered ideal as the intergranular concentrations of solutes are very high. So, the interactions between atoms cannot be neglected. The interaction coefficients α_{ij} in a regular solution can be related to the excess free enthalpy ΔG^E, or to the enthalpy of mixing ΔH^m . For a ternary system with solute 1 and 2 in a solvent 3, the excess free energy can be written

$$\Delta G^E = \Delta H^m = -\sum_{i<j} \alpha_{ij} N_i N_j = -\alpha_{12} N_1 N_2 - \alpha_{23} N_2 N_3 - \alpha_{13} N_1 N_3 \quad \text{A44}$$

where N_i is atomic concentration of solute *i*. In a single-phase, *i.e.*, homogeneous, ternary system

$$\Delta G^E = \sum_i N_i \mu_i = N_1\mu_1 + N_2\mu_2 + N_3\mu_3 \quad \text{A45}$$

$$\mu_1 - \mu_2 = \left(\frac{\partial \Delta G^E}{\partial N_1}\right)_{N_3} = RTln\left(\frac{f_1}{f_2}\right) \quad \text{A46}$$

$$\mu_1 - \mu_3 = \left(\frac{\partial \Delta G^E}{\partial N_1}\right)_{N_2} = RTln\left(\frac{f_1}{f_3}\right) \quad \text{A47}$$

$$\mu_2 - \mu_3 = \left(\frac{\partial \Delta G^E}{\partial N_2}\right)_{N_1} = RTln\left(\frac{f_2}{f_3}\right) \quad \text{A48}$$

In the boundaries, where $\Delta G^E \neq 0$ owing to the high values of the solute concentrations N_1^ϕ and N_2^ϕ, the activity coefficients are calculated by A44-A47

$$-RTlnf_1^\phi = \alpha_{13}^\phi\left(1 - N_1^\phi\right)^2 + \alpha_{23}^\phi\left(N_2^\phi\right)^2 + (\alpha_{12}^\phi - \alpha_{23}^\phi - \alpha_{13}^\phi)N_2^\phi(1 - N_1^\phi) \quad \text{A49}$$

$$-RTlnf_2^\phi = \alpha_{23}^\phi\left(1 - N_2^\phi\right)^2 + \alpha_{13}^\phi\left(N_1^\phi\right)^2 + (\alpha_{12}^\phi - \alpha_{23}^\phi - \alpha_{13}^\phi)N_1^\phi(1 - N_2^\phi) \quad \text{A50}$$

$$-RTlnf_3^\phi = \alpha_{13}^\phi\left(N_1^\phi\right)^2 + \alpha_{23}^\phi\left(N_2^\phi\right)^2 + (\alpha_{12}^\phi - \alpha_{23}^\phi - \alpha_{13}^\phi)N_1^\phi N_2^\phi \quad \text{A51}$$

The bulk phase where N_1^B and N_2^B and thus ΔG^E are small can be considered as ideal:

$$-RTlnf_i^B = \mu_i^B - \mu_j^{0B} - RTlnN_i^B \cong 0 \quad \text{A52}$$

Then the segregation free energy for solute *i* can be written as

$$\Delta G_i = \left(\mu_3^{0\phi} - \mu_3^{0B}\right) - \left(\mu_3^{0\phi} - \mu_3^{0B}\right) + RTln(\frac{f_3^\phi}{f_i^\phi}) \quad \text{A53}$$

Combining A49, A50, A51 and A53, the free energy for solute 1 and 2 can be obtained as

$$\Delta G_1 = \Delta G_1^0 + \alpha_{13}^\phi\left(1 - 2N_1^\phi\right) + (\alpha_{12}^\phi - \alpha_{23}^\phi - \alpha_{13}^\phi)N_2^\phi \quad \text{A54}$$

$$\Delta G_2 = \Delta G_2^0 + \alpha_{13}^\phi\left(1 - 2N_2^\phi\right) + (\alpha_{12}^\phi - \alpha_{23}^\phi - \alpha_{13}^\phi)N_1^\phi \quad \text{A55}$$

For a multicontinent system, the free energy of solute *i* can be written as

$$\Delta G_i = \Delta G_i^0 - \alpha_{iM}^M\left(1 - 2N_i^{\emptyset}\right) + \sum\nolimits_{j \neq i} \alpha_{ij}' N_j^{\emptyset} \quad \text{A56}$$

where ΔG_I^0 is the segregation energy of I without interaction with M and

$$\alpha_{ij}' = \alpha_{ij} - \alpha_{iM} - \alpha_{jM} \quad \text{A57}$$

8. NES kinetics by Wu (Equation 2.30)

Let the vacancy concentration (in atomic fraction) over the entire grain be $X_V(t)$, the vacancy concentration on the intergranular zone side of interface A as X_V^i, the volume of the segregation zone V_S, the surface area of the non-segregation zone S_N, the complex concentrations (in molar concentration) in the segregation and nonsegregation zones X_C^S and X_C^N, solute concentration (in atomic fraction) in the segregation zone be $X_S(t)$, the transformed solute concentration (in atomic fraction) in the non-segregation zone be X_S^i, the vacancy transfer coefficient in interface A β_V, and the complex transfer coefficient in interface B β_C.

According to the theory of convective mass transfer, at interface A,

$$\frac{V_G dX_V}{dt} = S_G \beta_V (X_V^i - X_V) \quad \text{A58}$$

With the initial condition, $X_V(0) = X_V^0$, it can be obtained

$$X_V(t) = X_V^i + (X_V^0 - X_V^i) exp(-k_V t) \quad \text{A59}$$

where

$$k_V = \beta_V S_G / V_G \quad \text{A60}$$

Similarly, at the interface B, we can get

$$\frac{V_S dX_C^S}{dt} = S_N \beta_C (X_C^N - X_C^S) \quad \text{A61}$$

The local equilibrium among the three concentrations of vacancies, solute atoms, and complexes can be formulized as

$$X_C = K_0 X_V X_S \exp(\frac{E_b}{kT}) \quad \text{A62}$$

X_C^S and X_C^N can then be given by

$$X_C^S = K_0 X_V X_S \exp(\frac{E_b}{kT}) \quad \text{A63}$$

$$X_C^N = K_0 X_V X_S^i \exp(\frac{E_b}{kT}) \quad \text{A64}$$

Substituting Eqs. A63 and A64 into Eq. A61 gives

$$\frac{X_S dX_V}{dt} + \frac{X_V dS_S}{dt} = k_C X_V (X_S^i - X_S) \quad \text{A65}$$

where

$$k_C = \beta_C S_N / V_S \quad \text{A66}$$

Substituting Eq. A65 into Eq. A59 and making use of the initial condition $X_S(0) = X_S^0$, one can acquire the segregation kinetics as

$$C_{gb}(t) = \frac{(k_V - k_C)C_{gb}^i - k_C(\alpha - 1)C_{gb}^i e^{-k_V t} + [k_V(\alpha C_{gb}^0 - C_{gb}^i) - k_C \alpha (C_{gb}^0 - C_{gb}^i)]e^{-k_C}}{(k_V - k_C)[1 + (\alpha - 1)e^{-k_V t}]} \quad \text{A67}$$

where C_{gb}^i is the transformed solute concentration in the non-segregation zone, C_{gb}^0 the initial concentration and k_V, k_C and α are defined as

$$k_V = 12 D_{0V} \exp\left(-\frac{Q_V}{kT}\right)/d^2 \quad \text{A68}$$

$$k_C = \frac{12(d - 2\theta) D_{0C} \exp\left(-\frac{Q_C}{kT}\right)}{d^3 - (d - 2\theta)^3} \quad \text{A69}$$

$$\alpha = \exp[Q_f(T_0 - T/kT_0 T] \quad \text{A70}$$

where Q_V and Q_C are the migration energies of the vacancies and complexes respectively and Q_f is the vacancy formation energy.

Appendix II: Monte Carlo simulation and theoretical calculation of SEM image intensity and its application in thickness measurement

1. Introduction

STEM-in-SEM reveals the internal structure of thin foil samples with high contrast and resolution due to the low voltage and thin sample utilized, which increase the electron scattering cross-sections and reduce the interaction volume [281]. In the last few years, thin foil samples have also been widely used for diffraction study in SEMs. The so-called transmission Kikuchi diffraction (TKD) technique employs the traditional EBSD detectors but very thin samples [282]. Compared with bulk sample, it is more complicated for the SEM imaging of thin samples as the image contrast may vary with thickness, as well as composition and topography. So it is quite important to understand the expected contrast seen in both secondary electron (SE) and back-scattered electron (BSE) modes. A combination of Monte Carlo (MC) simulation and experiments help to interpret the image contrast and how it varies with imaging conditions, such as sample thicknesses and voltages.

On the other hand, it is important to obtain accurately the thickness of thin samples when the density of microstructure features, such as precipitates, dislocations and dispersoids is needed. It is also important for absorption and fluorescence effect corrections when energy dispersive spectroscopy (EDS) is used for composition analysis. Focused ion beam (FIB) can be used to cut the sample to reveal the cross section and then directly measure the sample thickness. However, this method is destructive. Electron energy loss spectroscopy (EELS) and convergent beam electron diffraction (CBED) have also been used widely to determine the sample thickness. For EELS, the thickness calculation is based on a simple relationship between the

log-ratio intensity distribution and the ratio of mean free paths of electron inelastic scattering to sample thickness, that is $t = \lambda ln(I/I_0)$, where t is the sample thickness, λ the mean free path of inelastic scattering, I the total intensity of the zero loss peak and the plasma peak and I_0 the intensity of the zero loss peak [283]. In the CBED [284], the sample thickness can be linked to the fringe minima observed as $\left(s_i^2 + \frac{1}{\xi_g^2}\right) t^2 = n_i^2$, where s_i is the deviation of the ith minimum from the exact Bragg position, ξ_g is the extinction distance and n_i an integer. Thickness can be determined from the slope of the plot of s_i^2 versus n_i^2. Both EELS and CBED methods can give a reliable thickness. Especially for CBED, in which case the relative error is better than 2-5% even with the above simple version of the formula [285]. Even better accuracy can be obtained by quantitative many-parameter fits to the intensity profiles of the CBED discs [286]. However, both methods are time consuming, especially when many thickness measurements are needed.

Since the BSE coefficient and SE yield have been widely researched using experiments and theoretical calculations and for thin samples, both depend on the thickness [287]. There is a potentially more efficient way to determine the thickness of a specimen based on the BSE coefficient and SE yield obtained. In this paper, the intensity profiles of both BSE and SE images were measured experimentally vis-à-vis Monte Carlo (MC) simulations and theoretical calculations, and the application to thickness determination is discussed.

2. Experimental procedure and simulation

Pure Mg TEM samples of 3 mm diameter were prepared by twin-jet polishing using a solution containing lithium chloride 8.8 g, magnesium perchlorate 19.3 g, methanol 833 mL and butoxyethanol 167 mL, at a voltage of 70 V and a temperature of -45 ºC. Both BSE and SE images were taken at different acceleration voltages (HV) of 5, 10, 15, 20, 25 and 30 kV using two different sample holders (an STEM holder and a TKD holder) in a TESCAN Mira microscope (the configurations are shown in Figure 1). The SE and BSE detectors used are an

Everhart Thornley detector with standard grid bias and a YAG detector with a single annular scintillator, respectively. The other imaging conditions were kept the same. The image intensity profiles versus distance from the edge of the hole were obtained from defined positions. The sample was finally cut apart using the FIB at these defined locations to directly measure the thickness of the sample.

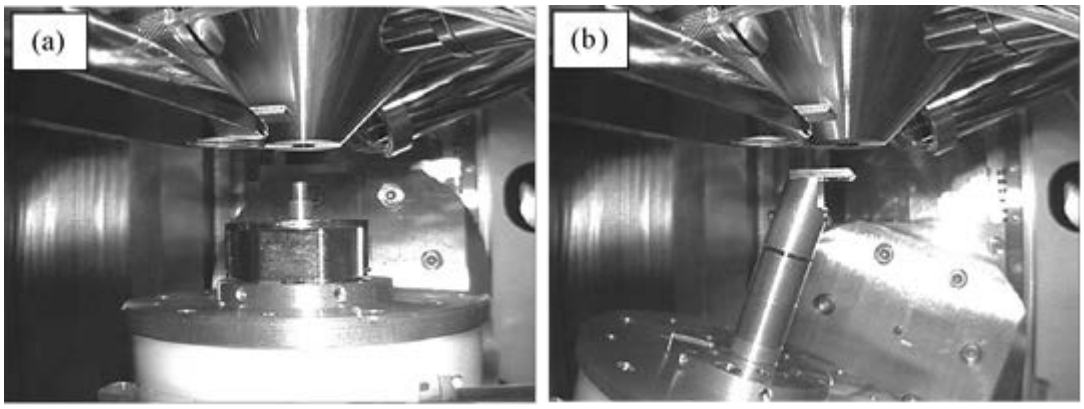

Fig.1 two types of holders used in this study: (a) STEM holder and (b) TKD holder

MC simulation of the SE and BSE yields was done using CASINO version 3.3 [288] with a thickness step of 0.1 μm from 0.1 μm to a thickness when no electrons can get through the sample and with different energies from 5 to 30 keV in steps of 5 keV. At 5 keV, the initial thickness was set as 10 nm with a step size of 10 nm. In every case, 1,000,000 electrons were considered. The cut-off energy was set to 50 eV for all the conditions. It has been shown that the mean penetration depth in aluminium is less than 1 Å when the cut-off energy changed from 100 eV to 20 eV [289]. So the effect of cut-off energy used in the current work on the SE and BSE signals and therefore the thickness determination was regarded as negligible. The modified Bethe formula given by Joy and Luo [290] and Lowney [291] was used to determine the stopping power and the scattering cross section was calculated by ELSEPA model [292].

The BSE coefficient of bulk samples has been widely researched using both experiment and theoretical calculation as it is the foundation of the BSE imaging. Hunger [293] measured the BSE coefficients of 28 elements and derived an analytical expressions of the dependence of

BSE coefficient on the electron energy and the atomic number. For light elements with Z smaller than about 50, the BSE coefficient decreased with increasing incident electron energy and vice versa. However Everhart [294] derived a formula which showed that the BSE coefficient was independent of the incident electron energy, which is consistent with the MC simulations using both single and plural scattering models. Joy [287] suggested the inconsistences between the experimental results [293] and computed data [294] probably arose from the variety of methods used to measure the BSE coefficient. Compared with bulk samples, BSE coefficients of thin samples have received little attention with regard to the relationship between BSE coefficients and thickness. Niedrig [295] reported a linear relationship between BSE efficiency and the sample thickness for most elements (except those with low atomic number) in the low thickness region which is much smaller than the penetration depth of the incident electrons, and proposed a model to interpret the experimental results. Nakhodkin [296] extended the Everhart model to films with thicknesses between 0 and R/2, where R is the maximum penetration depth. Using a simple potential between electron and atom, Kanaya [297] obtained an equation which can be used to calculate the BSE coefficient over the whole range 0 to R, the predicted BSE coefficients were much bigger than the experimental results [298]. MC simulation has therefore been carried out to determine the dependence of BSE coefficient on the thickness.

In contrast to BSE coefficients, SE yields do not depend upon the atomic number, while strongly depend on the incident electron energy [287]. Baroody [299] formulated a theory based on the Sommerfeld model [300] and pointed out that the dependence of SE yield on incident electron energy can be described using a single curve. However, the calculated data were lower than the experimental results [299]. After that, several theories were proposed to calculate the SE yield, e.g. by Seiler [301], Dionne [302]. Joy [303] thoroughly examined the

correlation between SE yields (δ) and the primary electron energy (E_{PE}) for 44 elements and proposed a semi-empirical law to describe the correlation

$$\frac{\delta}{\delta^m} = 1.28(\frac{E_{PE}}{E_{PE}^m})^{-0.67}\left\{1 - \exp[-1.614(\frac{E_{PE}}{E_{PE}^m})^{1.67}]\right\}$$

where δ^m is the maximum SE yield and E_{PE}^m the corresponding energy for the maximum SE emission. For Mg, the parameters were set as 0.8 and 240 eV respectively, which agree reasonably well with the experimental results of 0.8 and 300 eV and the calculated results of 0.67 and 280 eV by Kanaya [304]. Only those SE excited near the surface can reach the surface and escape from it. The escape depth had been revealed by MC simulation, indicating that the escape depth in Cr for 20 keV electrons was about 3 nm [305]. This is consistent with the result of Seiler [301], which showed that the escape depth of SE is about 5λ where λ is the mean free path of SE and of the order of 5 nm and 75 nm for metals and insulators, respectively. This can be used to explain why the SE intensity profiles had a step at the edge of the holes. As the sample thickness is much greater than 5 nm, the SE yields by PE saturated immediately even at the edge.

Considering the contribution of BSE, the total SE yields from the top surface of a thin sample can be derived as

$$\delta = \delta_{PE}(1 + \beta\eta)$$

where δ_{PE} is SE yield by primary electrons (PE), β is the ratio of the SE generated by a BSE and by a PE, and η the BSE coefficient. BSE energy is smaller than the PE energy but larger than E_{PE}^m (240 eV for Mg) and within this energy range, the SE yields increased with decreasing incident electron energy [303]. Also, the BSE had a broad angular distribution and Kanter's experiment [306] showed that the SE yields increased with the tilt angle when the incident electron energy was above 5 keV. Both of the above factors indicated that β should be larger than unity 1. This was confirmed by experiments and MC simulations [307-309]. Reimer's

results indicated β is in the range of 1.5 - 3 for both Al and Au with the incident electron energy in the range of 10 – 35 keV [309]. This is smaller than the MC simulation predicted value of 2 – 5 [308] and Drescher's [307] experimental results of 4 - 6. As the BSE energy and angular distribution depend on the thickness of the sample, β also should be related to the thickness and can be described by a distribution function f (E, θ). However, an accurate expression of f(E, θ) is not available. As a simplification, f(E, θ) can be estimated as $f_1(E)*f_2(\theta)$, i.e. β can be calculated by considering the contributions of energy and angular distribution separately. The contribution of energy distribution has been discussed by Joy [303], while the contribution of angular broadening can be calculated by [309]

$$\beta_\theta = \frac{\int_0^{\pi/2} f_2(\theta) \sec\theta \sin\theta d\theta}{\int_0^{\pi/2} f_2(\theta) \sin\theta d\theta}$$

Both the energy and angular distribution can be obtained by MC simulation. In this work, the SE yield excited by PE was calculated and the BSE coefficient derived from MC simulation. The calculated results were compared with the MC simulation.

As MC simulation did not provide the SE yield from both surfaces, calculations were conducted. To calculate the SE yield from the bottom surface, we started with the calculation of the maximum range (R) the electrons can get through and the transmission possibility in Mg. The transmitted electron energy and the exit angle from the bottom surface will also be considered to calculate the SE yield caused by the transmitted electrons. The maximum range of electron can be calculated by the integration of dE/ds, the stopping power proposed by Bethe [310] as

$$\frac{dE}{ds} = -78500 \frac{\rho Z}{AE} \ln\left(\frac{1.166E}{J}\right)$$

where Z is the atomic number, ρ the density of material, A the atomic weight and J the mean ionization potential. Based on experimental measurements, Burger [311] proposed the dependence of J on Z as

$$J = \left(9.76Z + \frac{58.5}{Z^{0.19}}\right).10^{-3}$$

For Mg, J was determined to be 154 eV.

This model is consistent with the results of Tung [312] calculated based on a statistical model when E is larger than 1 keV, while it gives a much smaller prediction in the lower energy range because J is energy dependent rather than a constant. Joy [290] modified Bethe's model to incorporate this energy dependence by adding a correction term:

$$\frac{dE}{ds} = -78500\frac{\rho Z}{AE}\ln[\frac{1.166(E + 0.85J)}{J}]$$

The modified model is consistent with Bethe's model in the high energy range, and the accuracy was improved in the low energy range. According to Lowney [291], a residual term of 0.4 eV/nm showed the best fit with experimental results. The same residual term was used in the present simulation using CASINO v3.3. The maximum range of the electrons can then be calculated by the integration of the stopping power. In this paper, R was determined to be 0.50, 1.6, 3.2, 5.2, 7.6 and 10.3 μm for HV used at 5, 10, 15, 20, 25 and 30 kV, respectively.

The transmission possibility calculated by Kanaya's semi-empirical formula was smaller for elements of low atomic number in the range of 0-0.3 R due to the overestimation of the scattering cross section [297]. Fitting [313] also formulated a normalized formula to describe the experimental data

$$\eta_T = \exp[-4.605\left(\frac{x}{R}\right)^p]$$

where p is a transmission parameter which reflected the different efficiency ratios of elastic and inelastic processes in different target materials and dependent on the atomic number and the initial electron energy. Experimental results [314] indicated that p is about 2 for Al and 2.2 for Si in the energy range of 5-30 keV and can be written for a wide range of atomic number and energy (3<Z<80, 1 keV < E < 1 MeV) as

$$p = (0.8 + 2B_0)\ln(\frac{1}{B_0})$$

where B_0 is the backscattering coefficient. According to this relationship, p was determined as 2.2 for all the energy ranges used in the current work.

The electron energy after getting through the material can be calculated by integration of the stopping power. However, this overestimates the energy as the beam broadening has not been taken into consideration.

Similar to SE excited by BSE, the energy and angular distribution should be taken into consideration when calculating the SE yields from the bottom surface. The energy distribution can be obtained by MC simulation. However, the angular distribution is not provided by MC simulation. As a simplification, the most probable angle of the transmitted electron was used. Cosslett's experiments [315] indicated that the most probable angle increases with increasing sample thickness as

$$\lambda_A^2 = 1.2 \times 10^7 \frac{Z^{3/2}}{E_0}\frac{\rho x}{A}$$

where λ_A is the most probable angle and the other parameters as defined earlier.

The total SE yields can then be obtained as the sum of the SE excited by primary electrons, BSEs and transmitted electrons.

3. Results and Discussions

The experimental SE and BSE images and the corresponding image intensity profiles obtained using *Image-Pro Plus* versus the sample thickness using different holders and HVs are shown in figure 2 and figure 3. The red line in figure 2 shows the position where intensity profile was obtained. Noticeably strong SE signals were detected in the hole with TKD holder but not with the STEM holder. This is probably due to the interaction between electrons and the stage underneath the specimen, which may generate SE and reach the detector. While for STEM holder, electrons going through the hole are all trapped by the tube.

It can be seen from figure 3 that the intensity profiles of the BSE images were quite similar for both holders, increasing with thickness until saturation. However, the trends were different with different holders for the SE image intensity. Using the STEM holder, the SE image intensity profile increased with the thickness until saturation, which is similar to the BSE profiles though the SE profiles had a step at the edge of the hole. With the TKD holder, the intensity increased to a maximum value and then decreased.

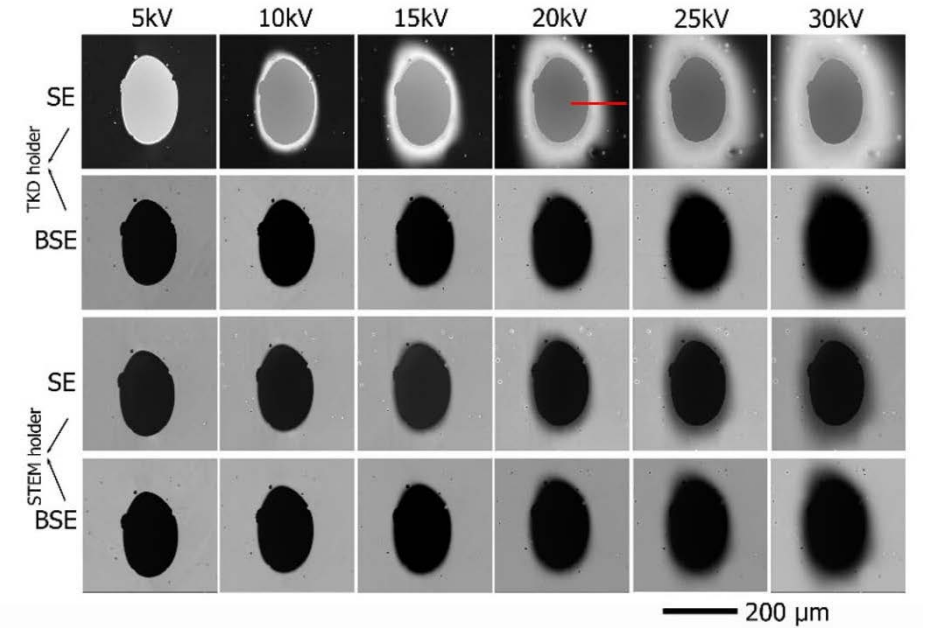

Figure 2 BSE and SE images obtained under different HVs with holders. Red line shows the position where intensity profile was obtained.

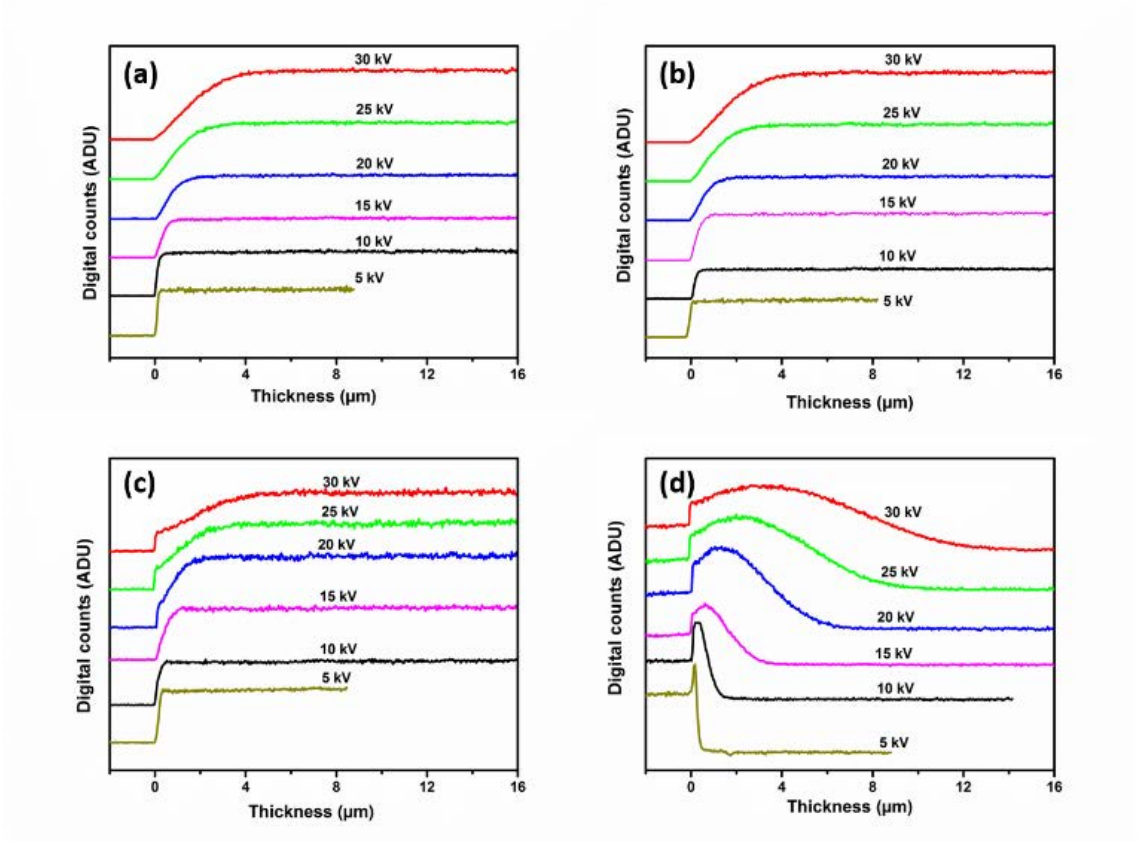

Figure 3 Intensity profiles versus thickness extracted from: (a) BSE image with STEM holder, (b) BSE image with TKD holder, (c) SE image with STEM holder and (d) SE image with TKD holder

3.1 BSE intensity

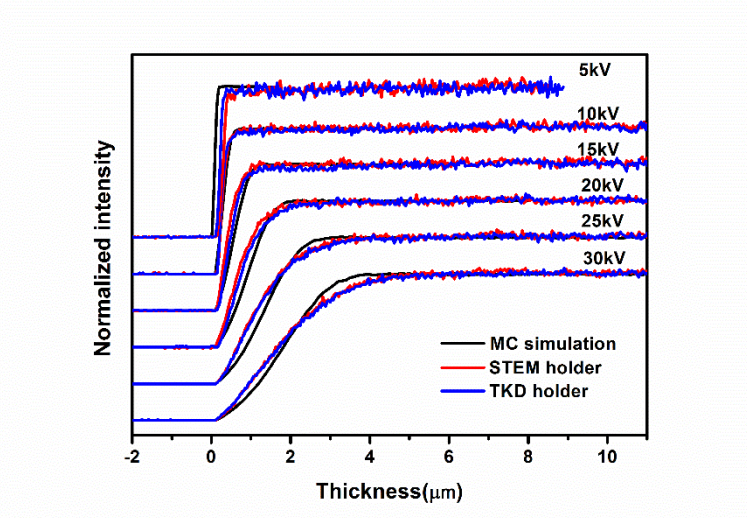

Figure 4 Comparison of normalized BSE intensity profiles between simulations and experiments

The BSE yields in the MC simulation and experiments are illustrated in figure 4. To make a direct comparison, the profiles were normalized by setting the minimum and maximum as 0 and 1 respectively. From figure 4 it can be seen the simulated curve is consistent with the experimental curve, increasing with thickness to a saturation value. The thickness when the BSE reached to saturation can be obtained from the simulation (experimental) curves as 0.18 (0.38), 0.7 (0.82), 1.2 (1.34), 2.0 (2.27), 3.0 (3.53) and 3.9 μm (4.51 μm) with an HV of 5, 10, 15, 20, 25 and 30 kV, respectively. The simulated value is lower than that of the experimental results. Residual terms of smaller values than 0.4 eV/nm have been assessed which obviously generated slightly larger thickness calculated. However the material dependence of the residual term needs to be defined as future work.

3.2 SE yields

The resultant SE yields from the top surface are shown in figure 5. Similar to BSE, the image intensity profiles were normalized. The trend that SE yields increased with thickness until saturation is consistent with the SE image intensity profiles obtained. There is a sudden change of the intensity profile between hole and sample, resulting in the formation of a step. The point when the intensity profile deviated at the step was determined and set as the zero point. The experimental results and MC simulated results agree reasonably well except that the thickness when SE yields reach to saturation for simulation and calculation is lower than experimental results. This is reasonable as it has been shown that the increasing SE yields are due to the increasing BSE yields and the saturation thickness for BSE curve is lower by simulation than experiment.

When using the STEM holder, only electrons excited from the top surface were collected by the detector as electrons exited from the bottom surface were confined within the tube of the holder. However, the TKD holder offers no shielding of the electrons exited from the bottom surface. With the bias of the SE detector, those SE exited from the bottom surface can also be detected, thus resulted in different SE image intensity profiles compared with those used the STEM holder.

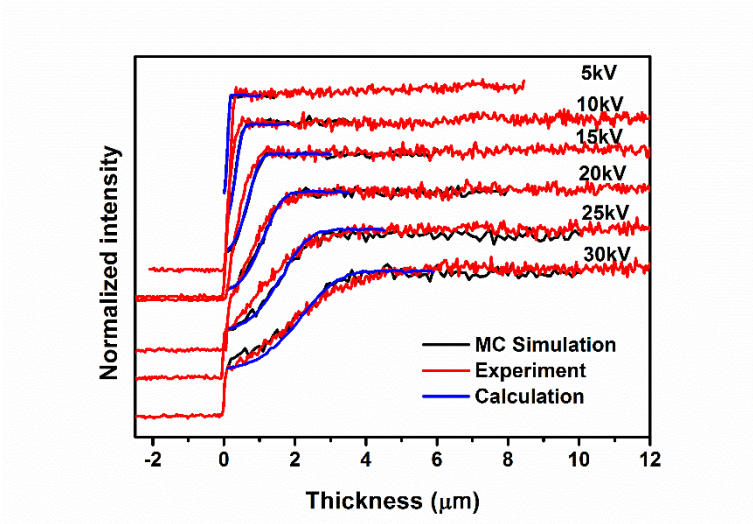

Figure 5 Comparison of normalized SE intensity in the top surface between simulation, experiments and calculation.

The normalized result is shown in figure 6. With increasing sample thickness, the SE yield increases to a maximum value and then decreases. The total SE yields can be divided into three parts, i. e. the contribution from the PE, BSE, and the transmission electrons. SE generated by PE is a constant. Contributions from BSE increased until saturation. SE yields from the bottom surface decrease to 0 as the transmission possibility decreases. The sum of these three parts results in a peak. Also, with increasing incident electron energy, the peak shifted towards larger thickness side. This is consistent with experimental results. To compare quantitatively the result of MC simulation and that of the experiment measurement, the image intensity profiles were normalized and are shown in figure 6. It can be seen that there were deviations between

the experimental and the simulation results though the trends of the intensity profiles are consistent. There are two characteristic thicknesses, one is the peak thickness, and the other is the saturation thickness. The peak thickness for calculation (experiment) is determined to be 0.08 (0.17), 0.2 (0.25), 0.6 (0.61), 0.9 (1.06), 2.3 (2.58) and 2.7μm (3.22μm), for 5, 10, 15, 20, 25 and 30kV, respectively. The simplification of the contribution of angular distribution used and the neglect of collection efficiency may contributed to the difference between the simulation and the experimental results observed. The saturation thickness is 0.5 (0.61), 1.6 (1.74), 3.2 (3.68), 5.2 (6.85), 7.6 (10.32) and 10.3μm (13.86μm) for simulation (experiment) and for 5, 10, 15, 20, 25 and 30kV. This difference is due to the penetration depth which is determined by stopping power which was in turn affected by the residual terms used. The application of the residual term and the exact values for different materials may need further study.

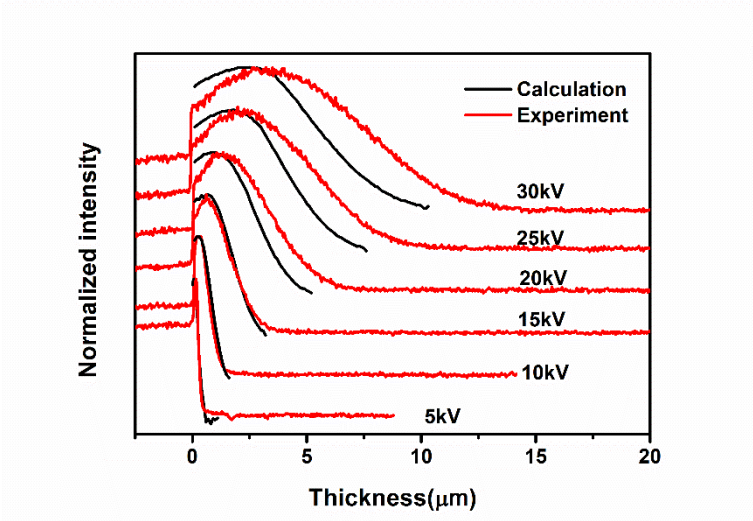

Figure 6 Comparison of normalized total SE yield between the calculation and the experiments.

3.3 Application to thickness determination

As discussed in the above section, the SEM image intensity is related to sample thickness and thus in principle can be used to measure thin foil sample thickness. Figure 4 indicated that BSE

image intensity profiles with different holders were identical while the SE image intensity profiles vary depending on the holder used. Also, for SE image, more factors had to be taken into consideration because SE can be generated by primary electrons, BSEs and transmitted electrons and the collection efficiency might be different for SE yielded at the top and bottom surfaces. Moreover, it has been stated that to normalize or fit the intensity profiles of SE image obtained using the STEM holder, the height of the steps due to the sudden change of the intensity had to be determined, which could not be done precisely. For the SE images obtained using the TKD holder, it is difficult to find accurate mathematical expressions to calculate the SE yield. On the other hand, the electron backscattering process is less sensitive to the surface condition and surface texture than the SE emission. As such the BSE image intensity profiles are more reliable for the sample thickness determination. Experimental profiles can be used as references to determine sample thickness by comparing the intensity profiles with that of samples whose thickness were unknown. A four-parameter (t_0, A_1, A_2, A_3) sigmoidal curve

$$\eta = A_2 + \frac{A_1 - A_2}{1 + \exp(\frac{t - t_0}{A_3})}$$

has been shown to provide the best description of the experimental BSE intensity profile [316]. Using the same equation, a normalized experimental intensity profile of the BSE image with the incident electron energy of 30 kV using the STEM holder is shown in figure 7(a), together with a fitting curve using the same equation above. The parameters used are also shown in figure 7(a). Similar results could be obtained for other incident electron energies. By using this profile as a reference, the thickness of other samples with same composition can be directly derived by measuring the normalized intensity profile. An example was shown in figure 7(b) where the thickness derived using the above method is compared with the thickness measured from a FIB prepared sample. The difference between the two is less than 10%. Compared with other thickness measurement techniques like CBED and EELS, this method is much more

efficient as only a BSE image is required. This could be useful when the sample thickness at various positions needs to be determined repeatedly on different samples of the same material composition.

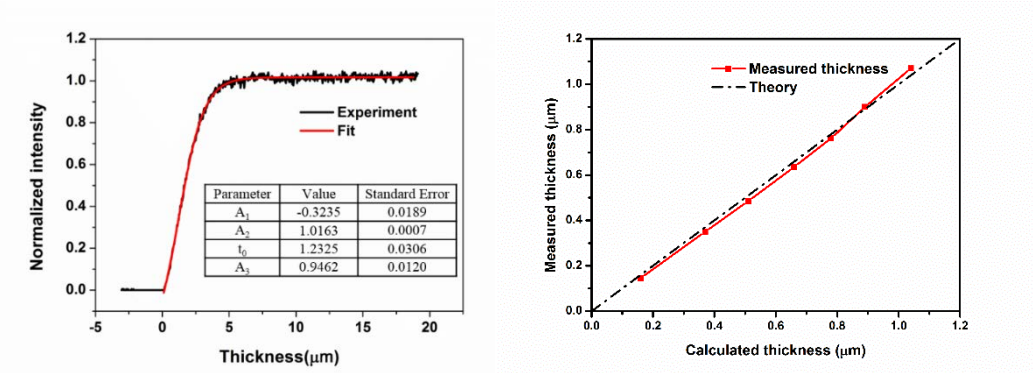

Figure 7 (a) Normalized experimental and fitted curves with HV of 30kV and STEM holder with fitted parameters embedded, (b) comparison of the measured and calculated thickness

4. Conclusion

Both the BSE image and SE image intensity profiles obtained from samples of different thicknesses and incident electron energies were studied using MC simulation and analytical calculation using either the STEM holder or the TKD holder. The results obtained agree reasonably well with the experimental obtained image intensity profiles. The BSE image intensity profile can be used to determine the sample thickness with a reasonably good accuracy.

References

1. Faulkner R.G., *Non-equilibrium grain-boundary segregation in austenitic alloys.* Journal of Materials Science, 1981. **16**(2): p. 373-383.
2. Faulkner R.G., *Combined grain boundary equilibrium and non-equilibrium segregation in ferritic/martensitic steels*, Acta Metallurgica, 1987. **35** (12): p. 2905-2914.
3. Xu T.D., *Non-equilibrium grain-boundary segregation kinetics.* Journal of Materials Science, 1987. **22**(1): p. 337-345.
4. Wu J. and Song S.H., *A unified model of grain-boundary segregation kinetics.* Journal of Applied Physics, 2011. **110**(6): p. 063531.
5. Reed R.C., *The Superalloys: Fundamentals and Applications*. 2006, Cambridge: Cambridge University Press.
6. McLean M. and Strang A., *Effects of trace elements on mechanical properties of superalloys.* Metals Technology, 1984. **11**(1): p. 454-464.
7. Guo J.T. and Zhou L.Z., *The effect of phosphorus, sulphur and silicon on segregation, solidification and mechanical properties in cast alloy 718*, in *Superalloy 1996*. 1996. p. 451-455.
8. Sun W.R., Guo S.R., Lee J.H., Park N.K., Yoo Y.S., Choe S.J. and Hu Z.Q., *Effects of phosphorus on the δ-Ni_3Nb phase precipitation and the stress rupture properties in alloy 718.* Materials Science and Engineering: A, 1998. **247**: p. 173-179.
9. Yang S.L., Sun W.R., Wang J.X., Ge Z.M., Guo S.R. and Hu Z.Q., *Effect of phosphorus on mechanical properties and thermal stability of fine-grained GH761 alloy.* Journal of Materials Science and Technology, 2011. **27**(6): p. 539-545.

10. Wang M.Q., Du J.H., Deng Q., Tian Z.L. and Zhu, J., *The effect of phosphorus on the microstructure and mechanical properties of ATI 718Plus alloy*. Materials Science and Engineering: A, 2015. **626**: p. 382-389.

11. Guan S., Cui C.Y., Yuan Y. and Gu Y.F., *The role of phosphorus in a newly developed Ni-Fe-Cr-based wrought superalloy*. Materials Science and Engineering: A, 2016. **662**: p. 275-282.

12. Sun W. R., Guo S. R., Lu D. Z. and Hu Z.Q., *Effect of phosphorus on the microstructure and stress rupture properties in an Fe-Ni-Cr base superalloy*. Metallurgical And Materials Transactions A, 1997. **28**: p. 649-654.

13. Cao W.D. and Kennedy R.L., *Phosphorus-boron interaction in nickel-base superalloys.* in *Superalloys 1996*, 1996: p. 589-597.

14. Sun W.R., Guo S.R., Guo,J.T., Tong B.Y., Yang Y.S., Sun X.F., Guan H.R. and Hu, Z.Q., *The common strengthening effect of phosphorus, sulfur, and silicon in lower contents and a problem of a net superalloy*. in *Superalloys 2000*, 2000: p. 467-476.

15. Sun W.R., Guo S.R., Lu D.Z., Li Z.C., Tong B.Y. and Z.Q. Hu, in *PRICM-4*. 2001: Honolulu. p. 2719.

16. McLean D., *Grain boundaries in metals*. 1957: Clarendon Press.

17. Lejček P., *Effect of variables on equilibrium grain boundary segregation*, in *grain boundary segregation in metals*, P. Lejcek, Editor. 2010, Springer Berlin Heidelberg: Berlin, Heidelberg. p. 103-152.

18. Randle V., *Grain boundary engineering: an overview after 25 years.* Materials Science and Technology, 2010. **26**(3): p. 253-261.

19. Weng Y.Q. and McMahon C.J., *Interaction of phosphorus, carbon, manganese, and chromium in intergranular embrittlement of iron.* Materials Science and Technology, 1987. **3**(3): p. 207-216.

20. Clayton J.Q. and Knott J.F., *Phosphorus segregation in austenite in Ni–Cr and Ni–Cr–Mn steels.* Metal Science, 1982. **16**(3): p. 145-152.

21. Li, L., Liu, E.B., Li Q.F. and Li Z., *Non-equilibrium grain boundary cosegregation of Mo and P.* Applied Surface Science, 2006. **252**(11): p. 3989-3992.

22. Dong J.X., Zhang M.C., Xie X.S. and Thompson R.G., *Interfacial segregation and cosegregation behaviour in a nickel-base alloy 718.* Materials Science and Engineering: A, 2002. **328**(1–2): p. 8-13.

23. Seah M.P., *Adsorption-induced interface decohesion.* Acta Metallurgica, 1980. **28**(7): p. 955-962.

24. Liu X., Liu H., Dong J.X., and Xie X.S., *Molecular dynamics simulation on phosphorus behavior at Ni grain boundary.* Scripta Materialia, 1999. **42**(2): p. 189-195.

25. Všianská M. and Šob M., *The effect of segregated sp-impurities on grain-boundary and surface structure, magnetism and embrittlement in nickel.* Progress in Materials Science, 2011. **56**(6): p. 817-840.

26. Liu W.G., Ren C.L., Han H., Tan J., Zou Y., Zhou X.T., Huai P., and Xu H.J., *First-principles study of the effect of phosphorus on nickel grain boundary.* Journal of Applied Physics, 2014. **115**(4): p. 043706.

27. Zhu Y.X., Zhang S.N., Zhang T.X., Lou, L.H., Tong Y.J., Ning X.Z., Hu Z.Q. and Xie X.S., *Effect of P, S, B and Si on the solidification segregation of inconel 718 alloy*. in *Superalloys 718, 625 and Various Derivative*, 1994: p. 89-98

28. Thompson R.G., Koopman M.C. and King B.H., *Grain boundary chemistry of alloy 718 type alloy*, in *Superalloys 718, 625 and Various Derivative*. 1991, TMS-AIME. p. 53-70.

29. Dong J.X., Thompson R.G., Xie X.S. *Multi-component intergranular and interracial segregation in Alloy 718 with correlations to stress rupture behavior,* in *superalloys 718, 625, 706 and Various Derivative*. 1997. p. 553-566.

30. Chen C., Thompson R.G. and Davis D.W., *A study of effects of phosphorus, sulfur, boron and carbon on laves and carbide formation in alloy 718.* in *Superalloys 718, 625, 706 and Derivatives,* 1991: p. 81-96.

31. Miao Z.J., Shan A.D., Lu J. and Song H.W., *Microstructure and solidification behaviour characterisation of phosphorus and boron doped IN718 superalloy.* Materials Science and Technology, 2012. **28**: p. 334-341.

32. Yu L.X., Sun Y.R., Sun W.R., Sun X.F., Guo S.R. and Hu Z.Q., *The influence of phosphorus on the microstructure and stress-rupture properties in a low thermal expansion superalloy.* Materials Science and Engineering: A, 2010. **527**(4–5): p. 911-916.

33. Hu Z.Q., Sun W.R. and Guo S.R., *Effect of P, S and Si on the solidification, segregation, microstructure and mechanical properties in Fe-Ni base superalloys.* Acta Metallurgica Sinica (English letters), 1996. **9**: p. 443-452.

34. Was G.S., Sung J.K. and Angeliu T.M., *Effects of grain boundary chemistry on the intergranular cracking behavior of Ni-16Cr-9Fe in high-temperature water*. Metall. Trans. A, 1992. **23**: p. 3343-3359.

35. Guo S.R., Sun W.R., Lu D.Z., Hu Z.Q., *Effect of minor elements on microstructure and mechanical properties of IN 718 alloy* in *Superalloys 718, 625, 706 and Various Derivatives*. 1997. p. 521-530.

36. Cao W.D. and Kennedy R. L., *The effect of phosphorous on mechanical properties of Alloy 718,* in *Superalloys 718, 625, 706 and Various Derivatives*. 1994. p. 463-477.

37. Xie X.S., Liu X.B., Dong J.X., Hu Y.H., Xu Z.C., Zhu Y.X., Luo W.B., Zhang Z.W., and Thompson R.G., *Segregation behavior of phosphorus and its effect on microstructure and mechanical properties in alloy system Ni-Cr-Fe-Mo-Nb-Ti-Al.* in *Superalloys 718, 625, 706 and Various Derivatives*, 1997: p. 531-542.

38. Song H.W., Guo S.R., and Hu Z.Q, *Beneficial effect of phosphorus on the creep behavior of INCONEL 718.* Scripta Materialia, 1999. **41**(2): p. 215-219.

39. Zhang S., Xin X., Yu L.X., Zhang A.W., Sun W.R., and Sun X.F., *Effect of phosphorus on the grain boundary cohesion and γ′ precipitation in IN706 alloy.* Metallurgical and Materials Transactions A, 2016. **47**(8): p. 4092-4103.

40. Prokoshkina D., Esin V.A., Wilde G. and Divinski S.V., *Grain boundary width, energy and self-diffusion in nickel: Effect of material purity.* Acta Materialia, 2013. **61**(14): p. 5188-5197.

41. Yip S. and Wolf D., *Atomistic concepts for simulation of grain boundary fracture.* Materials Science Forum. 1991. **46**: p. 77-168.

42. Wolf D., *Structure-energy correlation for grain boundaries in F.C.C. metals—III. Symmetrical tilt boundaries.* Acta Metallurgica et Materialia, 1990. **38**(5): p. 781-790.

43. Burgers J.M., *Geometrical considerations concerning the structural irregularities to be assumed in a crystal.* Proceedings of the Physical Society, 1940. **52**(1): p. 23.

44. Taylor G.I., *The mechanism of plastic deformation of crystals. Part I. Theoretical.* Proceedings of the Royal Society, 1934. **145**: p. 362-387.

45. Bollmann W., *Crystal Defects and Crystalline Interfaces*. 1970: Springer.

46. Brandon D.G., Ralph B., Ranganathan S., and Wald M.S., *A field ion microscope study of atomic configuration at grain boundaries.* Acta Metallurgica, 1964. **12**(7): p. 813-821.

47. Ishida Y. and McLean M., *Burgers vectors of boundary dislocations in ordered grain boundaries of cubic metals.* Philosophical Magazine, 1973. **27**(5): p. 1125-1134.

48. Déchamps M., Baribier F., and Marrouche A., *Grain-boundaries: Criteria of specialness and deviation from CSL misorientation.* Acta Metallurgica, 1987. **35**(1): p. 101-107.

49. Jang H., Farkas D., and De Hosson J.T.M., *Determination of grain boundary geometry using TEM.* Journal of Materials Research, 1992. **7**(07): p. 1707-1717.

50. Read W.T. and Shockley W., *Dislocation models of crystal grain boundaries.* Physical Review, 1950. **78**(3): p. 275-289.

51. Brandon D.G., *The structure of high-angle grain boundaries.* Acta Metallurgica, 1966. **14**(11): p. 1479-1484.

52. Glicksman M.E. and Vold C.L., *Heterophase dislocations — An approach towards interpreting high temperature grain boundary behavior.* Surface Science, 1972. **31**: p. 50-67.

53. Winning M., Gottstein G., and Shvindlerman L.S., *On the mechanisms of grain boundary migration.* Acta Materialia, 2002. **50**(2): p. 353-363.

54. Sakaguchi N., Watanabe S., Takahashi H., Faulkner R.G., *A multi-scale approach to radiation-induced segregation at various grain boundaries*, Journal of Nuclear Materials, 2004. **329-333**: p. 1166-1169.

55. Tschopp M.A., Tucker G.J. and McDowell D.L., *Structure and free volume of <110> symmetric tilt grain boundaries with the E structural unit.* Acta Materialia, 2007. **55**(11): p. 3959-3969.

56. Bean J.J. and McKenna K.P., *Origin of differences in the excess volume of copper and nickel grain boundaries.* Acta Materialia, 2016. **110**: p. 246-257.

57. Chen T.F., Gyanendra P.T., Iijima Y. and Yamauchi K., *Volume and grain boundary diffusion of chromium in Ni-base Ni-Cr-Fe alloys.* Materials Transactions, 2003. **44**(1): p. 40-46.

58. Bokstein B., Ivanov V., Oreshina O., Peteline A. and Peteline S., *Direct experimental observation of accelerated Zn diffusion along triple junctions in Al.* Materials Science and Engineering: A, 2001. **302**(1): p. 151-153.

59. Arjhangmehr A., Feghhi S.A.H., Esfandiyarpou, A. and Hatami F., *An energetic and kinetic investigation of the role of different atomic grain boundaries in healing radiation damage in nickel.* Journal of Materials Science, 2016. **51**(2): p. 1017-1031.

60. Gleiter H. and Chalmers B., *Grain-boundary diffusion.* Progress in Materials Science, 1972. **16**: p. 77-112.

61. Sommer J., Herzig C., Mayer S. and Gust W., *Grain boundary self-diffusion in silver bicrystals.* Defect and Diffusion Forum, 1989. **66-69**: p. 843-848.

62. Guttmann M., *Equilibrium segregation in a ternary solution: A model for temper embrittlement.* Surface Science, 1975. **53**(1): p. 213-227.

63. Ogura T., *A method for evaluation of the amount of grain boundary segregation during quenching.* Transactions of the Japan Institute of Metals, 1981. **22**(2): p. 109-117.

64. Connétable D., Andrieu É. and Monceau D., *First-principles nickel database: Energetics of impurities and defects.* Computational Materials Science, 2015. **101**: p. 77-87.

65. LarÈre A., Guillopé M. and Masuda-Jindo K., *Segregation energies of phosphorus and sulfur in various relaxed structures of grain boundaries in Ni by tight-binding approximation.* Journal de Physique Colloques, 1988. **49**(C5): p. C5-447-C5-450.

66. Kegg G.R., Silcock J.M. and West D.R.F., *The effect of phosphorus additions and cooling rate on the precipitation of $M_{23}C_6$ in austenite.* Metal Science, 1974. **8**(1): p. 337-343.

67. *8 - Thermochemical data*, in *Smithells Metals Reference Book (Eighth Edition)*, Gale W.F. and Totemeier T.C., Editors. 2004, Butterworth-Heinemann: Oxford. p. 8-1-8-58.

68. Wang K., Si H., Yang C. and Xu T.D., *Nonequilibrium grain boundary segregation of phosphorus in Ni-Cr-Fe superalloy.* Journal of Iron and Steel Research, International, 2011. **18**(1): p. 61-67.

69. Langmuir I., *The adsorption of gases on plane surfaces of glass, mica and platinum.* Journal of the American Chemical Society, 1918. **40**(9): p. 1361-1403.

70. Lejček P. and Hofmann S., *Grain boundary segregation diagrams of α-iron.* Interface Science, 1993. **1**(2): p. 163-174.

71. Larere A., Guttmann M., Dumoulin P. and Roques-Carmes C., *Auger electron spectroscopy study of the kinetics of intergranular and surface segregations in nickel during annealing.* Acta Metallurgica, 1982. **30**(3): p. 685-693.

72. Muschik T., Gust W., Hofmann S. and Predel B., *The temperature dependence of grain boundary segregation in Ni-In bicrystals studied with auger electron spectroscopy.* Acta Metallurgica, 1989. **37**(11): p. 2917-2925.

73. Lejček P. and Hofmann S., *Segregation enthalpies of phosphorus, carbon and silicon at {013} and {012} symmetrical tilt grain boundaries in an Fe-3.5 at.% Si alloy.* Acta Metallurgica et Materialia, 1991. **39**(10): p. 2469-2476.

74. Clayton J.Q. and Knott J.F., *Effects of nickel and antimony on temper embrittlement in alloy steels*, in *The Physical Metallurgy of Fracture*, Taplin D.M.R., Editor. 1978, Pergamon. p. 287-296.

75. Powell B.D. and Mykura H., *The segregation of bismuth to grain boundaries in copper-bismuth alloys.* Acta Metallurgica, 1973. **21**(8): p. 1151-1156.

76. Powell B.D. and Woodruff D.P., *Anisotropy in grain boundary segregation in copper-bismuth alloys.* Philosophical Magazine, 1976. **34**(2): p. 169-176.

77. Watanabe T., Kitamura S. and Karashima S., *Grain boundary hardening and segregation in alpha Iron-Tin alloy.* Acta Metallurgica, 1980. **28**(4): p. 455-463.

78. Hofmann S., Lejček P. and Adámek J., *Grain boundary segregation in [100] symmetrical tilt bicrystals of an Fe-Si alloy.* Surface and Interface Analysis, 1992. **19**(1-12): p. 601-606.

79. Erhart H. and Grabke H.J., *Site competition in grain boundary segregation of phosphorus and nitrogen in iron.* Scripta Metallurgica, 1981. **15**(5): p. 531-534.

80. Suzuki S., Obata M., Abiko K. and Kimura H., *Effect of carbon on the grain boundary segregation of phosphorus in α-iron.* Scripta Metallurgica, 1983. **17**(11): p. 1325-1328.

81. Lejček P. and Hofmann S., *Temperature dependence of the phosphorus segregation at the twin boundary in an Fe–4 at.% Si alloy.* Surface and Interface Analysis, 1990. **16**(1-12): p. 546-551.

82. Ishida K., *Effect of grain size on grain boundary segregation.* Journal of Alloys and Compounds, 1996. **235**(2): p. 244-249.

83. Kim J.I., Pak J.H., Park K.S., Jang J.H., Suh D.W. and Bhadeshia H.K.D.H., *Segregation of phosphorus to ferrite grain boundaries during transformation in an Fe–P alloy.* International Journal of Materials Research, 2014. **105**(12): p. 1166-1172.

84. Zhao Y., Song S.H., Si H. and Wang K., *Effect of grain size on grain boundary segregation thermodynamics of phosphorus in interstitial-free and 2.25Cr-1Mo steels.* Metals, 2017. **7**(11): p. 470.

85. Gruffel P. and Carry C., *Effect of grain size on yttrium grain boundary segregation in fine-grained alumina.* Journal of the European Ceramic Society, 1993. **11**(3): p. 189-199.

86. Aoki M., Chiang Y.M., Kosacki I., Lee L.J.R., Tuller H. and Liu Y., *Solute segregation and grain-boundary impedance in high-purity stabilized zirconia.* Journal of the American Ceramic Society, 1996. **79**(5): p. 1169-1180.

87. Menyhard M., Blum B. and McMahon Jr C.J., *Grain boundary segregation and transformations in Bi-doped polycrystalline copper.* Acta Metallurgica, 1989. **37**(2): p. 549-557.

88. Lejček P., Krajnikov A.V., Ivashchenko Y.N., Militzer M. and Adámek J., *Solute segregation to grain boundaries and free surfaces in an Fe-Si multicomponent alloy.* Surface Science, 1993. **280**(3): p. 325-334.

89. Briant C.L. and Messmer R.P., *An electronic model for the effect of alloying elements on the phosphorus induced grain boundary embrittlement of steel.* Acta Metallurgica, 1982. **30**(9): p. 1811-1818.

90. Li Q.F., Li L., Liu EB., Liu D., and Cui, X.F., *Temper embrittlement dynamics induced by non-equilibrium segregation of phosphorus in steel 12Cr1MoV.* Scripta Materialia, 2005. **53**(3): p. 309-313.

91. Williams T.M., *The segregation and effects of boron in an austenitic stainless steel.* Metal Science, 1972. **6**(1): p. 68-69.

92. Williams T.M., Stoneham A.M. and Harries D.R., *The segregation of boron to grain boundaries in solution-treated Type 316 austenitic stainless steel.* Metal Science, 1976. **10**(1): p. 14-19.

93. Okamoto P.R. and Rehn L.E., *Radiation-induced segregation in binary and ternary alloys.* Journal of Nuclear Materials, 1979. **83**(1): p. 2-23.

94. Was G.S., Wharry J.P., Frisbie B., Wirth B.D., Morgan D., Tucker J.D. and Allen T.R., *Assessment of radiation-induced segregation mechanisms in austenitic and ferritic–martensitic alloys.* Journal of Nuclear Materials, 2011. **411**(1): p. 41-50.

95. Wiedersich H., Okamoto P. and Lam N., *Solute segregation during irradiation.* Radiation Effects in Breeder Reactor Structural Materials, 1977: p. 801-819.

96. Faulkner R.G., Song S.H. and Flewitt P.E.J., *Determination of impurity–point defect binding energies in alloys.* Materials Science and Technology, 1996. **12**(11): p. 904-910.

97. Aust K.T., Hanneman R.E., Niessen P. and Westbrook J.H., *Solute induced hardening near grain boundaries in zone refined metals.* Acta Metallurgica, 1968. **16**(3): p. 291-302.

98. Anthony T.R., *Solute segregation in vacancy gradients generated by sintering and temperature changes.* Acta Metallurgica, 1969. **17**(5): p. 603-609.

99. Song S.H. and Weng L.Q., *Diffusion of vacancy-solute complexes in alloys.* Materials Science and Technology, 2005. **21**(3): p. 305-310.

100. Huffman R., Pikus F. and Ward R., *Self-diffusion in solid nickel.* Transactions of the Metallurgical Society of AIME, 1956. **206**: p. 483-486.

101. Smallman R.E. and Ngan A.H.W., *Chapter 7-Diffusion*, in *Modern Physical Metallurgy (Eighth Edition)*. 2014, Butterworth-Heinemann: Oxford. p. 287-316.

102. Zhang S.H., He X.L., and Ko T., *Non-equilibrium segregation of solutes to grain boundary*. Journal of Materials Science, 1994. **29**(10): p. 2663-2670.

103. Xu T.D., *The critical time and critical cooling rate of non-equilibrium grain-boundary segregations.* Journal of Materials Science Letters, 1988. **7**(3): p. 241-242.

104. Gay A.S., Fraczkiewicz A. and Biscondi M. *Mechanisms of the intergranular segregation of boron in (B2) FeAl alloys*. Materials science forum. 1998. **294**: p.453-456.

105. Briant C.L., Feng H.C. and McMahon C.J., *Embrittlement of a 5 Pct Nickel high strength steel by impurities and their effects on hydrogen-induced cracking.* Metallurgical Transactions A, 1978. **9**(5): p. 625-633.

106. Misra R.D.K. and Balasubramanian T.V., *Co-operative and site-competitive interaction processes at the grain boundaries of a Ni-Cr-Mo-V steel.* Acta Metallurgica, 1989. **37**(5): p. 1475-1483.

107. Xu T.D. and Cheng B.Y., *Kinetics of non-equilibrium grain-boundary segregation.* Progress in Materials Science, 2004. **49**(2): p. 109-208.

108. Ding R.G., Rong T.S. and Knott J.F., *Phosphorus segregation in 2.25Cr–1Mo steel.* Materials Science and Technology, 2005. **21**(1): p. 85-92.

109. Li Q.F., Yang S.L., Li L., Zheng L. and Xu T.D., *Experimental study on non-equilibrium grain-boundary segregation kinetics of phosphorus in an industrial steel.* Scripta Materialia, 2002. **47**(6): p. 389-392.

110. Zhang Z.L., Xu T.D., Lin Q.Y. and Yu Z.S., *A new interpretation of temper embrittlement dynamics by non-equilibrium segregation of phosphor in steels.* Journal of Materials Science, 2001. **36**(8): p. 2055-2059.

111. Briant C.L., *Grain boundary segregation of phosphorus in 304L stainless steel.* Metallurgical Transactions A, 1985. **16**(11): p. 2061-2062.

112. Briant C.L., *Grain boundary segregation of phosphorus and sulfur in Types 304L and 316L stainless steel and its effect on intergranular corrosion in the Huey test.* Metallurgical Transactions A, 1987. **18**(5): p. 691-699.

113. Wang K., Wang M.Q., Si H., and Xu T.D., *Critical time for non-equilibrium grain boundary segregation of phosphorus in 304L stainless steel.* Materials Science and Engineering: A, 2008. **485**(1–2): p. 347-351.

114. Xu T.D., *Critical time for Mg grain-boundary segregation in Ni–Cr–Co alloy.* Philosophical Magazine Letters, 2006. **86**(8): p. 501-510.

115. Xu T.D. and Song, S.H., *A kinetic model of non-equilibrium grain-boundary segregation.* Acta Metallurgica, 1989. **37**(9): p. 2499-2506.

116. Wang K., Xu T.D., Song S.H, and Shao C., *Graphical representation for isothermal kinetics of non-equilibrium grain-boundary segregation.* Materials Characterization, 2011. **62**(6): p. 575-581.

117. Xu T.D., *Non-equilibrium cosegregation to grain boundaries.* Scripta Materialia, 1997. **37**(11): p. 1643-1650.

118. Doig P. and Flewitt P.E.J., *Segregation of chromium to prior austenite boundaries during quenching of a 2.25%Crl%Mo steel.* Acta Metallurgica, 1981. **29**(11): p. 1831-1841.

119. Doig P. and Flew P.E.J., *Nonequilibrium solute segregation to austenite grain boundaries in low alloy ferritic and austenitic steels.* Metallurgical Transactions A, 1987. **18**(3): p. 399-406.

120. Thuvander M. and Stiller K., *Evolution of grain boundary chemistry in a Ni–17Cr–9Fe model alloy.* Materials Science and Engineering: A, 1998. **250**(1): p. 93-98.

121. Faulkner R.G., *Impurity diffusion constants and vacancy–impurity binding energies in solids.* Materials Science and Technology, 1985. **1**(6): p. 442-447.

122. Domain C., *Ab initio modelling of defect properties with substitutional and interstitials elements in steels and Zr alloys.* Journal of Nuclear Materials, 2006. **351**(1): p. 1-19.

123. Olsson P., Domain C. and Wallenius J., *Ab initio study of Cr interactions with point defects in bcc Fe.* Physical Review B, 2007. **75**(1): p. 014110.

124. Terentyev D., Olsson P., Klaver T.P.C. and Malerba L., *On the migration and trapping of single self-interstitial atoms in dilute and concentrated Fe-Cr alloys: Atomistic study and comparison with resistivity recovery experiments.* Computational Materials Science, 2008. **43**(4): p. 1183-1192.

125. Ohnuma T., Soneda N. and Iwasawa M., *First-principles calculations of vacancy–solute element interactions in body-centered cubic iron.* Acta Materialia, 2009. **57**(20): p. 5947-5955.

126. Choudhury S., Barnard L., Tucker J.D., Allen T.R., Wirth B.D., Asta M. and Morgan D., *Ab-initio based modeling of diffusion in dilute bcc Fe–Ni and Fe–Cr alloys and implications for radiation induced segregation.* Journal of Nuclear Materials, 2011. **411**(1): p. 1-14.

127. Bakaev A., Terentyev D., He X.L., Zhurkin E.E. and Van Neck D., *Interaction of carbon-vacancy complex with minor alloying elements of ferritic steels.* Journal of Nuclear Materials, 2014. **451**(1): p. 82-87.

128. Gorbatov O.I., Delandar A.H., Gornostyrev Y.N., Ruban A.V. and Korzhavyi P.A., *First-principles study of interactions between substitutional solutes in bcc iron.* Journal of Nuclear Materials, 2016. **475**: p. 140-148.

129. Terentyev D.A., Malerba L., Chakarova R., Nordlund K., Olsson P., Rieth M. and Wallenius J., *Displacement cascades in Fe-Cr: A molecular dynamics study.* Journal of Nuclear Materials, 2006. **349**(1): p. 119-132.

130. Möslang A., Albert E., Recknagel E., Weidinger A. and Moser P., *Investigation of electron irradiated iron alloys and nickel.* Hyperfine Interactions, 1984. **17**(1): p. 255-259.

131. Ding R., *Phosphorus segregation in ferritic steel*. 2003, Thesis (PhD) - University of Birmingham, Department of Metallurgy & Materials.: Birmingham.

132. Duh T.S., Kai J.J. and Chen F.R., *Effects of grain boundary misorientation on solute segregation in thermally sensitized and proton-irradiated 304 stainless steel.* Journal of Nuclear Materials, 2000. **283–287, Part 1**: p. 198-204.

133. Kai J.J., Chen, F.R. and Duh T.S., *Effects of grain boundary misorientation on radiation-induced solute segregation in proton irradiated 304 stainless steels.* Materials Transactions, 2004. **45**(1): p. 40-50.

134. Shen Q.Z. and Du J.M., *Metallurgy Transport Principle*. 2006, Beijing: Metallurgical Industry Press.

135. Tang F., Emura S. and Hagiwara M., *Tensile properties of Tungsten-modified orthorhombic Ti-22Al-20Nb-2W alloy.* Scripta Materialia, 2001. **44**(4): p. 671-676.

136. Pike L.M. and Liu C.T., *Environmental effects on the tensile properties of two Ni3Si-Based alloys.* Scripta Materialia, 2000. **42**(3): p. 265-270.

137. Horikawa K., Kuramoto S. and Kanno M., *Intergranular fracture caused by trace impurities in an Al-5.5 mol% Mg alloy.* Acta Materialia, 2001. **49**(19): p. 3981-3989.

138. Xu T.D., *Critical time and temper embrittlement isotherms.* Materials science and technology, 1999. **15**(6): p. 659-665.

139. Otsuka M. and Horiuchi R., *Ductility loss of Al-Mg alloys at high temperatures.* Japan Institute of Metals, Journal, 1984. **48**: p. 688-693.

140. He L.Z., Zheng Q., Sun X.F., Hou G.C., Guan H.R. and Hu Z.Q., *Low ductility at intermediate temperature of Ni–base superalloy M963.* Materials Science and Engineering: A, 2004. **380**(1–2): p. 340-348.

141. Seah M.P., *Grain boundary segregation and the T-t dependence of temper brittleness.* Acta Metallurgica, 1977. **25**(3): p. 345-357.

142. Seah M. P. and Hondros E.D., *Grain boundary segregation.* Proceedings of the Royal Society of London. A. Mathematical and Physical Sciences, 1973. **335**(1601): p. 191-212.

143. Tomita M., Kinno T., Koike M., Tanak H., Takeno S., Fujiwara Y., Kondou K., Teranishi Y., Nonaka H., Fujimoto T., Kurokawa A. and Ichimura S., *Depth resolution improvement in secondary ion mass spectrometry analysis using metal cluster complex ion bombardment.* Applied Physics Letters, 2006. **89**(5): p. 053123.

144. Christien F., Downing C., Moore K.L. and Grovenor C.R.M., *Quantification of grain boundary equilibrium segregation by NanoSIMS analysis of bulk samples.* Surface and Interface Analysis, 2012. **44**(3): p. 377-387.

145. Cadel E., Lemarchand D., Chambreland S. and Blavette D., *Atom probe tomography investigation of the microstructure of superalloys N18.* Acta Materialia, 2002. **50**(5): p. 957-966.

146. Doig P. and Flewitt P.E.J., *Microanalysis of Grain Boundary Segregation in Embrittled Iron-3wt% Nickel Alloys Using STEM.* Journal of Microscopy, 1978. **112**(3): p. 257-267.

147. Keast V.J. and Williams D.B., *Quantification of boundary segregation in the analytical electron microscope.* Journal of Microscopy, 2000. **199**(1): p. 45-55.

148. Faulkner R.G., Song S.H. and Flewitt P.E.J., *Combined quenching and tempering induced phosphorus segregation to grain boundaries in 2·25Cr–1 Mo steel.* Materials Science and Technology, 1996. **12**(10): p. 818-822.

149. Vorlicek V. and Flewitt P.E.J., *Cooling induced segregation of impurity elements to grain boundaries in Fe-3 wt%Ni alloys, 214wt%Cr-1 wt%Mo steel and submerged arc weld metal.* Acta Metallurgica et Materialia, 1994. **42**(10): p. 3309-3320.

150. Papworth A.J. and Williams D.B., *Segregation to prior austenite grain boundaries in low-alloy steels.* Scripta Materialia, 2000. **42**(11): p. 1107-1112.

151. Faulkner R.G., Morgan T.S., Little E.A., *Analytical electron microscopy of thin segregated layers*, X-Ray Spectrometry, 1994. **23**: p. 195-202.

152. Carter R.D., Damcott D.L., Atzmon M., Was G.S., Bruemmer S.M., Kenik E.A., *Quantitative analysis of radiation-induced grain-boundary segregation measurements*, Journal of Nuclear Materials, 1994. **211** (1): p. 70-84.

153. Kreye H., Hornbogen E. and Haessner F., *Recrystallization of supersaturated and plastically deformed solid solutions of nickel.* Physica Status Solidi (a), 1970. **1**(1): p. 97-108.

154. http://www.totalmateria.com/Article32.htm.

155. Schlossmacher P., Klenov D.O., Freitag B. and von Harrach H.S., *Enhanced detection sensitivity with a new windowless XEDS system for AEM based on silicon drift detector technology.* Microscopy Today, 2010. **18**(4): p. 14-20.

156. Cliff G. and Lorimer G.W., *The quantitative analysis of thin specimens.* Journal of Microscopy, 1975. **103**(2): p. 203-207.

157. Goldstein J.I., Costley J.L., Lorimer G.W. and Reed S.J.B., Proceedings of the 10th Annual Scanning Electron Microscope Symposium and Workshop on Materials and Component Characterization/Quality Control with the SEM/STEM, 1977: p. 315-324.

158. Song S.H., Faulkner R.G., Flewitt P.E.J., Marmy P. and Victoria M., *Grain boundary phosphorus and molybdenum segregation under irradiation and thermal conditions in a 2.25Cr1Mo steel.* Materials Science and Engineering: A, 2000. **286**(2): p. 230-235.

159. Watanabe T., Tsurekawa S., Zhao X. and Zuo L., *The coming of grain boundary engineering in the 21st century*, in *Microstructure and Texture in Steels*. 2009, Springer. p. 43-82.

160. Sinha S., Kim D.I., Fleury E. and Suwas S., *Effect of grain boundary engineering on the microstructure and mechanical properties of copper containing austenitic stainless steel.* Materials Science and Engineering: A, 2015. **626**: p. 175-185.

161. King A.H., *Triple lines in materials science and engineering.* Scripta Materialia, 2010. **62**(12): p. 889-893.

162. Chellali M.R., Balogh Z., Bouchikhaoui H., Schlesiger R., Stender P., Zheng L. and Schmitz G., *Triple Junction Transport and the Impact of Grain Boundary Width in Nanocrystalline Cu.* Nano Letters, 2012. **12**(7): p. 3448-3454.

163. Frolov T. and Mishin Y., *Molecular dynamics modeling of self-diffusion along a triple junction.* Physical Review B, 2009. **79**(17): p. 174110.

164. Portavoce A., Chow L. and Bernardini J., *Triple-junction contribution to diffusion in nanocrystalline Si.* Applied Physics Letters, 2010. **96**(21): p. 214102.

165. Chellali M. R., Balogh Z. and Schmitz G., *Nano-analysis of grain boundary and triple junction transport in nanocrystalline Ni/Cu.* Ultramicroscopy, 2013. **132**: p. 164-170.

166. Wegner M., Leuthold J., Peterlechner M., Song X., Divinski S.V. and Wilde G., *Grain boundary and triple junction diffusion in nanocrystalline copper.* Journal of Applied Physics, 2014. **116**(9): p. 093514.

167. Morris D.G. and Harries D.R., *Wedge crack nucleation in Type 316 stainless steel.* Journal of Materials Science, 1977. **12**(8): p. 1587-1597.

168. Sorbello F., Hughes G.M., Lejček P., Heard P.J and Flewitt, P.E.J., *Preparation of location-specific thin foils from Fe–3% Si bi- and tri-crystals for examination in a FEG-STEM.* Ultramicroscopy, 2009. **109**(2): p. 147-153.

169. Miyazawa N., Suzuki S., Mabuchi M. and Chino Y., *An atomistic study of Y segregation at a {101¯1}–{101¯2} double twin in Mg.* AIP Advances, 2017. **7**(3): p. 035308.

170. Simonen E.P. and Bruemmer S.M., *Cr-Vacancy Elastic and Chemical Interactions in Irradiated Stainless Steels.* MRS Proceedings, 2011. **540**: p. 501.

171. Karakostas T., Bleris G.L. and Antonopoulos J.G., *Grain boundary analysis in TEM III. Determination of conditions for csl and application in copper.* physica status solidi (a), 1979. **55**(2): p. 801-809.

172. Liu Q., *A simple and rapid method for determining orientations and misorientations of crystalline specimens in TEM.* Ultramicroscopy, 1995. **60**(1): p. 81-89.

173. Liu Q., *A simple method for determining orientation and misorientation of the cubic crystal specimen.* Journal of applied crystallography, 1994. **27**(5): p. 755-761.

174. Liu Q., Huang X.X., and Yu M., *New method for determining grain boundary parameters.* Ultramicroscopy, 1992. **41**(4): p. 317-321.

175. Bunge H.J., *Texture Analysis in Materials Science* 1982, London: Butterworth and Co.

176. Kempshall B.W., Prenitzer B.I., and Giannuzzi L.A., *Grain boundary segregation: equilibrium and non-equilibrium conditions.* Scripta Materialia, 2002. **47**(7): p. 447-451.

177. Goodwin C.C., *The mathematical modelling of grain boundary segregation in austenitic alloys*. 1998, Loughborough University.

178. Zhang X.F., *In-situ transmission electron microscopy*, in *In-situ Materials Characterization: Across Spatial and Temporal Scales*, A. Ziegler, et al., Editors. 2014, Springer Berlin Heidelberg: Berlin, Heidelberg. p. 59-109.

179. Duh T.S., Kai J.J., Chen F.R. and Wang L.H., *Effects of grain boundary misorientation on the solute segregation in austenitic stainless steels.* Journal of Nuclear Materials, 1998. **258–263**: p. 2064-2068.

180. Yin K.M., King A.H., Hsieh T.E Chen, F.R., Kai J.J. and Chang L., *Segregation of bismuth to triple junctions in copper.* Microscopy and Microanalysis, 1997. **3**(5): p. 417-422.

181. Zheng L., Chellali M.R., Schlesiger R., Meng Y., Baither D. and Schmitz G., *Non-equilibrium grain-boundary segregation of Bi in binary Ni(Bi) alloy.* Scripta Materialia, 2013. **68**(10): p. 825-828.

182. Herbig M., Raab D., Li, Y.J., Choi P., Zaefferer S. and Goto S., *Atomic-scale quantification of grain boundary segregation in nanocrystalline material.* Physical Review Letters, 2014. **112**(12): p. 126103.

183. Chellali M.R., Zheng L., Schlesiger R., Bakhti B., Hamou A., Janove J. and Schmitz G., *Grain boundary segregation in binary nickel–bismuth alloy.* Acta Materialia, 2016. **103**: p. 754-760.

184. Karkin I.N., Karkina L.E., Kuznetsov A.R., Petrik M.V., Gornostyrev Y.N. and Korzhavyi P.A., *Segregation of Mg to generic tilt grain boundaries in Al: Monte Carlo modeling.* Materials Physics and Mechanics, 2015. **24**(3): p. 201-210.

185. Adlakha I. and Solanki K.N., *Structural stability and energetics of grain boundary triple junctions in face centered cubic materials.* Scientific Reports, 2015. **5**: p. 8692.

186. Purohit Y., Sun L., Irving D.L., Scattergood R.O. and Brenner D.W., *Computational study of the impurity induced reduction of grain boundary energies in nano- and bi-crystalline Al–Pb alloys.* Materials Science and Engineering: A, 2010. **527**(7): p. 1769-1775.

187. Uberuaga B.P., Vernon L.J., Martinez E. and Voter A.F., *The relationship between grain boundary structure, defect mobility, and grain boundary sink efficiency.* Scientific Reports, 2015. **5**: p. 9095.

188. Murzaev R.T. and Nazarov A.A., *Activation energy for vacancy migration in [001] tilt boundaries in nickel.* The Physics of Metals and Metallography, 2006. **101**(1): p. 86-92.

189. Shekhar S. and King A.H., *Strain fields and energies of grain boundary triple junctions.* Acta Materialia, 2008. **56**(19): p. 5728-5736.

190. Shinoda T. and Nakamura T., *The effects of applied stress on the intergranular phosphorus segregation in a chromium steel.* Acta Metallurgica, 1981. **29**(9): p. 1631-1636.

191. Song S.H., Wu J., Wang D.Y., Weng L.Q. and Zheng L., *Stress-induced non-equilibrium grain boundary segregation of phosphorus in a Cr–Mo low alloy steel.* Materials Science and Engineering: A, 2006. **430**(1): p. 320-325.

192. Medina S.F. and Mancilla J.E., *Influence of alloying elements in solution on static recrystallization kinetics of hot deformed steels.* ISIJ International, 1996. **36**(8): p. 1063-1069.

193. Chen D., Gao F., Hu W.Y., Hu S.Y., Terentyev D., Sun X., Heinisch H.L., Henager C.H., and Khaleel M.A., *Migration of Cr-vacancy clusters and interstitial Cr in α-Fe using the dimer method.* Physical Review B, 2010. **81**(6): p. 064101.

194. Li Y.J., Ponge D., Choi P. and Raabe D., *Segregation of boron at prior austenite grain boundaries in a quenched martensitic steel studied by atom probe tomography.* Scripta Materialia, 2015. **96**: p. 13-16.

195. Li Y.J., Ponge D., Choi P. and Raabe D., *Atomic scale investigation of non-equilibrium segregation of boron in a quenched Mo-free martensitic steel.* Ultramicroscopy, 2015. **159**: p. 240-247.

196. Tucker J., Allen T. and Morgan D., *Ab initio defect properties for modeling radiation-induced segregation in Fe-Ni-Cr alloys*, in *13th International conference on*

environmental degradation of materials in nuclear power systems. 2007, Canadian Nuclear Society: Canada.

197. Tucker J.D., Najafabadi R., Allen T.R. and Morgan D., *Ab initio-based diffusion theory and tracer diffusion in Ni–Cr and Ni–Fe alloys.* Journal of Nuclear Materials, 2010. **405**(3): p. 216-234.

198. Tucker J.D., *Solute-Vacancy Interactions in Nickel.* MRS Proceedings, 2014. **1645**.

199. Li H., Xia S., Liu W.Q., Liu T.G. and Zhou B.X., *Atomic scale study of grain boundary segregation before carbide nucleation in Ni–Cr–Fe Alloys.* Journal of Nuclear Materials, 2013. **439**(1): p. 57-64.

200. Li H., Xia S., Zhou, B.X. and Liu, W.Q., *C–Cr segregation at grain boundary before the carbide nucleation in Alloy 690.* Materials Characterization, 2012. **66**(0): p. 68-74.

201. Tytko D., Choi P.P., Klöwer J., Kostka A., Inden G. and Raabe D., *Microstructural evolution of a Ni-based superalloy (617B) at 700°C studied by electron microscopy and atom probe tomography.* Acta Materialia, 2012. **60**(4): p. 1731-1740.

202. Briant C.L., *Grain boundary segregation in the Ni-base alloy 182.* Metallurgical Transactions A, 1988. **19**(1): p. 137-143.

203. Zhang X., Ren C.L., Han H., Ye X.X., Kuo E., Wang C.B., Zhang W., Jiang L., Lumpkin G., Huai P. and Zhu Z.Y., *Theoretical study of the substitutional solute effect on the interstitial carbon in nickel-based alloy.* RSC Advances, 2017. **7**(33): p. 20567-20573.

204. Dumbill S., Boothby R.M. and Williams T.M., *Grain boundary segregation in Nimonic PE16.* Materials Science and Technology, 1991. **7**(5): p. 385-390.

205. Thuvander M., Miller M.K. and Stiller K., *Grain boundary segregation during heat treatment at 600°C in a model Alloy 600.* Materials Science and Engineering: A, 1999. **270**(1): p. 38-43.

206. Baik S.I., Olszta M.J., Bruemmer S.M. and Seidman D.N., *Grain-boundary structure and segregation behavior in a nickel-base stainless alloy.* Scripta Materialia, 2012. **66**(10): p. 809-812.

207. Benhadad S., Richards N.L. and Chaturvedi M.C., *The influence of minor elements on the weldability of an INCONEL 718-type superalloy.* Metallurgical and Materials Transactions A, 2002. **33**(7): p. 2005-2017.

208. Ojo O.A. and Zhang H.R., *Analytical electron microscopy study of boron-rich grain boundary microconstituent in directionally solidified Rene 80 superalloy.* Metallurgical and Materials Transactions A, 2008. **39**(12): p. 2799-2803.

209. Misra R.D.K., Balasubramanian T.V. and Rao P.R., *On interactions amongst trace and alloying elements at the grain boundaries of a low alloy steel.* Acta Metallurgica, 1987. **35**(12): p. 2995-3000.

210. Misra R.D.K., *Grain boundary segregation and fracture resistance of engineering steels.* Surface and Interface Analysis, 2001. **31**(7): p. 509-521.

211. Dumoulin P. and Guttmann M., *The influence of chemical interactions between metallic and metalloid solutes on their segregation in α-Fe I: Co-segregation at free surface studied by Auger electron spectroscopy.* Materials Science and Engineering, 1980. **42**: p. 249-263.

212. Woodward J. and Burstein G.T., *Surface segregation in a 3Cr-0.5Mo steel.* Metal Science, 1980. **14**(11): p. 529-533.

213. Greeff A.P., Louw C.W., Terblans J.J and Swart, H.C., *The influence of sulphur segregation on the oxidation of industrial FeCrMo steel.* Corrosion Science, 2000. **42**(6): p. 991-1004.

214. Burton J.J., Berkowitz B.J. and Kane R.D., *Surface segregation in an engineering alloy: Hastelloy C-276.* Metallurgical Transactions A, 1979. **10**(6): p. 677-682.

215. Ding R.G. and Knott J.F., *Grain boundary segregation of phosphorus and molybdenum in 2.25Cr-1Mo steel.* Materials Science and Technology, 2008. **24**(10): p. 1189-1194.

216. Bowen A.W. and Leak G.M., *Diffusion in Bcc iron base alloys.* Metallurgical Transactions, 1970. **1**(10): p. 2767-2773.

217. Braun R. and Feller-Kniepmeier M., *Diffusion of chromium in α-iron.* Physica Status Solidi (a), 1985. **90**(2): p. 553-561.

218. Ding R.G., *Grain boundary segregation in Ni-base (718 plus) superalloy.* Materials Science and Technology, 2010. **26**(1): p. 36-40.

219. Ping D.H., Gu Y.F., Cui C.Y. and Harada H., *Grain boundary segregation in a Ni-Fe-based (Alloy 718) superalloy.* Materials Science and Engineering: A, 2007. **456**(1-2): p. 99-102.

220. Lee C.G., Iijima Y., Hiratani T. and Hirano K.I., *Diffusion of chromium in α-iron.* Materials Transactions, JIM, 1990. **31**(4): p. 255-261.

221. Guttmann M., Dumoulin P. and Wayman M., *The thermodynamics of interactive co-segregation of phosphorus and alloying elements in iron and temper-brittle steels.* Metallurgical Transactions A, 1982. **13**(10): p. 1693-1711.

222. Gorbatov O.I., Korzhavyi P.A., Ruban A.V., Johansson B. and Gornostyrev Y.N., *Vacancy–solute interactions in ferromagnetic and paramagnetic bcc iron: Ab initio calculations.* Journal of Nuclear Materials, 2011. **419**(1): p. 248-255.

223. Olsson P., Klaver T.P.C. and Domain C., *Ab initio study of solute transition-metal interactions with point defects in bcc Fe.* Physical Review B, 2010. **81**(5): p. 054102.

224. Sergej S., Jutta R. and Ralf D., *Vacancy mobility and interaction with transition metal solutes in Ni.* Journal of Physics: Condensed Matter, 2014. **26**(48): p. 485014.

225. Karlsson L. and Norden H., *Grain boundary segregation of boron: An experimental and theoretical study.* J. Phys. Colloques, 1986. **47**(C7): p. 257-262.

226. Takahashi J., Ishikawa K., Kawakami K., Fujioka M. and Kubota N., *Atomic-scale study on segregation behavior at austenite grain boundaries in boron- and molybdenum-added steels.* Acta Materialia, 2017. **133**: p. 41-54.

227. Karlsson L., Nordén H. and Odelius H., *Overview no. 63 Non-equilibrium grain boundary segregation of boron in austenitic stainless steel—I. Large scale segregation behaviour.* Acta Metallurgica, 1988. **36**(1): p. 1-12.

228. Blavette D., Letellier L., Duval P. and Guttmann M., *Atomic-scale investigation of grain boundary segregation in Astroloy with a three dimensional atom-probe.* Materials Science Forum, 1996. **207-209**: p. 79-92.

229. Miller M.K., Anderson I.M., Pike L.M. and Klarstrom D.L., *Microstructural characterization of Haynes® 242™ alloy.* Materials Science and Engineering: A, 2002. **327**(1): p. 89-93.

230. Song S.H., Yuan Z.X., Shen D.D., Liu J. and Weng L.Q., *Grain boundary segregation of phosphorus and molybdenum in a Cr – Mo low alloy steel.* Materials Science and Technology, 2004. **20**(1): p. 117-120.

231. Viljoen E.C. and Uebing C., *Effect of nitrogen and sulphur on the segregation of molybdenum on single crystalline Fe–3.5%Mo–N,S alloys.* Surface Science, 1998. **410**(1): p. 123-131.

232. Jordaan W.A., Terblans J.J. and Swart H.C., *The effect of nitrogen on the co-segregation with molybdenum in a Fe-3.5wt%Mo-N(100) single crystal.* South African Journal of Science, 2008. **104**: p. 393-397.

233. Karunaratne M.S.A. and Reed R.C., *Interdiffusion of niobium and molybdenum in nickel between 900 -1300 °C.* Defect and Diffusion Forum, 2005. **237-240**: p. 420-425.

234. Lindwall G. and Frisk K., *Assessment and evaluation of mobilities for diffusion in the bcc Cr-Mo-Fe system.* Journal of Phase Equilibria and Diffusion, 2012. **33**(5): p. 375-389.

235. Versteylen C.D., van Dijk N.H. and Sluiter M.H.F., *First-principles analysis of solute diffusion in dilute bcc Fe-X alloys.* Physical Review B, 2017. **96**(9): p. 094105.

236. Ševc P., Janovec J., Koutník M. and Výrostková A., *Equilibrium grain boundary segregation of phosphorus in 2.6Cr-0.7Mo-0.3V steels.* Acta Metallurgica et Materialia, 1995. **43**(1): p. 251-258.

237. Ševc P., Janovec J. and Katana V., *On kinetics of phosphorus segregation in Cr-Mo-V low alloy steel.* Scripta Metallurgica et Materialia, 1994. **31**(12): p. 1673-1678.

238. Menyhard M. and McMahon C.J., *On the effect of molybdenum in the embrittlement of phosphorus-doped iron.* Acta Metallurgica, 1989. **37**(8): p. 2287-2295.

239. Zacherl C.L., *A computational investigation of the effect of alloying elements on the thermodynamic and diffusion properties of fcc Ni alloys, with application to the creep rate of dilute Ni-X alloys*. 2012, The Pennsylvania State University.

240. Hargather C.Z., Shang S.L., and Liu Z.K., *A comprehensive first-principles study of solute elements in dilute Ni alloys: Diffusion coefficients and their implications to tailor creep rate.* Acta Materialia, 2018. **157**: p. 126-141.

241. Sprung I.R. and Olen K.R., *Temper embrittlement response and toughness of a rare earth treated Ni-Cr-Mo steel.* Metallurgical Transactions, 1972. **3**(11): p. 2939-2941.

242. Low J., Stein D., Turkalo A. and Laforce R., *Alloy and impurity effects on temper brittleness of steel.* Trans Met Soc AIME, 1968. **242**(1): p. 14-24.

243. Kubaschewski O. and Catterall J.A., *Thermodynamics of Alloys*. 1956: Oxford.

244. Bennett L.H. and Watson R.E., *A database for enthalpies of formation of binary transition metal alloys.* Calphad, 1981. **5**(1): p. 19-23.

245. Whalen T.J., Kaufman S.M. and Humenik M., Trans. ASM, 1962. **55**: p. 778-85.

246. Do K.H., Nam H.S., Jang J.M., Kim D.S. and Pak J.J., *Thermodynamic interaction between chromium and phosphorus in high Cr containing liquid iron.* ISIJ International, 2017. **57**(8): p. 1334-1339.

247. Takiguchi S.I. and Sano N., *Phosphorus distribution between Fe-Cr-C melts and CaO bearing fluxes.* Tetsu-to-Hagané, 1988. **74**(5): p. 809-815.

248. Kanzaki Y., Tsukihashi F. and Sano N., *The solubility of $CaO\cdot Cr_2O_3$ in the CaO-CaF_2 system associated with dephosphorization of Fe-Cr-C melts.* Tetsu-to-Hagané, 1994. **80**(1): p. 13-17.

249. Hara T., Tsukihashi F. and Sano N., *Phosphorus partition between Fe-Cr-C melts and BaO-BaF_2 fluxes and the activity of BaO.* Tetsu-to-Hagané, 1990. **76**(3): p. 352-359.

250. Dalaker H., *Thermodynamic computations of the interaction coefficients between boron and phosphorus and common impurity elements in liquid silicon.* Computer Methods in Materials Science, 2013. **13**(1-3): p. 407-411.

251. Guttmann M., *Interfacial segregation in multicomponent systems*, in *Atomistics of Fracture*, R.M. Latanision and J.R. Pickens, Editors. 1983, Springer US: Boston, MA. p. 465-494.

252. Ustinovshikov Y.I., *Effects of alloying elements, impurities, and carbon on temper embrittlement of steels.* Metal Science, 1984. **18**(12): p. 545-548.

253. Janovec J., Výrostková A., Ševc P. and Lejček P., *Phosphorus grain boundary segregation in polycrystalline low alloy steels.* J Surf Anal 1999. **5**(2): p. 294-297.

254. Guillou R., Guttmann M. and Dumoulin P., *Role of molybdenum in phosphorus-induced temper embrittlement of 12%Cr martensitic stainless steel.* Metal Science, 1981. **15**(2): p. 63-72.

255. Nakamura T., Shinoda T. and Watanabe H., *Grain boundary segregation of phosphorus in 2.25 wt.% chromium steels with variations in molybdenum and carbon contents.* Trans. Iron Steel Inst. Jpn., 1979. **19**(6): p. 365-373.

256. Schlesinger M.E., *The thermodynamic properties of phosphorus and solid binary phosphides.* Chemical Reviews, 2002. **102**(11): p. 4267-4302.

257. Guttmann M., *The link between equilibrium segregation and precipitation in ternary solutions exhibiting temper embrittlement.* Metal Science, 1976. **10**(10): p. 337-341.

258. Pankratz L.B., *Thermodynamic properties of carbides, nitrides, and other selected substances*. 1995: United States Department of the Interior, Bureau of Mines.

259. Guttmann M., *Thermochemical interactions versus site competition in grain boundary segregation and embrittlement in multicomponent systems.* Journal de Physique IV Colloque, 1995. **05**(C7): p. C7-85-C7-96.

260. Jones R.B., Lu Z., Flewitt P.E.J., and Faulkner, R. G, *Grain boundary impurity segregation and neutron irradiation effects in ferritic alloys.* Philosophical Magazine, 2005. **85** (19): p. 2065-2099.

261. Suzuki S., Tanii S., Abiko K. and Kimura H., *Site competition between sulfur and carbon at grain boundaries and their effects on the grain boundary cohesion in iron.* Metallurgical Transactions A, 1991. **18**(6): p. 1109-1115.

262. Abel K.A., Boyer J.C., Andrei C.M. and van Veggel F.C.J.M., *Analysis of the shell thickness distribution on $NaYF_4/NaGdF_4$ core/shell nanocrystals by EELS and EDS.* The Journal of Physical Chemistry Letters, 2011. **2**(3): p. 185-189.

263. Doig P., Lonsdale D. and Flewitt P.E.J., *X-Ray microanalysis of grain boundary segregations in steels using the scanning transmission electron microscope.* Metallurgical Transactions A, 1981. **12**(7): p. 1277-1282.

264. Doig P. and Flewitt P.E.J., *STEM-EDS X-ray microanalysis of grain boundary segregations: The influence of electron probe size and grain boundary orientation.* Micron and Microscopica Acta, 1983. **14**(3): p. 225-231.

265. Jones I.P. and Loretto M.H., *Some aspects of quantitative STEM X-ray microanalysis.* Journal of Microscopy, 1981. **124**(1): p. 3-13.

266. Goldstein J., Costley J.L., Lorimer G. and Reed S.J.B., *Quantitative X-ray microanalysis in the electron microscope*, in *Scanning Electron Microscopy*, O. Johari, Editor. 1977.

267. Reed S., *The single-scattering model and spatial resolution in X-ray analysis of thin foils.* Ultramicroscopy, 1982. **7**(4): p. 405-409.

268. Goldstein J.I., *Principles of Thin Film X-Ray Microanalysis*, in *Introduction to Analytical Electron Microscopy*, J.J. Hren, J.I. Goldstein, and D.C. Joy, Editors. 1979, Springer US: Boston, MA. p. 83-120.

269. Hutchings R., Loretto M.H., Jone, I.P. and Smallman R.E., *Spatial resolution in x-ray microanalysis of thin foils in stem.* Ultramicroscopy, 1978. **3**: p. 401-405.

270. Keast V.J. and Williams D.B., *Quantitative compositional mapping of Bi segregation to grain boundaries in Cu.* Acta Materialia, 1999. **47**(15–16): p. 3999-4008.

271. Watanabe M., Ackland D.W., Burrows A., Kiely C.J., Williams D.B., Krivanek O.L., Dellby N., Murfitt M.F. and Szilagyi Z., *Improvements in the X-Ray analytical capabilities of a scanning transmission electron microscope by spherical-aberration correction.* Microscopy and Microanalysis, 2006. **12**(06): p. 515-526.

272. Watanabe M. and Williams D.B., *Atomic-level detection by X-ray microanalysis in the analytical electron microscope.* Ultramicroscopy, 1999. **78**(1–4): p. 89-101.

273. Nakata K., Okada O. and Ueki Y., *Measurement of electron beam broadening in stainless steels during EDS analysis in the FEG-TEM.* Journal of Electron Microscopy, 2001. **50**(2): p. 89-96.

274. O'Neill J.P., Ross I.M., Cullis A.G., Wang T. and Parbrook P.J., *Electron-beam-induced segregation in InGaN/GaN multiple-quantum wells.* Applied Physics Letters, 2003. **83**(10): p. 1965.

275. Lai W., Barashev A. and Bacon D., *Multiscale modeling of surface sputtering in a scanning transmission electron microscope.* Physical Review B, 2004. **70**(19).

276. Tang B.B., Jones I.P., Lai W.S. and Bacon D.J., *Sputtering-induced nanometre hole formation in Ni3Al under intense electron beam irradiation.* Philosophical Magazine, 2005. **85**(17): p. 1805-1817.

277. Bradley C., *Calculations of atomic sputtering and displacement cross-sections in solid elements by electrons with energies from threshold to 1.5 MV*. 1988, Argonne National Lab., IL (USA).

278. Lorimer G., *Quantitative X-ray microanalysis of thin specimens in the transmission electron microscope; a review.* Mineralogical Magazine, 1987. **51**(359): p. 49-60.

279. Thomas G., Fulrath R.M. and Fisher R.M., *Electron microscopy and structure of materials: Proceedings*. 1972: University of California Press.

280. Jiang N., *Electron beam damage in oxides: a review.* Rep Prog Phys, 2016. **79**(1): p. 016501.

281. Merli P.G. and Morandi V., *Low-energy STEM of multilayers and dopant profiles.* Microscopy and Microanalysis, 2005. **11**(1): p. 97-104.

282. Trimby P.W., *Orientation mapping of nanostructured materials using transmission Kikuchi diffraction in the scanning electron microscope.* Ultramicroscopy, 2012. **120**: p. 16-24.

283. Egerton R.F., *Electron energy-loss spectroscopy in the electron microscope*. 1996: Plenum Press.

284. Mac Gillavry v.C.H., *Zur prüfung der dynamischen theorie der elektronenbeugung am kristallgitter.* Physica, 1940. **7**(4): p. 329-343.

285. Allen S.M. and Hall E.L., *Foil thickness measurements from convergent-beam diffraction patterns An experimental assessment of errors.* Philosophical Magazine A, 1982. **46**(2): p. 243-253.

286. Spence J.C.H. and Zuo J.M., *Electron microdiffraction*. 1992: Plenum Press.

287. Joy D.C., *Monte Carlo modeling for electron microscopy and microanalysis*. 1995: Oxford University Press.

288. Demers H., Poirier-Demers N., de Jonge N. and Drouin D., *Three-dimensional electron microscopy simulation with the CASINO Monte Carlo software.* Microscopy and Microanalysis, 2017. **17**(S2): p. 612-613.

289. Valkealahti S. and Nieminen R.M., *Monte Carlo calculations of keV electron and positron slowing down in solids. II.* Applied Physics A, 1984. **35**(1): p. 51-59.

290. Joy D.C. and Luo S., *An empirical stopping power relationship for low-energy electrons.* Scanning, 1989. **11**(4): p. 176-180.

291. Lowney J.R., *MONSEL-II: Monte Carlo simulation of SEM signals for linewidth metrology*. Microbeam Analysis, 1995. **4**(3): p. 131-136.

292. Salvat F., Jablonski A. and Powell C.J., *ELSEPA—Dirac partial-wave calculation of elastic scattering of electrons and positrons by atoms, positive ions and molecules.* Computer Physics Communications, 2005. **165**(2): p. 157-190.

293. Hunger H.J. and Küchler L., *Measurements of the electron backscattering coefficient for quantitative EPMA in the energy range of 4 to 40 keV.* physica status solidi (a), 1979. **56**(1): p. K45-K48.

294. Everhart T.E., *Simple theory concerning the reflection of electrons from solids.* Journal of Applied Physics, 1960. **31**(8): p. 1483-1490.

295. Niedrig H., *Electron backscattering from thin films.* Journal of Applied Physics, 1982. **53**(4): p. R15-R49.

296. Nakhodkin N.G., Ostroukhov A.A. and Romanovskii V.A., *Electron inelastic scattering in thin films.* Soviet Phys.-Solid State, 1962. **4**: p. 1112-1119.

297. Kanaya K. and Okayama S., *Penetration and energy-loss theory of electrons in solid targets.* Journal of Physics D: Applied Physics, 1972. **5**(1): p. 43.

298. Joy D.C., *A database on electron-solid interactions.* Scanning, 1995. **17**(5): p. 270-275.

299. Baroody E.M., *A theory of secondary electron emission from metals.* Physical Review, 1950. **78**(6): p. 780-787.

300. Sommerfeld A., *Zur Elektronentheorie der Metalle auf Grund der Fermischen Statistik.* Zeitschrift für Physik, 1928. **47**(1): p. 1-32.

301. Seiler H., *Secondary electron emission in the scanning electron microscope.* Journal of Applied Physics, 1983. **54**(11): p. R1-R18.

302. Dionne G.F., *Origin of secondary-electron-emission yield-curve parameters.* Journal of Applied Physics, 1975. **46**(8): p. 3347-3351.

303. Lin Y. and Joy D.C., *A new examination of secondary electron yield data.* Surface and Interface Analysis, 2005. **37**(11): p. 895-900.

304. Kanaya K. and Kawakatsu H., *Secondary electron emission due to primary and backscattered electrons.* Journal of Physics D: Applied Physics, 1972. **5**(9): p. 1727.

305. Joy D.C., *Monte Carlo studies of high resolution imaging*, in *Microbeam Analysis*. 1984, San Francisco Press: Pennsylvania. p. 81.

306. Kanter H., *Contribution of backscattered electrons to secondary electron formation.* Physical Review, 1961. **121**(3): p. 681-684.

307. Drescher H., *Ruckstreukoeffizient und Sekundarelektronen-Ausbeute von 10-100 keV-Elektronen und Beziehungen zur Raster-Elektronenmikroskopie*. Z. angew. Physik, 1970. **29**: p. 331-336.

308. Shimizu R., *Secondary electron yield with primary electron beam of kilo-electron-volts.* Journal of Applied Physics, 1974. **45**(5): p. 2107-2111.

309. Reimer L. and Drescher H., *Secondary electron emission of 10-100 keV electrons from transparent films of Al and Au.* Journal of Physics D: Applied Physics, 1977. **10**(5): p. 805.

310. Bethe H., *Zur Theorie des Durchgangs schneller Korpuskularstrahlen durch Materie.* Annalen der Physik, 1930. **397**(3): p. 325-400.

311. Berger M. and Seltzer S., *10. Tables of energy-losses and ranges of electrons and positrons*, in *Studies in penetration of charged particles in matter*. 1964, National Academy of Sciences-National Research Council: Washington. p. 205.

312. Tung C.J., Ashley J.C. and Ritchie R.H., *Electron inelastic mean free paths and energy losses in solids II: Electron gas statistical model.* Surface Science, 1979. **81**(2): p. 427-439.

313. Fitting H.J., *Transmission, energy distribution, and SE excitation of fast electrons in thin solid films.* physica status solidi (a), 1974. **26**(2): p. 525-535.

314. Makhov A.F., *Sur la pénétration des électrons dans les corps solides.* Sov. Phys.-Solid State, 1960. **2**: p. 1934-1951.

315. Cosslett V.E. and Thomas R.N., *Multiple scattering of 5-30 keV electrons in evaporated metal films: I. Total transmission and angular distribution.* British Journal of Applied Physics, 1964. **15**(8): p. 883.

316. Haimovich J., Leibold K. and Staudt G., *Estimating and measuring thickness of thin layers by Monte Carlo simulation and backscattered electron image analysis.* AMP J. Techn, 1996. **5**: p. 65-78.